UNIVERSITY OF OKLAHOMA

GRADUATE COLLEGE

Measurement of the top quark pair production cross section with a tau lepton in the final state at $\sqrt{s} = 8$ TeV

A DISSERTATION

SUBMITTED TO THE GRADUATE FACULTY

in partial fulfillment of the requirements for the

Degree of

DOCTOR OF PHILOSOPHY

By

AHMED HASIB
Norman, Oklahoma
2016

Measurement of the top quark pair production cross section with a tau lepton in the final state at $\sqrt{s} = 8$ TeV

A DISSERTATION APPROVED FOR THE
DEPARTMENT OF PHYSICS AND ASTRONOMY

BY

Dr. Phillip Gutierrez, Chair

Dr. Braden Abbott

Dr. Ronald Kantowski

Dr. Chung Kao

Dr. James Hawthorne

Table of Contents

Abstract

This dissertation presents the measurement of the inclusive cross section of the top quark pair production in the final state of a tau lepton with associated jets. The dataset used in this measurement is collected by the ATLAS detector from proton-proton collisions during the 2012 operation of the Large Hadron Collider at the center-of-mass energy, $\sqrt{s} = 8$ TeV. This dataset corresponds to an integrated luminosity of 20.2 fb^{-1}. The inclusive $t\bar{t}$ production cross section, $\sigma_{t\bar{t}}$ is found to be $\sigma_{t\bar{t}} = 231 \pm 3(\text{stat.})^{+25}_{-25}(\text{syst.}) \pm 3(\text{lumi.})$ pb for a top quark mass of 172.5 GeV. This result is consistent with the theoretical prediction $\sigma^{\text{SM}}_{t\bar{t}} = 253^{+13}_{-15}$ pb. Statistical analysis is performed to set a model independent upper limit on the visible cross section of any non Standard Model processess following frequentist probability. An upper limit on the branching ratio of the flavor changing neutral Higgs decay of the top quark to a charm quark is also calculated. The observed (expected) limit on the branching ratio at 95% CL is BR($t \to ch^0$) $< 10\%$ (15%).

CHAPTER 1

Introduction

The Standard Model (SM) of particle physics is a quantum field theory that explains the behavior of the elementary particles and the fundamental forces that govern their interactions. The SM was developed in the 1960s from experimental research efforts that have probed interactions at successively higher energies. Thus far, the SM, which encompasses all our current understanding of particle physics, has been incredibly successful as a descriptive and predictive theory. Notably, the prediction and subsequent discovery of the Higgs boson. However, the SM, is a low energy approximation of a more fundamental theory of nature and is only valid up to a certain energy scale (TeV scale). The framework of the SM does not include gravity and cannot unify the strong interaction with the electroweak interaction. Furthermore, it cannot explain the hierarchy problem [1]. Only visible matter, which makes up 5% of the universe, can be explained by the SM.

The Large Hadron Collider (LHC) at the European Organization of Nuclear

Research (CERN) is currently the world's highest energy particle collider. The LHC provides a new energy regime, where the SM has never been tested and is expected to unveil its problems. A promising avenue to test the SM are the final states in the decay of the heaviest elementary particle, the top quark, which was first discovered at the Tevatron [2, 3]. The top quark has a lifetime smaller than the hadronization time and provides a unique opportunity to explore the interactions of a *bare* quark at the TeV-scale. Due to its high mass, the top quark is also an excellent probe of the mechanism that breaks the electroweak symmetry [4]. Furthermore, since all properties of the top quark, with the exception of its mass, are predicted by the SM, by measuring all of its properties, including all possible decays, one can search for deviations from SM predications to discover new physics or consistency with the SM to set limits on possible extensions.

In this dissertation, a measurement of the inclusive $pp \to t\bar{t}$ production cross section at the center-of-mass energy ($\sqrt{s}$) of 8 TeV is presented with data collected by the ATLAS experiment. The cross section is measured using the decay mode where one top quark decays to a tau lepton with an associated neutrino, while the other decays to light quarks, in the final state: $t\bar{t} \to [Wb]\,[Wb] \to [\tau\nu_\tau b]\,[qqb]$.

The theoretical prediction, for inclusive $pp \to t\bar{t}$, at $\sqrt{s} = 8$ TeV is calculated to be 253^{+13}_{-15} pb [5–10]. In the ATLAS experiment, the cross section ($\sigma_{t\bar{t}}$) is measured at the center-of-mass energy of 8 TeV, in the single lepton final state of a electron or a muon, with $\sigma_{t\bar{t}} = 260 \pm 1(\text{stat.})^{+20}_{-21}(\text{syst.})$ pb [11] and in two leptons final state of a electron and a muon, with $\sigma_{t\bar{t}} = 242 \pm 1.7(\text{stat.}) \pm 9.3(\text{syst.})$ pb [12]. None of these analyses, however, consider decay modes with tau leptons. At $\sqrt{s} = 7$ TeV, the cross section in

the final state of one tau lepton is measured by both ATLAS and CMS experiments, with $\sigma_{t\bar{t}} = 194 \pm 18(\text{stat.}) \pm 46(\text{syst.})$ pb [13], and $\sigma_{t\bar{t}} = 152 \pm 2(\text{stat.}) \pm 32(\text{syst.})$ pb [14], respectively. Both measurements, although consistent with the SM prediction, have large systematic uncertainty. The analysis presented in this dissertation is the first measurement with a tau lepton in the final state, at $\sqrt{s} = 8$ TeV, and improves on the associated uncertainties compared to the previous measurements.

In the $t\bar{t} \to [\tau\nu_\tau b]\,[qqb]$ decay, the leptonic part of the top decay, $t \to \tau\nu_\tau b$ involves third generation fermions. Hence, this decay mode can be exploited to investigate the coupling of the third generation fermions in a single process. In the SM, the t quark branching ratio (BR) to a W boson and a b quark is $\approx 100\%$, and the final state is determined by the SM branching ratios of the W boson, which are very well measured. A combination of this measurement with other top quark final states can be used to extract an independent measurement of the relative BR. Furthermore, this decay mode involves the heaviest quark (t) and the heaviest lepton (τ), and the presence of a non-SM mass or flavor dependent coupling could change the decay rate of the top quark into final states with tau leptons. Therefore, any deviation in the BR of $t \to \tau\nu_\tau b$ from that predicted by the SM can be an indication of non-SM physics. The Type 2 two Higgs doublet model (2HDM) [15], an extension of the SM, can be taken as an example. In the 2HDM, the top quark can decay to a light charged Higgs boson ($H^\pm$) in association with a b-quark and if the ratio of the vacuum expectation values of the two-Higgs double ($\tan\beta$) is large, the $H^\pm$ would preferentially decay to $\tau\nu_\tau$. Therefore, the measured $\sigma(p\bar{p} \to t\bar{t}) \cdot \text{BR}(t\bar{t} \to \tau + \text{jets})$ would be larger compared to the SM prediction [16–18].

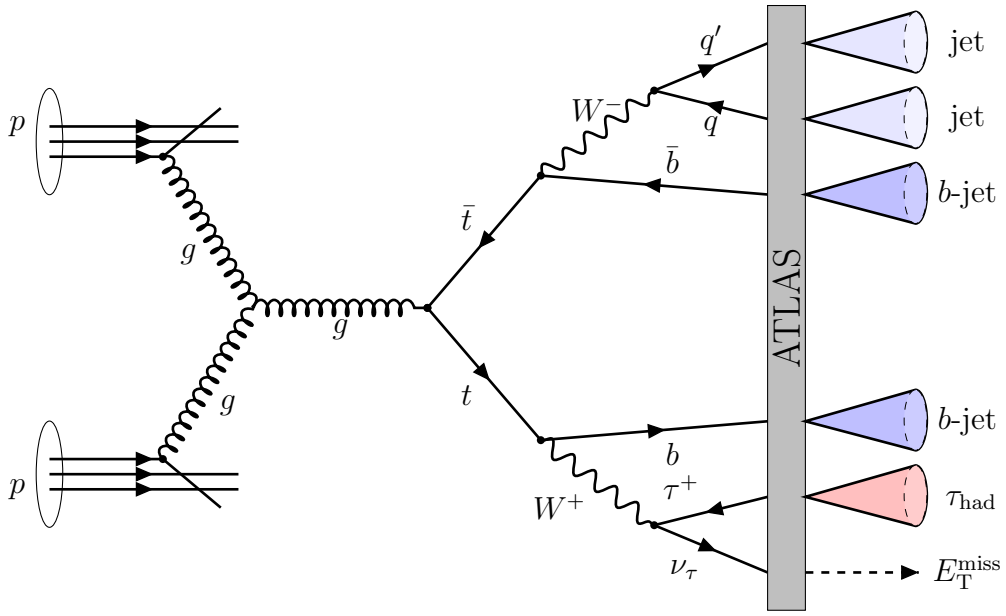

Figure 1.1: Feynman diagram for $t\bar{t}$ production through gg fusion and the decay products of interest along with the detector signature associated to each object.

The 2HDM can also produce an excess of $t \to \tau$ events if the restriction on flavor changing neutral couplings is lifted, which is allowed in "so called" type 3 models. For example, this would allow $t \to ch^0$ and if $h^0 \to \tau^+\tau^-$, an excess of $t \to \tau$ events would be observed relative to the SM, where the SM predicts $\text{BR}(t \to ch^0) \approx 10^{-15}$ [19]. Therefore, a deviation in the BR would be an indication of non-SM physics.

Figure 1.1 illustrates the various steps involved in the measurement of the top quark pair production cross section in the tau lepton final state. First, we need to understand the theoretical framework that describes the proton-proton collisions, the mechanism behind top quark pair production after these collisions and their subsequent decay. In order to interpret the results we also need to have a prediction from this theoretical framework that would allow us to investigate any discrepancy. In Chapter 2 a brief overview of this theoretical framework (i.e. the SM of particle

physics) is outlined. The phenomenology of the proton-proton collision, production of the top quark pair and the various decay modes of the top quark are then discussed in the context of the SM. In addition, several exotic decay modes of the top quark especially the flavor changing neutral current interaction of the top quark in various beyond the SM scenarios are described. To perform this experiment, we need a particle collider capable of colliding two proton beams and a detector that would record these collisions. Chapter 3 describes such a collider, the LHC, and a detector, the ATLAS detector, which are the experimental apparatus used in this research. The output from the various subdetectors of ATLAS recording these collisions are then analyzed to identify the various final state particles that are produced. Chapter 4 discusses the detector signature associated with each of the final state particles and the process by which detector outputs are interpreted and classified as particles. With the information of the final state particles produced in the proton-proton collision we can then proceed to measure the top quark pair production cross section. Chapter 5 details how physics processes relevant to final state particles are classified and the method to extract the $t\bar{t}$ cross section. Chapter 6 discusses the statistical analyses performed to set upper limits on beyond the SM processes, in particular, upper limits on the branching ratio of flavor changing $t \to ch^0$ decay. Finally, Chapter 7 concludes this dissertation with a synopsis.

CHAPTER 2

Top Quark Physics

The measurement of the top quark pair production cross section, presented in this dissertation is compared with the theoretical prediction calculated in the context of the Standard Model. A theoretical overview of top quark physics related to this measurement is presented in this chapter from a phenomenological point of view. First, a overview of the Standard Model to describe the elementary particles and their interactions is described, followed by the production mechanism of top quark pairs. The subsequent decay of top quark in the context of Standard Model and beyond the Standard Model processes are also discussed.

2.1 Overview of the Standard Model

The Standard Model of particle physics [20–29], is a mathematical construct that combines quantum mechanics and special relativity to describe the elementary particles and their interactions. The elementary particles are grouped into two categories: fermions with spin $\frac{1}{2}$, obeying Fermi-Dirac statistics, and bosons with spin 1 characterized by Bose-Einstein statistics. The fermions can interact with

each other through three fundamental forces: electromagnetic, weak and strong. The bosons act as a force carrier or mediators between interacting fermions. The fourth fundamental force, the gravitational force is negligible at the distances these elementary particle interact and is not accommodated in the SM. Each fermion is represented by a massless fermion field and its interaction is described by the Lagrangian density, ($\mathcal{L}$). The Lagrangian is required to be invariant under the local transformation of fields in space-time, referred to as *gauge invariance*. Gauge invariance of the Lagrangian introduces fields that correspond to gauge bosons. The gauge boson that mediates electromagnetic interaction is based on the $U_{\text{EM}}(1)$ symmetry group and is described in a theory of quantum electrodynamics (QED). The weak interaction is based on the $SU(2)$ symmetry group. Finally, the strong interaction is represented by the $SU(3)$ symmetry group and formulated into a theory of quantum chromodynamics (QCD).

The SM Lagrangian for massless fermions and bosons can be written as,

$$\mathcal{L} = \bar{\psi}\left(i\gamma^{\mu}D_{\mu} - m\right)\psi \qquad \text{where,} \tag{2.1}$$

$$D_{\mu} = \partial_{\mu} - \underbrace{ig_1\frac{Y}{2}B_{\mu} - ig_2 t^i W_{\mu}^i}_{U_Y(1)\times SU_L(2)} - \underbrace{ig_3 T^a G_{\mu}^a}_{SU(3)}. \tag{2.2}$$

In equation 2.1, ψ represents the fermionic field and the term D_{μ}, is the covariant derivative associated to the SM. Each term of the covariant derivative shows the generator of the term's symmetry group (Y, t^i, T^a), the gauge field that mediate the particular interaction (B_{μ}, W_{μ}^i, G_{μ}^a) and the coupling constant associated to each interaction (g_i). Requiring gauge invariance of the Lagrangian, generates four

massless gauge bosons for $U_Y(1) \times SU_L(2)$ electroweak (EW) theory which are the linear combinations of the massless gauge fields, B_μ and W^i_μ $(i = 1, 2, 3)$. Similarly, for $SU(3)$ QCD, there are eight massless gauge bosons, gluons (g) which are linear combinations of gauge fields G^a_μ ($a = 1, ..., 8$).

The masses of weak gauge bosons are generated through the Brout-Englert-Higgs [30, 31] mechanism by introducing an additional term to the Lagrangian in equation 2.1 associated to a scalar field. This scalar field i.e. the Higgs field, breaks the $U_Y(1) \times SU_L(2)$ symmetry of the vacuum to $U_{\rm EM}(1)$ and $SU(2)$, by generating a non-zero vacuum expectation value, while keeping the Lagrangian invariant. The non-zero vacuum expectation value gives mass to three linear combinations of the B_μ and W^i_μ gauge fields, i.e. $W^\pm$ and Z^0 gauge bosons, responsible for weak interactions. While, the fourth linear combination of B_μ and W^i_μ gauge fields remain invariant with a massless gauge boson, the photon (γ), responsible for the electromagnetic interacton.

The Higgs field also couples to the fermions through the *Yukawa coupling*, g_f, which adds another term to the SM Lagrangian in equation 2.1 leading to non-zero fermion masses proportional to the Yukawa coupling and the vacuum expectation value.

In the SM, there are three generation of fermions with increasing mass in each generation. The fermions are grouped into two categories: leptons with integer charge (relative to the charge of the proton) and quarks with fractional charge (relative to the charge of the proton). Each fermion has its anti-particle counterpart with the same property but opposite charge. The properties of these leptons along

Particle	Generation	Charge (e)	Mass	Interactions
$e^{\pm}$	1	± 1	0.51 MeV	Electromagnetic, weak
ν_e	1	0	$<$2 eV	Weak
$\mu^{\pm}$	2	± 1	105.66 MeV	Electromagnetic, weak
ν_μ	2	0	$<$0.19 MeV	Weak
$\tau^{\pm}$	3	± 1	1.78 GeV	Electromagnetic, weak
ν_τ	3	0	$<$18.2 MeV	Weak

Table 2.1: Lepton and their properties in the Standard Model [32].

Particle	Generation	Charge (e)	Mass	Interactions
u	1	2/3	1.8 - 3.0 MeV	Strong, electromagnetic, weak
d	1	-1/3	4.5 - 5.3 MeV	Strong, electromagnetic, weak
c	2	2/3	1.27 GeV	Strong, electromagnetic, weak
s	2	-1/3	90 - 100 MeV	Strong, electromagnetic, weak
t	3	2/3	173.2 GeV	Strong, electromagnetic, weak
b	3	-1/3	4.18 GeV	Strong, electromagnetic, weak

Table 2.2: Quarks and their properties in the Standard Model. The quark masses are calculated using the $\overline{\text{MS}}$ factorization scheme, except the top quark mass, where the measured world average is quoted [32].

Gauge Boson	Interaction	Charge (e)	Isospin	Color	Mass
γ	Electromagnetic	0	0	–	$< 1 \times 10^{-18}$ eV
$W^{\pm}$	Weak	± 1	± 1	–	80.39$\pm$ 0.0012GeV
Z^0	Weak	0	0	–	91.19$\pm$0.0023 GeV
Gluon	Strong	0	0	8 combinations	0
H^0	–	0	–	–	125.09$\pm$0.24 GeV

Table 2.3: Gauge bosons of the Standard Model with their associated interactions, charges and masses. The Higgs boson of the SM is also included [32].

with their associated neutrinos are listed in Table 2.1. Similarly, the six quarks are also categorized into three generation with a "down-type" (charge $-\frac{1}{3}e$) and "up-type" (charge $+\frac{2}{3}e$) isospin doublet. The properties of these quarks are listed in Table 2.2. The weak eigenstates of the quarks are found to be different from their mass eigenstate. A unitary CKM matrix [33, 34] is used to transform the quark weak eigenstates to their mass eigenstates. The CKM matrix allows the mixing of the quarks only through their interaction with $W^{\pm}$ bosons. Since this interaction changes the flavor of the quark, this type of interaction is referred to as a *flavor changing charged current*. Note, in the SM at leading order the *flavor changing neutral current* interaction, i.e. flavor change through interaction with a Z^0 boson is forbidden.

The properties of the gauge bosons are outlined in Table 2.3. In QED, the electromagnetic interaction between two charged particles (carrying electric charge Q) is mediated by the massless and neutral photon, γ. Since the photon do not carry a electric charge, they do not couple with themselves. The quantum number for weak interaction is isospin. The weak gauge bosons interact with fermions which carry weak isospin of $\frac{1}{2}$. Since the $W^{\pm}$ boson carry isospin, they exhibit self-couplings.

In QCD, gluons mediate the strong interactions between quarks. The quantum number of strong interaction is called "color" which occurs in three types, *red*, *green* and *blue*, and the respective anti-colors. The eight flavor of gluons are linear combinations of each of these color charges. The ninth flavor is a "colorless" singlet and has never been observed experimentally. The quarks carry single color charge, however, no free particles with color charge have been observed experimentally and the quarks form colorless bound states. The possible configurations are the bound state of quark and anti-quark of same color charge ($|q_{r/g/b}\bar{q}_{\bar{r}/\bar{g}/\bar{b}}\rangle$), referred to as *mesons* and bound state of three quarks or anti-quarks with three different color charge ($|q_r q_g q_b\rangle$ or $|\bar{q}_{\bar{r}}\bar{q}_{\bar{g}}\bar{q}_{\bar{b}}\rangle$), referred to as *baryons*. The mesons and baryons are collectively referred to as *hadrons* and the process of formation of hadrons is called *hadronization*. An important aspect of colorless bound state, is *quark confinement*, i.e. quarks cannot appear as a free particle. As a consequence, when trying to separate quarks from one another, it becomes energetically preferable to create another pair of quarks with opposite color charge from the vacuum, which then creates a new bound state. When quarks are generated in high energy particle collisions, like at the LHC, they transform into a collimated shower of hadrons. The process is referred to as *parton shower* and the collimated cone of hadrons are called *jets*. The phenomenology of proton-proton collisions is discussed in Section 2.2.1. The top quark, however, is an exception. Due to its large mass, the top quark will decay before it can form a bound state.

In QCD, the coupling constant, $\alpha_s(\equiv \frac{g_3^2}{4\pi})$, that appears in the covariant derivative of the SM Lagrangian in equation 2.2 is dependent on momentum transfer (Q^2).

Hence, α_s is defined for an arbitrary momentum transfer scale, μ^2, to account for any divergences that can occur. For Q^2 larger than μ^2, the coupling constant, $\alpha_s \left(\sim \left(\ln\left(Q^2/\mu^2\right)\right)^{-1}\right) \ll 1$ and QCD processes can be calculated perturbatively (pQCD) up to a certain order in α_s. QCD processes for which $Q^2 < \mu^2$ are usually factored out using a mathematical technique from the perturbative part. The mathematical technique to separate this long distance effect from the short distance effect is called *factorization* and the energy scale is referred to as factorization scale, μ_F^2. In the context of the SM, it is common to take the factorization scale close to the QCD energy scale, $\Lambda_{\mathrm{QCD}} \approx 200\,\mathrm{MeV}$.

The SM with 18 free parameters is an "effective" field theory meaning it is only valid up to a certain energy scale, called the *cut-off* scale. Above the cut-off scale, i.e. at shorter distances, certain divergences occur in the mathematical formulation, thus the SM is realized as a low energy approximation of a more fundamental theory. Several such mathematical models exist that can accomodate the fourth fundamental force, gravity, and can also explain certain experimental observations that the SM cannot. However, the predictions of such models have not yet been experimentally observed. One possible way to look for such new physics phenomenon is to measure the predictions of the SM precisely and look for any possible deviation. The analysis presented in this dissertation tests the prediction of the SM prediction for the top quark pair production at the center of mass energy of 8 TeV discussed in Section 2.2.2

2.2 Phenomenology

2.2.1 Proton-proton collisions

The constituent of the proton are the valence quarks (uud), a sea of gluons being exchanged by the valence quarks and a sea of quark-antiquark pairs produced through gluon interactions. These constituents are collectively called *partons*. In proton-proton collision these constituent partons carry some fraction, x, of the proton's momentum and take part in scattering process. These hadronic interactions are described by the QCD formalism and can be factorized into high momentum transfer (Q^2), hard scattering process and low momentum transfer, soft interactions. The soft interactions occur between the proton remnants left over after the hard scattering and during parton shower and hadronization process. As discussed in Section 2.1, this means the hard scattering process can be separated from the soft interactions through a factorization scheme and can be described through pQCD. The soft interactions are described through non-perturbative QCD. The cross section of pp interactions is then obtained from the hard scattering cross-section above the factorization scale.

To calculate the cross section of the hard scattering process, knowledge of the momentum fraction of the proton carried by the constituent partons is important. Parton distribution functions (PDFs), which are defined as the probability density to find a parton with longitudinal momentum fraction, x, at momentum transfer Q^2, are determined empirically and used in the calculation of the cross-section. The rate of change of parton distribution with the variation of Q^2 is governed by the QCD evolution equation of parton densities (DGLAP) [35].The equations can be

formulated in the domain where perturbative calculations can be applied at different level of approximation, i.e. different orders in α_s^2. However, the DGLAP equations cannot make definitive predictions on the x dependence of the parton distributions at a given Q^2. Data from the deep inelastic scattering processes such as fixed-target lepton-nucleon experiments and electron-proton experiments are used to extract this information. PDF sets are then obtained by a fit on a large number of cross section data points from these experiments, in a large grid of Q^2 and x values. Figure 2.1 shows one such PDF calculated for two different Q^2 values at next-to-next-to-leading order in α_s^2 using a particular factorization scheme. The number of partons increases at low x with Q^2, and falls at high x. At low Q^2, the three valence quarks become more dominant and at high Q^2, there are more valence quarks with low momentum fraction x. The fraction of gluons also increases with increasing Q^2. As can be seen in the figure, at the energy scale of the LHC, more gluons carry the momentum fractions of the proton compared to the valence and sea quarks for low x.

Considering a and b as constituents of protons A and B, respectively, the hard scattering part of the proton-proton interaction can be defined as, $a + b \to c + X$ and the cross section can be written as:

$$\sigma_{pp\to c+X} = \sum_{a,b} \int dx_a dx_b f_{a/A}\left(x_a, \mu_F\right) f_{b/B}\left(x_b, \mu_F\right) \hat{\sigma}_{a+b\to c+X} \tag{2.3}$$

The sum runs over all the quarks and gluons contributing, x is the parton momentum fraction with respect to the proton momentum, μ_F is the factorization scale separating

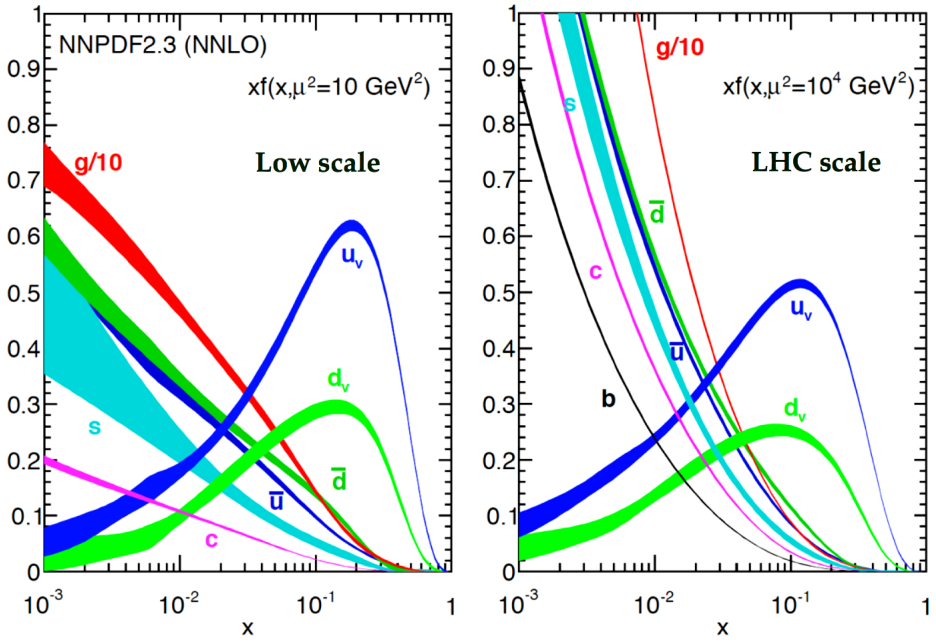

Figure 2.1: Parton distribution functions for proton using the NNPDF sets for $Q^2 = 10\,\text{GeV}$ (left) and $Q^2 = 10^4\,\text{GeV}$ (right) calculated at next-to-next-to-leading order (NNLO) in α_s^2 [36].

the hard and soft scattering processes. The functions $f_{a/A}$ and $f_{b/B}$ represents the PDF sets for proton.

The hard scattering process produces additional quarks and gluons, which further radiates to produce new quark-antiquark pairs to form parton shower. Initial partons that do not participate in the hard scattering can also produce a parton shower. As discussed in Section 2.1, due to quark confinement, the quarks hadronize to form bound states resulting in collimated jets of hadrons. Contributions to the final state of proton-proton collisions that do not originate from hard scattering, such as, the initial, final state radiation and soft interactions are referred to as the underlying event (UE). An schematic diagram of the processes involved in a proton-proton collision, starting from the hard scattering to the final state, is shown in Fig. 2.2.

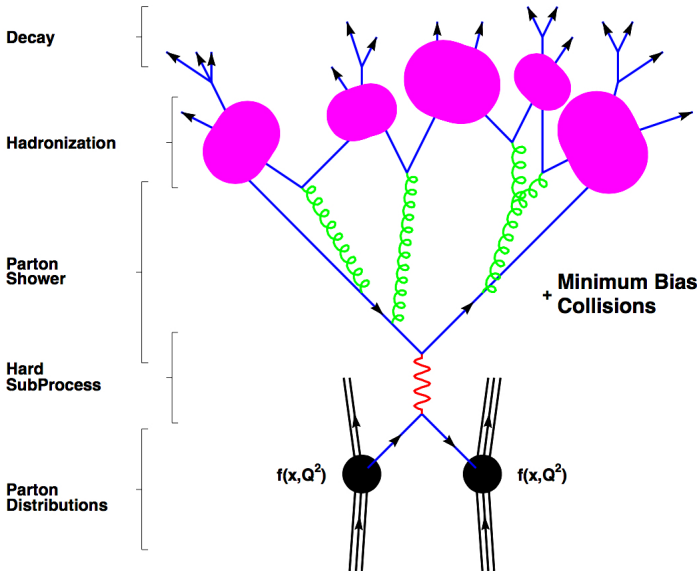

Figure 2.2: A schematic diagram of the processes involved in a proton-proton collision [37].

2.2.2 Top quark pair production at the LHC

In the SM, the dominant mechanism for top quark pair production is the strong interaction. As discussed in Section 2.1, since the mass of a top quark pair is larger than Λ_{QCD}, perturbative QCD can be used to describe its production mechanism. Top quark pairs can be produced through gluon-gluon fusion and quark anti-quark annihilation. The Feynman diagrams at leading order for these two mechanisms are shown in Fig. 2.3. In proton-proton collisions, gluon-gluon fusion is the dominant mechanism due to the fact that valence anti-quarks are absent in the proton and as shown in Fig. 2.1, at the LHC energy scale, gluons dominate the PDFs. At the center-of-mass energy of 8 TeV, about 85% of top quark pairs are produced through gg fusion and about 15% are produced through $q\bar{q}$ annihilation. Following the discussion in Section 2.2.1, equation 2.3 can be used for the specific case of top

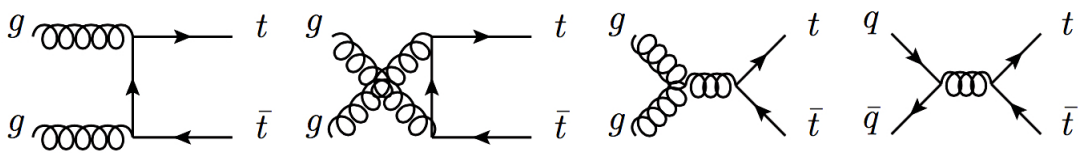

Figure 2.3: Feynman diagram for the $t\bar{t}$ production at leading order QCD.

quark pair production,

$$\sigma_{pp\to t\bar{t}} = \sum_{a,b} \int dx_a dx_b f_{a/A}\left(x_a, \mu_F\right) f_{b/B}\left(x_b, \mu_F\right) \hat{\sigma}_{a+b\to t\bar{t}}\left(s, m_t, \mu_F^2, \alpha_s\right) \tag{2.4}$$

The inclusive $pp \to t\bar{t}$ cross section depends on the mass of the top quark, m_t and the center-of-mass energy squared (s) of the collider. The theoretical prediction for top quark pair production cross section is calculated at the center-of-mass energy of 8 TeV, considering a top quark mass of 172.5 GeV. The calculation is performed at the next-to-next-to leading order (NNLO) in QCD including resummation of next-to-next-to leading logarithmic (NNLL) soft gluon terms with Top++2.0 [38–44]. The PDF and α_s uncertainty is calculated using the PDF4LHC prescription [45] with the MSTW2008 68% CL NNLO [46, 47], CT10 NNLO [48, 49] and NNPDF 2.35f [36] PDF sets. The central value of the calculated prediction is,

$$\sigma_{t\bar{t}}\left(m_t = 172.5 \text{ GeV}; \sqrt{s} = 8 \text{ TeV}\right) = 252.89^{+6.39}_{-8.64}\,(\text{scale}) \pm 11.67\,(\text{PDF} + \alpha_s) \tag{2.5}$$

Figure 2.4 shows the comparison of the prediction with the measured top quark pair production cross section at different center-of-mass energies for pp collisions at the LHC and $p\bar{p}$ collisions at the Tevatron colliders. As can be seen in the figure,

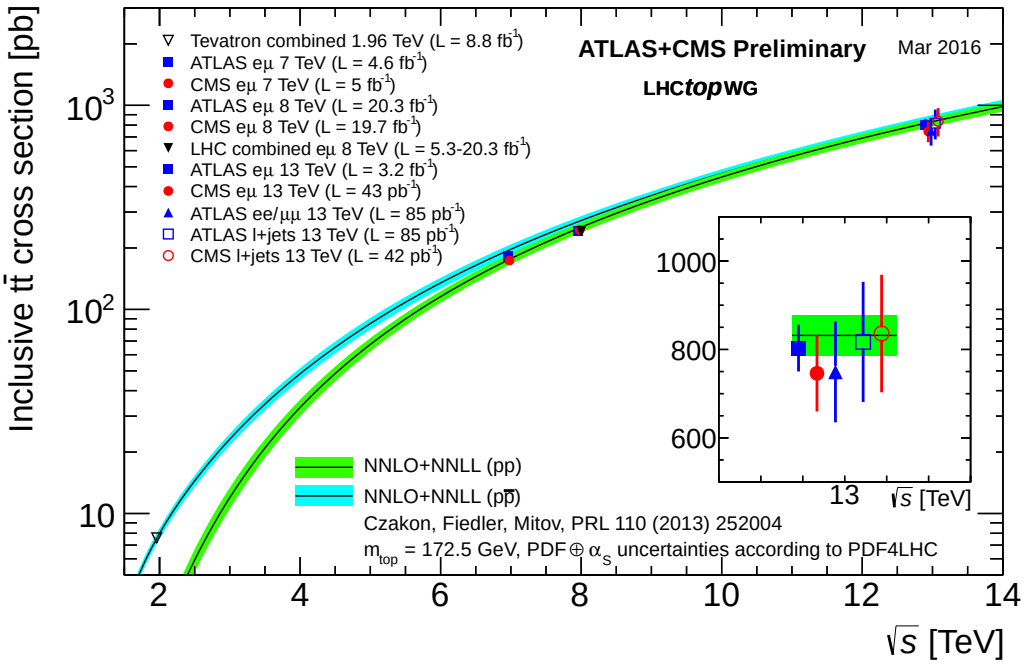

Figure 2.4: Summary of LHC and Tevatron measurements of the top-pair production cross-section as a function of the center-of-mass energy compared to the NNLO QCD calculation complemented with NNLL resummation (top++2.0). The theory band represents uncertainties due to renormalisation and factorisation scale, parton density functions and the strong coupling. The measurements and the theory calculation are quoted at $m_t = 172.5$ GeV. Measurements made at the same centre-of-mass energy are slightly offset for clarity [50].

the measurement of the cross section in the tau lepton final state is missing and this dissertation measures the cross section in that final state.

2.2.3 Top quark decay in the Standard Model

In the SM, the top quark decays through electroweak interactions. As discussed in Section 2.1, the charged current $W^{\pm}$ couples to the physical or mass eigenstate of the quarks. The mass eigenstate of the quarks are obtained using CKM matrix [33, 34] from the weak eigenstate which allows the mixing of the quarks. The elements of the CKM matrix are fundamental parameters of the SM and their values give the strength of the flavor changing weak decays for each quark.

$$V_{\text{CKM}} \equiv \begin{pmatrix} V_{ud} & V_{us} & V_{ub} \\ V_{cd} & V_{cs} & V_{cb} \\ V_{td} & V_{ts} & V_{tb} \end{pmatrix} \text{ where, } \quad V_{\text{CKM}} V_{\text{CKM}}^{\dagger} = 1. \tag{2.6}$$

The probability of the top quark to decay to a down-type quark of each generation in association with $W^{\pm}$ is determined by the elements V_{td}, V_{ts} and V_{tb}, which are measured experimentally. The values of $|V_{td}|$ and $|V_{ts}|$ are measured from the measurement of mixing of $B^0 - \bar{B}^0$ mesons from different experiments [51–55]. The world average is,

$$|V_{td}| = (8.4 \pm 0.6) \times 10^{-3} \quad |V_{ts}| = (40.0 \pm 2.7) \times 10^{-3} \tag{2.7}$$

The direct measurement of $|V_{tb}|$ is performed in the single top quark decay.

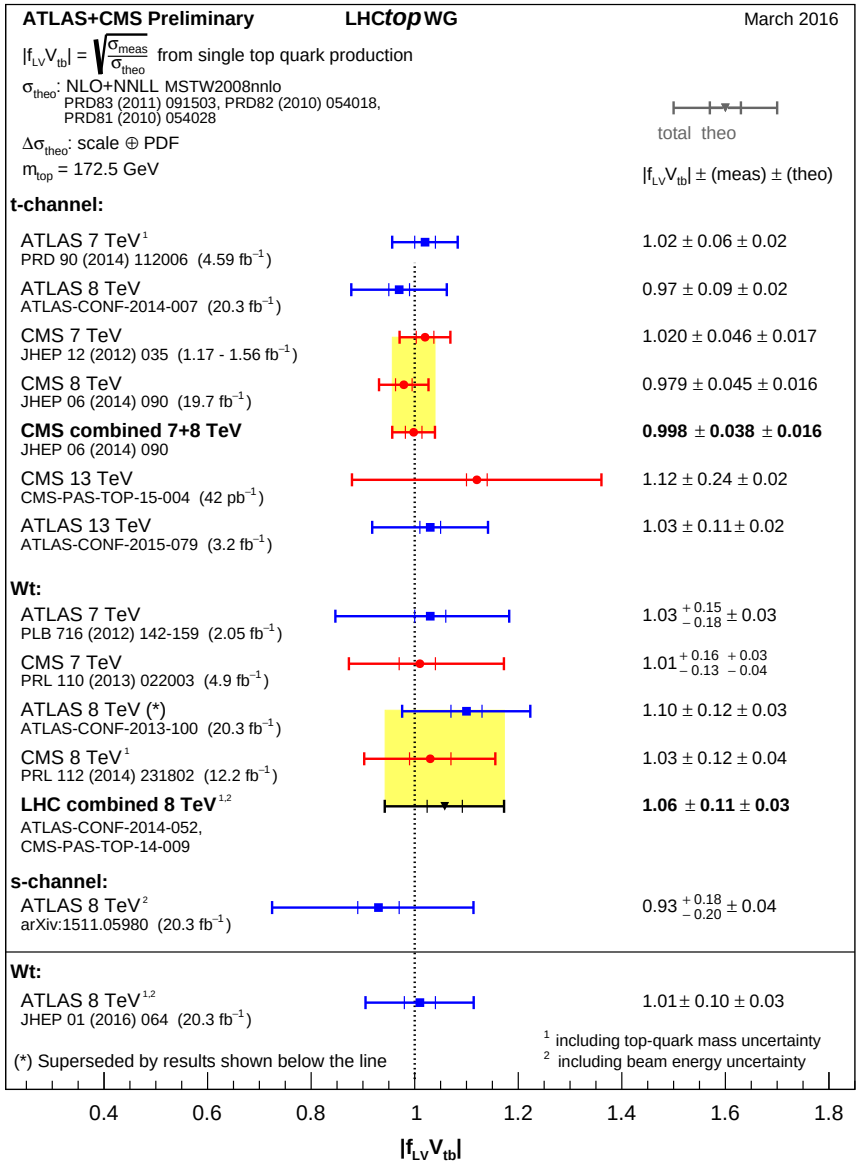

Figure 2.5: Summary of the ATLAS and CMS extractions of the CKM matrix element V_{tb} from single top quark measurements. For each result, the contribution to the total uncertainty originating from the uncertainty on the theoretical prediction for the single top production cross section is shown along with the uncertainty originating from the experimental measurement of the cross section. The measurements below the line were made after the LHC combination that is shown in the upper part of the figure [50].

Figure 2.5 shows the summary of the ATLAS and CMS extraction of the CKM matrix element. The current world average is [56–61]:

$$|V_{tb}| = 1.021 \pm 0.032 \tag{2.8}$$

The top quark thus decays $\sim 100\%$ of the time into a b-quark. The lifetime of the top quark is $\sim 3 \times 10^{-24}$ s [32, 62], which is an order of magnitude smaller than the typical formation time of hadrons. This means the top quarks decay before they can hadronize, providing a rare opportunity to measure the properties of a free quark. The final state of the top quark decay is determined by the decay of the W bosons:

- Dilepton channel: both the W bosons in this channel, decay to leptons (electron, muon or tau) along with their associated neutrino, $t\bar{t} \to W^+bW^-\bar{b} \to \bar{l}\nu_l b l'\bar{\nu}_{l'}\bar{b}$. The total branching ratio (BR) in this final state $\sim 9\%$.

- Lepton+jets channel: one of the W boson in this final state decays to a light quark anti-quark pair with $\mathrm{BR}\big(t\bar{t} \to l\nu_l bq\bar{q}'\bar{b}\big) \sim 45\%$.

- Hadronic (all jets) channel: both the W bosons decay to a light quark anti-quark pair. The branching ratio for this final state is $\mathrm{BR}(t\bar{t} \to q\bar{q}'bq''\bar{q}''') \sim 46\%$

The Feynman diagrams for each final state along with their branching ratios is shown in Fig. 2.6. The signal over background ratio is largest for the final state with the smallest branching ratio and vice versa. The featured final state particle in this thesis, the tau lepton is the heaviest lepton (see Table 2.2) and can decay to electron, muon and hadrons. At the ATLAS detector, only the hadronic

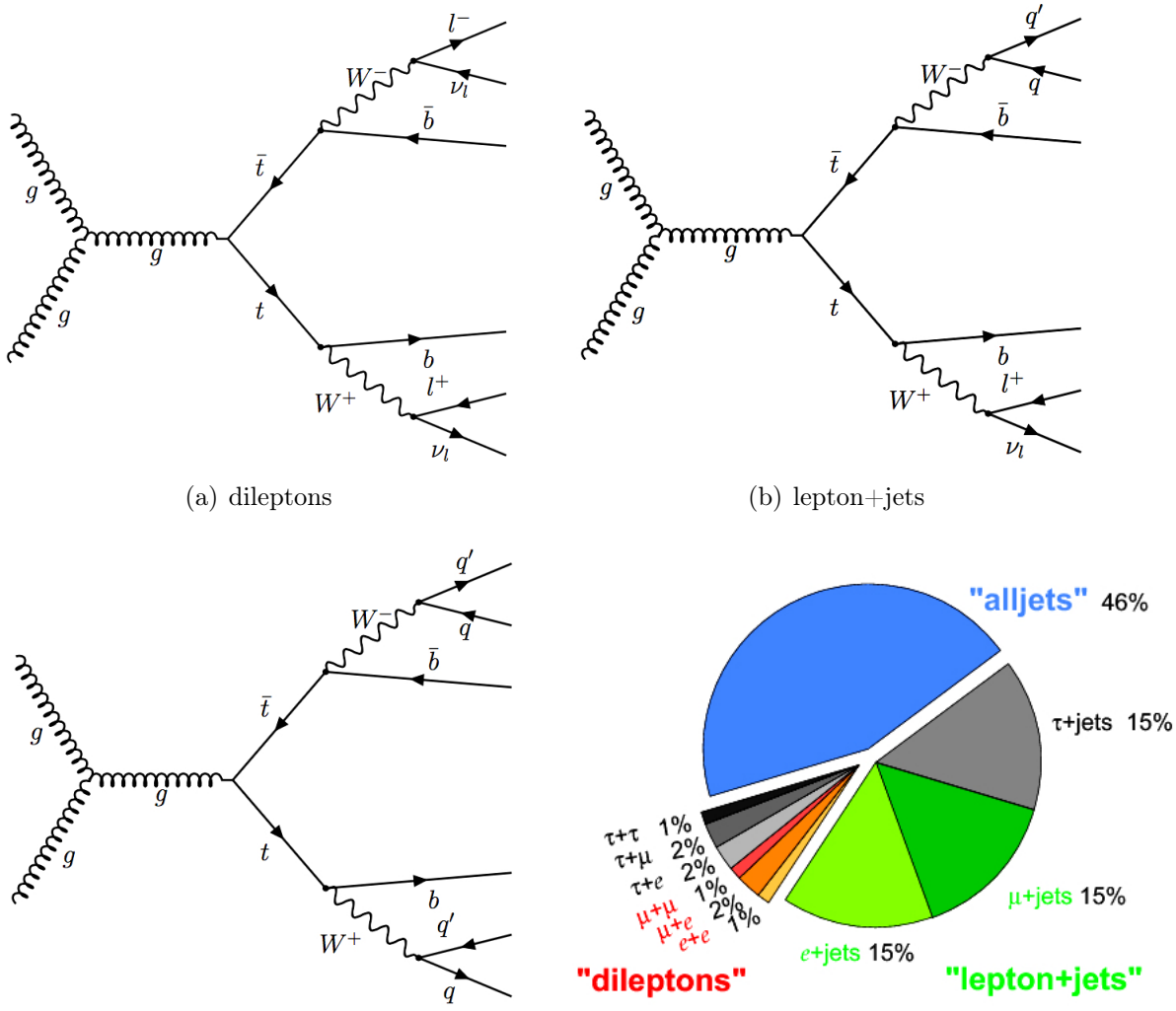

(a) dileptons (b) lepton+jets

(c) all jets (d) branching ratio

Figure 2.6: Feynman diagrams of the top quark decay into different final states along with the branching ratio in each final state. Here, l represents e, μ, τ.

decay mode, corresponding to 65% of all decay modes of tau leptons is used for their identification. The details of tau lepton identification and reconstruction are discussed in Section 4.5. Thus, the branching ratio of the final state considered in this measurement is $\mathrm{BR}\left(t\bar{t} \to \tau\nu_\tau bq\bar{q}'\bar{b}\right) \sim 10\%$. This is also the most difficult final state due to the difficulty in the identification and background estimations of tau leptons.

2.3 Top quark in beyond the SM scenarios

In the framework of the SM, the mass of the Higgs boson becomes divergent due to radiative corrections from fermions through Yukawa couplings. The divergent Higgs mass in the SM is a direct violation of the experimental observation [63]. This is known as the hierarchy problem [64, 65]. The top quark being the heaviest of the fermions (large Yukawa coupling) contributes significantly to this mechanism. As a result, the top quark also plays an important role in the SM extensions that can solve the hierarchy problem. Thus, the top quark can be a sensitive probe for fundamental interactions beyond the SM (BSM). All BSM models introduce new particles in addition to the ones predicted by the SM. If these new particles are heavier than the top quark, they can lead to an excess in the production of top quarks. Supersymmetry (SUSY) [66] is one such extension where a supersymmetric partner of the top quark, the top squark, can decay to a top quark. The two Higgs doublet model (2HDM) [67] can be another example where an additional Higgs doublet is added to the SM Lagrangian resulting in five different Higgs boson. In

that scenario, a heavy charged Higgs can decay to a top quark, $H^+(\text{heavy}) \to tb$. These type of searches rely on the specific predictions from the models. Another effective way to search for these heavy particles without relying on specific predictions from any model is to look for resonances into top quark pairs. Top quark pairs produced in these heavy particle decays are usually boosted. Both ATLAS and CMS have searched for $t\bar{t}$ resonances in different final states and both in resolved and boosted scenarios [68–72]. BSM models also predict production of new particles in the decay of the top quark. For example, in the 2HDM, the light charged Higgs can be produced in the decay of the top quark, $t \to bH^+(\text{light})$. In certain SUSY scenarios, the top squark is light and can be produced in the decay of top quark. In the SM, every other decay mode apart from $t \to Wb$ are suppressed even at higher order loop corrections. However, several BSM extensions predict that these exotic decay modes have a branching ratio higher than that predicted by the SM and can be observed at the LHC. The flavor changing neutral current (FCNC) decays of the top quark is an example of such exotic decay modes and will be discussed in detail in the next section.

2.3.1 FCNC decays of the top quark

Flavor changing neutral current decay referes to the decay of a fermion into another fermion of different flavor in interaction with neutral bosons (Z, γ, g, H). Tree level FCNC decays have not yet been discovered experimentally. In the framework of the SM, the absence of FCNC decays has been explained by the GIM mechanism [73]. According to this mechanism such decays do not exist at the tree level and are

Process	BR (SM)
$t \to uZ$	8×10^{-17}
$t \to u\gamma$	3.7×10^{-16}
$t \to ug$	3.7×10^{-14}
$t \to uH$	2×10^{-17}
$t \to cZ$	1×10^{-14}
$t \to c\gamma$	4.6×10^{-14}
$t \to cg$	4.6×10^{-12}
$t \to cH$	3×10^{-15}

Table 2.4: Predictions for the branching ratios of the FCNC $t \to qX^0 (q = uc;\ X = Z, \gamma, g, H)$ in the SM [74–78].

suppressed at higher order loop corrections. FCNC decay of the top quark is represented by $t \to u$ and $t \to c$ transitions. Table 2.4 lists the SM predictions for the branching ratios for $t \to qX^0\,(q = u, c;\ X^0 = Z, \gamma, g, H)$. In several BSM models, the GIM mechanism is relaxed and new heavy particles contribute to the loop diagram predicting significant enhancement of these branching ratios. Table 2.5 shows the predictions on the branching ratios from a two Higgs doublet model where no requirement of flavor conservation is applied (2HDM Type III), and 2HDM model where explicit flavor conservation is required, a minimal supersymmetric standard model and R parity violating supersymmetric models ($\not{R}$ SUSY).

The ATLAS and the CMS experiments have measured the branching ratios for each processes in different final states at the center-of-mass energies of 7 and 8 TeV. The gluon mediated FCNC process, $t \to u/cg$ is measured in single top events, where the top quark decays leptonically into a electron or muon. In the CMS analysis [85],

Process	BR(2HDM Type III)	BR(FC 2HDM)	BR(MSSM)	BR($\not{R}$ SUSY)
$t \to uZ$	–	–	2×10^{-6}	3×10^{-5}
$t \to u\gamma$	–	–	2×10^{-6}	1×10^{-6}
$t \to ug$	–	–	8×10^{-5}	2×10^{-4}
$t \to uH$	5.5×10^{-6}	–	10^{-5}	$\sim 10^{-6}$
$t \to cZ$	$\sim 10^{-7}$	$\sim 10^{-10}$	2×10^{-6}	3×10^{-5}
$t \to c\gamma$	$\sim 10^{-6}$	$\sim 10^{-9}$	2×10^{-6}	1×10^{-6}
$t \to cg$	$\sim 10^{-4}$	$\sim 10^{-8}$	8×10^{-5}	2×10^{-4}
$t \to cH$	1.5×10^{-3}	$\sim 10^{-5}$	10^{-5}	$\sim 10^{-6}$

Table 2.5: Predictions for the branching ratios (BR) of the FCNC $t \to qX^0 (q = uc;\ X = Z, \gamma, g, H)$ in models with two Higgs doublet of Type III (2HDM), a flavor conserving 2HDM (FC), in the MSSM and with R parity violating SUSY [74–78].

Collab.	Decay mode	$BR(t \to cH)$		$BR(t \to uH)$		Ref.
		Observed	Expected	Observed	Expected	
CMS	$t\bar{t} \to [Wb][H] \to [qqb][\gamma\gamma]$	0.47%	0.71%	0.42%	0.65%	[79]
	$t\bar{t} \to [Wb][H] \to [l\nu b][WW(l\nu l\nu)]$	0.93%	0.89%	–	–	[80]
	($3l$, same charge $2l$)					
CMS combination		0.56%	0.65%	–	–	
ATLAS	$t\bar{t} \to [Wb][H] \to [qqb][\gamma\gamma]$	0.79%	0.51%	0.79%	0.51%	[81]
	$t\bar{t} \to [Wb][H] \to [l\nu b][WW, \tau\tau]$	0.79%	0.54%	0.78%	0.57%	[82]
	($3l$, same charge $2l$, same charge $2l$ one τ)					
	$t\bar{t} \to [Wb][H] \to [qqb][bb]$	0.56%	0.42%	0.61%	0.64%	[83]
ATLAS combination		0.46%	0.25%	0.45%	0.29%	

Table 2.6: Summary of the 95% CL upper limits on the branching ratios of $t \to u/cH$ from the ATLAS and CMS experiments.

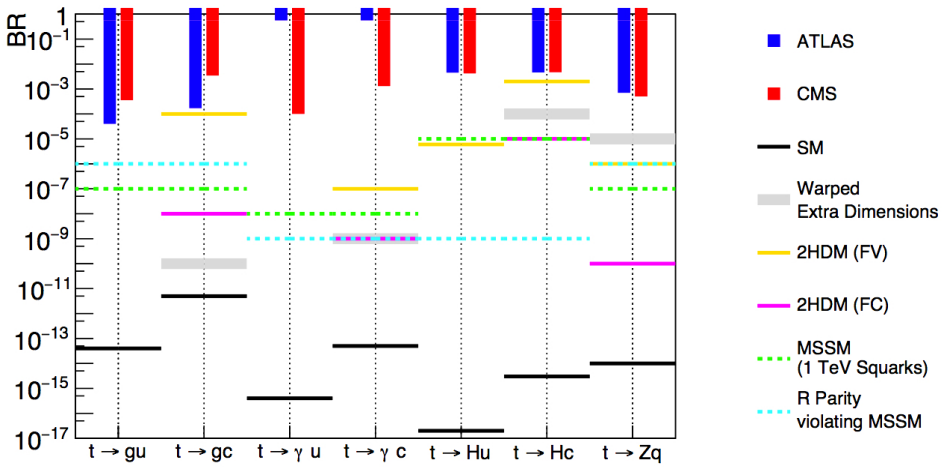

Figure 2.7: Summary of the measured 95% CL upper limits on the branching ratios (BR) of the FCNC $t \to qX^0 (q = uc;\ X = Z, \gamma, g, H)$, measured by the ATLAS and CMS collaborations. The limits are compared to the SM expectation for the branching ratios as well as predictions on the branching ratios from different BSM models [84].

the observed(expected) 95% CL upper limits on the branching ratios are $BR(t \to ug) < 3.55 \times 10^{-4} (1.58 \times 10^{-4})$ and $BR(t \to cg) < 3.44 \times 10^{-3} (1. - 05 \times 10^{-3})$. For the ATLAS analysis [86], observed(expected) 95% CL upper limits are $BR(t \to ug) < 4 \times 10^{-5} (3 \times 10^{-5})$ and $BR(t \to cg) < 17 \times 10^{-5} (15 \times 10^{-5})$. The $t \to u/c\gamma$ processes are measured in a similar fashion in single top events with muon final states by the CMS collaboration. The 95% upper limits observed(expected) by this analysis [87] are $BR(t \to u\gamma) < 1.3 \times 10^{-4} (1.9 \times 10^{-4})$ and $BR(t \to c\gamma) < 1.7 \times 10^{-3} (2.0 \times 10^{-3})$. FCNC processes mediated by the Z boson are searched in $t\bar{t}$ events, where one top is assumed to decay leptonically ($be\nu$ or $b\mu\nu$) and the other top decays via $t \to u/cZ$ with $Z \to ee/\mu\mu$. The ATLAS analysis [88] sets an 95% CL upper limit on the observed(expected) branching ratios, $BR(t \to qZ) < 0.07\%(0.08\%)$. The corresponding CMS analysis [89] yields an upper limit of $BR(t \to qZ) < 0.05\%(0.09\%)$.

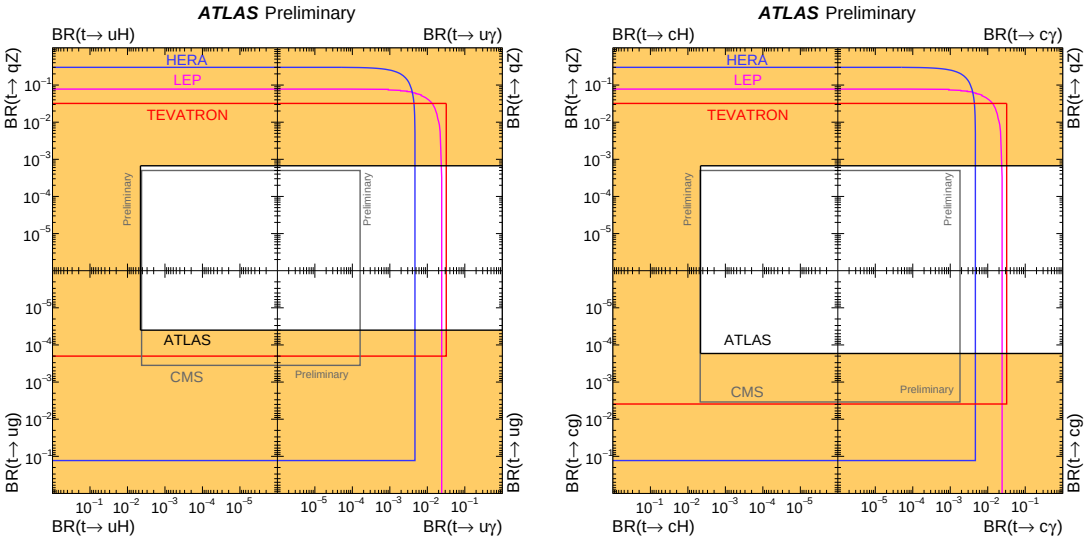

(a) $t \to uX^0$ (b) $t \to cX^0$

Figure 2.8: Summary of the current 95% confidence level observed limits on the branching ratios of the top quark decays via flavour changing neutral currents to a (a) up and a (b) charm quark and a neutral boson. The colored lines represent the results from HERA (the most stringent limits between the ones obtained by the H1 and ZEUS collaborations, in blue), LEP (combined ALEPH, DELPHI, L3 and OPAL collaborations result, in magenta), TEVATRON (the most stringent limits between the ones obtained by the CDF and D0 collaborations, in red) and the CMS Collaboration (in grey). The yellow area represents the region excluded by the ATLAS Collaboration [50].

The discovery of the SM like Higgs boson with a mass $\sim$ 125 GeV has been followed by comprehensive studies of its properties including FCNC decays. The mass of the Higgs boson being lighter than the mass of the top quark makes FCNC decays feasible. Besides, as can be seen in Table 2.5, the Higgs mediated processes, especially $t \to cH$ have the biggest enhancement from BSM. FCNC Higgs decays also known as, flavor changing neutral Higgs (FCNH), are searched in $t\bar{t}$ events. Table 2.6 gives a summary of the analyses from the ATLAS and CMS experiments. The analyses consider one of the top quark pairs decay through SM process and the other top quark decay via FCNH. Several different final states for the SM top quark and the Higgs have been considered. For the Higgs decay mode to two photons, the hadronic decay mode of the top quark is considered, i.e. $t\bar{t} \to [Wb][u/cH] \to [qqb][u/c\gamma\gamma]$. In contrast, for $H \to WW, \tau\tau$ decay modes, the leptonic top quark final state, $t \to Wb \to l\nu$ is considered. In these Higgs decay modes ($H \to WW, \tau\tau$) several combination of final state leptons are considered: 3 leptons (e or μ), 2 leptons (e or μ) with same charge, 2 leptons (e or μ) with same charge and a tau lepton. All the different final states are combined resulting a observed $BR(t \to u/cH) < 0.5\%$ limit at 95% CL.

The ATLAS and CMS measurement summary for all neutral boson FCNC interaction is shown in Fig. 2.6. In addition, the exclusion region for each case from all experiments (HERA, LEP, TEVATRON and LHC) is shown in Fig. 2.8.

In Table 2.6, the decay mode where the one top quark decays hadronically and the Higgs boson decays to two tau leptons, $t\bar{t} \to [Wb][cH] \to [qqb][c\tau\tau]$ has not been considered. In this disseration, in addition to the measurement of the top quark pair

production cross section, the measured value of the cross section is used to set an upper limit at 95% CL on $BR(t \to cH)$. The results are discussed in Chapter 6.

CHAPTER 3

The LHC and the ATLAS experiment

The Large Hadron Collider (LHC) is one of the largest scientific facilities in the history of humanity. The accelerator smashes protons, at higher speeds than any previous physics experiment. The ATLAS detector records these collisions and translates detector signals into physics phenomena. The data analyzed in this thesis have been recorded by the ATLAS experiment during the LHC Run 1 in the year 2012. A brief description of the accelerator focusing on the LHC conditions during 2012 operation is presented. The ATLAS detector with subsystems relevant to the analysis presented in this thesis are also described.

3.1 The Large Hadron Collider

The Large Hadron Collider [90] (LHC) was first conceived in the 1980s to test our understanding of particle physics and to answer unresolved questions by discovering physics beyond our current knowledge. The LHC is the most powerful accelerator ever built. This circular two-ring, hadron accelerator lies beneath the border of Switzerland and France, near the Swiss city of Geneva. It is operated by the European

Organization for Nuclear Research (CERN[1]) and occupies the underground tunnel originally constructed for the Large Electron Positron collider (LEP). The LHC became operational on 10th September, 2008.

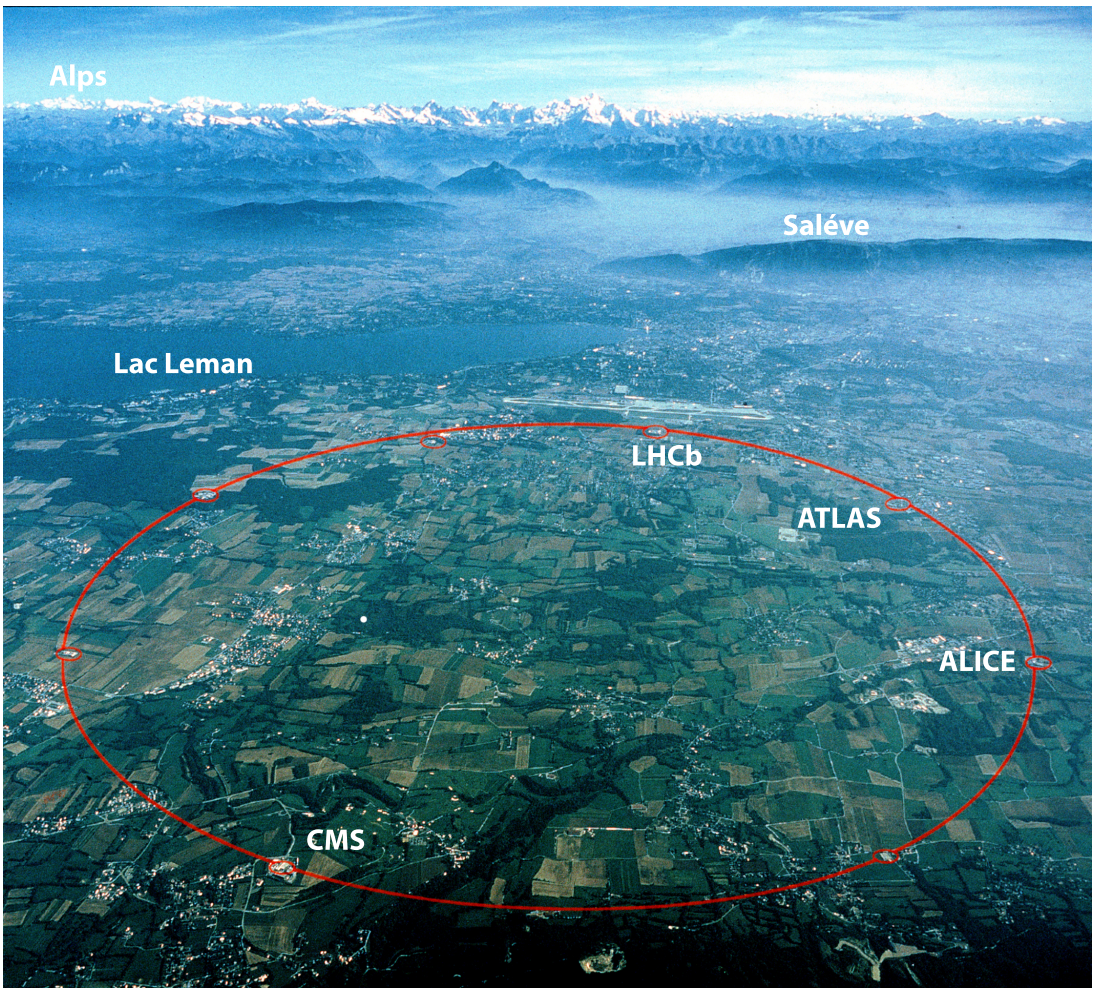

Figure 3.1: The area under which the tunnel for LHC can be found, near Geneva. The French Alps and Lac Leman can be seen in the background. The LHC tunnel location is indicated in red [91].

An aerial view of the region with the location of the tunnel indicated in red can be seen in Fig. 3.1. The tunnel has a circumference of 26.7 km and is located at a mean depth of 100 m at a gradient of 1.4%. The depth of the tunnel varies

[1]Conseil Européen pour la Recherche Nucléaire

between approximately 175 m (under the Jura mountain range) and approximately 50 m (towards Lac Leman).

The LHC is designed to accelerate beams of protons and heavy ions (Pb^{82+}), and to collide them along the tunnel at four points where the four major experiments – ATLAS [92], CMS [93], ALICE [94] and LHCb [95] are located. ATLAS (**A** **T**oroidal **L**HC **A**pparatu**S**) and CMS (**C**ompact **M**uon **S**olenoid) are general purpose particle physics detector experiments built for discovering the physics of and beyond the Standard Model. ALICE (**A** **L**arge **I**on **C**ollider **E**xperiment) is designed to provide insight into heavy ion collisions and the quark-gluon plasma. LHCb (LHC-**b**eauty) is a forward detector specialized to study b-hadrons and to understand the asymmetry between matter and antimatter. Three smaller experiments have also been commissioned at the LHC site: LHCf (LHC forward experiment) [96], MoEDAL(Monopole and Exotics Detector a the LHC) [97] and TOTEM (Total Cross-section, Elastic Scattering and Diffraction Dissociation at the LHC) [98].

3.1.1 The LHC complex

The LHC is the final component of a multi-stage chain of smaller accelerators, both circular and linear, called the accelerator complex [99]. A schematic of the CERN accelerator complex can be seen in Fig. 3.2. Protons are obtained by placing hydrogen atoms in a strong electric field to strip away the orbiting electron. The protons are then accelerated to 50 MeV in the LINAC2 linear accelerator (LINAC3 is used for heavy ions). The protons are then injected successively into the Proton Synchrotron Booster (PSB), Proton Synchrotron (PS) and Super Proton Synchrotron

(SPS) where they are accelerated to 1.4 GeV, 25 GeV, and 450 GeV, respectively. These protons are then injected into the LHC where they are maximally accelerated to 4 TeV during 2012 operations, yielding a center-of-mass collision energy of 8 TeV. This chain of accelerators and the speed of a proton at the end of each acceleration step is summarized in Table 3.1.

The proton beams are segmented into groups of protons called *bunches* to maximize the number of collisions. During the 2012 LHC operation, a 50 ns spacing is used between each bunches resulting a total of 1380 bunches. The proton intensity in each bunch is $\sim 10^{11}$.

The protons are accelerated using 8 superconducting radio frequency (RF) cavities per beam. The RF cavities also ensure the protons in each bunch are clumped tightly to provide high luminosity at the collision point. Inside each RF cavity, a voltage oscillating longitudinally with a frequency of 400 MHz is generated. The amplitude of the voltage is 2 MV and corresponds to an accelerating field of 5 MV m^{-1}.

A total of $\approx$ 6700 magnets are installed along the LHC ring to keep the proton beams confined. These magnets can be classified into more than 50 categories based on their functionality and geometrical configuration. Out of these 50 categories, the superconducting magnets are the most complex. To bend the proton beams along the ring, 1232 superconducting dipole magnets are used. The dipole magnets are cooled to a temperature of 1.9 K using superfluid helium. At this temperature, the dipoles can produce a current of 11 850 A, creating a magnetic field of 8.4 T. In order to constrain the width and height of each beam, 392 superconducting quadrupole magnets are used. These magnets ensure that the beam dimension is smaller than

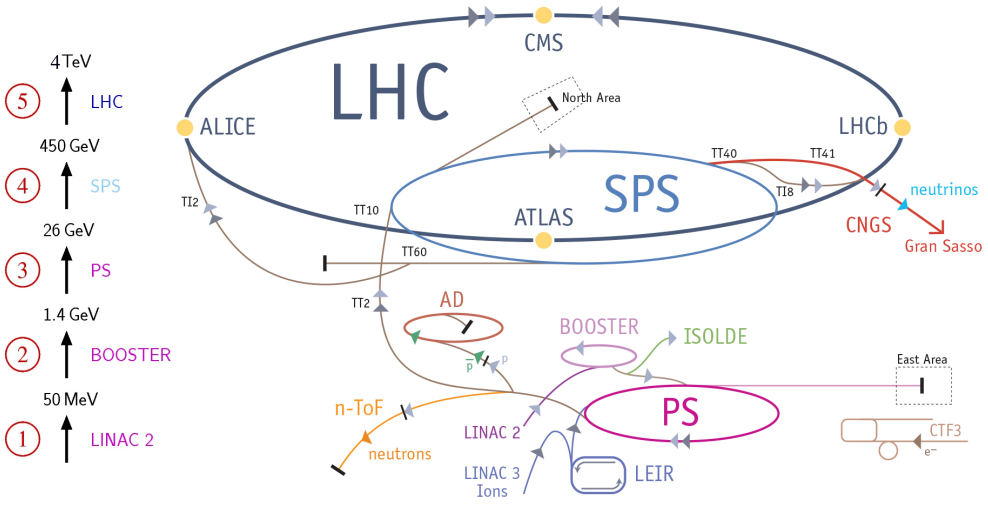

Figure 3.2: The LHC accelerator complex. Before reaching the LHC, protons are accelerated at Linac 2, Proton Synchrotron Booster (PSB), the Proton Synchrotron (PS), and the Super Proton Synchrotron (SPS) [100].

proton energy (GeV)	speed of light (%)	accelerator
0.05	31.4	LINAC 2
1.4	91.6	PSB
25	99.93	PS
450	99.9998	SPS
4000	99.999997	LHC

Table 3.1: The accelerators of the LHC accelerator chain and the speed at which they accelerate protons during 2012 [100]

the dimension of the beam pipes.

3.1.2 Physics goal and performance

The physics program at the LHC is diverse and driven by the physics each experiment is designed to study. The different experiments at the LHC are listed in section 3.1. The design parameters of the LHC, therefore, are based on the physics goals of each experiments and are tuned to deliver maximum performance.

The main physics goal of the ATLAS and CMS experiments at the LHC is to

reveal new physics by searching for rare processes. The rare processes are associated with small cross sections and production of massive particles. The rate of production of a process during a collision is given by the product of the luminosity of the beams, $\mathcal{L}$, and the cross section of the process, σ, that depends on the center-of-mass energy of the collider $\sqrt{s}$, i.e. $\mathcal{L}\sigma\left(\sqrt{s}\right)$. The center-of-mass energy represents the energy available in a collision. This parameter defines the phase space accessible to the final state particles as well as the mass of the particles that can be created. Figure 3.3 shows the cross section of different processes in different center-of-mass energy for pp and $p\bar{p}$ collisions. As can be seen in the Fig., the production cross section increases with increasing center-of-mass energy. For a fixed center-of-mass energy, the total delivered luminosity, $L = \int \mathcal{L}dt$, measured in inverse barns ($1\,\mathrm{b} = 10^{-8}\,\mathrm{m}^2$) increases the total number of generated events. Therefore, LHC is designed to operate at a large center-of-mass energy and to deliver large integrated luminosity.

The luminosity depends on the beam parameters and is defined as

$$\mathcal{L} \propto \frac{f_{rev} n_b N_p^2}{4\pi\sigma_T^2}, \tag{3.1}$$

where f_{rev} represents the frequency of revolution of the beam, n_b is the number of bunches per beam, N_p is the number of protons per bunch and σ_T the transverse beam size at the interaction point. These are the performance parameters of the LHC. The increase of instantaneous luminosity however, would increase the number of proton-proton collisions a single bunch crossing. The probability of more than one hard scattering event per bunch crossing is low with additional collisions being

Beam Parameter	value in 2012
Center-of-mass energy, $\sqrt{s}$ [TeV]	8
Peak Luminosity, $\mathcal{L}$ [$10^{33}\,\mathrm{cm}^{-2}\,\mathrm{s}^{-1}$]	7.73
Delivered integrated luminosity, L [fb^{-1}/year]	23.1
Integrated luminosity recorded by ATLAS [fb^{-1}/year]	21.7
Maximum number of colliding bunches	1380
Number of protons in a bunch [$\times\ 10^{11}$]	1.6
Minimum bunch spacing [ns]	50
Average number of interactions per bunch crossing $\langle\mu\rangle$	20.7

Table 3.2: The LHC beam parameters and performance in the year 2012 [102].

soft interactions between the constituent quarks and gluons. The number of such events is described by a Poisson distribution with a mean value,

$$\mu = \frac{\mathcal{L}\sigma_{inelastic}}{n_b f_{rev}}, \tag{3.2}$$

where $\sigma_{inelastic}$ is the inelastic pp cross section taken to be 73 mb for 8 TeV collision. The average number of such events over all bunch crossing, $\langle\mu\rangle$ is referred to as *pileup*.

During the 2012 operation, the LHC delivered an integrated luminosity of 23.1 fb^{-1} of which 21.7 fb^{-1} were recorded by the ATLAS detector. The high luminosity resulted on average of 20.7 interactions per bunch crossing ($\langle\mu\rangle$). Figure 3.4 shows the integrated luminosity delivered by the LHC during 2012 along with average number of collisions per bunch crossing, $\langle\mu\rangle$. Table 3.2 lists the beam conditions during this period of operation.

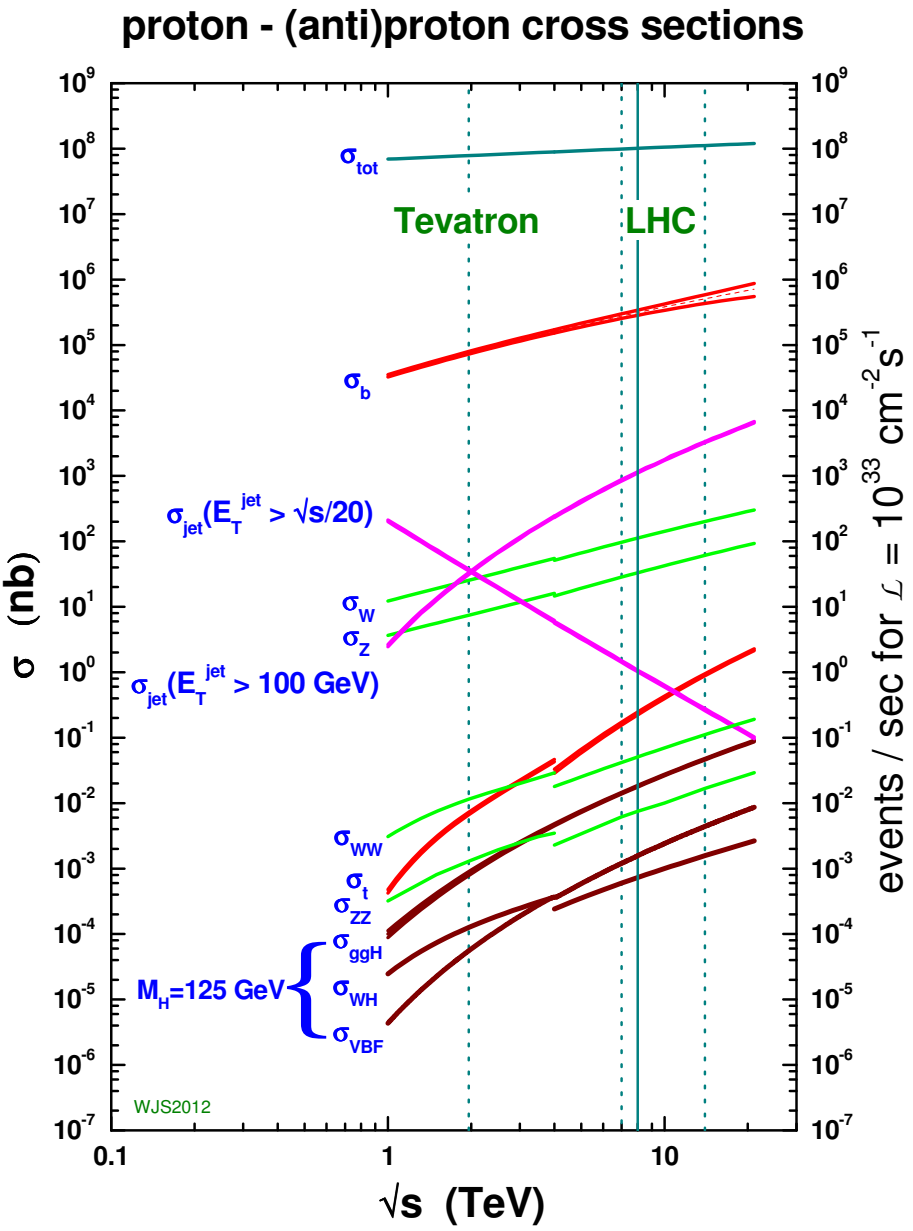

Figure 3.3: Cross sections of pp and $p\bar{p}$ processes in the center-of-mass energy regime relevant to the Tevatron and LHC. Courtesy W.J. Stirling [101].

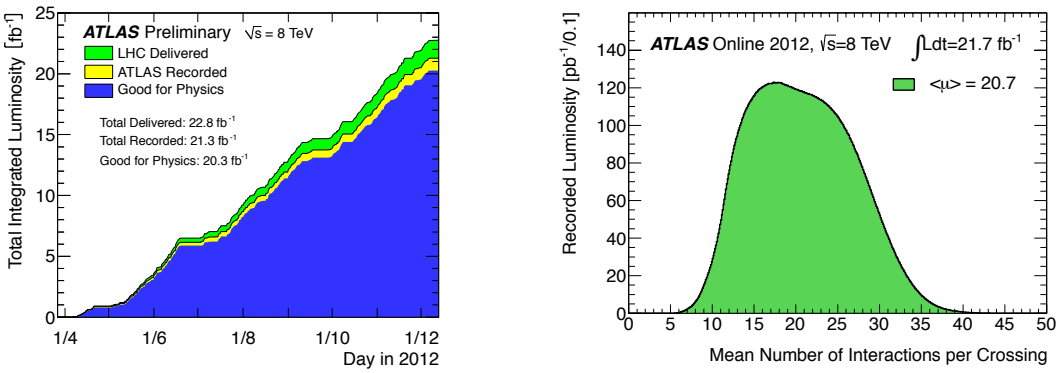

(a) (b)

Figure 3.4: The integrated luminosity delivered by the LHC and recorded by the ATLAS detector (a) and the average number of interactions per bunch crossing (b) in 2012 [103].

The LHC operation during 2012 has been a huge success with many Standard Model precision measurement as well as the discovery of the Higgs boson by ATLAS and CMS experiments. During spring 2013 – 2015, the LHC went through a long shut down for upgrades. These upgrades allow the LHC to run at its design collision energy of $\sqrt{s} = 14\,\text{TeV}$. At the moment of writing this thesis, the LHC has successfully completed the 2015 operation with collisions at $\sqrt{s} = 13\,\text{TeV}$ and delivered an integrated luminosity of $4\,\text{fb}^{-1}$.

3.2 The ATLAS detector

The ATLAS detector is located at one of the collision points of the LHC. It is 46 m in length, 26 m in diameter, and weighs 7000 tons, making it the largest detector at the LHC. The construction of the detector began in 2003 and was completed in 2008. It is a general purpose detector designed to be sensitive to large areas of high energy physics phenomena including high precision measurement of the Standard Model

properties, the newly discovered Higgs boson, measurement of the properties of the Higgs boson, and searches for new and exotic phenomena. The ATLAS detector and its physics performance goals are described in detail in Technical Design Reports (TDRs) [104, 105] and a paper published by the ATLAS collaboration [92]. The content of this chapter is intended to be an overview of the ATLAS detector and its physics and performance goal.

ATLAS uses a right-handed coordinate system with its origin at the nominal interaction point (IP) and the z-axis along the beam line, with the side-A of the detector defined to be positive in z. The x-y plane is orthogonal to the beam line, with the positive y-axis pointing upward towards the surface and the positive x-axis pointing from the detector to the center of the LHC ring. The azimuthal angle ϕ is measured around the beam axis while the polar angle, θ is measured relative to the positive z-axis. The pseudorapidity η, is typically used in place of the polar angle θ since $\Delta\eta$ is invariant under boost along the beam line. The pseudorapity is defined in terms of the polar angle θ as,

$$\eta = -\ln\left(\tan\frac{\theta}{2}\right). \tag{3.3}$$

The distance, ΔR, measured in (η, ϕ) plane is defined as,

$$\Delta R = \sqrt{\Delta\eta^2 + \Delta\phi^2} \tag{3.4}$$

The momentum of each particle can then be decomposed in longitudinal and

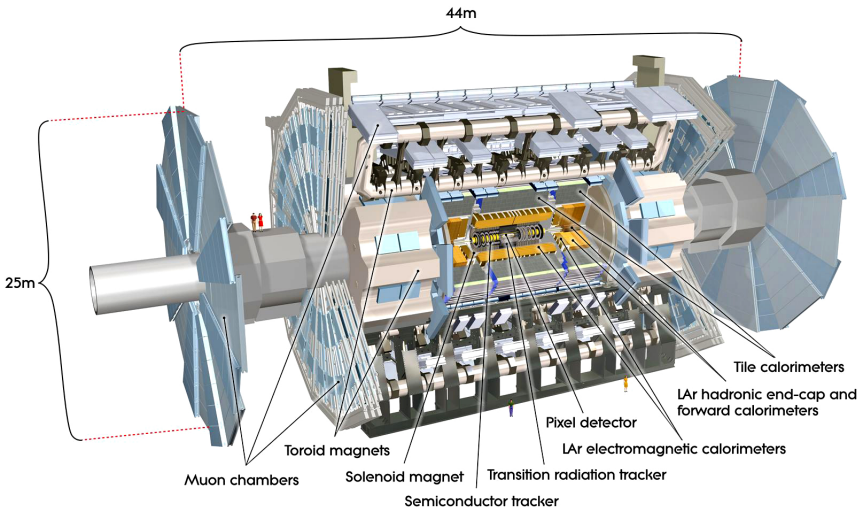

Figure 3.5: A schematic representation of the ATLAS detector, showing the various sub-detectors labeled and models of people shown for scale [106].

transverse components. The transverse momentum, p_T, of each particle, which is also invariant under Lorentz transformations, is another useful quantity that is defined as,

$$p_T = p \sin(\theta) \tag{3.5}$$

The protons in the LHC collide almost head-on. Hence there is negligible transverse momentum before the hard-scattering, which means the sum of the transverse momenta of the final state particles should be approximately zero. However, neutrinos generally escape the detector without any interaction. In processes that contain neutrinos in the final state, their momenta cannot be measured, therefore resulting in missing transverse momentum, yet another useful quantity.

ATLAS can classify and detect particles with energies as low as a few hundred

MeV to as high as multiple TeV. To cover these broad range of spectra, the ATLAS detector is designed to be as close to hermetic as possible with multiple subdetectors concentric about the proton-proton interaction point as depicted in Fig. 3.5. The innermost layers, collectively known as the inner detector (ID), provide information on the trajectories of charged particles and have a coverage up to $|\eta| < 2.5$. The ID is surrounded by a solenoid magnet with a magnetic field of 2 T. The magnetic field bends the tracks of charged particles and allows for a measurement of their charge over momentum ratio. The middle layer of subdetectors, collectively know as the calorimeters, are responsible for measuring the energy of a particle. The calorimeters provide coverage all the way up to $|\eta| < 4.9$. The outermost layer is the muon spectrometer (MS), which is immersed in a toroidal magnetic field of 2 T to 8 T (depending on endcap or barrel) and is designed to measure the momentum and direction of a muon. The MS provides coverage up to $|\eta| < 2.7$. Figure 3.6 shows the trajectories and detection points of the final state particles that are observed in ATLAS.

3.2.1 Inner detector and tracking

The ATLAS inner detector is designed to precisely measure the trajectory and momentum of charged particles such as electrons, muons and charged pions [92]. The ID consists of three highly granular, independent but complementary subsystems: the Pixel detector, the Semiconductor Tracker (SCT) and the Transition Radiation Tracker (TRT). In addition to trajectory and momentum measurements, the TRT can also provide particle identification (PID) through the detection of transition

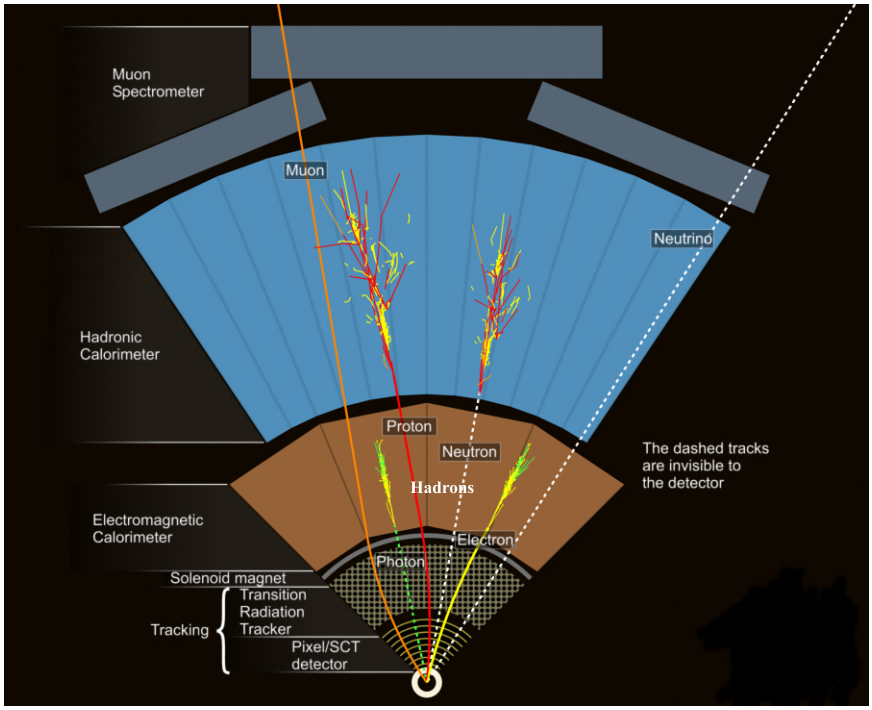

Figure 3.6: A computer generated transverse schematic view of a wedge of the ATLAS detector. Charged particles leave tracks in the tracker, electrons and photons typically stop in the electromagnetic calorimeter, hadrons like proton, neutron or charged pions typically stop in the hadronic calorimeter, and muons are tagged at the muon spectrometer as they exit. Neutrinos escape the detector without interacting [107].

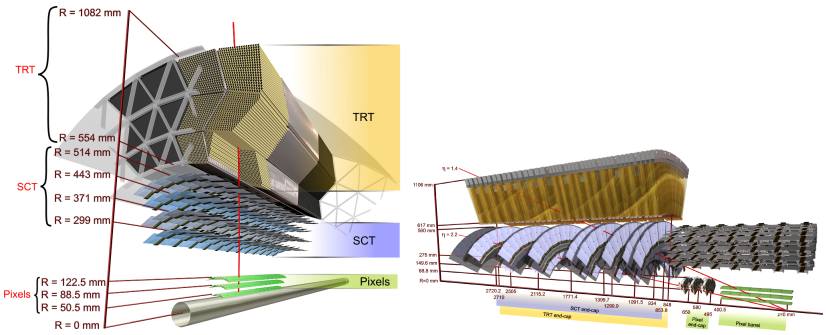

Figure 3.7: A diagram of the barrel (left) and end cap (right) of the Inner Detector showing the layers in the Pixel, SCT and TRT sub-detectors [108]

.

radiation. Each of these subdetectors are split into barrel and endcap components, providing full 2π coverage in ϕ, and up to 2.5 in $|\eta|$. Figure 3.7 shows each component of the ID in the barrel and endcap regions.

The Pixel detector is the innermost layer of the ID, composed of high-precision, high-granularity semiconductor modules [92]. In the barrel they consist of three cylinders of differing radii, while in the endcaps they consist of three disks on each side (6 in total) at different locations along the beam line. There are 1744 semiconductor modules, each one containing 47232 pixels. The dimension of each pixel module is $50\,\mu\text{m} \times 400\,\mu\text{m}$ and has an intrinsic resolution of $115\,\mu\text{m}$ in the longitudinal (z-axis) direction and $10\,\mu\text{m}$ in the transverse direction ($r - \phi$). The purpose of the Pixel detector is to deliver precise measurement of the tracking parameters as close to the interaction point as possible. Measurement of tracking parameters with high accuracy is extremely important to determine the precise location of the interaction point, the impact parameter resolution and identification (via the measurement of secondary vertex) of short lived particles such as τ lepton and b hadrons

The SCT is the middle layer of the ID, surrounding the Pixel detector and is made up of silicon detector elements, using strips instead of pixels [92]. In the barrel SCT, the strips are arranged in four double layers and mounted on carbon fiber cylinders of varying radii . The SCT endcap sensors are mounted onto nine wheels of varying radii at different z locations. In the barrel region, each strip is 80 µm in width and 126.1 mm long. The intrinsic resolution of each strip module is 16 µm in the transverse plane and 580 µm in the longitudinal direction.

The TRT is the outermost subdetector of the ID and is a combined transition radiation and tracking detector. The intrinsic resolution of the TRT is only 130 µm in the transverse direction and complements the tracking capabilities of the Pixel and the SCT. The TRT employs 300,000 gas (mixture of 70% Xe, 27% CO_2 and 3% O_2) filled polymer straw drift tubes and can additionally classify charged particles as electrons or pions via the detection of transition radiation in the gas mixture. This radiation is produced when a charged particle crosses the boundary between two media of different dielectric constants and is proportional to the Lorentz boost of a particle. Therefore, for an electron and charged pion of equal momentum, the electron is much more likely to produce transition radiation than the pion since its mass is 200 times smaller. Transition radiation in the TRT is observed as hits that are well above the threshold for tracking and is referred to as *high threshold* hits, as opposed to *low threshold*.

A comparison of the ID subdetector features in the barrel region are shown in Table 3.3. As a charged particle travels through the ID, it leaves *hits* in each subdetector along its trajectory, as shown in Fig. 3.8. Information from these

Subdetector	Channels	Element size	Resolution [µm]	Layer radii [mm]
Pixels	80×10^6	$50\,\mu m \times 400\,\mu m$	10×115	50.5, 88.5, 122.5
SCT	6.3×10^6	$80\,\mu m \times 126\,mm$	17×580	299, 371, 443, 514
TRT	350×10^3	4 mm	130×0	554 – 1082

Table 3.3: Comparison of the features of the three subdetectors: the Pixel detector, the SCT and the TRT in the barrel region of the ATLAS Inner Detector [108].

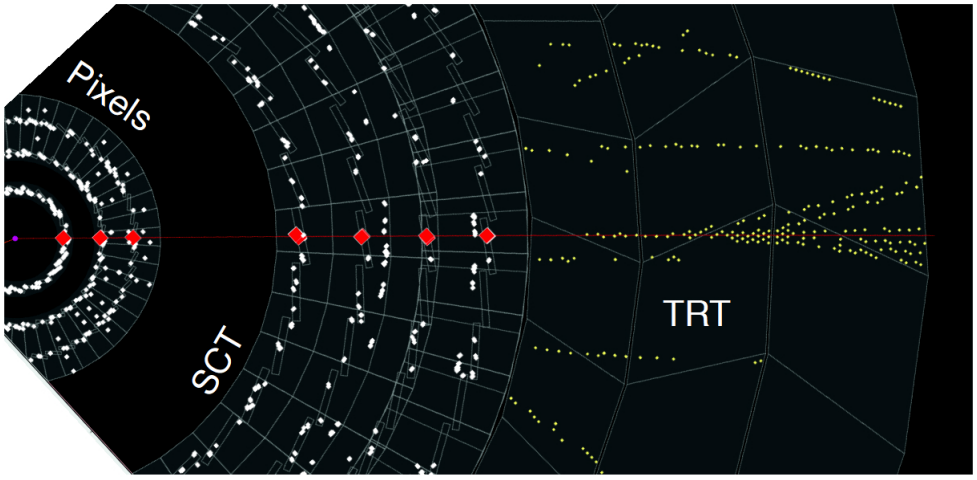

Figure 3.8: A event display of a charged particle traveling from left to right, through the three layers of the Pixel detector, four layers of the SCT, and many layers of the TRT [109]. The particle undergoes a material reaction at the TRT and produces multiple additional particles.

subdetectors are combined to reconstruct *tracks*, which have a unique correspondence to charged particles and are meant to describe their trajectory and momentum. The details of tracking and vertex reconstruction algorithms is discussed in Chapter 4.

3.2.2 Calorimeters and clustering

The ATLAS calorimeters surround the ID and the solenoid magnet, and is designed to precisely measure the energy of charged and neutral particles. The calorimeters used in the ATLAS detector are *sampling* devices, meaning only a fraction of a

particle shower energy is observed, and the full shower energy must be inferred. The calorimeters are composed of several alternating layers of a dense absorbing material and an active medium. Particles traversing the calorimeter interact with the dense absorbing material creating a cascade of secondary particles, called a *shower*, which is then measured in the subsequent active medium.

The interactions of various charged and neutral particles can be classified into two types: electromagnetic (e, γ) and strong (hadrons such as pions and tau leptons). Due to the different nature of these two interactions, the response of a material is different for electromagnetic (EM) and hadronic objects. The EM objects produce narrow calorimeter showers while hadrons tend to produce wider showers. Figure 3.9 shows a comparison of the showers produced by an electron and a pion of the same energy passing through iron. The ATLAS calorimeter system is therefore, divided into EM and hadronic components that are based on different technologies. The EM calorimeter covers the pseudorapidity range $|\eta| < 3.2$ and the hadronic calorimeter covers the region $|\eta| < 4.9$. An schematic representation of the ATLAS calorimeter system with different subdetectors is shown in Fig. 3.10.

The EM calorimeter uses liquid argon (LAr) as an active material and lead (Pb) plates as an absorber. To provide uniform coverage in the full azimuthal angle, a accordion-style geometry is used. The EM calorimeter is subdivided into barrel (EMB) and endcap (EMEC) components, which cover $|\eta| <$1.4 and $1.4 < |\eta| < 3.2$, respectively. The total thickness of a EMB module is $\sim$ 22 radiation lengths [2] (X_0) and the EMEC module has a thickness of $\sim 24X_0$. The EMB is further subdivided

[2]The radiation length is the mean length traversed by an electromagnetically-interacting particle until it has $1/e$ of its initial energy left.

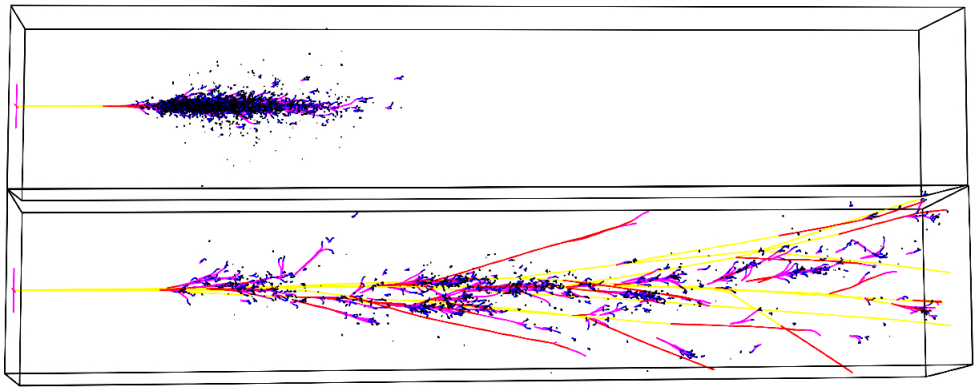

Figure 3.9: Simulated electron (top) and charged pion (bottom) showers, where both particles are 50 GeV and passes through iron.

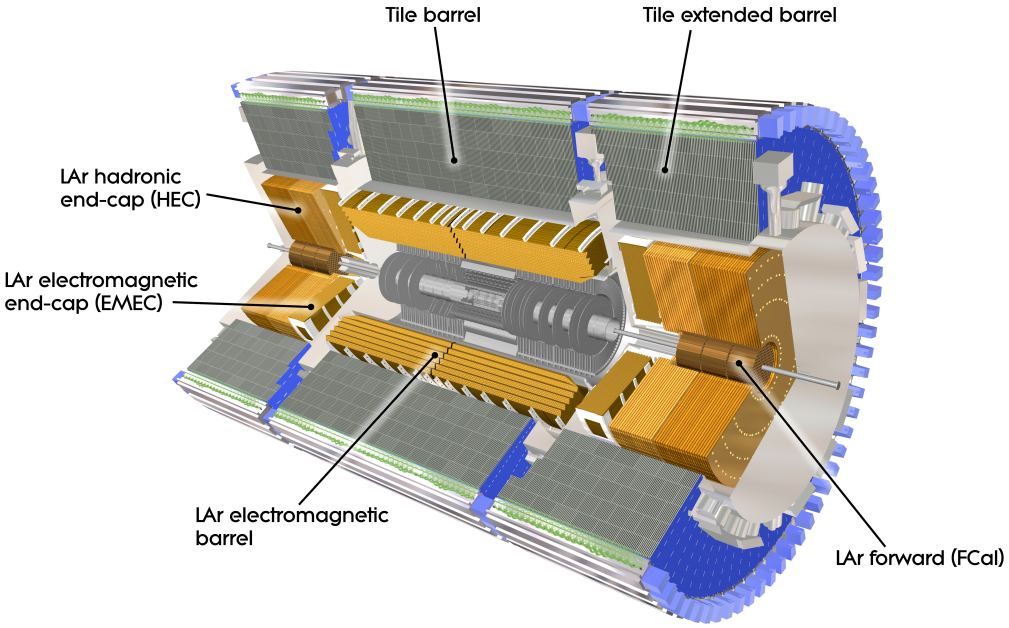

Figure 3.10: A computer generated schematic representation of the ATLAS calorimeters [110].

radially into first, second and third layers away from the beamline. The first layer has the smallest granularity with $\Delta\eta \times \Delta\phi = 0.003 \times 0.1$, providing detailed descriptions of shower shapes, which are important for the particle identification algorithm. The second layer with granularity $\Delta\eta \times \Delta\phi = 0.025 \times 0.025$ is the largest layer and usually contains most of the energy of an electromagnetic shower. The third and the outermost layer provide confinement of the showers and has coarse segmentation.

The hadronic calorimeter is subdivided into three components. The barrel and the endcap (HEC) covers a pseudorapidity range of $|\eta| < 1.7$ and $1.5 < |\eta| < 3.2$, respectively. The very forward region, $3.1 < |\eta| < 4.9$, is covered by the forward calorimeter (FCal). The barrel region uses steel as the absorber material and scintillating tiles as the active material. The HEC and the FCal uses LAr as the active material but for the absorber material, the HEC uses copper, while the FCal uses both copper and tungsten. In order to reduce the punch-through into the muon system, the nuclear interaction length [3] (λ) of the hadronic calorimeter is typically $\sim$10.

Each particle traversing the calorimeter deposit energy in the adjacent calorimeter cells along its path. To measure the total energy deposited by each of these particles, calorimeter cells from all subdetectors are combined using different algorithms known as *clustering*.

[3] The interaction length λ, is the mean length traversed by a hadronically-interacting particle until it has $1/e$ of its original energy left.

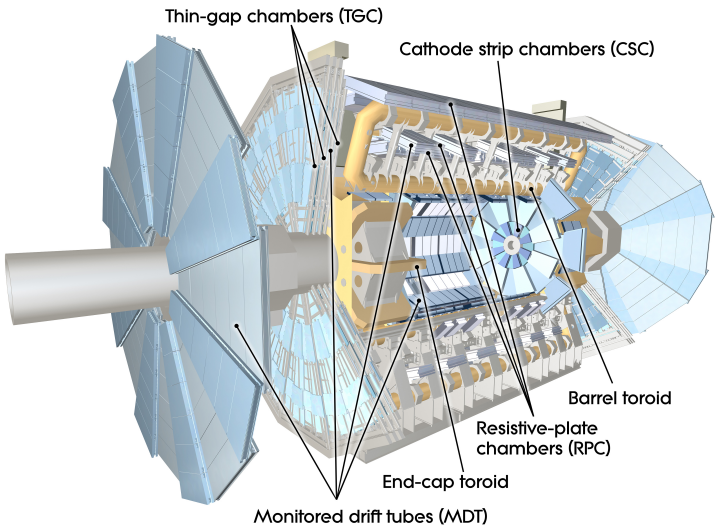

Figure 3.11: A computer generated schematic representation of the ATLAS muon system, with the various sub-systems labeled [112].

3.2.3 Muon spectrometry

The muon spectrometer (MS) is designed to measure the trajectory and momentum of muons [111], especially at high p_{T}. Muons are minimum ionizing particles and traverse the complete ATLAS detector without being stopped in the calorimeters. Therefore, the MS is built as a separate system, furthest from the interaction point, surrounding the calorimeters. The MS is comprised of four subdetectors: the Monitored Drift Tubes (MDTs), the Cathode Strip Chambers (CSCs), the Resistive Plate Chambers (RPCs), and the Thin Gap Chambers (TGCs), shown in Fig. 3.11.

The RPCs and TGCs are intended to provide fast, coarse measurement for use in the trigger system and are designed to provide a signal within 25 ns, i.e. the nominal bunch crossing time at the LHC. The RPCs are located at the barrel region covering a pseudorapidity range up to $|\eta| < 1.05$, while TGCs covers a range of $1.05 < |\eta| < 2.04$ and located at the endcap region. The trigger systems have a lower spatial

resolution, the RPCs(TGCs) provide a resolution of around 10 mm (2 mm to 6 mm) in the $r - z$ plane and an azimuthal resolution of 10 mm (3 mm to 7 mm).

The MDTs and CSCs are the slower but more precise muon systems and require around 700 ns to readout a signal. MDTs and CSCs provide a spatial resolution of 35 µm and 40 µm, respectively, in the $r - z$ plane.

The MS is integrated with a system of air-core toroidal magenets, which bend the tracks of muons and allow for their momentum to be measured. The large barrel toroid magnet provides the magnetic field in the central region out to $|\eta| < 1.4$, while in the range $1.6 < |\eta| < 2.7$ the magnetic field is provided by two end cap toroid magnets.

3.2.4 Trigger and data acquisition

The ATLAS trigger system is crucial in recording events that are interesting for physics analyses. The majority of the *pp* collisions produce low transverse momentum QCD dijet events, mostly uninteresting from a physics point of view. The bunch crossing rate at the LHC during $\sqrt{s} = 8$ TeV was approximately 20 MHz, corresponding to a bunch crossing every 50 ns, far too high a rate to readout signal from the ATLAS detector and then store the data from each collision. A huge reduction of data is necessary immediately after each collision and this reduction process must be careful not to remove events with interesting signatures. This scheme of fast reduction is called *triggering*. Reconstruction and decision making at the trigger level, that occurs in real-time is referred to as *online*, whereas, the nominal ATLAS reconstruction that is done at a later time is termed *offline*.

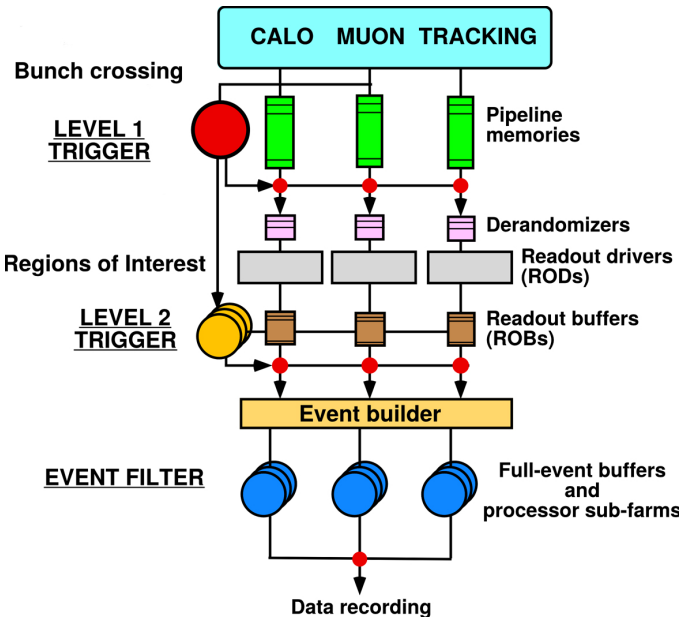

Figure 3.12: Block diagram of the ATLAS trigger and data acquisition (TDAQ) system [104, 105]

The ATLAS trigger and data acquisition (TDAQ) system is designed to select and record interesting events from the enormous number of collisions, such that the rate at which events are collected for storage is ∼700 Hz. This storage rate sets stringent requirements on the speed of signal collection from the sub-detectors, the speed of the reconstruction algorithms used by the trigger system, and the efficiency of the recording system for the collected data. To meet these requirements, the ATLAS trigger system is split into three levels, where at each level the number of accepted events is significantly reduced. Figure 3.12 shows a simplified block diagram of the TDAQ system. First, all *pp* collisions are sent to the hardware trigger, called *Level 1* (L1), which uses information from subdetectors in a reduced granularity compared to the offline reconstruction. Events satisfying the hardware trigger are then sent to the software trigger, called *High Level Trigger* (HLT). The HLT uses information

system	input rate	output rate	reduction	latency
L1	20 MHz	70 kHz	300×	2.5 µs
L2	70 kHz	5 kHz	15×	75 ms
EF	5 kHz	700 Hz	7×	1 s

Table 3.4: Approximate average trigger rates and latencies during 2012 data-taking with $\sqrt{s} = 8$ TeV [92, 113].

with a granularity comparable to the offline reconstruction and is divided into two steps, *Level 2* (L2) and *Event Filter* (EF). The reduction in rate and latency at each step is shown in Table 3.4.

The L1 trigger uses information only from the calorimeters and the MS as the ID is not equipped to process events at tens of MHz. The calorimeter granularity available at the L1 trigger is shown in Fig. 3.13, where performance is sacrificed for faster processing. The L1 trigger selection looks for muons in the trigger chambers of MS, and high transverse momentum e/γ and jet objects or missing transverse momentum (see Chapter 4 for definition of these objects) in the calorimeter. Once the object satisfying the selection is identified, the region in the detector where it is located, is defined as Region of Interest (RoI), where RoI is a cone with its apex at the interaction point and extending to the outer parts of the ATLAS detector in the direction of the selected object. The L1 trigger can then make a decision about whether to keep an event based on the presence of the required object.

Data selected by the L1 trigger is held at the readout buffers (ROBs) until it can be processed by the L2 trigger. The L2 trigger makes use, at full granularity and precision, of the subdetector information from the RoIs. Events selected by the L2 trigger system are passed to Event Builder (EB), which performs a full reconstruction

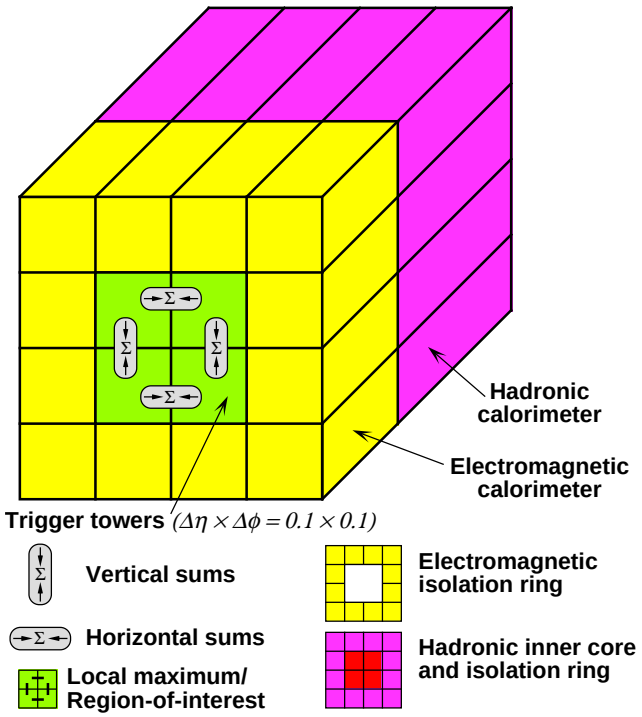

Figure 3.13: Schematic view of the calorimeter granularity at the L1 trigger [104, 105]

of each event, before being processed at EF, the final stage of the trigger system. The EF employs reconstruction and identification algorithm comparable to the nominal offline ATLAS algorithms, to ensure that selected data matches as closely as possible to the offline data that will finally be used for physics analyses.

3.2.5 Monte Carlo simulation

It is important to compare the collision data recorded by ATLAS to theoretical predictions to test our understanding of physics processes. The theoretical predictions are tested by generating simulated events using Monte Carlo (MC) methods. Generation of reliable MC simulated events is also crucial as they are used to estimate yields of SM background processes and to test different signal process hypothesis.

The response of the ATLAS detector to different objects, crucial to physics analyses, can also be studied using MC simulated events. In MC events, the true energy of an object is known and can be used to validate the ATLAS reconstruction algorithms. Multiple steps are involved toward producing MC simulated events: event generation, detector simulation, digitization and reconstruction.

Event generation refers to the process of simulating proton-proton interactions and involves the modeling of hard scattering between proton constituents, parton showering, hadronization, and the underlying event. Monte Carlo methods are used to randomly generate the initial hard interactions between proton constituents according to the differential cross-section of the process of interest. First, the matrix elements (ME) are calculated up to a certain order in perturbation theory. The parton distribution functions (PDF) are then used to determine the total or differential cross section for a process in interest. The ME is usually calculated using the lowest order Feynman diagrams of the process of interest i.e. at leading order (LO). A correction for the next-leading-order (NLO) known as a k-factor is calculated by taking the ratio of the NLO and LO cross-sections for the process. There are a number of PDFs that can be used, and the differences in the cross-section using different PDFs are used to estimate the uncertainty on modeling the process.

The initial partons and particles producing the hard interactions can radiate gluons, which in turn can split into more gluons, or into quark-anti-quark pairs, producing a cascade of radiation referred to as the parton shower. Due to QCD color confinement, individual quarks and gluons do not exist, so during parton showering they will interact with other quarks and anti-quarks produced to form hadrons,

this process is referred to as hadronization. The product of parton showering and hadronization are hadrons (and other particles from the decays of these hadrons) that are seen in the detector as a cone of tracks (in the ID and MS) and energy deposits (in the calorimeters). The object reconstructed from these tracks and energy deposits is referred to as a jet. The dynamics of parton showering and hadronization are not well understood, and the existing models are approximations of the process, inheriting an uncertainty in the final distribution of partons within jets. Jet distributions in MC simulated events are often tuned to jet distributions in collision data where the approximate models are found to not perfectly match the data. The proton constituents often interact softly and do not undergo hard scattering process. The resulting event from this type of interaction is referred to as underlying event.

A wide variety of event generation algorithms with varying level of details in the calculation, are used in ATLAS. For example, the Pythia [114], Sherpa [115] and Herwig [116] generators are used to calculate the ME, parton shower, hadronization, and decay for $2 \rightarrow 1$ and $2 \rightarrow 2$ processes at LO. Other algorithms exist to calculate the ME for $2 \rightarrow$ n processes at LO, such as MadGraph [117, 118] and Alpgen [119], however they do not model the parton shower and are usually combined with another generator for calculations beyond the ME. Finally, there are also generators capable of calculating the ME at NLO with both real and virtual corrections, such as MC@NLO [120] and Powheg [121], but they also require the use of a different generator to model the parton shower and hadronization.

The event generation step does not account for the interaction between the particles produced and the material of the ATLAS detector and this effect is simulated

using the GEANT4 software package [122]. For example, the hits in the ID and MS which is used to reconstruct tracks are modeled in GEANT4. The modeling of electromagnetic and hadronic showers produced when particles interact with the calorimeter is also done at this stage, which is necessary to accurately simulate the energy deposited by electrons, photons and jets in the calorimeters. Electromagnetic showering is well understood, however modeling of hadronic showering is still an area of active research. ATLAS uses two algorithms for hadronic shower modeling: the QGSP_BERT, which uses the quark gluon string model [123] and the FTFP_BERT, which is based on the FRITIOF model [124]. The full GEANT4 simulation is time consuming and computationally expensive, particularly for modeling showers, so a faster simulation called AFII (ATLAS fast II) is often used as an alternative. The AFII framework parameterizes the average response of the GEANT4 model of the ATLAS calorimeters to different types of particles with different kinematic properties, providing look-up tables for energy depositions and interaction probabilities. The ID and MS are unchanged in AFII and only the modeling of the calorimeters is changed. AFII improves the computation time by approximately an order of magnitude but also lowers the precision in the modeling of the calorimeters. AFII simulated events are only used when increased mis-modeling can be neglected, or when it does not change the accuracy of the MC simulation with respect to data.

The particles produced in the event generation are passed through the GEANT4 model of ATLAS. The energy deposits in the calorimeters and hits in the ID and MS are assigned to each particle based on the part of the detector it traverses. This process is known as digitization [125]. After digitization, the MC simulated events

can be reconstructed using the same event reconstruction algorithms as collision data, discussed in Chapter 4.

CHAPTER 4

Event and object reconstruction

For each collision at the LHC, the information of the various ATLAS sub-detectors is combined and processed in order to identify the particles produced in the proton-proton interaction and to measure their properties. The processes of transforming raw data to well defined physics objects is called reconstruction. The definition of these objects and their identification criteria is presented in this chapter. First, a short description of the identification process of particle tracks and the associated vertices is outlined, followed by the reconstruction and identification performance of electrons, muons, particles jets originated from the production of quarks, taus and missing transverse momentum resulted from escaping particles. In addition to these identification criteria a set of quality criteria is also applied to each object relevant to the measurement presented in this thesis and discussed in a later chapter.

4.1 Tracks and vertices

The trajectories of charged particles are identified using various algorithms and consequently their momenta are measured using the curvature of these tracks in the

magnetic field. Tracks are characterized through five parameters: curvature q/p, the impact parameters in the longitudinal, transverse and $r-z$ planes, i.e. d_0 and z_0, and the azimuthal and polar angles, θ and ϕ. The tracks are reconstructed within the ID acceptance ($|\eta| < 2.5$) using a sequence of two algorithms [126]:

i) the *inside-out algorithm:* is responsible for the reconstruction of the primary charged particles, i.e. particles which are directly produced in pp collisions. The algorithm starts with the formation of 3-dimensional space points from hits in the Pixel and SCT detector. A set of three space points, with each point originating from a unique layer of the silicon detectors is used to form a seed. Seeds are then extended into other layers of the Pixel and SCT detectors in search of further hits. A hit that degrades the quality of the fit to the track candidate is called an *outlier*, and if no hit is found where it is expected, it is termed a *hole*. The quality of a track candidate is determined from the number of good hits, outliers, and holes. Once ambiguities between track candidates are resolved, a more refined fitting procedure using global-χ^2 and Khalman fitting techniques is performed [127]. Finally tracks are extended and combined with the hits in the TRT.

ii) the *outside-in algorithm:* is responsible for track reconstruction of secondary particles i.e. particles which are produced in the decay of the primary particles. This algorithm starts from seeds in the TRT and traces the tracks backward into the inner Pixel and SCT layers.

Increasing pile-up, i.e. the average number of interactions per bunch crossing,

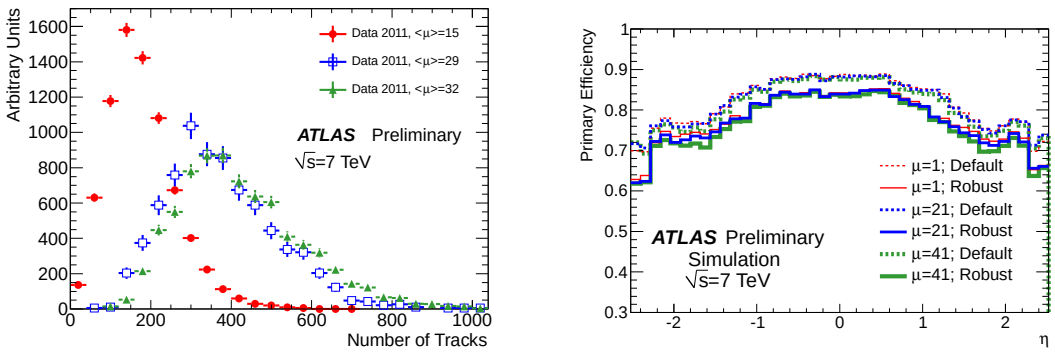

(a) (b)

Figure 4.1: Distributions of (a) number of tracks for different pile-up conditions and (b) track reconstruction efficiency for different pile-up conditions passing the default(dashed) and robust (solid) requirements in a especial high pile-up LHC fill at $\sqrt{s} = 7$ TeV [127].

increases the detector occupancy. The pile-up at the LHC during the 2012 data taking is shown in Fig. 3.4. The increasing detector occupancy leads to an increase in fake tracks, i.e. reconstructed tracks that cannot be matched to either a primary or secondary particle. Figure 4.1(a) shows the distributions of the number of reconstructed tracks under various pile-up conditions. To reduce the number of fake tracks, a more robust requirement on the number of silicon hits and holes has been applied, leading to a reduction in the track reconstruction efficiency. Figure 4.1(b) show the track reconstruction efficiency as a function of η, for the robust requirement for different pile-up conditions. Increasing pile-up changes the track reconstruction efficiency by only a small amount, within 1%, independent of the quality cuts. The difference between the reconstruction efficiency for the default and robust requirements is roughly 5%, on average.

Primary vertices are reconstructed, first by using the z-position at the beamline of reconstructed tracks to obtain vertex seeds. An iterative χ^2 fit [128] is then performed

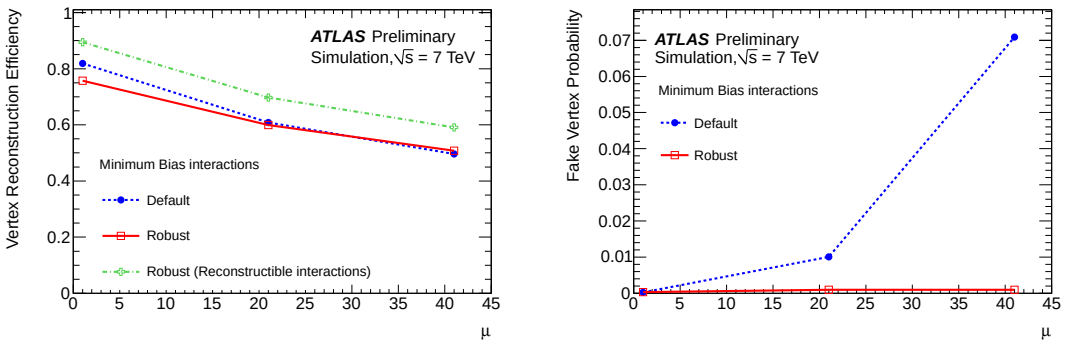

(a) (b)

Figure 4.2: The vertex reconstruction efficiency (a) and the probability for fake vertices (b) vs. pile-up (μ) in the simulation sample of minimum bias events for a especial high pile-up LHC fill at $\sqrt{s} = 7$ TeV [127].

using the seed and any nearby tracks. Each track is given a weight corresponding to a measure of its compatibility with the fitted vertex, which depends on the χ^2 fit. Tracks displaced by more than 7σ from the fitted vertex are used to obtain a new vertex seed, and this procedure is repeated until no additional vertices are found [127]. For events with more than one vertex, the vertex for which the sum of the square of transverse momentum (Σp_{T}^2) of associated tracks is largest, is selected as the one corresponding to the interaction of interest, and is called the primary vertex (PV).

The efficiency of vertex reconstruction decreases with increasing pileup due to the increased probability of fake tracks. Figure 4.2 shows the vertex reconstruction efficiency and probability of fake vertex for different pileup condition for the robust requirement. The vertex and track reconstruction are well understood in the 2011 data, however, a disagreement in the vertex multiplicity in minimum bias events, between simulation and the data at $\sqrt{s} = 8$ TeV, is observed. The disagreement can be attributed to observed differences in the minimum bias visible cross-section in data

and simulation [129]. In order to model the pile-up effects correctly in simulation a pileup rescaling is applied in the 2012 MC [130, 131].

4.2 Electrons

Electrons traverse the ATLAS detector leaving a track in the ID until they stop in the EM calorimeter, where they typically deposit all their energy. The reconstruction and identification of electron candidates start from the clusters of this energy deposit. Clusters are reconstructed from a set of seed clusters of longitudinal towers with total transverse energy above 2.5 GeV [132, 133]. In the central region of the detector ($|\eta| < 2.47$), the clusters are then associated with reconstructed tracks of charged particles in the ID by extrapolating the tracks from their last measurement point to the middle layer of the detector. This offers no rejections against other charged particles, however, so identification algorithms are designed to exploit discriminating features of electrons. Relative to backgrounds, electrons are more likely to leave longitudinally narrow calorimeter deposits in the EM calorimeter, deposit very little energy in the hadronic calorimeter, and be isolated in the ID and the EM calorimeter.

Three sets of selection requirements are applied on these discriminating variables to define *loose*, *medium* and *tight* quality electrons and corresponds to decreasing signal efficiency and increasing background rejection. The cuts are optimized in bins of η and E_{T}. The *loose* selection makes use of shower shape variables in the middle layer of the EM calorimeter and variables related to energy deposit in the hadronic calorimeter. The *medium* selection includes all of the cuts in the *loose*

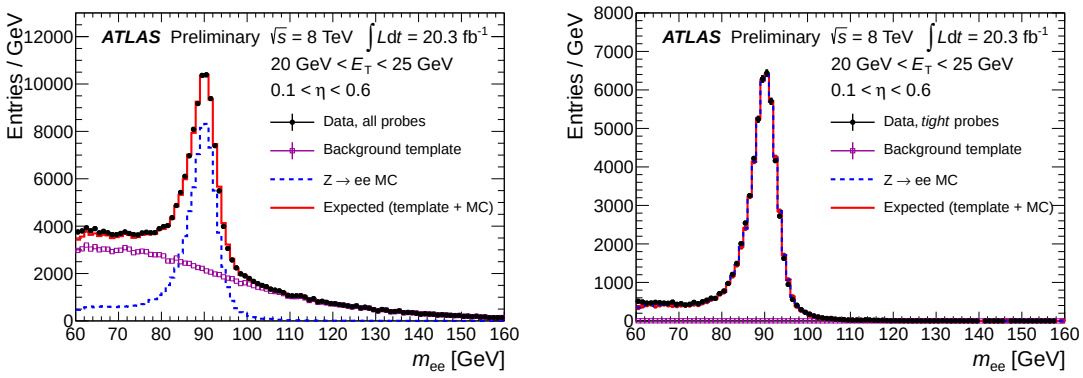

(a) (b)

Figure 4.3: Data and predictions of the invariant mass of two electrons (m_{ee}) before the electron identification algorithm is applied (a) and after (b) [134].

selection, and adds cuts on variables from the EM calorimeter strip layer, track quality requirements and track to cluster matching requirements. The *tight* selection, adds further requirements on E/p criteria (where E is the energy measurement in the calorimeter and p is the momentum measured in the tracking detectors), particle identification from the TRT, and discrimination against photon conversions [135,136]. Figure 4.3 shows the performance of the electron identification algorithm indicating huge rejection of backgrounds.

The reconstruction and identification efficiency for electrons in MC and data is measured using a tag and probe method in $Z \to ee$ and $J/\Psi \to ee$ events. In this method, an electron in each event is selected using the standard identification criteria discussed above (called the *tag* electron) and the second electron (called the *probe* electron) is selected with a looser set of criteria. The reconstruction efficiency is then determined, by checking how often the *probe* electron passes the standard criteria. Figure 4.4 shows the electron reconstruction efficiency versus E_{T} and η. The

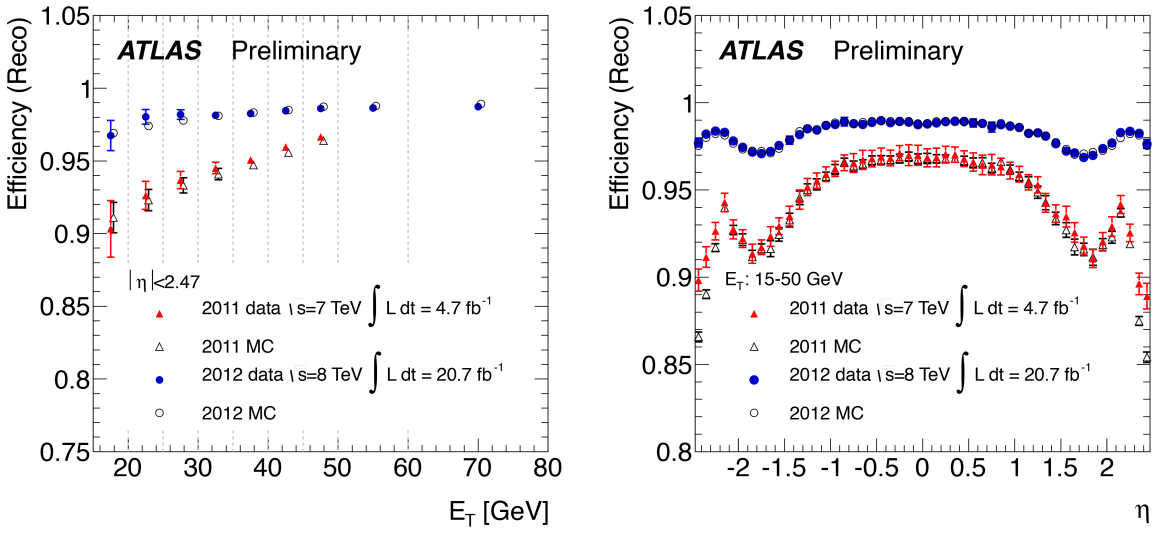

(a) (b)

Figure 4.4: Electron reconstruction efficiency in data and prediction binned in transverse energy (a) and pseudorapidity (b) [134].

small differences for the electron efficiency in data and MC are taken into account by calculating a scale factor to correct the MC simulation to what is observed in data.

4.3 Muons

Muons are minimum ionizing particles and do not deposit significant energy in the calorimeters, hence they are the only particles expected to reach and interact with the MS. Since, MS is specifically designed to identify muons, they are the simplest physics object to reconstruct in the ATLAS detector.

Muon tracks are reconstructed only in the MS. Impact parameters and direction of flight are determined by extrapolating the track in MS back to the point of closest approach to the beamline. Energy lost by the muon in the calorimeters is taken into account in the extrapolation. Muons are then reconstructed by matching the tracks

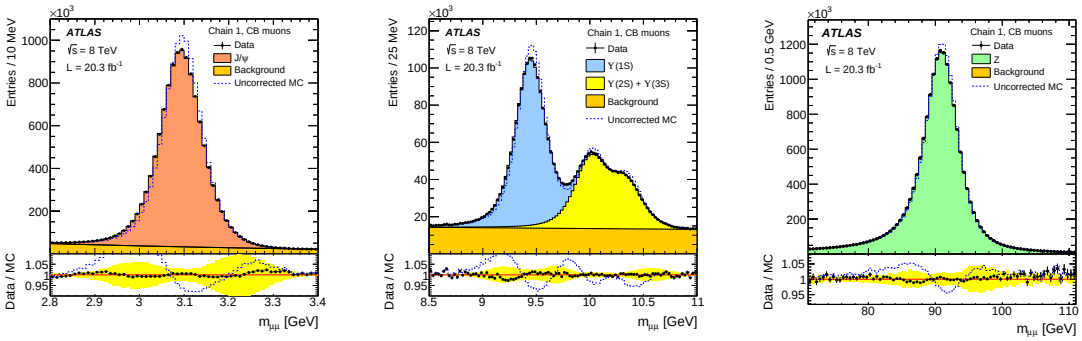

(a) $J/\Psi \to \mu\mu$ (b) $\Upsilon \to \mu\mu$ (c) $Z \to \mu\mu$

Figure 4.5: Data and predictions of the invariant mass of two mouns ($m_{\mu\mu}$) in J/Ψ, Υ and Z events [137].

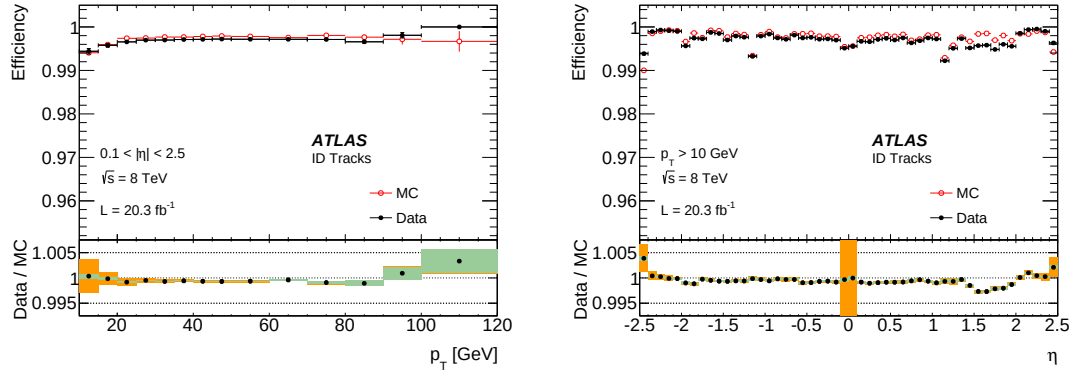

(a) (b)

Figure 4.6: Muon reconstruction efficiency in data and prediction binned in transverse momentum (a) and pseudorapidity (b) [137].

in MS to the tracks reconstructed in ID [137].. The muons that are reconstructed using information from both MS and ID are called combined (CB) muons.

The reconstruction efficiency of muons is measured using a tag and probe technique in $Z \to \mu\mu$ events, similar to the one described for electrons in the previous section. Figure 4.6 shows the reconstruction efficiency vs p_{T} and η in both data and MC simulation. The efficiency is $\approx 99\%$ and is limited by lack of coverage of the MS at $|\eta| < 0.1$ and $1.1 < |\eta| < 1.3$. Differences in the efficiency measurement for data and MC simulation are corrected by applying scale factors to the MC simulated events.

Muons are most often used in ATLAS as the electroweak decay products of W and Z bosons. However, they are also produced in the decays of some hadrons, but muons from these processes can be rejected by requiring that the muon is isolated in the detector, both in ID and in the calorimeters.

4.4 Jets originated from hadrons

Due to color confinement, quarks and gluons produced in pp collisions, fragment and hadronize, and manifest themselves as a cone of collimated particles in the final state. The particles are clustered into physically measurable objects, referred to as *jets*. In terms of the detector signature, jets can be loosely defined "as a cone of tracks", and energy deposits in the calorimeters, and thus should be considered as a composite object in $\eta - \phi$ space. Jets in the ATLAS detector are fully reconstructed in order to unfold the kinematics of the particles or partons that generated the jets to the energy measured in the detector. First, the calorimeter energy deposits are associated to a single jet with a jet finding algorithm. Subsequently, a calibration procedure is used to translate the signals read out from the calorimeters into a measurement of the energy of the particles forming the jet.

4.4.1 Jet reconstruction

Jets can be reconstructed from tracks in the ID (*track jets*) or from the energy deposits in the calorimeter (*calo jets*). The reconstruction of jets starts by combining basic calorimeter cells (both electromagnetic and hadronic) clustered into three-dimensional energy deposits exploiting the longitudinal and transverse calorimeter

segmentation. These clusters of cells are called *topoclusters* and are used as inputs to the jet finding algorithms [138].

A jet algorithm is required to be well behaved against possible QCD divergences such as infrared and collinear emissions. Both infrared and collinear emissions manifest themselves as soft particles radiated by the primary partons. The number of jets in the jet finding algorithm should not be altered by the presence or absence of soft particles. Furthermore, jets should not be sensitive to particles radiated at very small angle with respect to the original parton. In addition, a jet algorithm should reproduce the sample physics in the final state regardless of the input type: partons, particles and calorimeter objects. Beside the theoretical requirement, a jet algorithm should also follow experimental guidelines, which include: independence of detector technology, minimal effect on spatial and energy resolution (beyond intrinsic detector limitations), stability with luminosity (i.e. control of underlying event and pile-up contributions), ease of calibration and efficient use of computing resources.

Several jet finding algorithms are studied in ATLAS and a anti-k_t [139] algorithm is used as a default method. The algorithm sequentially recombines the input objects based on the distance, d_{ij}, between them and the distance between the beam and the object, d_{iB}. The definition of d_{ij} and d_{iB} are shown in equations 4.1 and 4.2 respectively.

$$d_{ij} = \min\left(k_{T,i}^{-2}, k_{T,j}^{-2}\right) \frac{\Delta R_{ij}^2}{R^2} \tag{4.1}$$

$$d_{iB} = k_{T,i}^{-2} \tag{4.2}$$

Where, $k_{T,i}$ is the transverse momentum of the object i, ΔR is the seperation of the two objects in $\eta - \phi$ space. The parameter R is the distance parameter and can be considered as a weight to seperation of the two objects. The larger the R, the wider the jets and R =0.4 is used for this algorithm. If the minimum between all d_{ij} and d_{iB} is a d_{ij}, object i and j is recombined, otherwise object i is considered stable and is not included in the next iteration. With this algorithm, soft radiation is effectively clustered around the harder core of the process. The anti-k_t jets have a regular, conical shape which is experimentally desirable since it allows for a well defined jet area. The four-momentum of the jet is obtained from summing the four-momenta of its constituents in a way that conserves energy and momentum, and allows a meaningful definition of the jet mass.

4.4.2 Jet energy scale

Jets are reconstructed from the calorimeter energy deposits at the electromagnetic scale. The EM energy scale provides a baseline calibration for electromagnetically interacting particles and is determined using electron test-beam measurements. The local cell signal weighting (LCW) method is used to calibrate topoclusters for energy deposits from hadrons [140]. The LCW method uses information on the measured energy density and longitudinal shower depth to classify topoclusters as either electromagnetic or hadronic. Since the calorimeters are non-compensating – response to hadrons is lower than response to EM particles, a calibration scheme is required to restore the correct hadronic energy scale starting from the electromagnetic scale. In addition, several corrections are applied to account for pileup effects, origin of

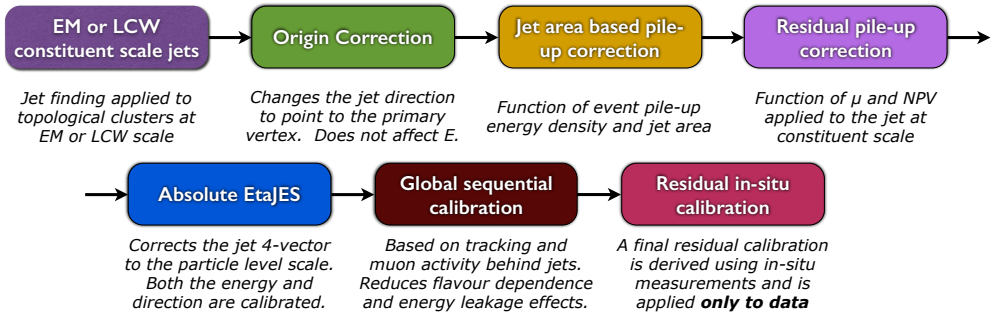

Figure 4.7: Schematic representation of the various stages used in the calibration of EM and LCW jets [141].

primary vertex, energy lost in the non-instrumented regions of the calorimeter and to improve the energy resolution. The subsequent steps in the calibration process is shown in Fig. 4.7 and discussed in the following sections [141].

Origin correction: Calorimeter jets are reconstructed using the geometrical center of the ATLAS detector as reference to calculate the four-momentum of the constituents. The direction of each topocluster or tower in a jet is corrected to point back to the primary vertex (highest $\sum p_{T,\text{track}}^2$) in the event. Figure 4.8 shows the effect of origin correction on the η and ϕ resolutions.

Pile-up correction: The energy of jets can include energy that does not come from the interaction of interest, but is instead produced from multiple proton-proton interactions within the same bunch crossing. To reduce the effects of such contribution, an area based subtraction method is used [142], which removes the effect of pile-up by using the pile-up energy density (ρ) in the $\eta - \phi$ plane. Figure 4.9(a) shows the ρ distribution for events with different number of reconstructed primary

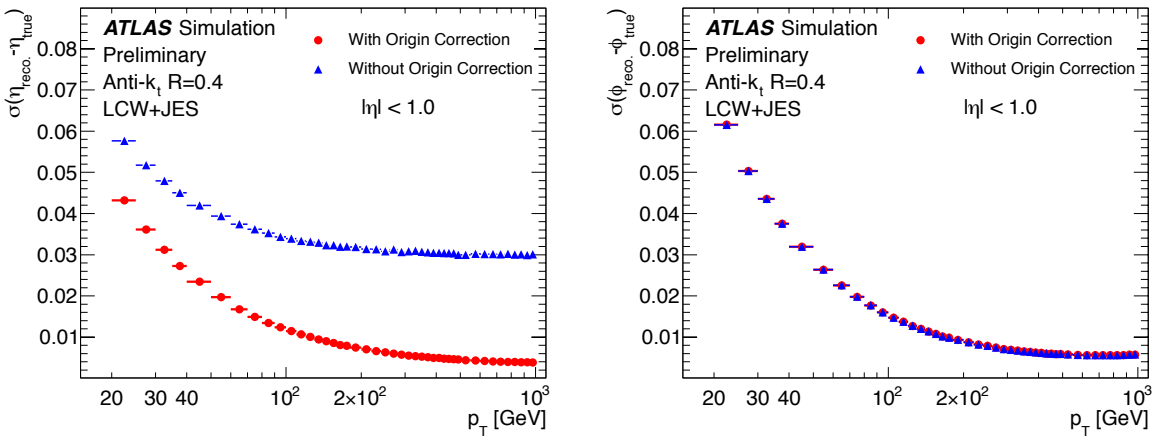

(a) (b)

Figure 4.8: The effect of the origin correction on the η resolution (vertical axis) (a) and ϕ resolution (vertical axis) (b) for $R = 0.4$ jets [141].

vertices (N_{PV}), as expected, the ρ increases with the increase of N_{PV}. After the area based correction, a small dependence of the jet-p_{T} on the pile-up remains and a residual correction is applied. This residual correction is parameterized in terms of N_{PV} and the average number of interactions per bunch crossing $\langle\mu\rangle$. Figure 4.9(b) shows the dependence of jet-p_{T} before and after pile-up correction.

Jet Energy Scale calibration: The jet energy scale (JES) calibration corrects for detector effects such as calorimeter non-compensation, energy leakage outside of jet cone, dead material. The calibration is derived as a correction that relates the reconstructed jet energy to the particle level truth jet energy [140]. The correction factors are derived in MC simulated events by taking the mean of the calorimeter response to jets, referred to as jet response, $\mathcal{R}$, in bins of p_{T} and η. The jet response is defined as the ratio of the reconstructed jet energy (pile-up corrections applied) and the energy of the same jet from stable simulated particles, i.e. $\mathcal{R} = E^{\mathrm{reco}}/E^{\mathrm{truth}}$.

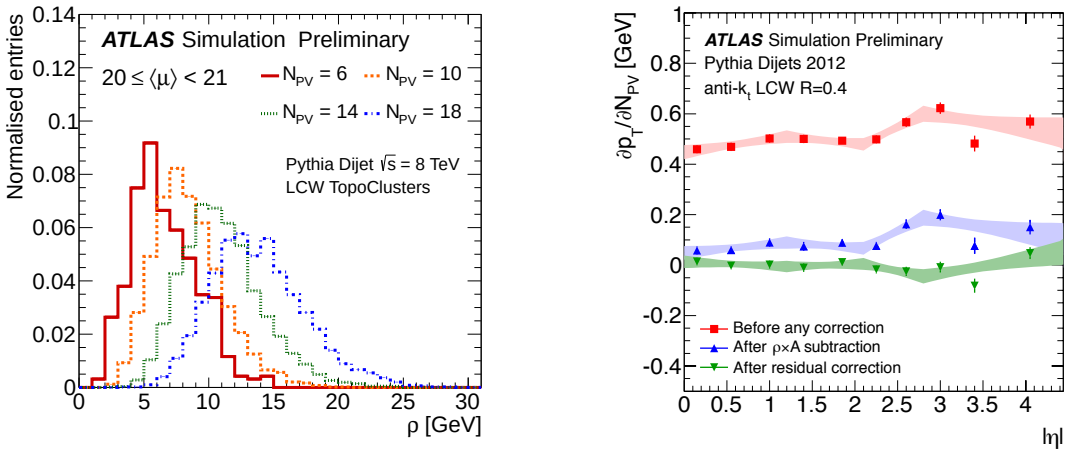

(a) (b)

Figure 4.9: (a) Distribution of the event p_{T} density, ρ, for an average number of interactions $20 < \langle\mu\rangle < 21$, for four different values of N_{PV}. (b) Dependence of the reconstructed jet-p_{T} at various correction stages in bins of jet-$|\eta|$ [141].

The correction factors are then obtained by taking the inverse of the mean of a Gaussian fit to the jet response distribution, i.e. $1/\langle\mathcal{R}\rangle$ [140]. Figure 4.10 shows the jet energy response in bins of η before and after the calibration is applied.

Global sequential correction: The calorimeter response to jets is sensitive to differences in fragmentation between light quark (LQ) and gluon initiated jets in different physics processes. The JES calibration scheme does not take into account the difference of response between LQ and gluon initiated jets, which is observed to be up to 8% [140]. To reduce this difference between the jet responses and thereby improve both jet resolution and jet energy scale uncertainties, further corrections, referred to as global sequential (GS) correction [143], are applied following the JES calibration. The corrections are applied depending on the topology of energy deposits in the calorimeter, tracking information and muon spectrometer information. Corrections

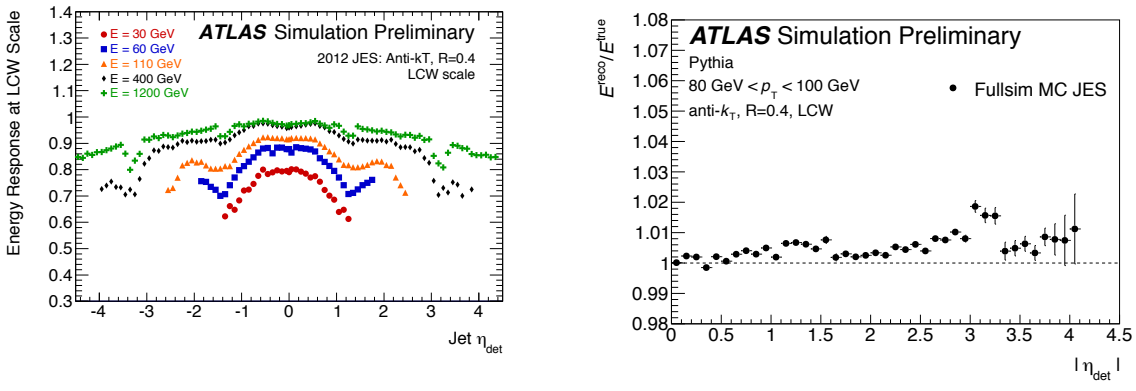

(a) (b)

Figure 4.10: Jet energy response as a function of η_{det} (the η of the jet relative to the geometric center of the detector) before calibration (a) and after calibration (b) for anti-k_t, $R = 0.4$ jets at LCW scale [141].

are applied sequentially and in such a way as the mean jet energy response is left unchanged. Figure 4.11 shows the performance of the GS correction for quark and gluon initiated jets.

In-situ energy calibration: To verify the MC-based calibration of jets, jet responses are also calculated in-situ, using p_{T} balance of physics objects in the transverse plane. The p_{T} of reference objects (e.g. photons, Z bosons or other jets) and the jet being calibrated are compared in both data MC simulation to measure the ratio,

$$\frac{\mathcal{R}_{\text{data}}}{\mathcal{R}_{\text{MC}}} = \frac{\langle p_{\text{T}}^{\text{jet}} / p_{\text{T}}^{\text{ref}} \rangle_{\text{data}}}{\langle p_{\text{T}}^{\text{jet}} / p_{\text{T}}^{\text{ref}} \rangle_{\text{MC}}}. \tag{4.3}$$

First, dijet events are used to calibrate the average p_{T} of the forward jets ($0.8 \leq |\eta| < 4.5$) against jets in the central region ($|\eta| < 0.8$) to remove the dependence of the calorimeter response on pseudorapidity [144]. Figure 4.12(a) shows these relative

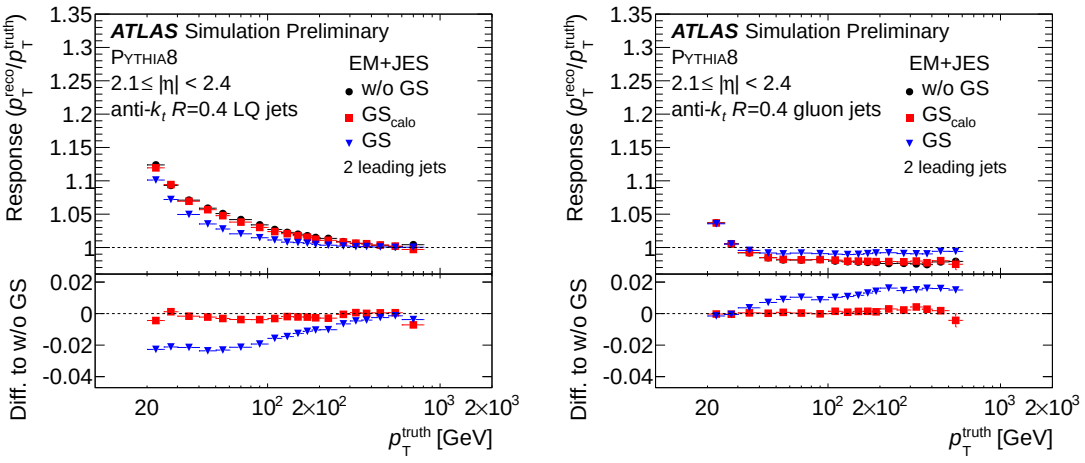

(a) (b)

Figure 4.11: Average jet response as a function of $p_{\mathrm{T}}^{\mathrm{truth}}$ for light quark (LQ)-initiated jets (a) and gluon-initiated jets (b). The average jet response after the EM+JES calibration without GS corrections (black circles), with calorimeter based GS corrections only (red squares) and including all the GS corrections (blue triangles) are shown. Only the two highest p_{T} jets in each event, reconstructed with the anti-k_t algorithm with R=0.4, are used. The lower part of each subfigure show the difference between the average jet response with the GS corrections and the average jet response at the EM+JES scale without the GS corrections [143].

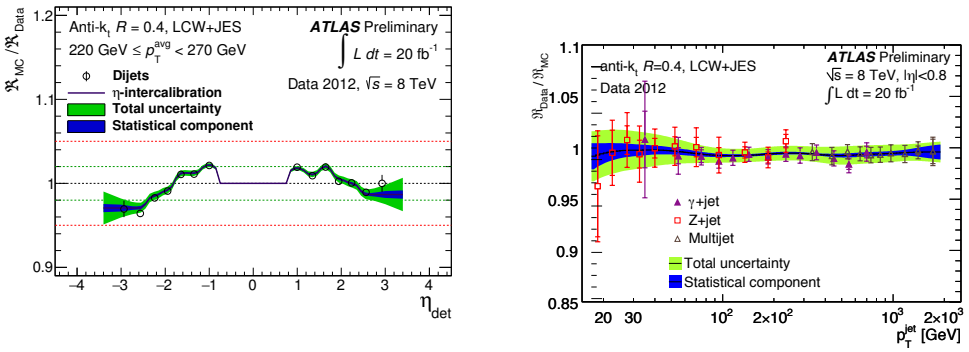

(a) (b)

Figure 4.12: (a) Relative jet response as a function of η_{det} (the η of the jet relative to the geometric centre of the detector) for anti-kt, R = 0.4, LCW jets. In the central region ($|\eta| < 0.8$) there is no calibration by construction. (b) Ratio of total response measured in data to response measured in data for Z+jet, γ+jet and multi-jet balance in-situ analyses [141].

jet response against pseudorapidity, from which the calibration factors are defined. In the next step, the balance of Z bosons and photons recoiling against jets is used to derived corrections for jets in the central region ($|\eta| < 0.8$) [144]. Finally, high-p_{T} jets are calibrated using events in which a system of low-p_{T} jets recoil against a single high-p_{T} jet in multi-jet processes [144]. Figure 4.12(b) summarizes the results of the $Z+$jets, $\gamma+$jets and multi-jet balance analysis showing the results of jet response in data and MC. The divergence of the response from unity defines the total in-situ correction and is applied to jets in data.

4.4.3 Jet energy scale uncertainty

The jet energy scale uncertainty has multiple components including statistical and systematic uncertainties from relative and absolute in-situ measurements, uncertainties associated to pile-up corrections and uncertainties due to jet flavor composition. The size of these uncertainties in events with an unknown flavor composition is shown in Fig. 4.13 for representative p_{T} and η regions. The effect of these uncertainties on the cross-section measurement presented in this thesis, is summarized later in Section 5.8.3.

4.4.4 Jets initiated by b-quarks

Jets which originate from the fragmentation of b-quarks, are referred to as b-jets. The significant lifetime of B-hadrons can be used to distinguish b-jets from jets originating from lighter sources like gluons or u-quarks [145]. An example of the B-hadron decay vertex is shown in Fig. 4.14(a).

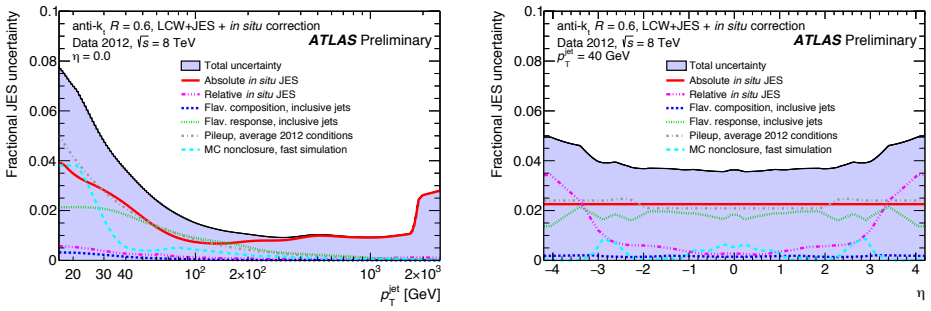

(a) (b)

Figure 4.13: Jet energy scale uncertainties (a) versus p_{T} in the central region and (b) versus η for jets with $p_{\mathrm{T}} = 40$ GeV [141].

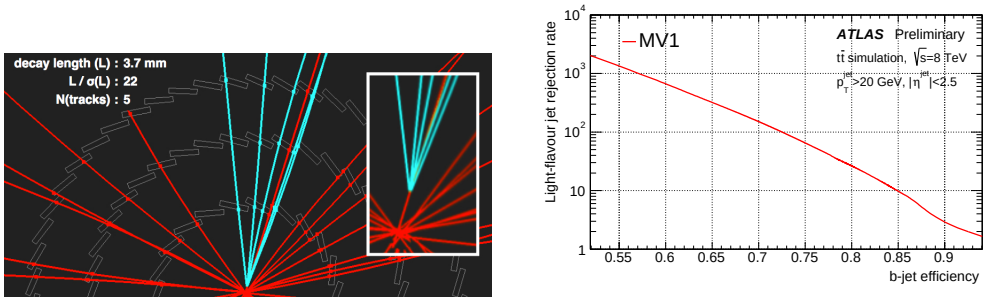

(a) (b)

Figure 4.14: (a) Event display of a displaced vertex consistent with the decay of a B-hadron [146] (b) Efficiency of MV1 algorithm for b-jet identification in simulation as a function of light jet rejection [145].

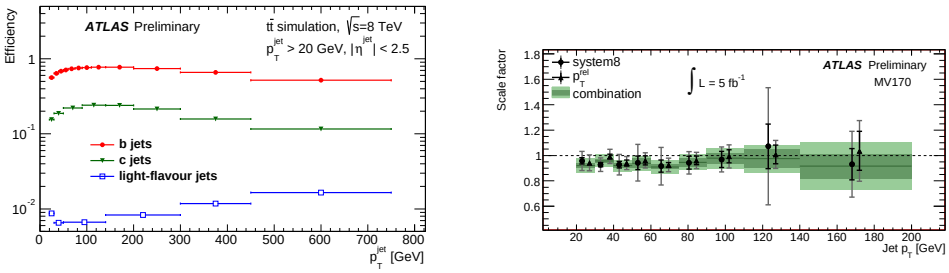

(a) (b)

Figure 4.15: (a) The efficiency of MV1 algorithm to select b-jet, c-jets or light-jets as a function of jet-p_{T} [145] (b) The b-taggging efficiency scale factors for the system8 method in data and MC simulation [147].

The b-jets can be identified through various algorithms based on impact parameters or secondary vertices. All these discriminating variables are used as an input to a multivariate algorithm, called the MV1 [145]. Figure 4.14 shows the output of the MV1 algorithm, where each point corresponding to a certain b-jet identification (b-tag) and light-jet rejection efficiency. Three different working points corresponding to three b-tag efficiency points are defined. The performance of the MV1 algorithm at 70% working point is shown in Fig. 4.15(a) and is measured in MC simulation. The b-tag efficiency is also measured in data using different methods. The system8 method discussed in detail in Reference [147], is used in this thesis to measure the b-tag efficiency in data. Figure 4.15(b) shows scale factors calculated by taking the ratio of the efficiencies measured in simulation and in data for the 70% working point of the MV1 algorithm, as a function of jet-p_{T}. These scale factors are applied to MC simulated events to account for the disagreement between data and simulation.

4.5 Tau leptons

The tau lepton is the final state particle of interest in this thesis. The tau lepton is a third generation fermion, first discovered in 1975 by Martin Pearl at the Mark I detector of the SPEAR e^+e^- collidier [148, 149]. The associated tau neutrino was first inferred from the Z boson width measurement [150] in 1990 and then discovered directly in 2000 by the DONUT experiment [151].

The taus lepton is the heaviest charged lepton with a mass of $\approx$1.8 GeV [32] and is the only lepton that can decay to hadrons. Their lifetime $c\tau = 87\,\mu\mathrm{m}$, however, is

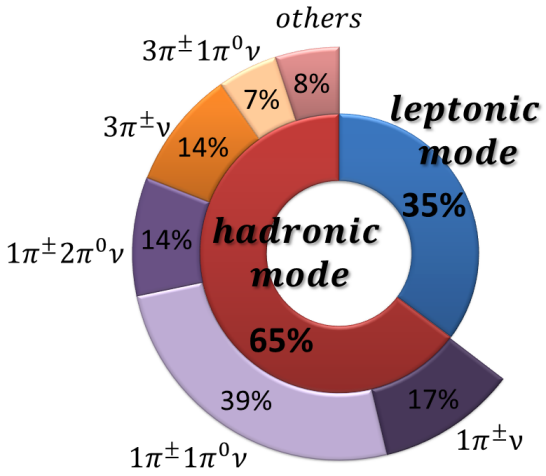

Figure 4.16: Pie chart of tau lepton decay modes. The branching ratios of hadronic decays are shown as the fraction of the total hadronic decay modes.

very short and tau leptons produced in the pp collisions at the LHC typically decay within the ATLAS beam pipe. Therefore, tau leptons can only be identified through their decay products which are observed in the ATLAS detector. Tau leptons decay leptonically ($\tau \to l\nu_l\nu_\tau$, $l = e, \mu$) and hadronically ($\tau \to$ hadron(s) ν_τ) in 35% and 65% of all decays, respectively. A pie chart of the tau lepton decay modes with corresponding branching fractions is shown in Fig. 4.16. These decay products can be used for reconstruction and identification of tau leptons.

To identify a tau lepton through its decay to light leptons (e, μ), the leptons need to be distinguished from prompt leptons in decays of W and Z bosons. The leptons from tau decay are less energetic due to the presence of two additional neutrinos ($\tau \to l\nu_l\nu_\tau$) compared to the prompt leptons ($W \to l\nu_l$, $Z \to ll$). However, the only useful quantity that can be used for their discrimination is the displaced tau vertex (i.e. the tau decay vertex different from the primary vertex). But due to the short

lifetime of the tau lepton, the discrimination power of the displaced tau vertex is weak. Therefore, in ATLAS, the leptons from tau decay is largely indistinguishable from the prompt leptons and only the hadronic decay mode is used to identify tau leptons.

In the hadronic decay mode, the final state predominantly consists of one or three charged pions, a associated tau neutrino and in some cases a few additional neutral pions. There are also some rare decays involving kaons, with a branching ratio of 2.9%. Majority of the hadronic decays of the tau lepton proceed through intermediate mesons like the $\rho^{\pm}(770\,\mathrm{MeV})$ and $a_1^{\pm}(1260\,\mathrm{MeV})$:

$$\tau \to \nu\rho^{\pm} \to \pi^{\pm}\pi^{+}\pi^{-}\pi^{0}\nu \qquad\qquad \tau \to \nu a_1^{\pm} \to \pi^{\pm}2\pi^{0}\nu$$

The hadronic decay mode, is generally characterized by the number of charged decay products, that is, the number of tracks or "prongs" observed in the detector. The hadronic $\tau_{\text{1-prong}}$ is the dominant decay mode with branching ratio (BR) of $\approx$ 49.5%, while the $\tau_{\text{3-prong}}$ has a BR of $\approx$ 15.2%. For reconstruction and identification purposes, however, only the visible hadronic decay products are used, as the neutrino escapes the ATLAS detector volume without being detected. The visible part of the hadronic decay mode, will henceforth be referred to as a hadronic tau (τ_{had}).

The identification of τ_{had} is challenging, as the detector signature for hadrons are jets as discussed in Section 4.4 and jets from tau decays have to be differentiated from quark or gluon initiated jets. This is especially difficult in hadron colliders where the cross section from QCD production of quark or gluon initiated jets is many orders

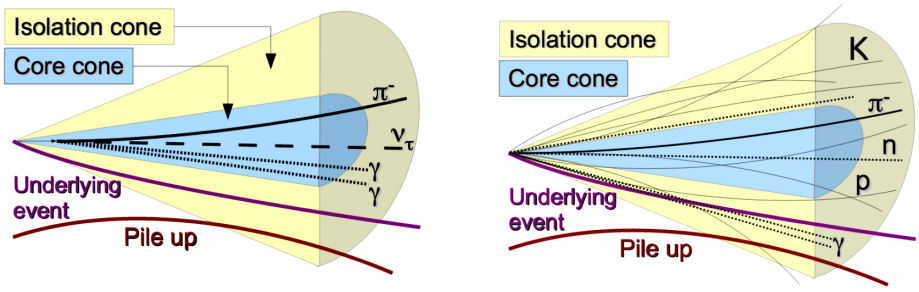

(a) (b)

Figure 4.17: Illustration of a hadronically decaying tau lepton (a) and a QCD induced jet (b). The track multiplicity inside a jet of cone $\Delta R = 0.4$ is lower for a tau lepton initiated jet compared to a QCD jet. The tau decay products are boosed, so that they are confined in a *core cone* ($\Delta R < 0.2$), leaving the *isolation annulus* ($0.2 < \Delta R < 0.4$) relatively empty, resulting in a narrow track clustering and calorimeter energy deposit [154].

of magnitude larger than the weak interaction processes involving tau leptons. For example, at $\sqrt{s} = 7$ TeV, the jet production cross section is $\approx 4 \times 10^3$ nb [152], while the cross section for $W \to \tau_{\text{had}}\nu$ is 6.8 nb [153]. Nonetheless, a few characteristic features of hadronic tau decays such as, low track multiplicity, narrow clustering of tracks and energy deposit, and existence of a possible displaced secondary vertex can be used to discriminate against QCD jets. Figure 4.17 illustrates the characteristic features of a hadronic tau decay and a QCD jet.

The reconstruction and identification process of hadronic tau occurs after tracks and clusters are reconstructed and the jet finding algorithm is used to reconstruct jets. First, τ_{had} reconstruction is seeded by each reconstructed jets. The list of calorimeter clusters associated to each hadronic tau candidate is then refined and calibrated to calculate the four momentum. Tracks are then associated to each candidate, and a list of identification variables is calculated from the combined track

and calorimeter information. The list of identification variables are combined into a multivariate discriminant to reject jets and electrons that can mimic (*fake*) a τ_{had} candidate. A cut based method is also used to reject muons that can fake a τ_{had}. The different algorithms used in these steps and their performance are described in the following sections [155] :

4.5.1 Reconstruction and energy calibration

Jet seeding: The τ_{had} reconstruction starts with the jets that are reconstructed using anti-k_t algorithm with cone size $R = 0.4$, from topoclusters that are calibrated using a local hadron calibration (LC) (see Section 4.4.1) as seed. Each such jet with $p_{\text{T}} > 10$ GeV and $|\eta| < 2.5$, is considered as a τ_{had} candidate. The initial τ_{had} four-momentum is calculated by summing the four-momentum of the constituent topoclusters within a cone of $\Delta R < 0.2$ (referred to as *core cone*) around the direction of the seeded jet. The mass of the τ_{had} is assumed to be identically zero, and therefore the transverse momentum, p_{T}, and the transverse energy, $E_{\text{T}} = E \sin\theta$, are identical.

Track and vertex association: Reconstructed tracks (see Section 4.1) are associated to each τ_{had} candidate, if they are within the core cone and satisfy the following criteria:

- $p_{\text{T}} > 1$ GeV,
- at least two hits in the pixel layer,
- at least seven hits in the pixel and SCT layers combined.

Tracks satisfying the same quality criteria within an *isolation annulus*, defined as, $0.2 < \Delta R < 0.4$ around the direction of the seeded jet, are also counted and are used for calculating identification variables.

In the next step, reconstructed vertices (see Section 4.1) are used to estimate the tau decay vertex (the vertex from which τ_{had} originates, denoted as TV), which is not necessarily the primary vertex of the event. A quantity, referred to as the tau vertex fraction (TVF), is defined as the ratio of track momenta originating from a certain vertex to the total track momenta:

$$\text{TVF} = \frac{\sum p_{\text{T}}^{\tau_{\text{had}}\text{tracks associated to a vertex}}}{\sum p_{\text{T}}^{\tau_{\text{had}}\text{tracks}}}. \tag{4.4}$$

The vertex that maximizes the TVF, is chosen to be the tau vertex. The is vertex association is called the Tau Jet Vertex Association (TJVA) algorithm [155]. Figure 4.18 shows the robustness of TJVA algorithm against pile-up compared to the default algorithm to associate primary vertex.

Once, the tau decay vertex is determined, following requirements on the impact parameter of the associated tracks are applied:

- $|d_{0,\text{TV}}| < 1.0\,\text{mm}$, where, $d_{0,\text{TV}}$ is the transverse impact parameter from the tau decay vertex.
- $|z_{0,\text{TV}} \sin\theta| < 1.5\,\text{mm}$, where $z_{0,\text{TV}}$ is the longitudinal impact parameter from the tau decay vertex.

τ_{had} candidates are classified as single- or multi-prong based on this set of tracks. The

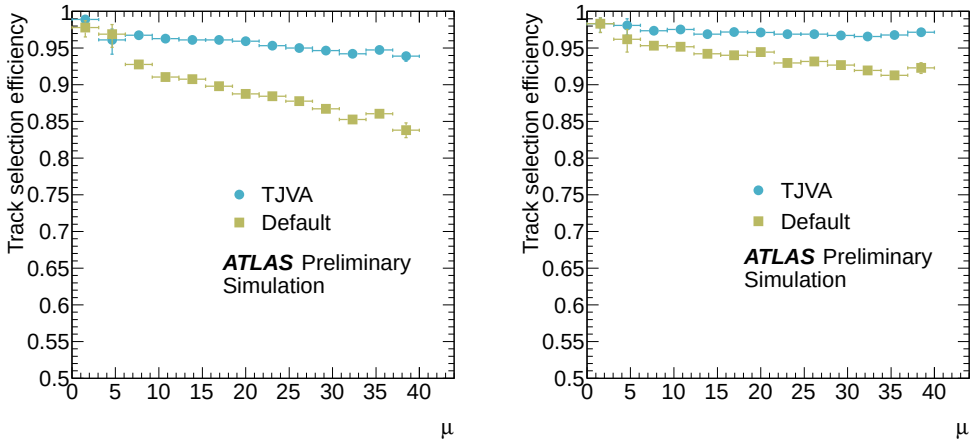

(a) (b)

Figure 4.18: Track selection efficiency for τ_{had} candidates with the default algorithm to find primary vertex ($\sum p_{\text{T}}^2$) and the TJVA algorithm to find tau decay vertex as a function of pile-up, for true $\tau_{\text{1-prong}}$ (a) and $\tau_{\text{3-prong}}$ (b) in simulated events [156].

charge of the τ_{had} candidate is determined by summing the charges of the associated tracks in side the core cone.

Energy calibration: The four-momentum of the τ_{had} candidate, at this stage, is at the LC scale and can be denoted as, E^{LC}, η^{LC}, and so on. The hadronic tau decays, however, consist of a specific mixture of charged and neutral pions, therefore, the energy scale of hadronic tau is calibrated independent of the jet energy scale. The calibration is applied as a correction, to bring the τ_{had} energy from the LC scale to the energy scale of a true visible hadronic tau, and accounts for effects such as, pile-up, the underlying event, and clusters falling out of core cone. This energy scale is referred to as tau energy scale (TES) and improves the energy resolution of τ_{had} candidates compared to the jet energy calibration.

The correction is derived in simulated $Z \to \tau\tau$, $W \to \tau\nu$, and $Z' \to \tau\tau$ events

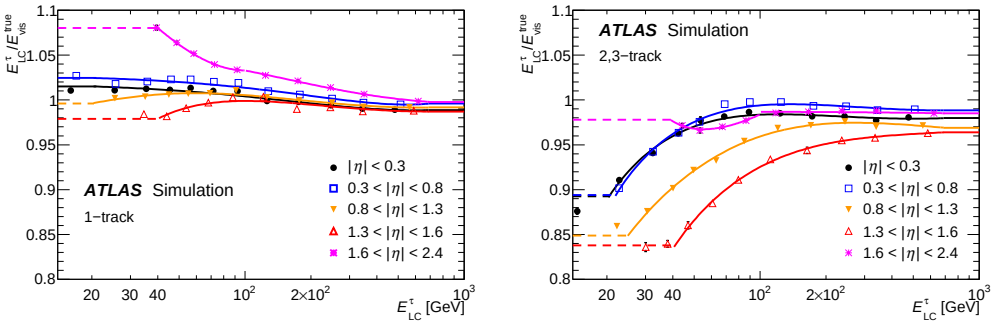

(a) (b)

Figure 4.19: τ_{had} energy response curves measured in simulated events, for τ_{had} associated with 1-track (a) and 2,3-track (b), as a function of the pre-calibration energy at the LC scale, E^{LC} [155].

where the true visible τ_{had} energy, E^{true}, is known, by defining a response function:

$$\mathcal{R}\left(E^{\text{LC}}\right) = \frac{E^{\text{LC}}}{E^{\text{true}}}. \tag{4.5}$$

Figure 4.19 shows the response curve as a function of pre-calibrated τ_{had} energy at the LC scale. The correction from these response curves, brings the mean energy of the reconstructed τ_{had} within 2% of the true visible energy.

A further correction is applied on the pseudorapidity to account for the bias from poorly instrumented regions of the detector. The correction is smaller than 0.01 units in the transition region between the barrel and endcap of the electromagnetic calorimeter and is negligible elsewhere. Finally, the effect of pile-up is corrected by subtracting an amount of energy proportional to the number of reconstructed primary vertices, in bins of pseudorapidity. The resulting τ_{had} energy resolution is shown in Fig. 4.20. The resolution is about 20% at very low energy and reduced to about 5% for energies above a few hundred GeV.

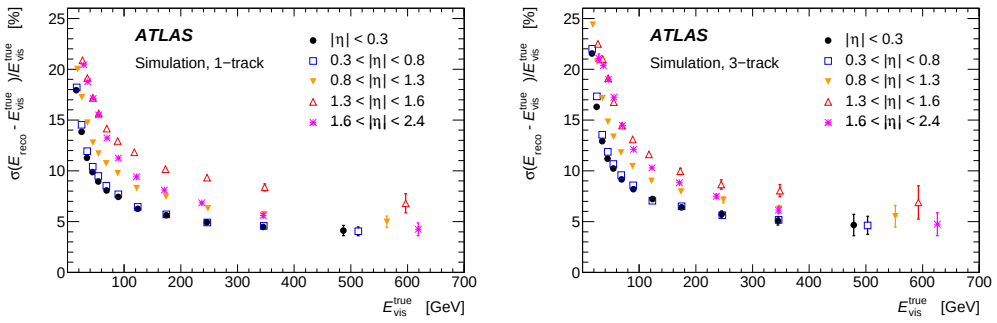

(a) (b)

Figure 4.20: τ_{had} energy resolution measured in simulated events, for τ_{had} associated with 1-track (a) and 3-track (b), as a function of the true visible energy [155].

To verify the calibration method derived in MC simulation and to calculate the systematic uncertainties, data driven methods are used to derive the energy calibration in two complementary methods: the *deconvolution* method and the *in-situ* method. The decomposition method relies on τ_{had} having a known composition of charged and neutral hadrons such that the response can be decomposed into individual sources. For charged hadrons, the response is estimated from test beam measurements and simulation with varied hadronic shower models. For showers from neutral pions, the response is estimated from $Z \to ee$ process. Pseudo-experiments are then designed to propagate and combine the single particle response uncertainties according to their branching ratio to the reconstructed τ_{had}.

The in-situ method relies on the sensitivity of the visible invariant mass, m_{vis}, in $Z \to \tau_{\mu}\tau_{\text{had}}$ events to the τ_{had} energy to measure a TES shift between data and simulation. Figure 4.21 shows the invariant mass distribution of two tau leptons, where one decays leptonically to a muon and the other decay hadronically and is measured in both data and simulation. Relative to τ_{had}, the muon energy is precisely

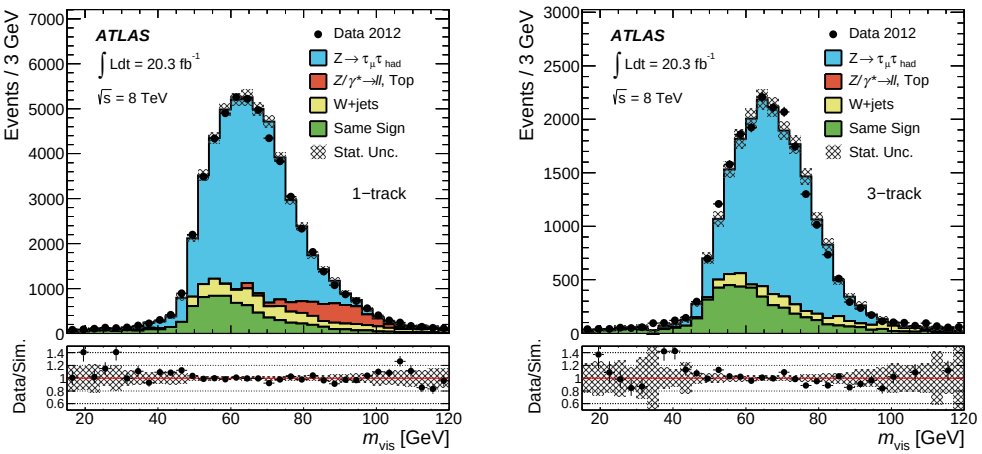

(a) (b)

Figure 4.21: The distribution of invariable mass, m_{vis} of two tau leptons, where, one decay leptonically to a muon and the other decay hadronically with 1-track (a) and 3-track (b), measured in data and simulation [155].

calibrated and validated in data with $Z \to \mu\mu$ events. The τ_{had} energy is then allowed to float like $(1+\alpha)E_{\text{T}}$ and the value of α for which m_{vis} agrees between data and simulation is calculated. The parameter α, is a measure of the TES shift and is estimated to be:

$$\alpha_{1-\text{track}} = 0.8\% \pm 1.3\%(\text{stat.}) \pm 0.6\%(\text{syst.}) \tag{4.6}$$

$$\alpha_{3-\text{track}} = 1.1\% \pm 1.4\%(\text{stat.}) \pm 0.7\%(\text{syst.}) \tag{4.7}$$

The value of the TES shift is applied to the transverse momentum in data. The effect of these uncertainties on the cross section measurement presented in this thesis is discussed in Section 5.8.1.

4.5.2 Discrimination against jets

The reconstructed τ_{had} provides little rejection against the jet background, as each τ_{had} candidate is seeded from a jet. As discussed earlier, the overwhelming majority of particles observed at ATLAS are hadrons and distinguishing quark or gluon like jets from τ_{had} is therefore extremely important for physics with tau leptons.

The characteristics of τ_{had} that can provide discrimination against jet backgrounds are the following:

Track multiplicity: τ_{had} typically have 1 or 3 reconstructed tracks, while QCD jets have a higher track multiplicity.

Narrow shower shape: The tau leptons produced in the electroweak decays of W and Z bosons, are boosted and thus tend to be more narrow in tracker and calorimeter compared to jets. Furthermore, τ_{had} does not undergo the same broadening fragmentation as quark and gluons from QCD processes.

Displaced tau vertex: Tau leptons with a finite lifetime have a decay vertex different from the primary vertex. Thus, tracks from τ_{had} tend to be more displaced from the primary vertex compared to tracks in jets.

Figure 4.22 shows the characteristic signature of a τ_{had} with low track multiplicity and narrow energy deposit compared to b-jets.

For track multiplicity, a requirement of exactly 1 or 3 reconstructed tracks associated to τ_{had} is effective to reject QCD jets. For shower shape and vertex displacement, information from tracker and calorimeters are used to form discriminating variables.

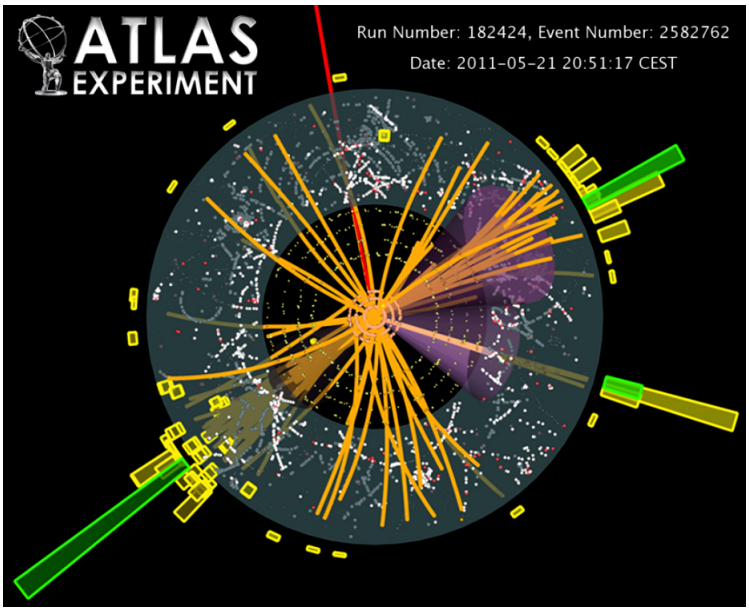

Figure 4.22: Event display of a $tt \to (b\mu\nu_\mu)(b\tau_{\text{had}}\nu_\tau)$ event in data [157]. The muon candidate is shown in red. The τ_{had} candidate has 3 tracks with narrow calorimeter energy deposite. The b-jet candidates each have more than 10 tracks with wider energy deposit.

The discriminating variables are combined into a multi-variate Boosted Decision tree (BDT) [158] algorithm and typically referred to as τ_{had} identification algorithm. The discriminating variables used as input to the BDT algorithm for jet discrimination are summarized in Table 4.1 and discussed below [155]:

Central energy fraction (f_{cent}): Fraction of transverse energy deposited inside a cone of $\Delta R < 0.1$ out of all energy deposited in a cone of $\Delta R < 0.2$, around the direction of the τ_{had} candidate. First, the total energy is calculate from the sum of the energy deposited in each constituent topoclusters. A correction based on the number of primary vertices in the event is then applied to remove biases due to pileup.

Leading track momentum fraction ($f_{\mathbf{track}}$): Ratio of the transverse momentum of the highest-p_{T}charged particle in a cone of $\Delta R < 0.2$ around the τ_{had} direction to the transverse energy sum in the same region. Biases due to pileup are removed by applying a correction based on the number of primary vertices in the event.

Track radius ($R_{\mathbf{track}}$): Distances of the all tracks in the core and isolation region from the τ_{had} direction. The distances are weighted by the p_{T} of the tracks.

Leading track interaction point (IP) significance ($S_{\mathbf{lead\ track}}$): Transverse impact parameter of the highest-p_{T} track with respect to the tau decay vertex divided by its estimated uncertainty.

Number of tracks in the isolation region ($N^{\mathbf{iso}}_{\mathbf{track}}$): Number of tracks associated to the τ_{had} in the isolation annulus, $0.2 < \Delta R < 0.4$.

Maximum ΔR ($\Delta R_{\mathbf{max}}$): The maximum ΔR between tracks associated to τ_{had} candidate in the core and the direction of τ_{had} candidate.

Transverse flight path significance ($S^{\mathbf{flight}}_{\mathbf{T}}$): The decay length of the secondary vertex (very reconstructed with tracks associated to τ_{had} candidate in the core region) in the transverse plane, divided by its estimated uncertainty. This variable is only defined for τ_{had} candidate with multiple associated tracks.

Track mass ($m_{\mathbf{tracks}}$): Invariant mass of the four-vector sum of all tracks associated to τ_{had} in the core and isolation regions.

Variable	1-track	3-track
f_{cent}	•	•
f_{track}	•	•
R_{track}	•	•
$S_{\text{lead track}}$	•	
$N_{\text{track}}^{\text{iso}}$	•	
ΔR_{max}		•
$S_{\text{T}}^{\text{flight}}$		•
m_{tracks}		•
$m_{\pi^0+\text{track}}$	•	•
N_{π^0}	•	•
$p_{\text{T}}^{\pi^0+\text{track}}/p_{\text{T}}$	•	•

Table 4.1: Discriminating variables used as input to τ_{had} identification algorithm for discriminating against jet backgrounds, for 1-track and 3-track candidates [155].

Track-plus-π^0-system mass ($m_{\pi^0+\text{track}}$): Invariant mass of the system composed of all tracks associated to τ_{had} and π^0 mesons in the core region.

Number of π^0 mesons (N_{π^0}): The number of π^0 mesons reconstructed in the core region.

Ratio track-plus-π^0-system p_{T} to total τ_{had} p_{T} ($p_{\text{T}}^{\pi^0+\text{track}}/p_{\text{T}}$): Ratio of estimated p_{T} using track and π^0 information to the calorimeter-only measurement.

The BDT algorithms are trained for $\tau_{\text{1-prong}}$ and $\tau_{\text{3-prong}}$ candidates separately. Figures 4.23 and 4.24 show the distribution of some of the important variables for $\tau_{\text{1-prong}}$ and $\tau_{\text{3-prong}}$ candidates respectively. The distributions are calculated in $Z \to \tau\tau$, $Z' \to \tau\tau$, $W \to \tau\nu$ simulated signal events and in multi-jet (QCD, all hadronic $t\bar{t}$ and $b\bar{b}$) background events selected in data. The output of the BDT algorithms is a weight distribution, where each weight correspond to a particular

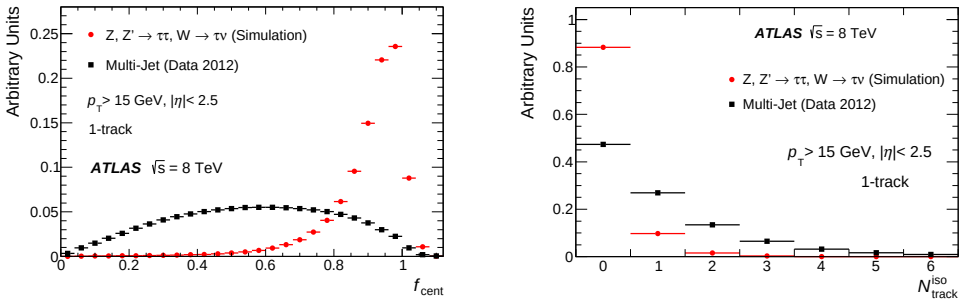

(a) (b)

Figure 4.23: Signal and background distribution for two of the variables used in 1-track τ_{had} BDT algorithm: (a) f_{cent} and (b) $N^{\text{iso}}_{\text{track}}$ [155].

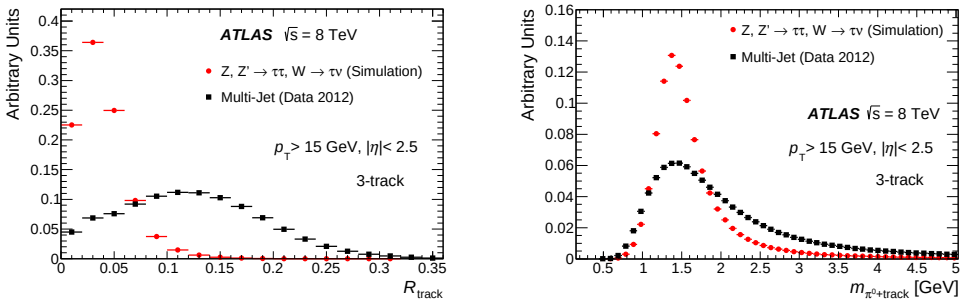

(a) (b)

Figure 4.24: Signal and background distribution for two of the variables used in 3-track τ_{had} BDT algorithm: (a) R_{track} and (b) $m_{\pi^0+\text{track}}$ [155].

signal and background efficiency. The signal efficiency is calculated as the ratio of the number of true reconstructed τ_{had} to the total reconstructed τ_{had}. The background efficiency is defined as the fraction of τ_{had} candidates that passes the identification criteria out of all reconstructed τ_{had} candidates, measured in background dominated sample. Three working points are defined labelled as *loose, medium, tight* corresponding to different efficiency values. Figure 4.25 shows output of the BDT algorithms corresponding to different efficiencies along with the three working points in different p_{T} regime, for 1-track and 3-track τ_{had} candidates.

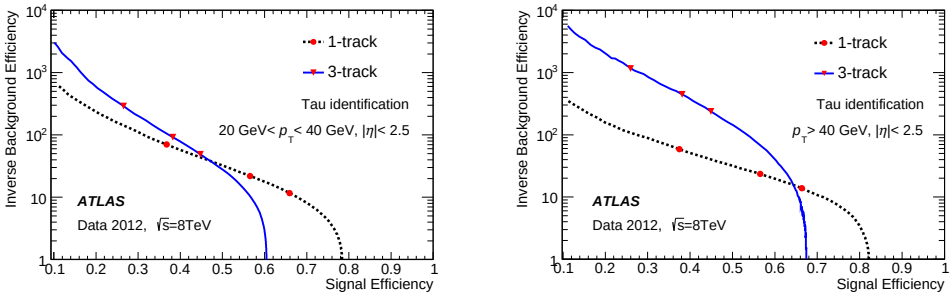

(a) (b)

Figure 4.25: Signal efficiency versus background rejection efficiency for 1-track and 3-track τ_{had} jet discrimination BDT algorithm for (a) 20 GeV $< p_{\text{T}} <$ 40 GeV and (b) $p_{\text{T}} >$ 40 GeV [155].

4.5.3 Discrimination against electrons

Electrons can mimic the characteristic signature of τ_{had} associated to 1-track, even those which fail dedicated electron identification algorithm discussed in Section 4.2. However, several distinguishing properties can be used to discriminate electrons from τ_{had}. Electrons produce narrower and shallow energy deposit in the calorimeter, and rarely any energy deposit in the hadronic calorimeter. In addition, electrons tend to produce more transition radiation in the TRT layer of the inner detector, compared to τ_{had}. These properties are used to calculate discriminating variables which are combined in another multivariate BDT algorithm referred to as electron veto algorithm. These input variables to the BDT algorithm is discussed below [155]:

TRT high threshold fraction ($f_{\text{TRT,HT}}$): This variable contains the transition radiation information and is calculated as the ratio of high-threshold to low-threshold hits on the TRT for the leading track. This ratio has a higher value for electrons compared to pions from τ_{had}.

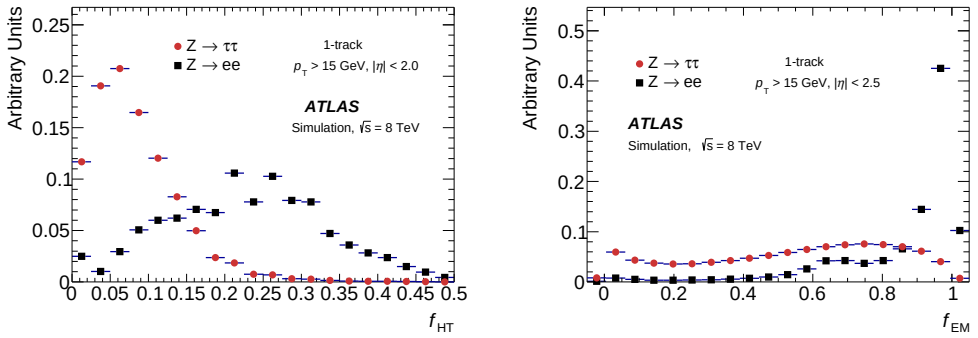

(a) (b)

Figure 4.26: Signal and background distributions for the TRT high threshold fraction (a) and EM fraction (b) in simulated events [155].

Pre-sampler and strip fraction ($f_{\mathbf{PS}}$): The fraction of cluster energy deposited in the pre-sampler and strips of the EM calorimeter.

Track-cluster $|\Delta\eta|$: The $|\Delta\eta|$ between the cluster and the leading track.

Track-cluster $|\Delta\phi|$: The $|\Delta\phi|$ between the cluster and the leading track.

Hadronic leakage ($f_{\mathbf{track}}^{\mathbf{Had.,0}}$): The ratio of the energy deposited in the first layer of the hadronic calorimeter to the leading track momentum.

EM fraction ($f_{\mathbf{EM}}$): The fraction of energy deposited in the EM calorimeter.

The discriminating variable are calculated in simulated $Z \to \tau\tau$ signal, and $Z \to ee$ background events, where only the τ_{had} candidate associated to 1-track is used. Figure 4.26 shows the distributions of two of the important variables. Separate BDT algorithms are trained for different η regions of the detector. The output of the BDT algorithms are weight distributions as shown in Fig. 4.27, where each point corresponds to different signal and background efficiencies. Similar to jet

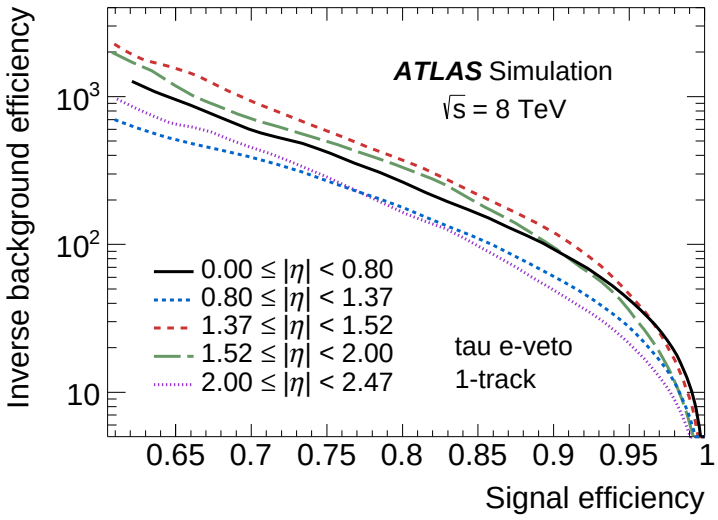

Figure 4.27: Electron veto inverse background efficiency versus signal efficiency in simulated samples [155].

discrimination, three working points, labelled *tight, medium,* and *loose* are chosen to yield signal efficiencies of 75, 85, and 95%, respectively.

4.5.4 Performance of the τ_{had} identification algorithms

The performance of the jet discrimination and electron veto algorithm can be seen in Fig. 4.28. A template fit is performed on the number of tracks associated to τ_{had} in $Z \to \tau_{\mu}\tau_{\text{had}}$ events, for both before and after the application for the τ_{had} identification requirements. The signal contribution in the 1-track and 3-track bins are more prominent after the identification requirements are applied, due to large amount of background rejection provided by the identification algorithms.

To verify the modeling of the input variables that are calculated using simulation, an in-situ method is used to calculate the efficiencies in $Z \to \tau_{\text{lep}}\tau_{\text{had}}$ events. A tag-and-probe method is implemented, where the lepton (μ for jet discrimination,

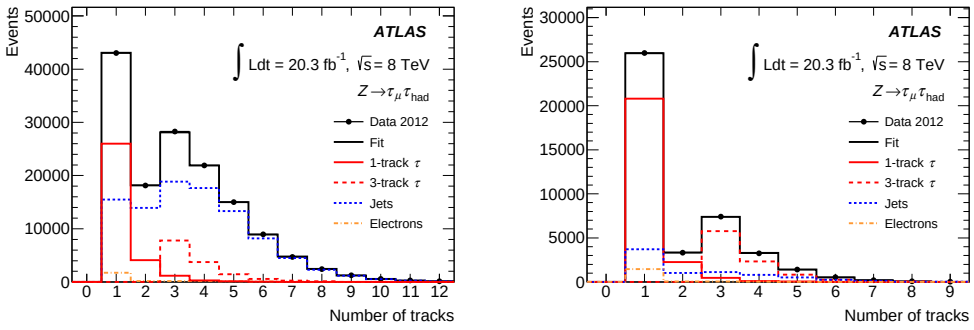

Figure 4.28: The performance of the τ_{had} identification algorithms. Results of the template fit in $Z \to \tau_{\mu}\tau_{\text{had}}$ events using a tag-and-probe method (a) before identification requirement and (b) after identification requirement [155].

and e for electron veto algorithm) from a tau lepton decay is tagged and a τ_{had} is probed which satisfies topological selections consistent with $Z \to \tau_{\text{lep}}\tau_{\text{had}}$ process. Correction factors are derived by comparing the efficiencies in data and simulation. Figure 4.29 shows the individual and combined correction factors derived for different pseudo-rapidity regions. These correction factors are then applied to simulated samples, to account for the slight discrepancy between data and simulated events. Uncertainties related to different sources such as, the underlying event, shower model, jet background fraction and tau energy scale on the signal and background efficiencies are also calculated. The effect of these uncertainties on the cross section measurement are discussed in Section 5.8.2.

4.5.5 Discrimination against muons

In addition to jets and electrons, muons can also mimic the characteristic signature of τ_{had} associated to 1-track. This is more rare than electron misidentified as τ_{had}

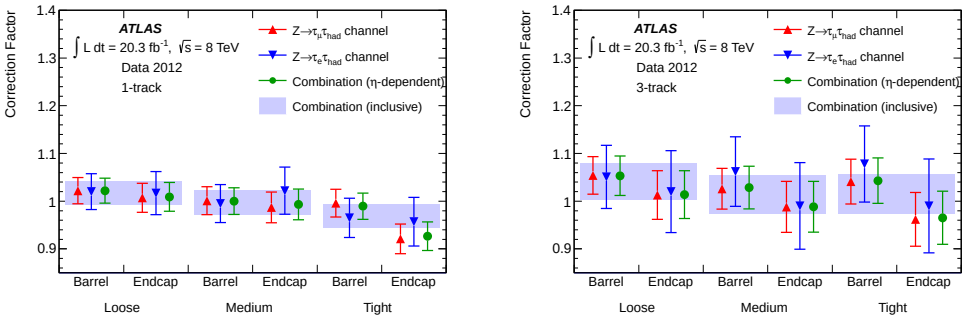

Figure 4.29: Correction factors for simulation for τ_{had} jet discriminant efficiency for 1-track (a) and 3-track (b) [155].

since muons are minimum ionizing particles and do not often deposit sufficient energy in the calorimeter to seed a τ_{had} candidate. However, if muons, deposit sufficient energy in the calorimeter and therefore fail muon spectrometer reconstruction or have sufficiently low p_{T} and stop in the calorimeter, they can be misidentified as τ_{had}. The former effect is characterized by a low EM energy fraction and a large ratio of track-p_{T}-to-E_{T} deposited in the calorimeter, while the later results in large EM energy fraction and small track-p_{T}-to-E_{T} ratio. Studies in $Z \to \mu\mu$ events have shown that only 2% of muon candidates arising from these effects are not reconstructed in the muon spectrometer. Most of these fake muon candidates are rejected using the dedicated muon identification algorithm discussed in Section 4.3. The remaining candidates are rejected by applying a cut based selection on the EM fraction and track-p_{T}-to-E_{T} variables with a signal efficiency of 96%.

4.6 Missing transverse momentum resulting from neutrinos

Neutrinos do not interact with the ATLAS detector volume and escape without detection. However, their presence can be inferred from momentum imbalance in the transverse plane since each pp collision should conserve the total momentum. The vector momentum imbalance in the transverse plane is obtained by taking the negative vector sum of the momenta of all particles detected in a collision, the magnitude of the resultant transverse momenta is denoted as, $E_{\mathrm{T}}^{\mathrm{miss}}$, and used as an experimental observable.

The calculation of the total momenta in the event is done in two steps. First, energy deposits in the calorimeters and tracks in the muon spectrometer are collected and their vector sum is calculated. This is referred to as the *hard term* in the $E_{\mathrm{T}}^{\mathrm{miss}}$ calculation. Tracks in the ID are used to account for the contribution from low-p_{T} particles which are missed in the calorimeters. Muons which cannot be reconstructed in the muon spectrometer due to low-p_{T} are recovered by matching extrapolated tracks from the ID. In the second step of $E_{\mathrm{T}}^{\mathrm{miss}}$ calculation, the tracks and calorimeter information unassociated to hard objects are combined, referred to as the *soft term* [159]. The calorimeter term can be further broken down to sum of the energy deposits from reconstructed objects, that is electrons, photons and jets. The τ_{had} is however treated as a jet in $E_{\mathrm{T}}^{\mathrm{miss}}$ calculation, i.e. no τ_{had} identification and energy calibration is applied.

$$E_{x,y}^{\mathrm{miss}} = E_{x,y}^{\mathrm{miss},e} + E_{x,y}^{\mathrm{miss},\gamma} + E_{x,y}^{\mathrm{miss,\ jets}} + E_{x,y}^{\mathrm{miss},\mu} + E_{x,y}^{\mathrm{miss,\ soft\text{-}term}} \tag{4.8}$$

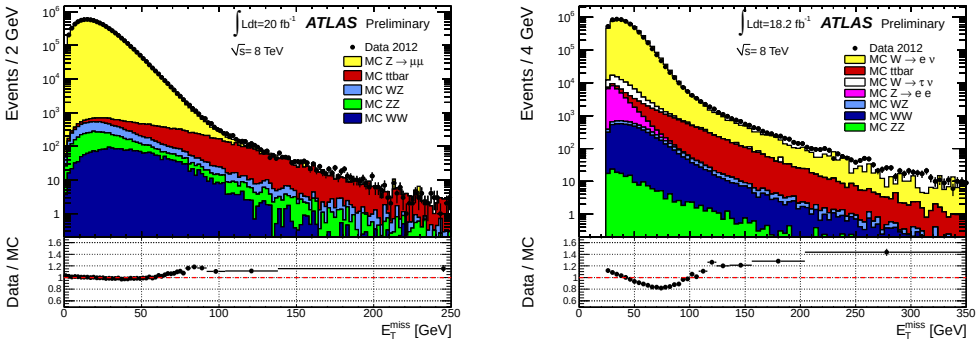

(a) (b)

Figure 4.30: The $E_{\mathrm{T}}^{\mathrm{miss}}$ distributions calculated in simulation and data corresponding to (a) fake contributions in $Z \to \mu\mu$ events (b) real contributions in $Z \to e\nu$ events [159].

The performance of the $E_{\mathrm{T}}^{\mathrm{miss}}$ calculation are studied in $Z \to ll$ and $W \to l\nu$ events, where the $E_{\mathrm{T}}^{\mathrm{miss}}$ originates from fake or real sources, respectively. Mis-reconstructed or mis-calibrated objects, detector inefficiencies and imperfect energy resolution are examples of fake sources of $E_{\mathrm{T}}^{\mathrm{miss}}$ and degrades the overall performance of $E_{\mathrm{T}}^{\mathrm{miss}}$ measurement. Figure 4.30 shows the $E_{\mathrm{T}}^{\mathrm{miss}}$ distributions in data and compared to simulated $Z \to \mu\mu$ and $W \to e\nu$ events.

CHAPTER 5

Measurement of $t\bar{t} \to \tau$ + jets cross section

This chapter presents the physics analysis performed to measure the top quark pair production cross section in the final state of a tau lepton with associated jets. First, the topology of the events of interest is discussed, followed by the physics object selection and event selection requirements. The signal and background contributions also are outlined in detail. Finally the results are presented along with all the associated sources of uncertainties.

5.1 Introduction

The semi-leptonic $t\bar{t}$ final state to a τ lepton has a signature that includes four jets that originate from different quarks. Two of these jets are produced from the hadronization of b quarks, while the other two are from light flavor quarks from the decay of one of the W bosons. The other W boson decays to a τ lepton and a ν_τ generating an observed transverse momentum imbalance ($E_{\mathrm{T}}^{\mathrm{miss}}$). The τ lepton has a mass of 1.77 GeV and a mean proper decay length of 87 μm [32]. In addition, it decays either to leptons (e, μ) or to neutral and charged hadrons with neutrinos in

all final states producing additional $E_{\mathrm{T}}^{\mathrm{miss}}$. Since the leptons from τ decay cannot be easily distinguished from prompt leptons, only the hadronic decay mode (denoted τ_{had}) is used for its identification. The hadronic tau lepton final states represent 65% of all possible decay modes [32]. The hadronic decay products are either one or three charged pions in 72% and 22% of all cases, respectively. Charged kaons represent the majority of the remaining hadronic decays. In 78% of all hadronic decays up to one associated neutral pion is also present. The neutral and charged hadrons make up the visible decay products of the tau lepton (denoted $\tau_{\text{had-vis}}$). The detector signature is a τ-jet with one (denoted $\tau_{\text{1-prong}}$) or three (denoted $\tau_{\text{3-prong}}$) associated tracks. This information is then used to identify and reconstruct the τ candidate [155]. The signal events therefore have the signature of a reconstructed τ candidate, large $E_{\mathrm{T}}^{\mathrm{miss}}$ and four jets. The number of reconstructed jets in the event, however, may be different from four for several reasons. Additional jets may be present in the final state due to initial/final state radiation and pile-up effects. Detector effects such as the acceptance or inefficiencies can also lead to jets that are not detected. Assuming the $t \to Wb$ branching ratio (BR) to be 100% [32], this final state corresponds to $\approx 10\%$, with $\tau_{\text{1-prong}}$ in the final state at $\approx 7.5\%$, and $\tau_{\text{3-prong}}$ in the final state at $\approx 2.5\%$ of all $t\bar{t}$ decays.

There are a number of different physical processes with similar topologies to this $t\bar{t}$ final state that constitute the background to this analysis. These backgrounds fall into two categories: The first consists of events in which prompt tau leptons are produced in hard interaction. The second class arises from non-prompt, non-isolated, fake lepton candidates. The first class of events are dominated by the production

of W bosons with associated jets and the production of t-channel single top. The production of Z bosons with associated jets and di-boson processes also contribute to this class of backgrounds.

The largest background contribution comes from the second class of events and is the most important for this measurement. The reducible background is dominated by multi-jet processes. These include QCD and the all hadronic final states of, for example, $t\bar{t}$, $W+\text{jets}$, and $Z+\text{jets}$, with the $E_{\text{T}}^{\text{miss}}$ generated through the mismeasurement of jet energies. Any one of the jets from these processes can be misidentified as a τ lepton which can then mimic the signal topology. The discriminating variables used to identify $\tau_{\text{had-vis}}$ are based on narrow shower shape, distinct number of charged particle tracks, and the displacement of the tau lepton decay vertex. These criteria generate a parton flavor dependency on the fake rate and lead to a difference in fake rates for $\tau_{\text{1-prong}}$ and $\tau_{\text{3-prong}}$. In order to take this into account, the analysis is performed on the $\tau_{\text{1-prong}}$ and $\tau_{\text{3-prong}}$ channels independently.

Both of these background categories can be reduced by applying a selection on the data that closely matches the phase space of $t\bar{t}$ topology. In addition, the selection of a jet originating from a b quark by using the flavor tagging algorithm, and a large $E_{\text{T}}^{\text{miss}}$ requirement is used to minimize the background contribution. The contribution from the remaining irreducible backgrounds are then estimated using simulation samples. While the reducible background is estimated from a method derived from data as will be discussed in section 5.5.

5.2 Data and simulation samples

The dataset used in this analysis are recorded in 2012 from pp collisions at $\sqrt{s} = 8$ TeV, during periods A to L (excluding periods F and K which are not standard physics runs). `Run 208261` is excluded from the analysis due to a corrupted data sample in this run. The total integrated luminosity corresponds to, $\int \mathcal{L}\, dt = (20.2 \pm 0.4)\text{fb}^{-1}$. This analysis is based on the release 17.2 processing of the data, using the COMMON D3PDs produced with `AtlasPhysics` cache 17.2.10.1.

5.2.1 Trigger

The unprescaled τ triggers available during the 2012 data taking period have very high p_T thresholds and are therefore not used in the selection of events for this analysis. Instead, the events are required to pass one of the lowest unprescaled $E_{\text{T}}^{\text{miss}}$ only triggers with a threshold of $E_{\text{T}}^{\text{miss}} > 80$ GeV at the event filter (EF) level. The trigger `EF_xe80_tclcw` uses the total energy deposited in the topological clusters of the calorimeter calibrated with local calibration weight (represented by `tclcw`) to calculate $E_{\text{T}}^{\text{miss}}$. The trigger `EF_xe80_tclcw` was active throughout the entire data taking period. In order to increase the statistics, a second trigger, in this case with a threshold 75 GeV, is also used by taking a logical OR of the two. The trigger `EF_xe75_tclcw` was only active during Period A (see Table 5.1).

2012 Period	Trigger Chain	L2 Chain	L1 Seed
Period A	EF_xe75_tclcw	L2_xe75	L1_xe50
Period A - L	EF_xe80_tclcw	L2_xe80	L1_xe50

Table 5.1: Triggers used for 2012 data periods *A* - *L*.

In order to calculate the efficiency of the trigger, a sample of $t\bar{t}$ events is constructed by applying the following requirements:

- a muon trigger, `EF_mu24i_tight`,
- one muon with $p_T > 25$ GeV to be in the muon trigger plateau,
- 2 inclusive jets, one or more of which is initiated by a b-quark. To identify the b-quark initiated jets a multivariate algorithm (MV1) with an efficiency of 70% and a mis-tag rate of $\sim 1\%$ was used [160].

The $E_{\mathrm{T}}^{\mathrm{miss}}$ calculation at the trigger level (online) uses only information from the calorimeters and does not include the transverse momentum deposited by muons in the muon spectrometer. In order to compensate for this effect, the transverse momentum deposited by muons in the muon spectrometer is subtracted from the offline $E_{\mathrm{T}}^{\mathrm{miss}}$ in calculating the efficiency. Only muons with $p_T > 25$ GeV are considered in this procedure. In the signal region for this analysis, muons are selected with the same selection criteria to veto events with a muon. Thus, soft ($p_T < 25$ GeV) muons are not subtracted from the offline $E_{\mathrm{T}}^{\mathrm{miss}}$ calculation. The contribution from these soft muons, however, is expected to be small due to the event selection and dilepton

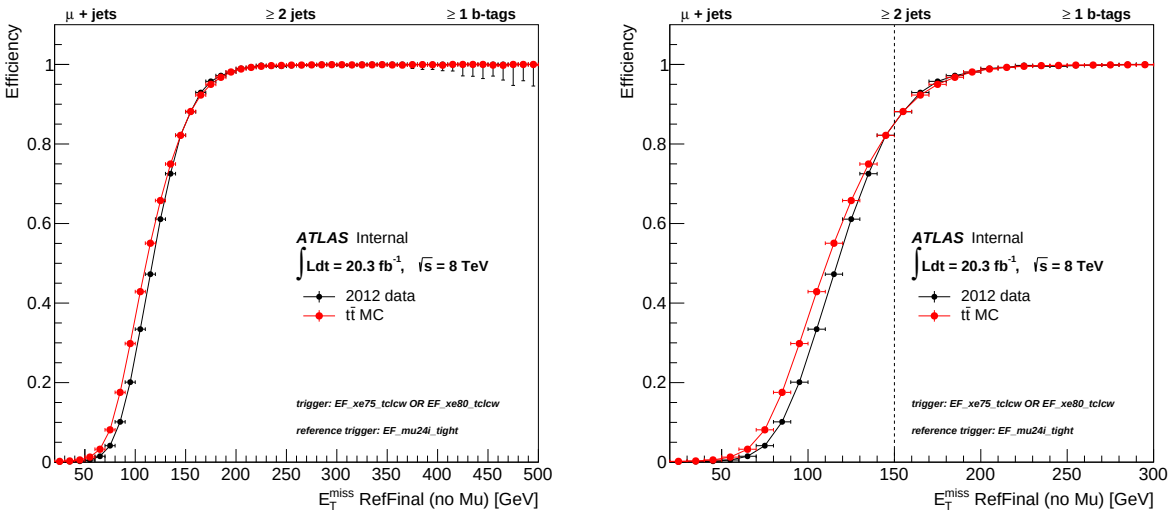

Figure 5.1: The trigger efficiencies for `EF_xe75_tclcw` OR `EF_xe80_tclcw` with respect to the muon trigger `EF_mu24i_tight` for a selection with one muon $p_T > 25$ GeV. The efficiency is plotted for data in black and $t\bar{t}$ in red. On the right, the plot is zoomed to better see the turn-on. The black dotted line represents the selection applied on offline $E_{\mathrm{T}}^{\mathrm{miss}}$ in the analysis.

branching ratios. Figure 5.1 shows the trigger efficiency as a function of offline $E_{\mathrm{T}}^{\mathrm{miss}}$, calculated with respect to the muon trigger.

The trigger is 100% efficient for events with offline $E_{\mathrm{T}}^{\mathrm{miss}} > 180$ GeV. For offline $E_{\mathrm{T}}^{\mathrm{miss}} > 150$ GeV, the trigger is $\approx 90\%$ efficient. The agreement between data and simulation, however, is excellent for $E_{\mathrm{T}}^{\mathrm{miss}} > 150$ GeV and is used as the minimum threshold in the signal region.

For different control and validation regions, other triggers are used and are described in the section on background estimation.

5.2.2 Monte Carlo Generators

Monte Carlo (MC) simulation samples are used in the analysis to

1) understand the composition of the data at various stages of selection,

2) directly estimate some of the smaller backgrounds and

3) compute signal acceptance and efficiency.

The standard MC12 samples are used and the analysis is based on COMMON D3PDs with tag `p1575`. The main $t\bar{t}$ signal and background samples were processed through the full ATLAS detector simulation based on GEANT4 [161] but some samples for evaluating systematic uncertainties use the `AtlFast2` [161] fast simulation instead. Pileup re-weighting is applied to full MC samples to match the distribution of the average number of interactions ($\langle\mu\rangle$) between data and MC. All samples are scaled such that the total number of events corresponds to the most recent theoretical predictions for the production cross sections.

The nominal MC sample of $t\bar{t}$ events is produced with the POWHEG [121] generator. A next-to-leading order (NLO) is used to calculate the matrix element (ME) for the $t\bar{t}$ hard scattering process and convoluted with the CT10 [162] parton distribution function (PDF) . The generator is interfaced to PYTHIAv6.427 [114] with Perugia 2011C [163] tune to simulate parton showering (PS) and the underlying event (UE). For the UE tune Perugia 2011C, a leading order (LO) PDF, CTEQ6L1 [164] is applied. The h_{damp} factor, which is a model parameter that controls ME/PS matching in POWHEG and effectively regulates high-p_T radiation is set to the top

quark mass, i.e. 172.5 GeV. The MC sample excludes the fully hadronic $t\bar{t}$ decay, where the cross section is scaled accordingly by applying the branching ratio of $W \to \ell\nu$ with the standard model expectation, 10.80±0.09 %, where l represents e, μ or τ lepton. The latest $t\bar{t}$ cross section is calculated at next-to-next-to-leading order (NNLO).

Alternative $t\bar{t}$ samples are used to evaluate the systematic uncertainties related to generator modeling and parton showering. One such sample is the POWHEG+PYTHIA sample described above but with $h_{\text{damp}} = \infty$. Another full simulation sample makes use of MC@NLO [120] interfaced to HERWIG [116] with JIMMY [165]. To estimate the model dependance of parton showering and fragmentation modeling, a fast simulation sample is used with POWHEG interfaced to HERWIG with JIMMY. The Initial/Final State Radiation (ISR/FSR) systematic uncertainty is estimated by using two $t\bar{t}$ fast simulation samples of low and high radiation (radLo/radHi), which are simulated with POWHEG interfaced to PYTHIA with Perugia 2012 [163] tuning.

The background associated with vector boson production plus additional jets, V+jets ($V = W, Z$) is simulated using ALPGEN interfaced to PYTHIA v6.426 using the CTEQ6L1 PDF set. The corresponding Perugia 2011C tune is used. The parton-jet matching (partons in matrix element to jets in parton showering) is applied inclusively for V + five light partons ($2 \to 7$) production and exclusively for lower multiplicity sub-samples. Production of vector bosons with heavy flavor partons ($V + c$, $V + c\bar{c}$ + jets, $V + b\bar{b}$ + jets) is simulated separately. Inclusive V + jets samples are formed by combining the light and heavy quark samples according to

their respective cross-sections. The heavy flavor overlap removal tool, HFOR, is used to avoid double counting the heavy flavor jets. The V+jets processes are calculated to NNLO.

The contribution from the single top production channels, including the t-, Wt- and s-channels, is simulated with POWHEG interfaced to PYTHIA and the CT10 PDF. The t-channel production is calculated at NNLO, while the productions of the s- and Wt-channels are calculated at next-to-next-to-leading-logarithm (NNLL). Finally, diboson production is simulated using HERWIG and the PDF set CTEQ6L1 and normalized to the next-to-leading order (NLO) calculation. A list of all simulation samples used in the analysis is shown is appendix A.

5.3 Physics object reconstruction and selection

The reconstruction of physics objects is discussed in Chapter 4. A set of selections are applied on these reconstructed objects. The selection requirements used in this analysis follow from the Top Working Group [166] and implemented in `AnalysisTop-1.9`

5.3.1 Jets

Jets are reconstructed from topological clusters in the calorimeters using the anti-k_t algorithm [167, 168] with a size parameter value of $R = 0.4$. A local calibration is applied [169, 170], which reduces fluctuations due to the non-compensating nature of the calorimeters, dead material, and out-of-cluster leakage. Calorimeter clusters are classified as either electromagnetic or hadronic by considering properties such

as the energy density of the cluster, isolation and shower depth in the calorimeters. Corrections, derived from simulations and based on jet areas [171], are then applied in order to reduce the effects of pile-up on the jet calibration [172]. In addition, a sequential correction using the global properties of the jets is applied [173]. The global sequential calibration uses tracking, calorimeter energy deposit and muon spectrometer information. The corrections are derived from simulated events. This correction improves the resolution of the jets and increases with p_T reaching a maximum of 35% depending on the η [173].

Only jets with a transverse momentum $p_T > 25$ GeV and a direction within $|\eta| < 2.5$ are considered in the following. A method that allows for the identification and selection of jets originating from the hard-scatter interaction through the use of tracking and vertexing information is used [172]. It is referred to as the "Jet Vertex Fraction" (JVF), defined as the fraction of the total momentum of the charged particle tracks associated to the jet that belongs to tracks that are also compatible with the primary vertex (pv):

$$\mathrm{JVF}(\mathrm{jet}_i, \mathrm{pv}) = \frac{\sum_k p_{\mathrm{T}}(\mathrm{trk}_k^{\mathrm{jet}_i}, \mathrm{pv})}{\sum_n \sum_l p_{\mathrm{T}}(\mathrm{trk}_l^{\mathrm{jet}_i}, \mathrm{vtx}_n)}. \tag{5.1}$$

The jet selection based on this discriminant is shown to be insensitive to pile-up. If no tracks are matched to a jet, a JVF value of -1 is assigned. In this analysis, $|\mathrm{JVF}| > 0.5$ is required for jets with $p_T < 50$ GeV and $|\eta| < 2.4$.

In order to identify the jets initiated by b quarks, the MV1 algorithm is used, which combines impact-parameter information with the explicit determination of an

inclusive secondary vertex [174]. MV1 is a neural network-based algorithm using the output weights of the IP3D, SV1 and JetFitterCombNN b-tagging algorithms. A working point is chosen that corresponds to an average efficiency of 70% for b jets in $t\bar{t}$ events (corresponding to a weight $w_{\mathrm{MV1}} > 0.7892$). Tagging and mis-tagging efficiency scale factors relate efficiencies as determined in various data samples to their counterparts in simulation. They are used in all simulated events, after having applied the b-tagging algorithm to the jets. Note that the b-tagged jets are required to pass the same p_T, η and JVF selection as all other jets. In order to calculate the data/MC scale factors and systematic uncertainty, a package provided by the flavor tagging group with `system8` calibration is used with `2014-Winter-8TeV-MC12-CDI.root` as the corresponding CDI file.

5.3.2 τ candidate

Jets formed using the anti-k_t algorithm with a distance parameter $R = 0.4$ with topological clusters calibrated using a local hadronic calibration (LC) are used as seeds of the $\tau_{\text{had-vis}}$ reconstruction algorithm. The reconstruction of the $\tau_{\text{had-vis}}$ candidate provides very little rejection against jet background. Jets initiated from quarks are on average more collimated and have fewer tracks and therefore, discrimination from $\tau_{\text{had-vis}}$ is less effective compared to jets initiated from gluons. A Boosted Decision Tree (BDT) algorithm is used to provide rejection agains jets. Separate BDT algorithms are trained for 1-track and 3-track $\tau_{\text{had-vis}}$ decays. The output of the algorithm is a score, labelled `BDTJetScore` and corresponds to different tau identification efficiency values. Three working points, `BDTTight`, `BDTMedium` and

BDTLoose, which depends on BDTJetScore and tau p_T, are available.

Another dedicated BDT algorithm is also used to reject electrons. Three working points, *tight*, *medium* and *loose* are available corresponding to different rejection rates. A simple cut based selection is used to reduce the muon contamination to a negligible level.

The energy of the reconstructed $\tau_{\text{had-vis}}$ is calibrated at the LC scale. However, it is not optimized to measure the $\tau_{\text{had-vis}}$ momentum and it does not correct for the underlying event or pile-up contributions. Hence, an additional correction is applied to obtain an energy scale which is in agreement to the true visible energy scale [155]. The $\tau_{\text{had-vis}}$ candidates calibrated at the tau energy scale (TES) are used and henceforth referred to as simply τ candidates.

The analysis uses tau candidates satisfying $p_T > 20$ GeV and pseudorapidity $|\eta| < 2.47$. To reject jets, the BDTTight working point is used for nominal selection (also referred to as identified-τ). The BDTTight working point has an efficiency of $\sim 40\%$ and a rejection factor of 100 to 1000. The rejection factor depends on the p_T and η of the candidate, as well as the associated track. An alternative working point is also used for estimation of reducible background discussed in section 5.5. Electrons are rejected with a *medium* working point only for $\tau_{\text{1-prong}}$ candidates while a cut based muon veto is applied to reject muons for all tau candidates.

5.3.3 Electrons

An event with a reconstructed electron is vetoed in this analysis. Electrons are reconstructed by matching clustered energy deposits in the electromagnetic calorime-

ter to tracks reconstructed in the inner detector [175]. Candidates are selected from `ElectronAODCollection`, with author 1 or 3, and they are required to meet quality requirements based on the shower shape [176], enclosed in the definition of `ElectronTight++`. The transverse energy $E_{\mathrm{T}} = E_{clus}/\cosh(\eta_{track})$, computed using the calorimeter cluster energy E_{clus} and the direction of the electron track η_{track}, is required to be larger than 25 GeV. The pseudo rapidity range for the electromagnetic cluster covers the fiducial volume of the detector, $|\eta| < 2.47$ (the transition region between the barrel and end-cap calorimeters, $1.37 < |\eta| < 1.52$, is excluded). The longitudinal impact parameter z_0 of the electron track relative to the primary vertex must be smaller than 2 mm. In addition, E_{T} and η-dependent calorimeter (tracking) isolation requirements are imposed in a cone with a radius $\Delta R = 0.2$ (0.3) around the electron position, with an efficiency of about 90% for true isolated electrons [177,178].

5.3.4 Muons

An event with a reconstructed muon is vetoed in this analysis. Muon candidates are required to contain matching inner detector and muon spectrometer tracks [179,180], as well as to have $p_T > 20$ GeV and $|\eta| < 2.5$. Combined and tight muons (i.e. with author 12) contained in `MuidMuonCollection`, with z_0 smaller than 2 mm, as well as a good track quality [181], are selected. Only isolated muons are accepted by requiring that the scalar sum of the track p_T in a cone of a variable radius, defined by $\Delta R < 10\mathrm{GeV}/p_T^{\mu}$ around the muon (while excluding the muon track itself) be less than 5% of the muon transverse momentum p_T^{μ}.

5.3.5 Removal of geometric overlaps between objects

When several selected objects satisfying the criteria above overlap geometrically, the following procedures are applied in this order:

- muons are rejected if found within $\Delta R < 0.4$ of any jet with nominal p_T, η and JVF selections,
- in order to avoid double-counting of electrons as jets, the single closest jet to an electron is removed if lying within $\Delta R < 0.2$ of an electron,
- electrons are rejected if found within $\Delta R < 0.4$ of any remaining jet with nominal p_T, η and JVF selections,
- a τ candidate is rejected if found within $\Delta R < 0.2$ of an electron,
- a τ candidate is rejected if found within $\Delta R < 0.2$ of a muon,
- jets are removed if they are within $\Delta R < 0.2$ of a selected τ candidate,
- when a muon shares the same track as a selected electron in the inner detector, the full event is discarded.

5.3.6 Missing transverse momentum

The magnitude of the missing transverse momentum $E_{\mathrm{T}}^{\mathrm{miss}}$ [159] is reconstructed from three-dimensional, noise-suppressed clusters of cells in the calorimeter, calibrated at the electromagnetic scale and corrected according to the energy scale of the associated objects, and from muon tracks reconstructed in the muon spectrometer and the

inner detector. Clusters of calorimeter cells belonging to jets with $p_T > 20$ GeV are calibrated to the hadronic energy scale, while clusters associated with jets having a transverse momenta in the range 7-20 GeV are included at the electromagnetic scale. Note that τ candidates are treated as jets for the $E_{\mathrm{T}}^{\mathrm{miss}}$ calculation. High-p_T electrons, photons, jets and muons are denoted by the `RefElec`, `RefPhoton`, `RefJet` and `RefMuon` terms in Eq. (5.2). Cells belonging to multiple objects are resolved using the first association in order to avoid double counting. Low-p_T jets are grouped into the `RefSoftJet` term. Calorimeter cells not associated with any object are also taken into account (in the `CellOut` term) and they are calibrated at the electromagnetic energy scale. In order to deal appropriately with the energy deposited by muons in the calorimeters, the contributions of muons to $E_{\mathrm{T}}^{\mathrm{miss}}$ are calculated differently for isolated and non-isolated muons. The total sum is then:

$$E_{x,y}^{\mathrm{miss}} = E_{x,y}^{\mathrm{RefElec}} + E_{x,y}^{\mathrm{RefPhoton}} + E_{x,y}^{\mathrm{RefJet}} + E_{x,y}^{\mathrm{RefSoftJet}} + E_{x,y}^{\mathrm{RefMuon}} + E_{x,y}^{\mathrm{CellOut}}, \quad (5.2)$$

and the magnitude is given by:

$$E_{\mathrm{T}}^{\mathrm{miss}} = \sqrt{(E_x^{\mathrm{miss}})^2 + \left(E_y^{\mathrm{miss}}\right)^2}. \quad (5.3)$$

The $E_{\mathrm{T}}^{\mathrm{miss}}$ definition used in this analysis is `MET_AntiKt4LCTopoJets_tightpp`, referring to the jet and electron selections as described in the previous sections.

5.4 Event selection

The events are selected according to $t\bar{t} \rightarrow \tau_{\text{had}} + \text{jets}$ signature discussed in section 5.1. The event selection is applied once all the physics objects are selected based on the definitions described in section 5.3 and the geometric overlap removal discussed in 5.3.5 is performed. In the first step, pre-selection criteria is applied and different discriminating variables are studied. In the next step, a discriminating variable that provides sufficient discrimination is chosen to select the signal events. The following pre-selection criteria is implemented to study discriminating variables:

- The event must pass a trigger requirement. Events are required to pass trigger `EF_xe80_tclcw` OR `EF_xe75_tclcw`, discussed in detail in section 5.2.1.
- The event must have a well defined primary vertex. Candidate events are selected if the reconstructed primary vertex has at least four associated tracks.
- An event is rejected if there is a `LooseBad` jet following the recommendation of jet cleaning [182].
- An event with either a reconstructed electron or a reconstructed muon defined in sections 5.3.3 and 5.3.4 is rejected.
- The event must have 2 inclusive jets where at least one of the jets must be identified as b-jet, defined in section 5.3.1.
- The event must have a significant amount of missing transverse energy, defined in section 5.3.6. Each event is required to pass a threshold, $E_{\text{T}}^{\text{miss}} > 150$ GeV. The

requirement is influenced by the trigger efficiencies in data and simulation samples discussed in section 5.2.1.

- The event must have at least one identified-τ as defined in section 5.3.2. In MC simulation, the identified-τ is required to overlap geometrically with a true-τ.

A discriminating criteria based on reconstructing the transverse mass of the W boson in $W \to \tau\nu$ candidate events that can significantly suppress the fake τ background is used. The W transverse mass is defined as,

$$m_{WT} = \sqrt{2p_{\mathrm{T}}^{\tau} E_{\mathrm{T}}^{\mathrm{miss}} \left(1 - \cos\Delta\phi\left(\tau, E_{\mathrm{T}}^{\mathrm{miss}}\right)\right)} \tag{5.4}$$

where, p_T^{τ} is the transverse momentum of the tau, $E_{\mathrm{T}}^{\mathrm{miss}}$ is the missing transverse momentum and $\Delta\phi$ is the angle between the directions of the tau and the direction of the $E_{\mathrm{T}}^{\mathrm{miss}}$ in the transverse plane.

Thus, in addition to the above requirements, each event is required to have a W transverse mass reconstructed from the tau leading in p_{T} and $E_{\mathrm{T}}^{\mathrm{miss}}$ to be less that 90 GeV.

Note, in determining this set of selections, listed above, different selection criteria is studied in detail to minimize the systematic uncertainties, contribution from reducible backgrounds, and to maximize the signal significance. These studies are done after all background estimation. The event yields from different processes are discussed in section 5.6. The selection criteria studied, is documented in appendix B and the optimized set of selections are used as the definition of the signal region. In addition, to the W transverse mass discriminant, different variables such as the sum

of the missing transverse energy ($\sum E_T$) , missing energy significance ($2E_T/\sqrt{\sum E_T}$), sum of all the jet p_{T} (H_T), di-jet invariant mass (M_{jj}) and tri-jet mass (M_{jjb}) are also studied. These variables do not provide sufficient discrimination of backgrounds from signal.

5.5 Estimation of fake tau background

The fake background arises from processes where a jet, an electron or a muon is misidentified as a τ. A dedicated BDT based electron veto is applied in the τ identification algorithm to reject electrons faking τ. The algorithm has a rejection rate of $\sim 99\%$ at the *medium* working point [155]. A simple cut based muon veto with a rejection rate of 60% is also applied reducing the number of fake muons to an negligible amount [155]. Therefore, jets, which are produced in abundance in proton-proton collision are the main source of misidentified taus leading to a large expected fake-rate. The jet fakes are not well modelled in simulation samples and a data driven method, called Fake Factor is used.

5.5.1 Definitions and method

The Fake Factor method uses a control sample with only the tau candidates that fail the nominal (identified-τ) tau identification criteria, referred to as the anti-τ candidates. All other selections are identical to the signal region (SR) definition. This sample is referred to as the anti-τ sample. The fake background in the SR can be estimated from the anti-τ sample with a transfer factor, referred to as the fake

factor (FF), using,

$$N_{\text{fakes,SR}} = \left(N^{\text{anti-}\tau}_{\text{data,SR}} - N^{\text{anti-}\tau}_{\text{prompt,SR}}\right) \times \text{FF}_{\text{CR}} \tag{5.5}$$

$$\text{FF}_{\text{CR}} \equiv \frac{N^{\text{identified-}\tau}_{\text{CR}}}{N^{\text{anti-}\tau}_{\text{CR}}} \tag{5.6}$$

where,

- $N^{\text{anti-}\tau}_{\text{data,SR}}$ is the number of events containing anti-τ candidates in data
- $N^{\text{anti-}\tau}_{\text{prompt,SR}}$ is the number of events containing prompt anti-τ, coming from $t\bar{t}$, W/Z+jets, single top and diboson events. The prompt contribution is estimated from simulation.

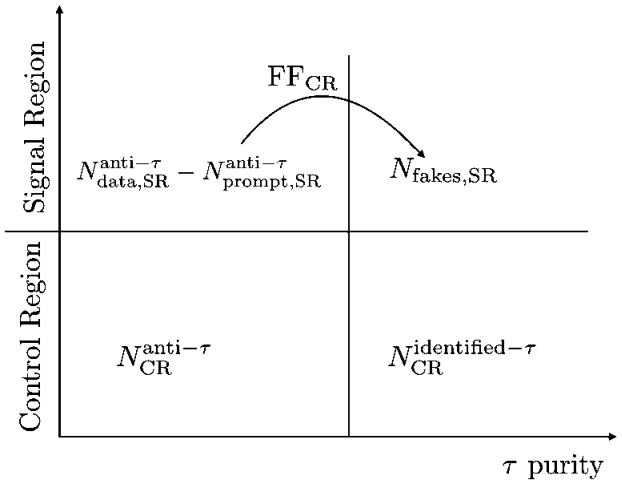

Figure 5.2: Schematic representation of the fake factor method. This method utilizes the purity of τ identification criteria to create a identified-τ and a anti-τ sample for both signal and control region selection. The transfer factor FF_{CR} defined in equation 5.6 is calculated in the control region and is used to estimate the number of fake events in the signal region ($N_{\text{fakes,SR}}$) from the signal-like anti-τ sample according to equation 5.5.

Figure 5.2 illustrates the FF method. The FF is measured in the data control

region (CR) where the signal doesn't contribute to $N_{\text{CR}}^{\text{identified-}\tau}$. Here, $N_{\text{CR}}^{\text{identified-}\tau}$ is the number of events with one and only one identified τ. However, a given anti-τ event can have several anti-τ candidates and only the leading anti-τ in p_T is used to calculate FF. Hence, the FF is object based instead of event based. If more than one identified-τ is allowed in SR, then an event based FF has to be calculated and is discussed in detail in section 5.5.5.

5.5.2 anti-τ selection

The fake factors are less sensitive to the jet flavor if a tighter efficiency working point is chosen for the anti-τ (as some shower shape requirements are already applied). However, it is important, to still choose a working point that is relaxed enough so that anti-τ statistics are sufficiently large. In order to minimize the differences between anti-τ and identified-τ samples, the very low-BDT score taus are not included. Fig. 5.3 shows how the quark/gluon changes at low-BDT score in the signal region. The selection criteria to define the signal region is discussed in detail in section 5.4. The study is performed in a simulation sample, where for each jet that fakes a tau, the largest p_T truth-parton present inside the tau reconstruction cone of $\Delta R < 0.2$ is taken as an estimation of the parton initiating the jet. The fake tau that doesn't match to a parton is considered to be a pile-up (PU) jet. To compromise between statistics and differences between anti-τ and identified-τ samples, a `BDTLoose` working point is chosen for anti-τ candidates. The working points are BDT score and p_T dependent. For reference, a 40 GeV $\tau_{\text{1-prong}}$ must have a BDT score above 0.72 to pass `BDTTight` working point (identified-τ). To be

considered as an anti-τ it would need a BDT score above 0.57 and below 0.72.

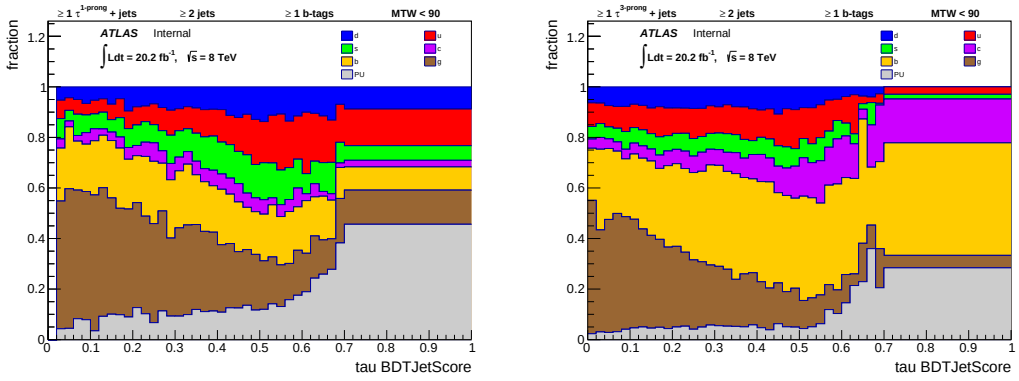

Figure 5.3: Origin of anti-τ candidates in terms of parton flavor, including pile-up jets, in $t\bar{t}$ simulated SR events for $\tau_{\text{1-prong}}$ (left) and $\tau_{\text{3-prong}}$ (right) candidate.

5.5.3 Fake-factor control region

The fake-factor should be calculated in a CR that is dominated by fake taus and have little contribution from the SR. For flavor composition, there is no observable that can be used, to directly and accurately classify each fake tau as potentially quark or gluon initiated in data events. Hence, the flavor composition of the SR and the CR is studied in simulated events. The selection criteria for the fake factor CR is first discussed and the validation studies are presented later in this section. The SR event selections are discussed in section 5.4. The following set of requirements are applied to select events in fake-factor control region (FFCR):

- The event must pass a trigger requirement. Events are required to pass a muon trigger, `EF_mu24i_tight`.

- The event must have a well defined primary vertex. Candidate events are selected

if the reconstructed primary vertex has at least four associated tracks.

- An event is rejected if there is a `LooseBad` jet following the recommendation of jet cleaning [182].

- The event must have 2 inclusive jets, where none of the jets are identified as b-jet, defined in section 5.3.1.

- Each event must have exactly one muon candidate with the criteria discussed in section 5.3.4. In addition, the muon is required to be trigger matched.

- The muon in the event must have a transverse moment, $p_{\mathrm{T}} > 25$ GeV to be on the plateau of the muon trigger.

- The event must have exactly one τ ($\tau_{\text{1-prong}}$ or $\tau_{\text{3-prong}}$ considered separately) candidate:

  (a) For the anti-τ sample, the τ candidate is selected with the `Loose!Tight` definition

  (b) For the identified-τ sample, the τ candidate is selected with the `Tight` definition

- In simulated events (for prompt subtraction), the τ candidate is geometrically matched to a true electron, muon or tau candidate

The distribution of the data events, thus created, is shown in Figs. 5.4 and 5.5 for anti-τ and identified-τ candidates along with the prompt contributions. Table 5.2

shows the number of data events and the prompt contribution from different processes for each sample.

Process	anti-$\tau_{\text{1-prong}}$	identified-$\tau_{\text{1-prong}}$	anti-$\tau_{\text{3-prong}}$	identified-$\tau_{\text{3-prong}}$
Data	84975 ± 291	28397 ± 168	39165 ± 198	9468 ± 98
Prompt contributions				
$t\bar{t} \to e, \mu, \tau$	688.2 ± 26.23	722.8 ± 26.88	472.4 ± 21.73	377.0 ± 19.42
Single top	110.8 ± 10.52	110.8 ± 10.52	106.2 ± 10.30	70.6 ± 8.40
W+jets	365.3 ± 19.11	116.1 ± 10.77	836.9 ± 28.92	436.3 ± 20.89
Z+jets	7028.7 ± 83.84	9750.3 ± 98.74	1496.7 ± 38.69	1889.2 ± 43.46
Diboson	234.3 ± 15.30	29.1 ± 5.39	88.6 ± 9.41	108.5 ± 10.41

Table 5.2: Number of events observed in data and simulation along with the associated statistical uncertainty for different processes with $\tau_{\text{1-prong}}$ and $\tau_{\text{3-prong}}$ candidate in the final state in the fake-factor control region.

A study of the flavor composition of FFCR is performed using a simulated sample and compared with that of the SR. In each case the flavor of the fake-τ is estimated by taking the largest p_T truth-parton inside the tau reconstruction cone of $\Delta R < 0.2$. Figures 5.6 and 5.7 show the flavor composition of FFCR and SR for both identified-τ and anti-τ samples as a function of `BDTJetScore`. In order to make a quantitative comparison, the flavor fraction inclusive of the `BDTJetScore`, in these two regions, are studied and the fake-factors are calculated for each type of parton flavor. Figure 5.8 shows the fraction of each parton flavor in identified-$\tau_{\text{1-prong}}$ and anti-$\tau_{\text{1-prong}}$ samples as well as the corresponding fake-factor for FFCR and SR. Figure 5.9 shows the same for $\tau_{\text{3-prong}}$. In both cases, good agreement in flavor composition between SR and FFCR is observed. The largest discrepancy in flavor

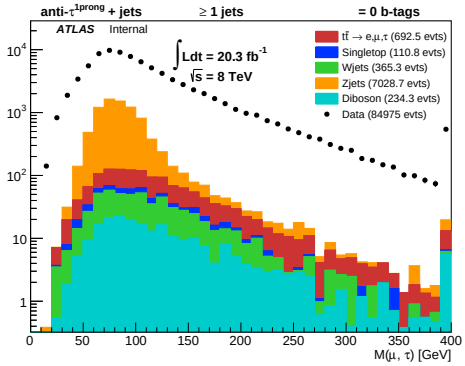

(a) invariant mass (μ, τ) : anti-$\tau_{\text{1-prong}}$

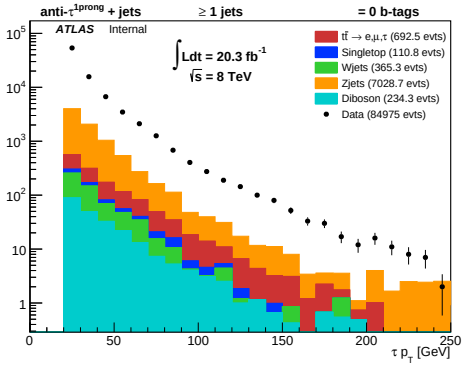

(b) p_T: anti-$\tau_{\text{1-prong}}$

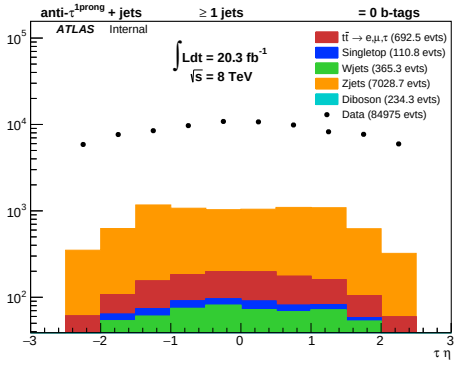

(c) η: anti-$\tau_{\text{1-prong}}$

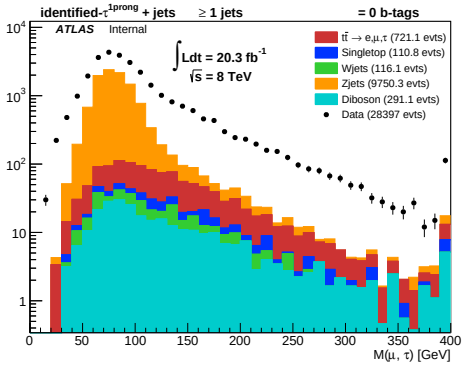

(d) invariant mass (μ, τ): identified-$\tau_{\text{1-prong}}$

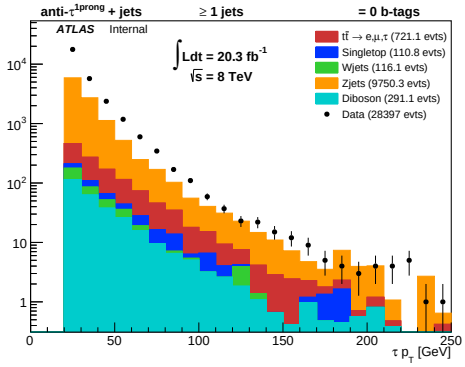

(e) p_T: identified-$\tau_{\text{1-prong}}$

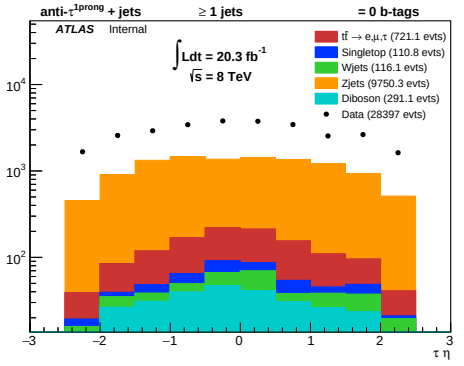

(f) η: identified-$\tau_{\text{1-prong}}$

Figure 5.4: Invariant mass distribution of the muon and the $\tau_{\text{1-prong}}$ candidate and the p_T, η of the corresponding $\tau_{\text{1-prong}}$ candidate for anti-τ with `BDTLoose!Tight` and identified-τ with `BDTTight` for $\tau_{\text{1-prong}}$ and $\tau_{\text{3-prong}}$. The prompt contribution estimated from simulation is shown along with the measured data.

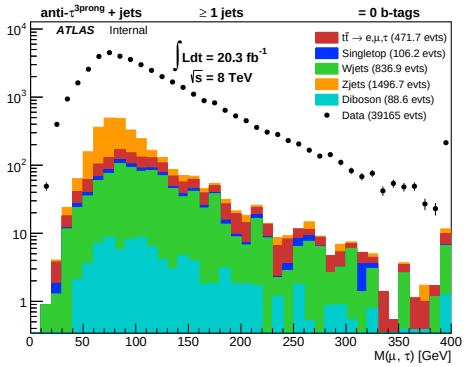

(a) invariant mass (μ, τ) : anti-$\tau_{3\text{-prong}}$

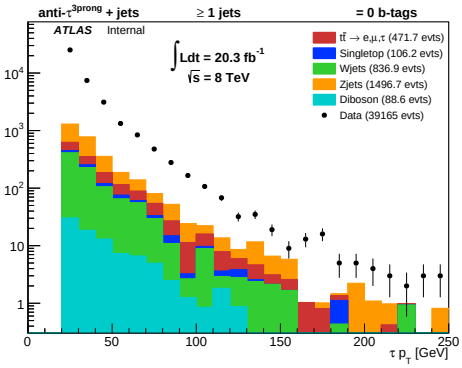

(b) p_T: anti-$\tau_{3\text{-prong}}$

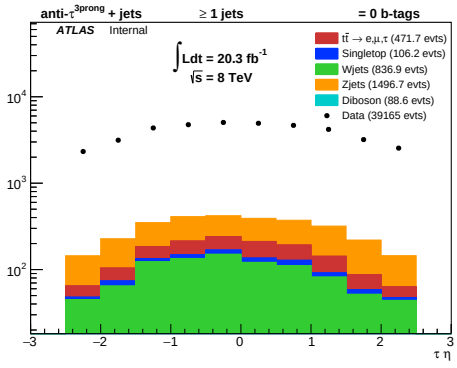

(c) η: anti-$\tau_{3\text{-prong}}$

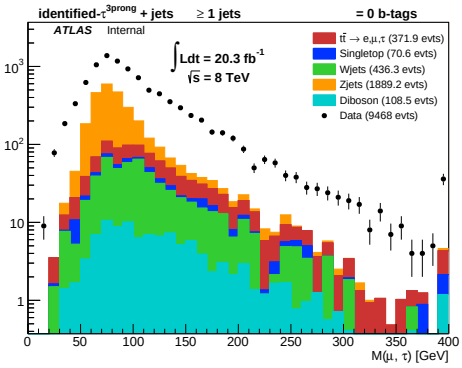

(d) invariant mass (μ, τ): identified-$\tau_{3\text{-prong}}$

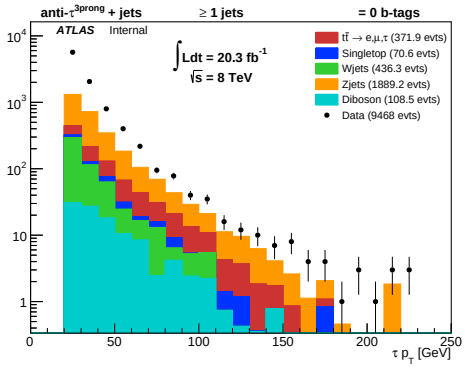

(e) p_T: identified-$\tau_{3\text{-prong}}$

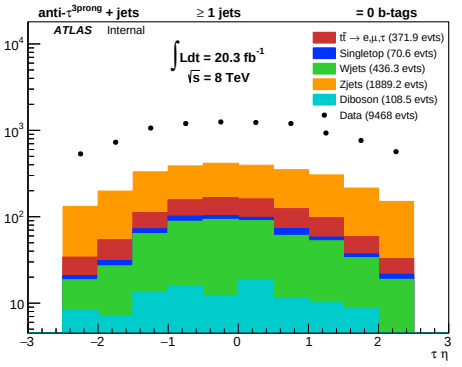

(f) η: identified-$\tau_{3\text{-prong}}$

Figure 5.5: Invariant mass distribution of the muon and the $\tau_{3\text{-prong}}$ candidate and the p_T, η of the corresponding $\tau_{3\text{-prong}}$ candidate for anti-τ with `BDTLoose!Tight` and identified-τ with `BDTTight` for $\tau_{3\text{-prong}}$ and $\tau_{3\text{-prong}}$. The prompt contribution estimated from simulation is shown along with the measured data.

composition between these two regions originate from the b-quark initiated jets as the reconstructed b-jets are vetoed in FFCR.

The total fake-factor in each region can be written as,

$$\begin{aligned} \mathrm{FF}_{\mathrm{total}} = \mathrm{FF}_{\mathrm{light-quark}} \times \text{light-quark fraction} \\ + \mathrm{FF}_{\mathrm{c-quark}} \times \text{c-quark fraction} \\ + \mathrm{FF}_{\mathrm{b-quark}} \times \text{b-quark fraction} \\ + \mathrm{FF}_{\mathrm{gluon}} \times \text{gluon fraction} \\ + \mathrm{FF}_{\text{pile-up jet}} \times \text{pile-up fraction} \end{aligned} \tag{5.7}$$

The difference in $\mathrm{FF}_{\mathrm{total}}$ between FFCR and SR is taken as the uncertainty on fake factor estimation due to flavor composition.

Effect of the presence of b-jet on the fake-factor: In order to estimate the effect of b-quark initiated jets on the fake-factor, an alternate FFCR (aFFCR) is designed by requiring at least one reconstructed b-jet. The other requirements are same as that of FFCR. Figure 5.10 shows the comparison of fake-factor for each flavor of jets between SR and aFFCR. The uncertainty on fake-factor is found to be $\sim 5\%$ and $< 1\%$ for $\tau_{\text{1-prong}}$ and $\tau_{\text{3-prong}}$ respectively.

Thus, the overall expected uncertainty on fake-factor due to the difference in flavor composition between SR and FFCR as derived in simulation is ~ 5 – 12 % and from the presence of b-jets $\sim 5\%$.

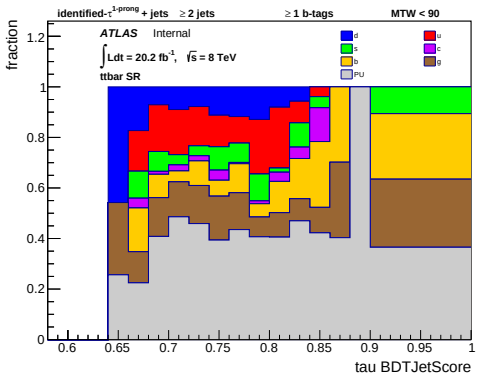

(a) SR: identified-$\tau_{\text{1-prong}}$

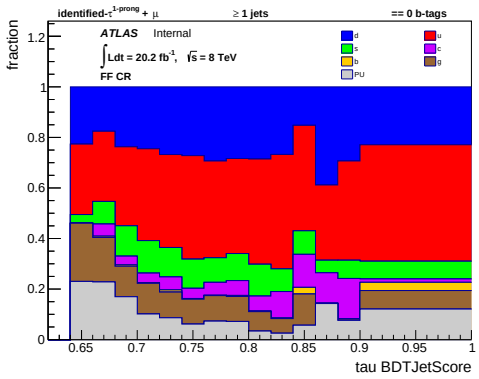

(b) FFCR: identified-$\tau_{\text{1-prong}}$

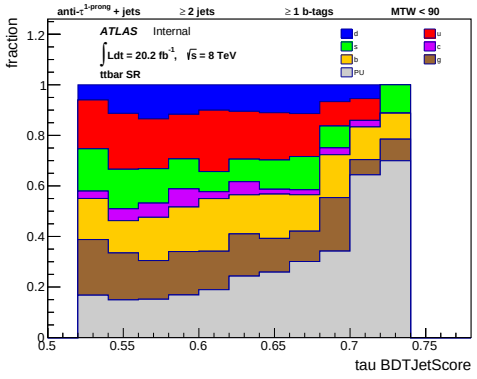

(c) SR: anti-$\tau_{\text{1-prong}}$

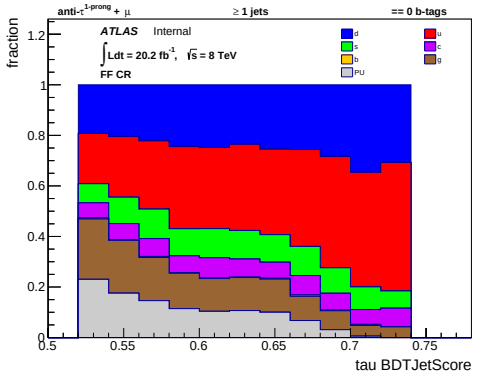

(d) FFCR: anti-$\tau_{\text{1-prong}}$

Figure 5.6: Comparison of the fake-tau flavor composition as a function of `BDTJetScore` between signal region (SR) and fake-factor control region (FFCR) for identified-$\tau_{\text{1-prong}}$ with `BDTTight` and anti-τ with `BDTLoose!Tight`. The flavor composition is estimated in a simulation sample.

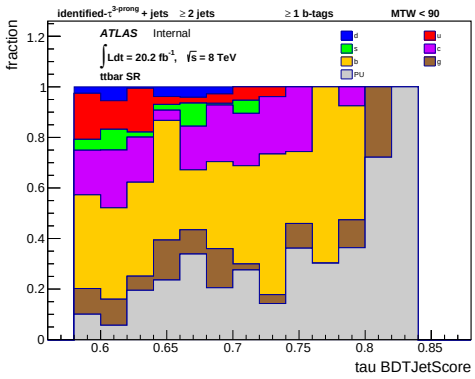

(a) SR: identified-$\tau_{3\text{-prong}}$

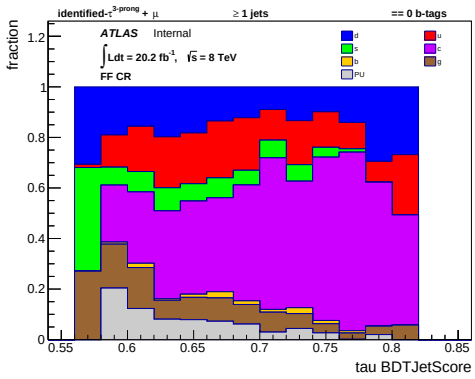

(b) FFCR: identified-$\tau_{3\text{-prong}}$

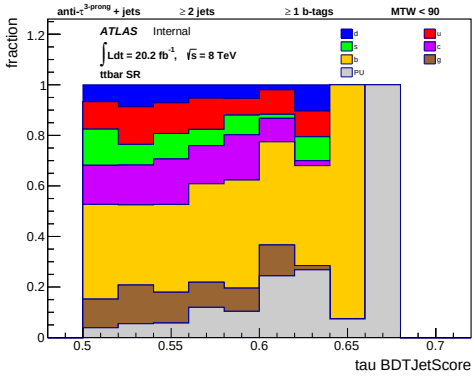

(c) SR: anti-$\tau_{3\text{-prong}}$

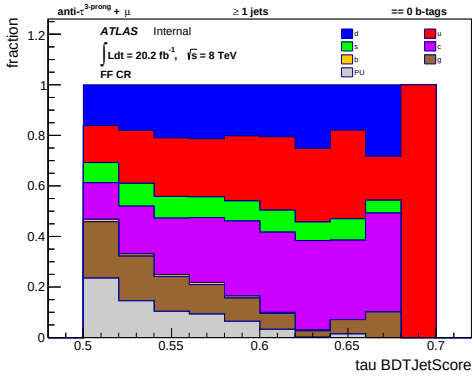

(d) FFCR: anti-$\tau_{3\text{-prong}}$

Figure 5.7: Comparison of the fake-tau flavor composition as a function of `BDTJetScore` between signal region (SR) and fake-factor control region (FFCR) for identified-$\tau_{3\text{-prong}}$ with `BDTTight` and anti-τ with `BDTLoose!Tight`. The flavor composition is estimated in a simulation sample.

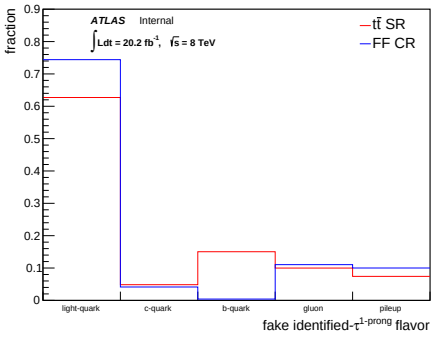

(a) inclusive in `JetBDTScore` : identified-$\tau_{\text{1-prong}}$

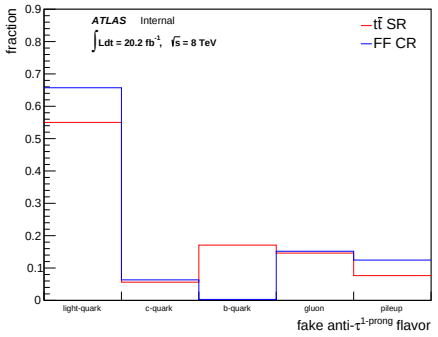

(b) inclusive in `JetBDTScore`: anti-$\tau_{\text{1-prong}}$ $\tau_{\text{1-prong}}$

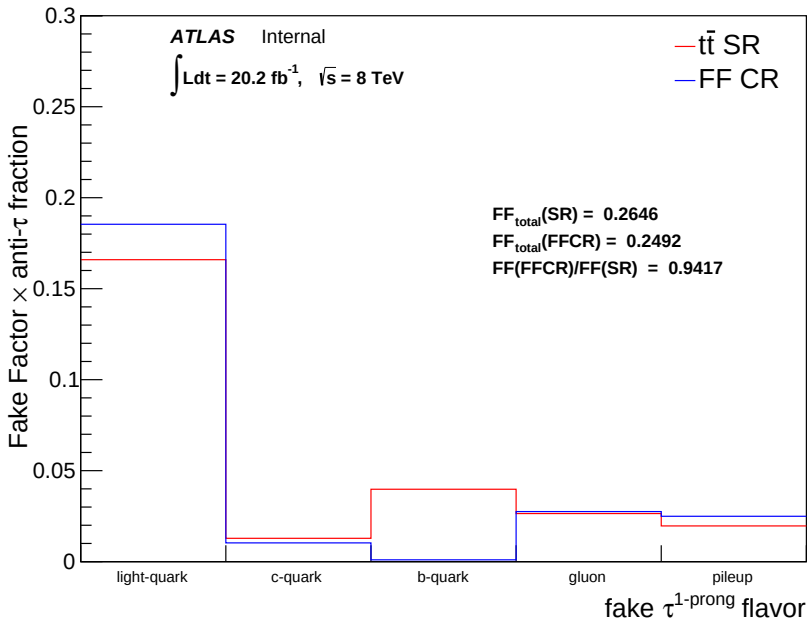

(c) FakeFactor $\times$ anti-$\tau_{\text{1-prong}}$ fraction

Figure 5.8: Top - Comparison of fake-$\tau_{\text{1-prong}}$ flavor composition inclusive in `BDTJetScore` between signal region (red) and fake-factor control region (blue) for identified-τ and anti-τ samples. Bottom - Comparison of the calculated fake-factor $\times$ anti-τ fraction between signal region (red) and fake-factor control region (blue).

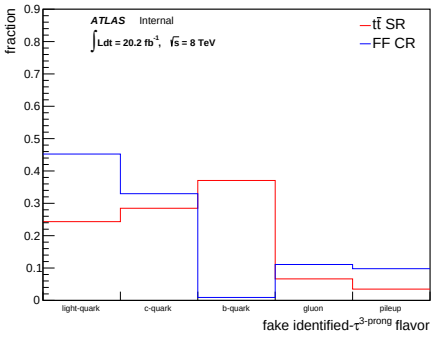

(a) inclusive in `JetBDTScore` : identified-$\tau_{\text{3-prong}}$

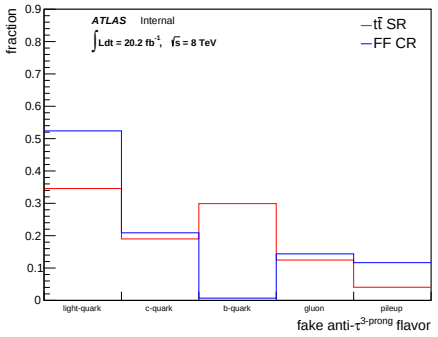

(b) inclusive in `JetBDTScore`: anti-$\tau_{\text{3-prong}}$

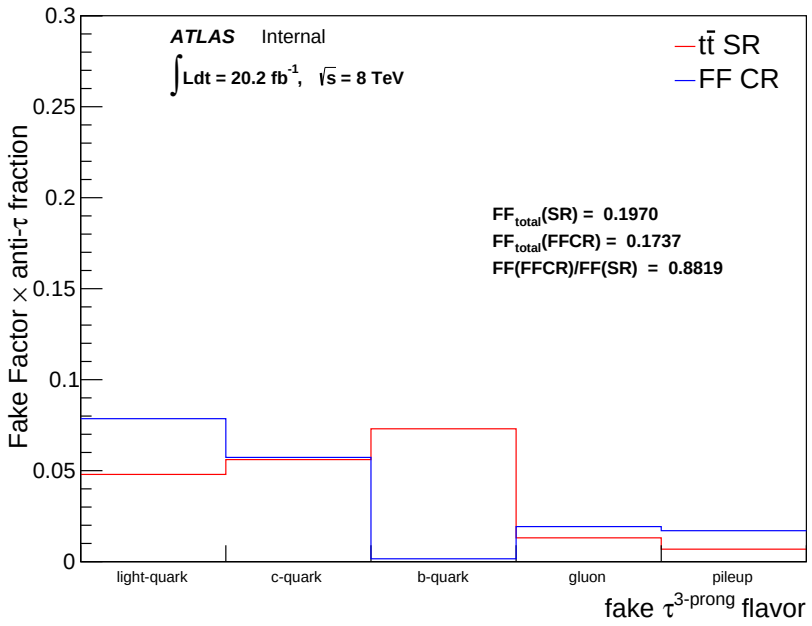

(c) FakeFactor × anti-$\tau_{\text{3-prong}}$ fraction

Figure 5.9: Top - Comparison of fake-$\tau_{\text{3-prong}}$ flavor composition inclusive in `BDTJetScore` between signal region (red) and fake-factor control region (blue) for identified-τ and anti-τ samples. Bottom - Comparison of the calculated fake-factor $\times$ anti-τ fraction between signal region (red) and fake-factor control region (blue).

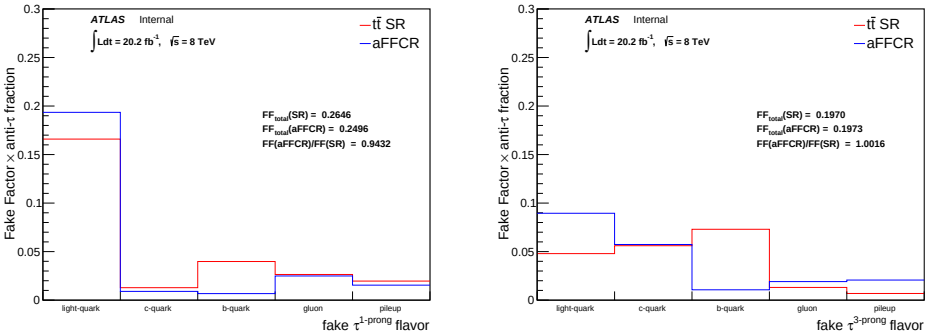

Figure 5.10: Effect of b-quark initiated jets on the fake-factor, estimated in the alternate fake-factor control region for $\tau_{\text{1-prong}}$ (left) and $\tau_{\text{3-prong}}$ (right).

5.5.4 Fake-factor derivation

The FFCR defined in section 5.5.3 is used to derive the fake-factor in data. The prompt-τ contribution in the data is estimated from simulation and subtracted.

The sensitivity of the fake-factor on different kinematic and topological variables are studied in detail and is found to be sensitive on the p_{T} and η of tau candidates. Thus, the fake factors are nominally parameterized as p_T and η of the tau candidate, binned in 2 dimensions to preserve the correlations. This parameterization is targeted to capture the dependencies associated with the jet shower shapes as a function of kinematics and detector homogeneity. Figures 5.11 and 5.12 show the measured fake factors for $\tau_{\text{1-prong}}$ and $\tau_{\text{3-prong}}$ candidate.

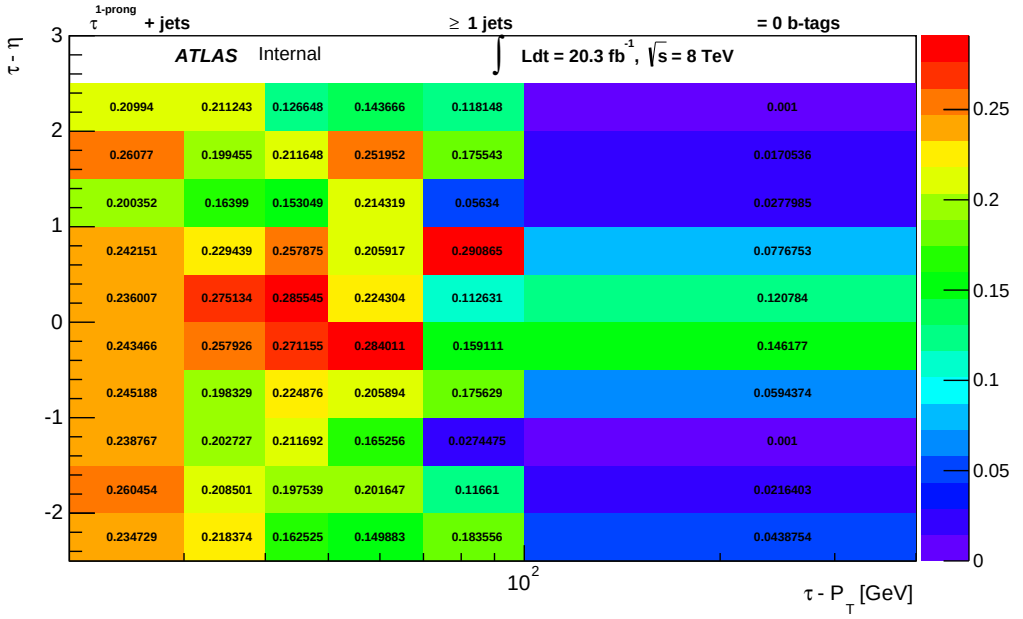

(a) fake-factor: $\tau_{\text{1-prong}}$

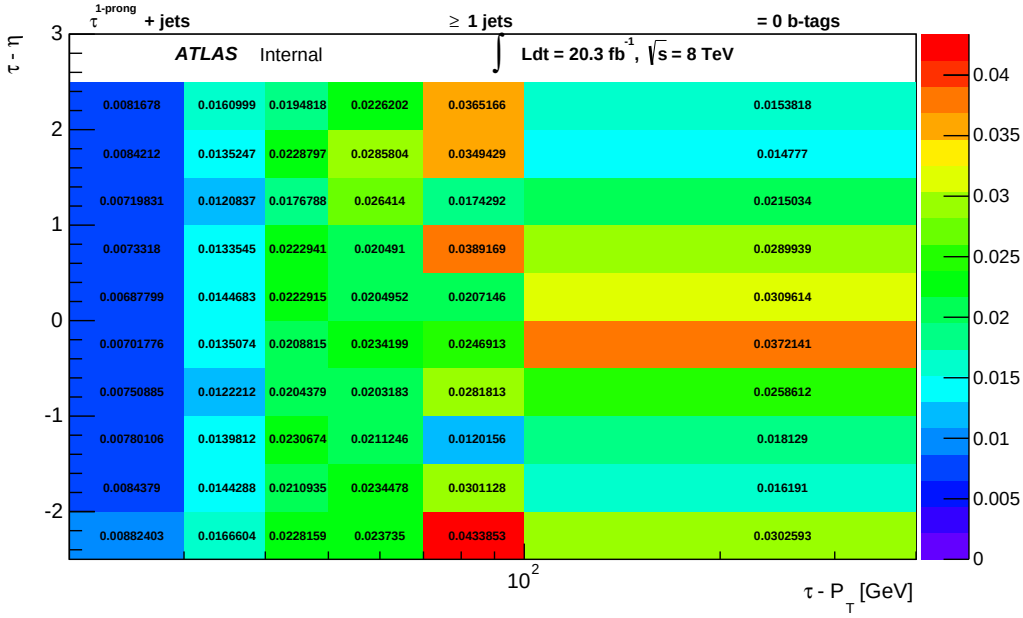

(b) statistical uncertainty on fake-factor: $\tau_{\text{1-prong}}$

Figure 5.11: The fake-factors measured as a function of p_T and η of the $\tau_{\text{1-prong}}$ candidate and the associated statistical uncertainty on the fake-factor.

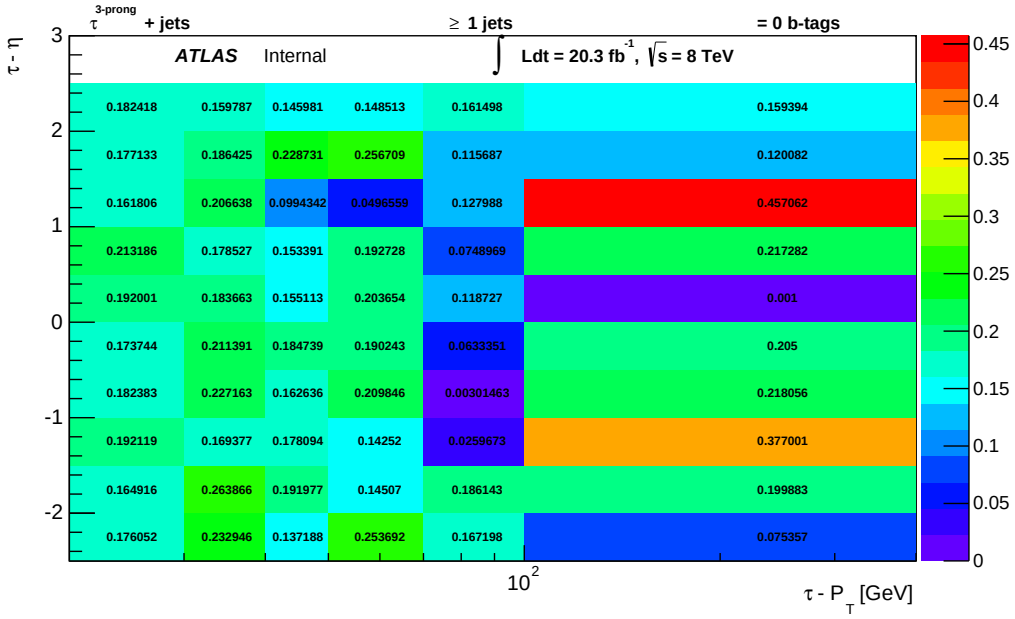

(a) fake-factor: $\tau_{\text{3-prong}}$

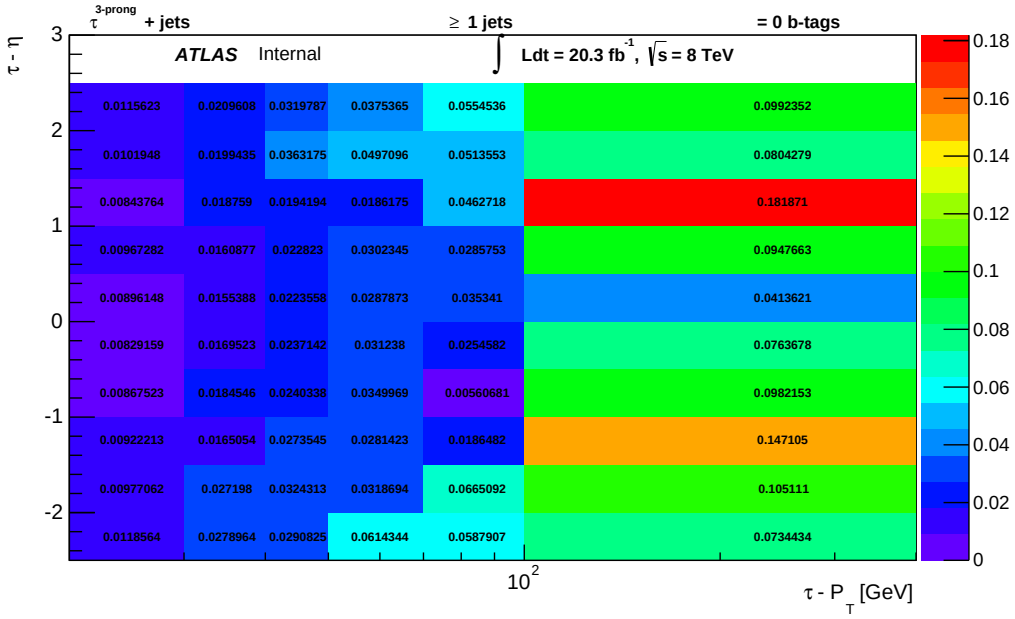

(b) statistical uncertainty on fake-factor: $\tau_{\text{3-prong}}$

Figure 5.12: The fake-factors measured as a function of p_T and η of the $\tau_{\text{3-prong}}$ candidate and the associated statistical uncertainty on the fake-factor.

5.5.5 Applying fake-factor to signal-like events

The fake-factors calculated from CR discussed in the previous section can be applied to signal-like anti-τ events, i.e. the events that pass full selection criteria but with anti-τ definition to estimate the fake background using equation 5.5. However, since the fake-factors are single τ based, their application to signal-like events would depend on the number of anti-τ candidates, which in turn depends on the identified-τ requirement in the event selection.

In the case where only one identified-τ is required the application of the fake factor to each event is trivial,

$$\mathrm{FF}_{\mathrm{evt}} = f_1 \tag{5.8}$$

where, $\mathrm{FF}_{\mathrm{evt}}$ is the event fake factor and f_1 is the fake factor of the anti-τ candidate leading in p_T and calculated using equation 5.6.

In an event with multiple taus, any subset of them can either be real or fake. Therefore, the fake factor has to be applied to each combination of taus in the event.

In an event with three identified-τ's τ_1, τ_2, τ_3, each τ_i could either be either real (τ_i^R) or fake(τ_i^F), as can each pair of taus or all three taus. Let us denote, a anti-τ_i candidate as $\tilde{\tau}_i$ and the fake-factor associated to it as f_i. All the τ candidates in the event are p_T-ordered.

Assuming that any combination of taus can be fakes, then an event of three identified-τ's can be decomposed as:

$$\begin{aligned}\tau_1\tau_2\tau_3 &= \tau_1^R\tau_2^R\tau_3^R + \tau_1^R\tau_2^R\tau_3^F + \tau_1^R\tau_2^F\tau_3^R + \tau_1^F\tau_2^R\tau_3^R \\ &\quad + \tau_1^R\tau_2^F\tau_3^F + \tau_1^F\tau_2^R\tau_3^F + \tau_1^F\tau_2^F\tau_3^R + \tau_1^F\tau_2^F\tau_3^F\end{aligned} \tag{5.9}$$

The fake factors are then applied to estimated τ_i^F. Assuming, $\tau_i^F = \tilde{\tau}_i \times f_i$,

$$\tilde{\tau}_1\tau_2\tau_3 \times f_1 = \tau_1^F\tau_2^R\tau_3^R + \tau_1^F\tau_2^R\tau_3^F + \tau_1^F\tau_2^F\tau_3^R + \tau_1^F\tau_2^F\tau_3^F \tag{5.10}$$

$$\tau_1\tilde{\tau}_2\tau_3 \times f_2 = \tau_1^R\tau_2^F\tau_3^R + \tau_1^F\tau_2^F\tau_3^R + \tau_1^R\tau_2^F\tau_3^R + \tau_1^F\tau_2^F\tau_3^F \tag{5.11}$$

$$\tau_1\tau_2\tilde{\tau}_3 \times f_3 = \tau_1^R\tau_2^R\tau_3^F + \tau_1^F\tau_2^R\tau_3^F + \tau_1^R\tau_2^F\tau_3^F + \tau_1^F\tau_2^F\tau_3^F \tag{5.12}$$

Thus the system has 4 equations and 8 unknowns. It also double counts the events with two fake taus, and triple counts the events with three fake taus. To cover these cases, events with two and three anti-τ's are selected, and multiplied by the product of the corresponding fake-factors:

$$\tilde{\tau}_1\tilde{\tau}_2\tau_3 \times f_1f_2 = \tau_1^F\tau_2^F\tau_3^R + \tau_1^F\tau_2^F\tau_3^F \tag{5.13}$$

$$\tilde{\tau}_1\tau_2\tilde{\tau}_3 \times f_1f_3 = \tau_1^F\tau_2^R\tau_3^F + \tau_1^F\tau_2^F\tau_3^F \tag{5.14}$$

$$\tau_1\tilde{\tau}_2\tilde{\tau}_3 \times f_2f_3 = \tau_1^R\tau_2^F\tau_3^F + \tau_1^F\tau_2^F\tau_3^F \tag{5.15}$$

$$\tilde{\tau}_1\tilde{\tau}_2\tilde{\tau}_3 \times f_1f_2f_3 = \tau_1^F\tau_2^F\tau_3^F \tag{5.16}$$

This now provides a complete system of equations that can be solved for $\tau_1^R\tau_2^R\tau_3^R$,

$$\begin{aligned}\tau_1\tau_2\tau_3 &= \tau_1^R\tau_2^R\tau_3^R \\ &+ (\tau_1\tau_2\tilde{\tau}_3 f_3 + \tau_1\tilde{\tau}_2\tau_3 f_2 + \tilde{\tau}_1\tau_2\tau_3 f_1) \\ &- (\tau_1\tilde{\tau}_2\tilde{\tau}_3 f_2 f_3 + \tilde{\tau}_1\tau_2\tilde{\tau}_3 f_1 f_3 + \tilde{\tau}_1\tilde{\tau}_2\tau_3 f_1 f_2) \\ &+ \tilde{\tau}_1\tilde{\tau}_2\tilde{\tau}_3 f_1 f_2 f_3 \end{aligned} \tag{5.17}$$

where the total reducible background is everything except the $\tau_1^R\tau_2^R\tau_3^R$ term and the $\mathrm{FF_{evt}}$ can be written as:

$$\mathrm{FF_{evt}} = f_1 + f_2 + f_3 - f_1 f_2 - f_1 f_3 - f_2 f_3 + f_1 f_2 f_3 \tag{5.18}$$

The case where two identified-τ's are present in an event, the derivation of $\mathrm{FF_{evt}}$ is now trivial following the same procedure.

Thus, the event based fake factor, $\mathrm{FF_{evt}}$ for events with two and three taus can be written respectively as,

$$\mathrm{FF_{evt}} = f_1 + f_2 - f_1 f_2 \tag{5.19}$$

$$\mathrm{FF_{evt}} = f_1 + f_2 + f_3 - f_1 f_2 - f_1 f_3 - f_2 f_3 + f_1 f_2 f_3 \tag{5.20}$$

The cross section measurement presented in section 5.4 uses at least one tau

requirement and thus the fake factor is applied depending on the number of taus in each event. For the upper limit on branching ratio of $t \to cH$, presented in section 6.1, two independent regions with exactly one tau and exactly two tau leptons are used. The fake factor is applied combinatorially for the exactly two tau region.

5.5.6 Systematic uncertainties on fake-factor measurement

Various studies are carried out to estimate the systematic uncertainty associated with the fake-factor measurement. The main sources of uncertainties are the following:

- Uncertainty associated to MC prompt subtraction.
- Uncertainty associated to binning choice.
- Uncertainty associated to the flavor dependence (gluon, light-quarks, heavy-quarks) of the fake-factor.

MC based prompt subtraction: The largest contribution for the prompts in the CR where fake-factors are derived, comes from Z+jets simulation sample through $Z \to \tau\tau \to \mu + \tau_{\text{had}}$ processes. The $Z+$jets normalization is varied by $\pm 1\sigma$ with the uncertainty associated its cross section(10%). The effect of the -1σ variation on the fake factor is shown in Fig. 5.13(a), while Fig. 5.13(b) shows the effect for the $+1\sigma$ variation for $\tau_{\text{1-prong}}$ prong. The largest difference of these variation from the nominal values of the fake factor is taken as an estimate of this uncertainty for each tau $p_{\text{T}} - \eta$ bin and shown in Fig. 5.13(c). The same is shown for $\tau_{\text{3-prong}}$ in Fig. 5.14.

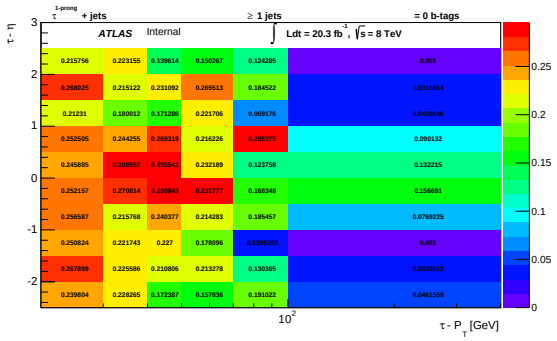

(a) Z+jets normalization varied by -1σ: $\tau_{\text{1-prong}}$

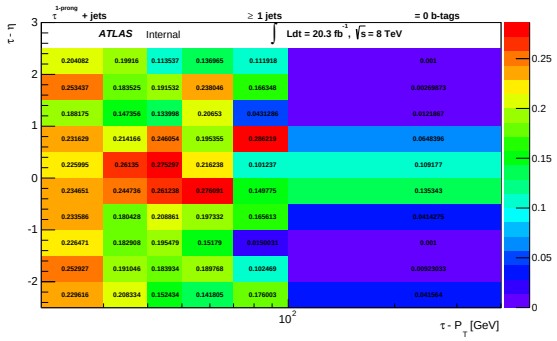

(b) Z+jets normalization varied by +1σ: $\tau_{\text{1-prong}}$

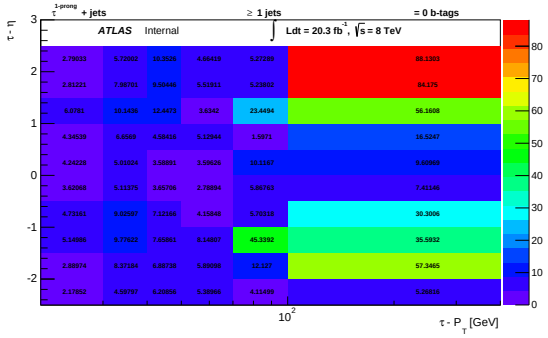

(c) prompt subtraction uncertainty (%) : $\tau_{\text{1-prong}}$

Figure 5.13: Fake-factors measured by varying the Z+jets normalization by its associated uncertainty (top) and the derived uncertainty on prompt subtraction(bottom) for the $\tau_{\text{1-prong}}$ candidate.

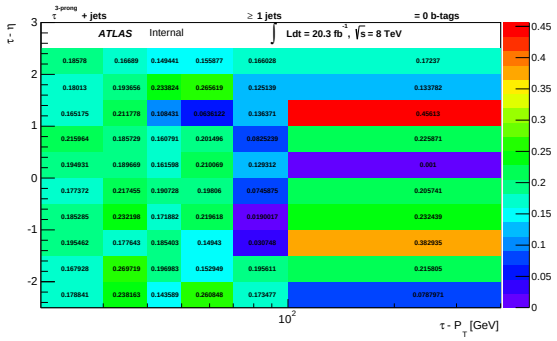

(a) Z+jets normalization varied by -1σ: $\tau_{\text{3-prong}}$

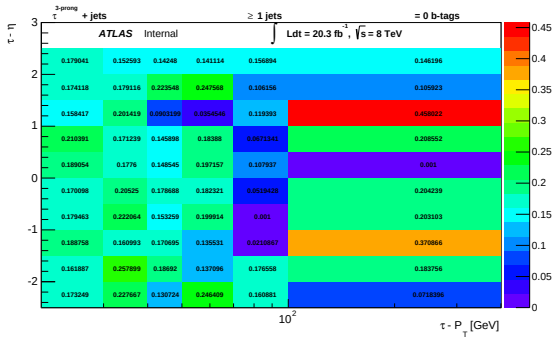

(b) Z+jets normalization varied by +1σ: $\tau_{\text{3-prong}}$

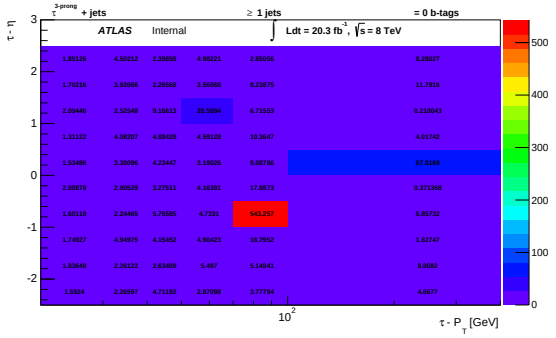

(c) prompt subtraction uncertainty (%) : $\tau_{\text{3-prong}}$

Figure 5.14: Fake-factors measured by varying the Z+jets normalization by its associated uncertainty (top) and the derived uncertainty on prompt subtraction(bottom) for the $\tau_{\text{3-prong}}$ candidate.

Bininng effect: The effect of different binning on the fake factor is also investigated. The effect is tested by applying the fake factor calculated using the binning described earlier, e.g. Fig. 5.11 to tau p_{T} and η distributions with different binning in a closure test. If the fake factor is applied to a distribution with the same binning it was derived from, perfect agreement is expected. For example, Fig. 5.15(b) show the $\tau_{\text{1-prong}}$-η distribution with the same binning shows perfect agreement between data and prediction. However, as shown in Fig. 5.15(a), the $\tau_{\text{1-prong}}$-p_{T} distribution with different binning, shows some level of disagreement. Several different binning schemes are investigated. In addition to tau p_{T} and η, other distributions such as the invariant mass of the muon and the $\tau_{\text{1-prong}}$ shown in Fig. 5.15(c) are also taken into account. The results for $\tau_{\text{3-prong}}$ candidates is shown in Fig. 5.16. The level of disagreement is taken as an estimate of this uncertainty, and a systematic of 5% is attributed to this effect.

Flavor composition: Finally, the sensitivity of the fake-factors to the flavor composition of the sample used to derive them is estimated. The fake-factors are derived in a quark dominated region. A QCD control region (QCR) is designed where the events are expected to be enriched with gluon initiated jets and therefore can be used to put a conservative systematic on this effect. The following requirements are applied to construct the QCR:

- A trigger with 4 jets where one of the jet identified as a b-jet, `EF_b45_4j45_a4tchad_L2FS`
- 4 leading jet $p_T > 50$ GeV to be on the trigger plateau

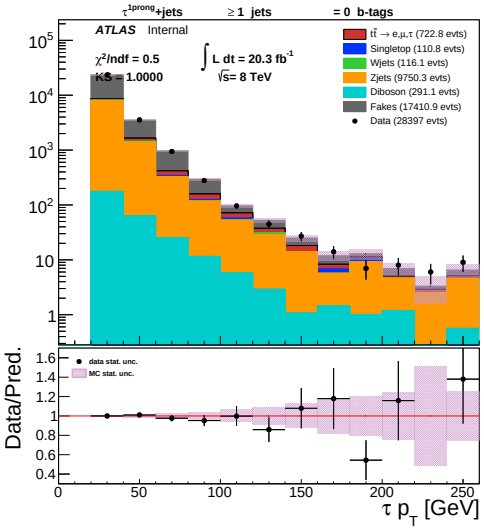

(a) p_T: $\tau_{\text{1-prong}}$

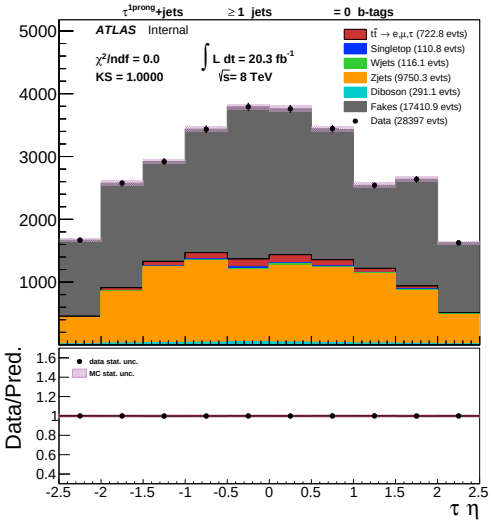

(b) η: $\tau_{\text{1-prong}}$

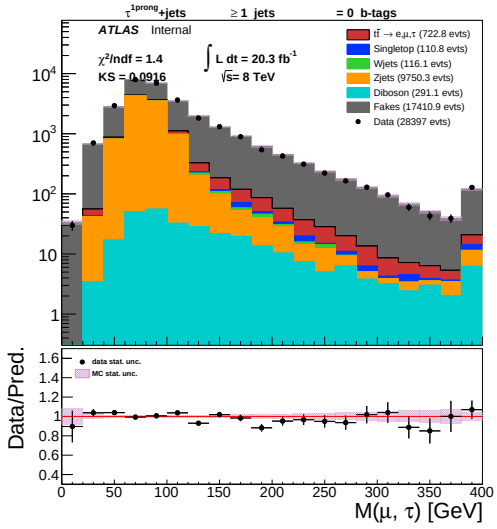

(c) invariant mass (μ, $\tau_{\text{1-prong}}$)

Figure 5.15: Distribution of the invariant mass of the muon and the $\tau_{\text{1-prong}}$ and the p_T and η of the corresponding tau candidate in closure test.

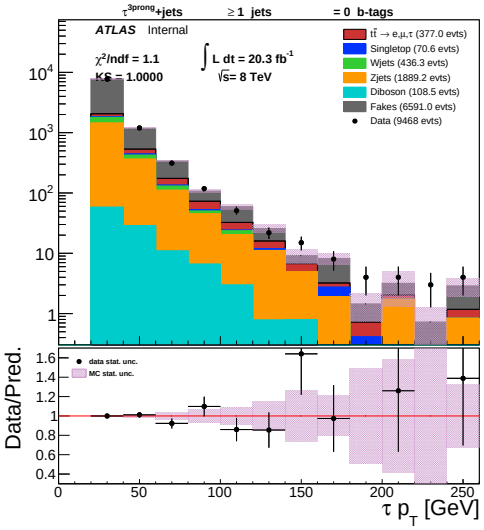

(a) p_T: $\tau_{\text{3-prong}}$

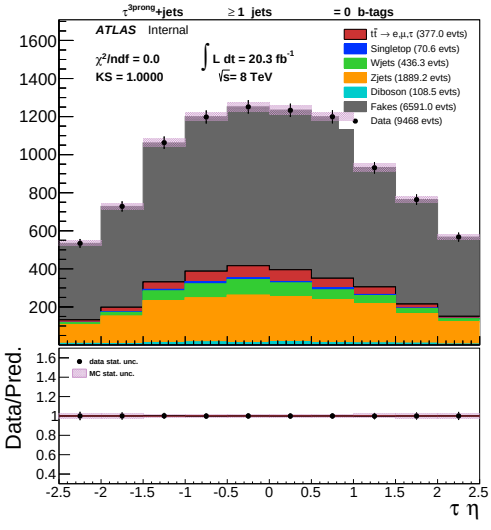

(b) η: $\tau_{\text{3-prong}}$

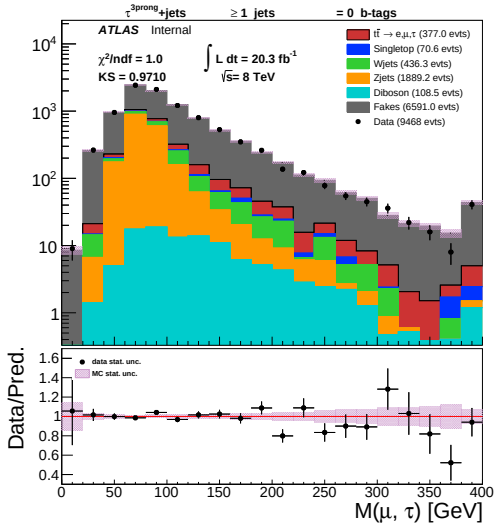

(c) invariant mass (μ, $\tau_{\text{3-prong}}$)

Figure 5.16: Distribution of the invariant mass of the muon and the $\tau_{\text{3-prong}}$ and the p_T and η of the corresponding tau candidate in closure test.

- one reconstructed identified-τ

- $E_{\mathrm{T}}^{\mathrm{miss}} < 100$ GeV to create a gluon dominated region. Note, in the SR $E_{\mathrm{T}}^{\mathrm{miss}} > 150$ GeV is required. Thus, this region is orthogonal to the SR.

  The results are shown in Fig. 5.17 for $\tau_{\text{1-prong}}$ and Fig. 5.18 for $\tau_{\text{3-prong}}$. A flat estimate of 20% is taken as a conservative uncertainty for this effect.

  The systematic uncertainties on the fake-factor measurement are propagated to the cross section measurement, discussed in section 5.8.11 in detail.

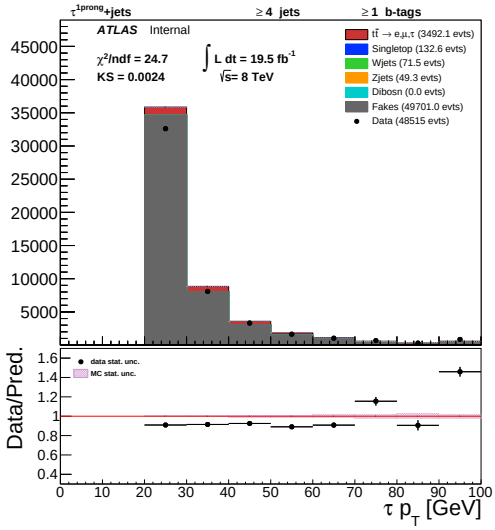

(a) $\tau_{\text{1-prong}}$ p_T

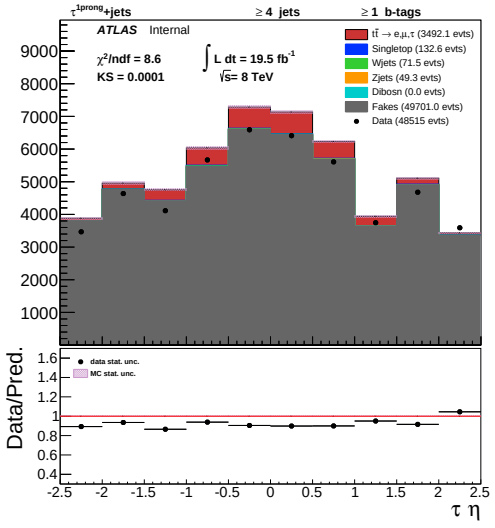

(b) $\tau_{\text{1-prong}}$ η

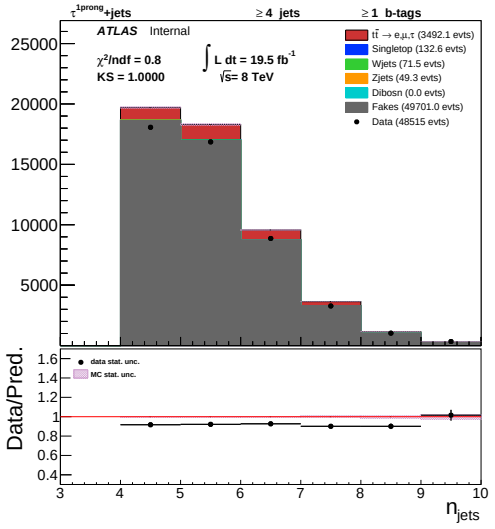

(c) jet multiplicity: $\tau_{\text{1-prong}}$

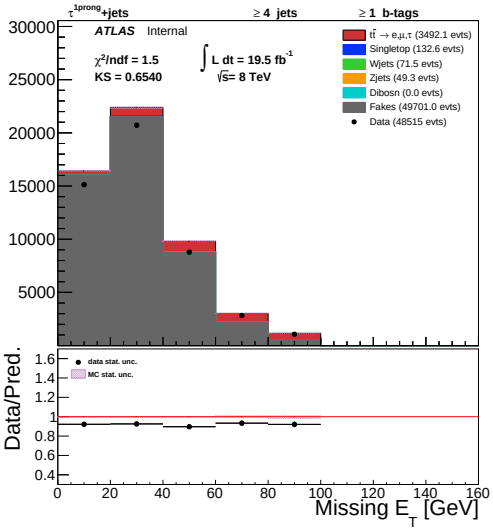

(d) $E_{\text{T}}^{\text{miss}}$: $\tau_{\text{1-prong}}$

Figure 5.17: QCD CR to estimate flavor composition uncertainty on fake-factor in $\tau_{\text{1-prong}}$ + jet final state. The disagreement in data/prediction is taken as an estimate of uncertainty.

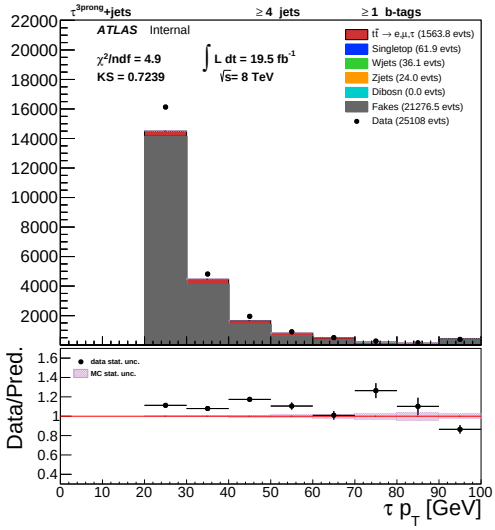

(a) $\tau_{\text{1-prong}}$ p_T

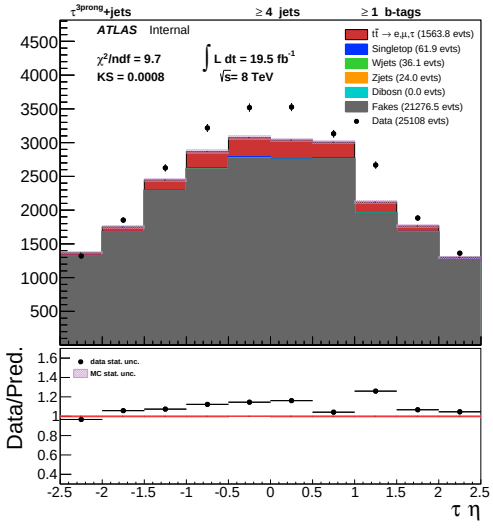

(b) $\tau_{\text{1-prong}}$ η

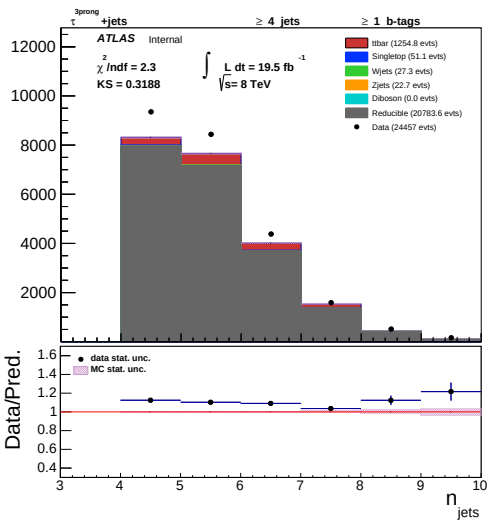

(c) jet multiplicity: $\tau_{\text{1-prong}}$

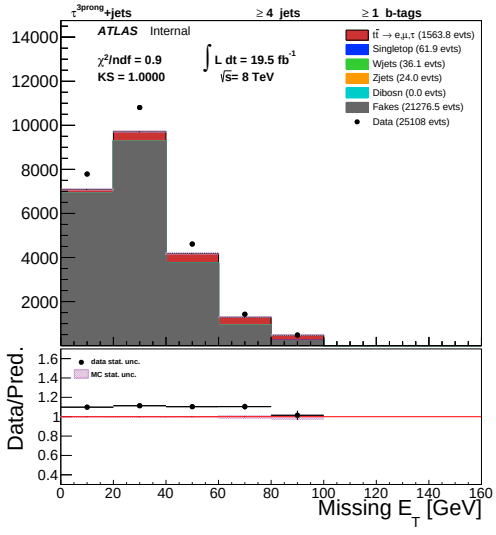

(d) $E_{\text{T}}^{\text{miss}}$: $\tau_{\text{1-prong}}$

Figure 5.18: QCD CR to estimate flavor composition uncertainty on fake-factor in $\tau_{\text{3-prong}}$ + jet final state. The disagreement in data/prediction is taken as an estimate of uncertainty.

5.5.7 Modeling of fake background in validation regions

The modeling of the fake background derived from use of the fake factor is verified using the validation regions (VR) created in data events that are orthogonal to the SR. These validation regions target specific effects and check the fake modeling for the following cases:

- regions with the presence of b-jets,
- regions of different topology, i.e. jet multiplicity,
- region dominated with true tau.

Modeling in regions of different topology with and without b-jets: Several μ+τ validation regions are created with and without b-jets to test the modeling of fake backgrounds for regions of different topology and the case where b-jets are present. The following requirements are applied for selecting events:

- Events are required to pass two single muon triggers, `EF_mu24i_tight` OR `EF_mu36_tight`.
- Exactly one muon with $p_{\mathrm{T}} > 25$ GeV and matched to the trigger muon.
- Exactly one identified-τ (separately for $\tau_{\text{1-prong}}$ and $\tau_{\text{3-prong}}$).
- Each event must have the following light and heavy flavor multiplicities:
  - i) 2 inclusive jets and 0 b-jet
  - ii) 3 inclusive jets and 0 b-jet

iii) 4 inclusive jets and 0 b-jet

iv) 2 inclusive jets and 1 inclusive b-jet

v) 3 inclusive jets and 1 inclusive b-jet

vi) 4 inclusive jets and 1 inclusive b-jet

Figures 5.19 - 5.30 show the results of these validation regions. The invariant mass of the muon and the tau candidate along with the tau p_T and η for $\tau_{\text{1-prong}}$ and $\tau_{\text{3-prong}}$ are shown. The fake-factors are found to be robust in these regions of varying flavor composition.

Modeling in region dominated by true taus: In addition, the selection of true τ's is verified by constructing a validation region of $Z \to \tau\tau$ events, in the $\mu\tau_{\text{had}}$ channel. The aim of the validation region is to test the tau selection as applied in this analysis. The reconstructed muon and event selection is thus tuned to maximize the true tau candidate. The event selection for this validation region is inspired by the selection and discussion in references [183, 184]. Without these specific requirements, the overwhelming contribution from fake τ's does not allow us to probe the prompt τ's with sufficient precision. The following event selection is applied:

- $\cos\Delta\phi\left(\mu, E_{\text{T}}^{\text{miss}}\right) + \cos\Delta\phi\left(\tau, E_{\text{T}}^{\text{miss}}\right) >$ -0.15
- $\Delta\phi\left(\mu, \tau\right) > 2.4$
- $m_T^{\mu} < 50$ GeV, where, m_T^{μ} is the transverse W mass with the muon candidate
- $42 < m_{\text{inv}}\left(\mu, \tau\right) < 82$ GeV, where, m_{inv} is the invariant mass of the muon and the tau candidate

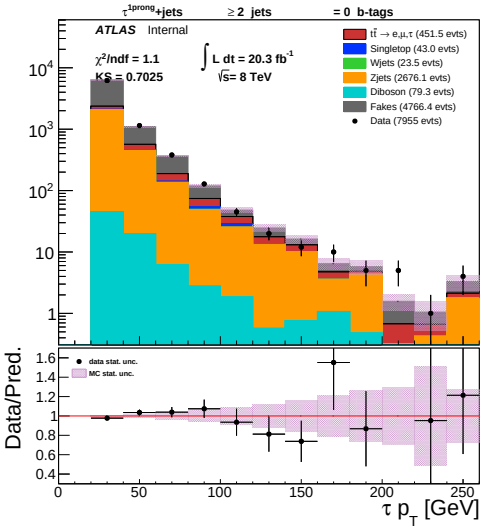

(a) p_T: $\tau_{\text{1-prong}}$

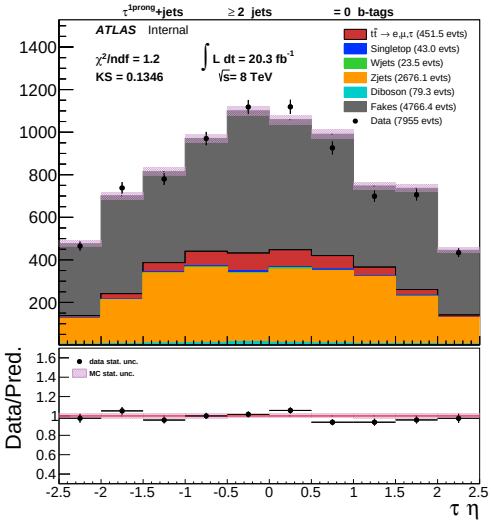

(b) η: $\tau_{\text{1-prong}}$

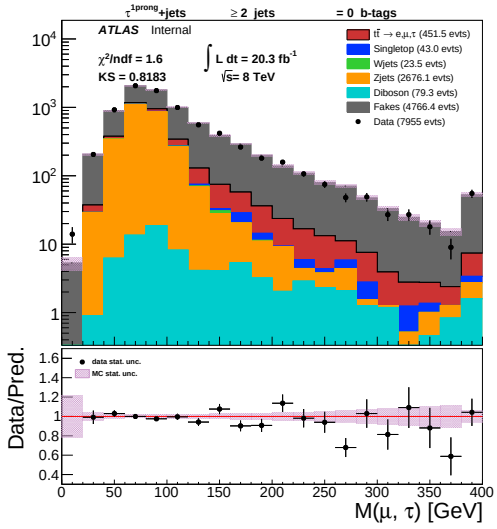

(c) invariant mass(μ, $\tau_{\text{1-prong}}$)

Figure 5.19: 2 inclusive jet and 0 b-jet validation region for $\mu + \tau_{\text{1-prong}}$ final state. Only the uncertainty related to statistic is shown in the plots and the systematic uncertainties are not included.

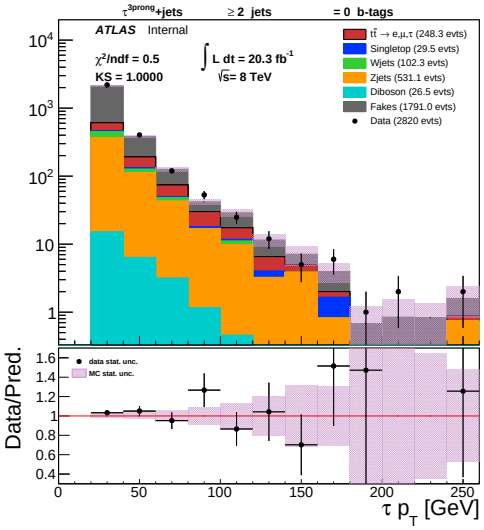

(a) p_T: $\tau_{\text{3-prong}}$

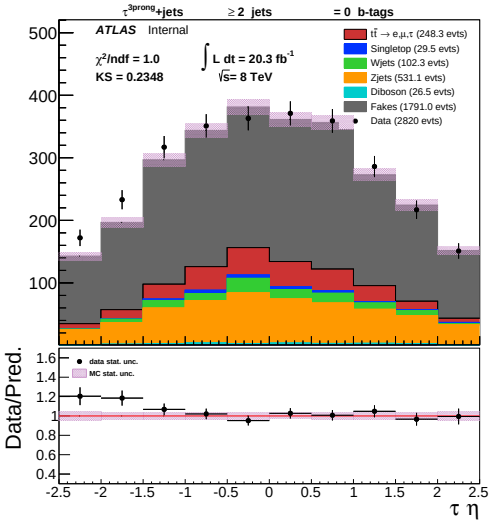

(b) η: $\tau_{\text{3-prong}}$

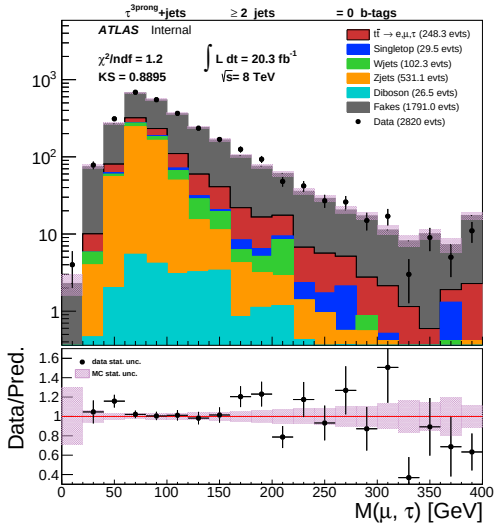

(c) invariant mass (μ, $\tau_{\text{3-prong}}$)

Figure 5.20: 2 inclusive jet and 0 b-jet validation region for $\mu + \tau_{\text{3-prong}}$ final state. Only the uncertainty related to statistic is shown in the plots and the systematic uncertainties are not included.

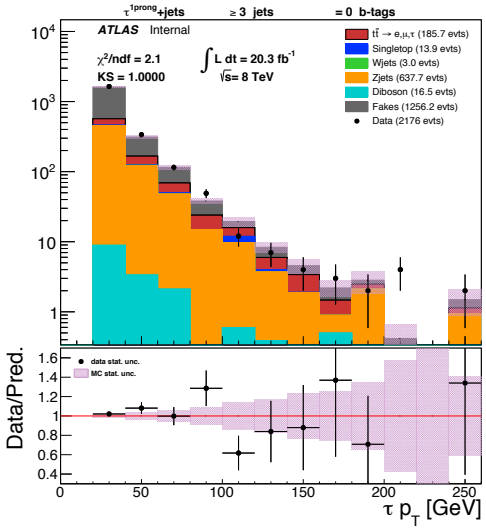

(a) p_T: $\tau_{\text{1-prong}}$

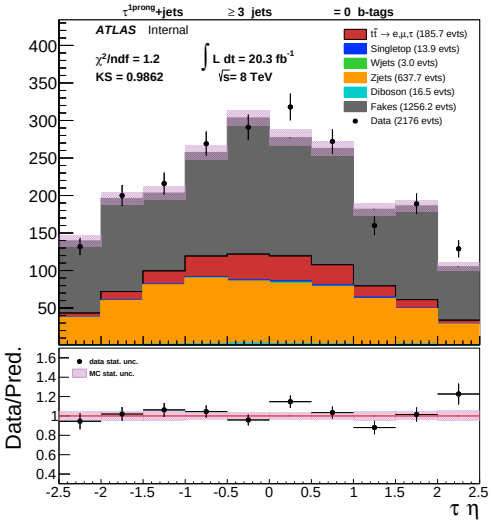

(b) η: $\tau_{\text{1-prong}}$

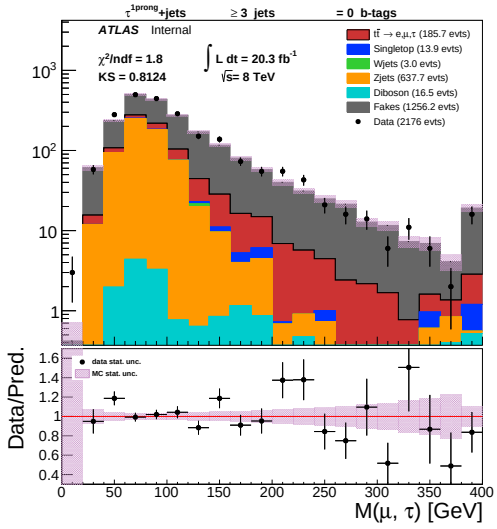

(c) invariant mass (μ, $\tau_{\text{1-prong}}$)

Figure 5.21: 3 inclusive jet and 0 b-jet validation region for $\mu + \tau_{\text{1-prong}}$ final state. Only the uncertainty related to statistic is shown in the plots and the systematic uncertainties are not included.

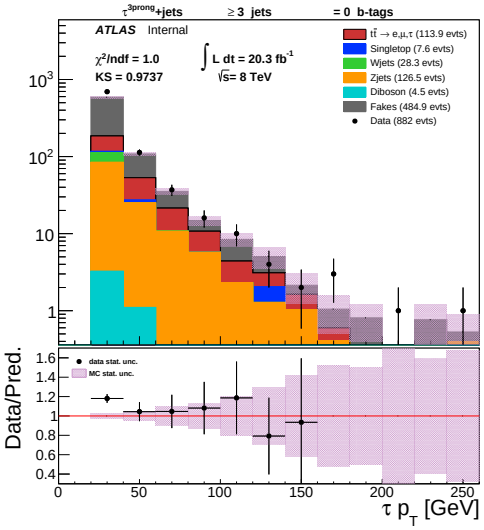

(a) p_T: $\tau_{\text{3-prong}}$

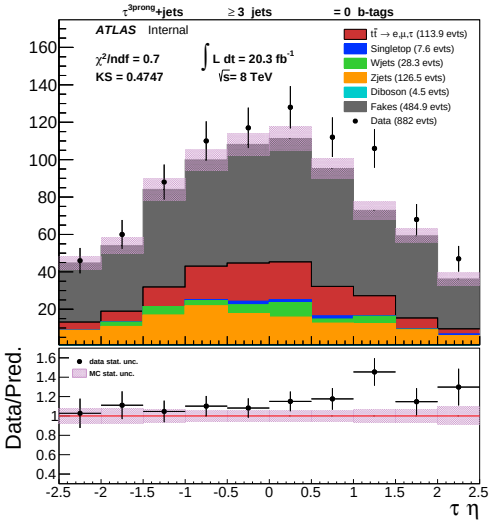

(b) η: $\tau_{\text{3-prong}}$

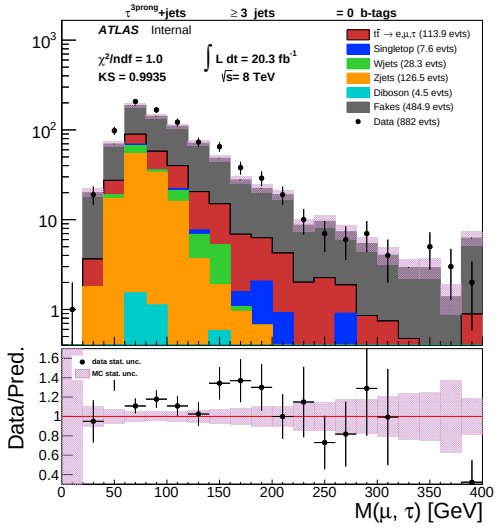

(c) invariant mass (μ, $\tau_{\text{3-prong}}$)

Figure 5.22: 3 inclusive jet and 0 b-jet validation region for $\mu + \tau_{\text{3-prong}}$ final state. Only the uncertainty related to statistic is shown in the plots and the systematic uncertainties are not included.

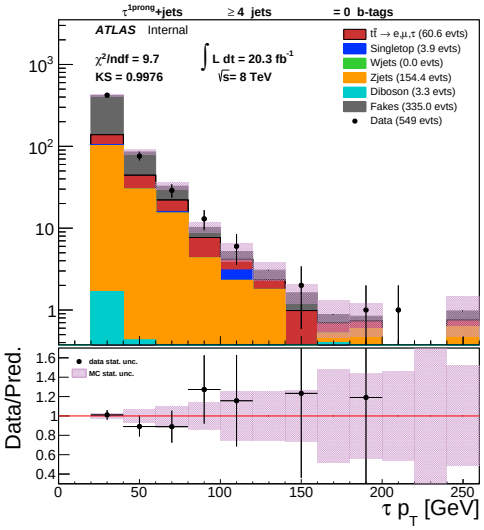

(a) p_T: $\tau_{\text{1-prong}}$

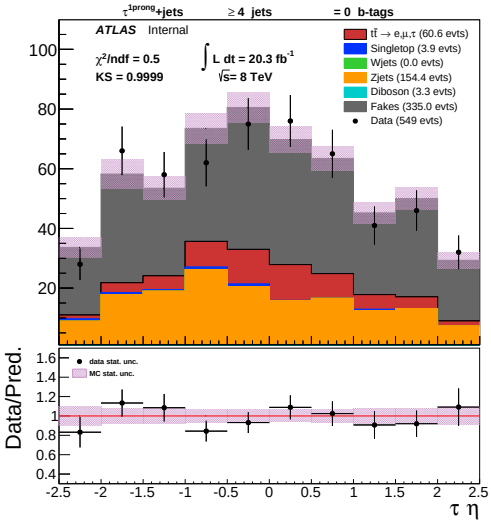

(b) η: $\tau_{\text{1-prong}}$

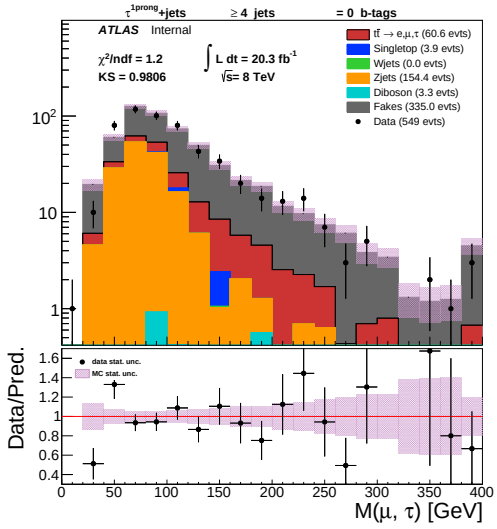

(c) invariant mass (μ, $\tau_{\text{1-prong}}$)

Figure 5.23: 4 inclusive jet and 0 b-jet validation region for $\mu + \tau_{\text{1-prong}}$ final state. Only the uncertainty related to statistic is shown in the plots and the systematic uncertainties are not included.

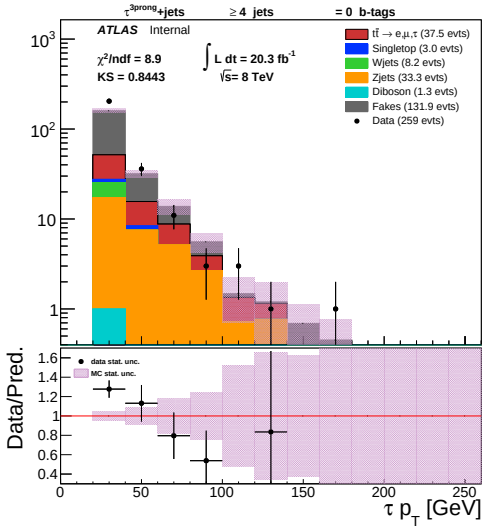

(a) p_T: $\tau_{\text{3-prong}}$

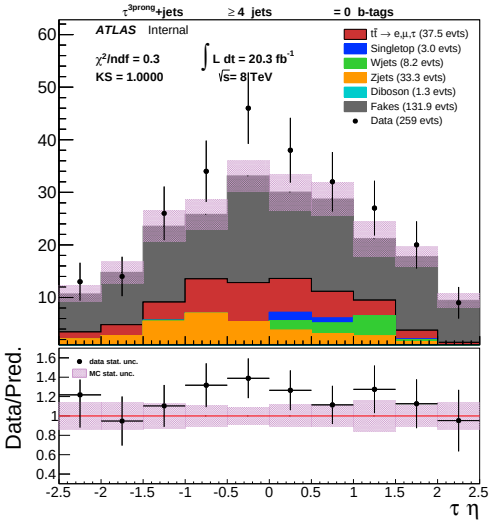

(b) η: $\tau_{\text{3-prong}}$

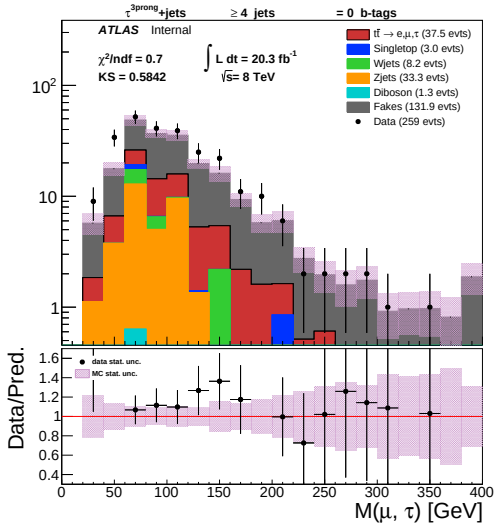

(c) invariant mass (μ, $\tau_{\text{3-prong}}$)

Figure 5.24: 4 inclusive jet and 0 b-jet validation region for $\mu + \tau_{\text{3-prong}}$ final state. Only the uncertainty related to statistic is shown in the plots and the systematic uncertainties are not included.

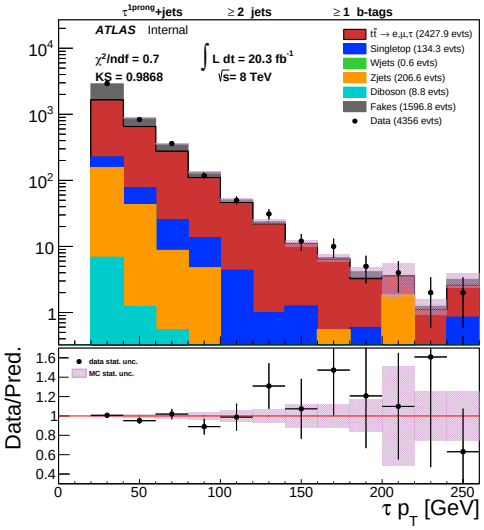

(a) p_T: $\tau_{\text{1-prong}}$

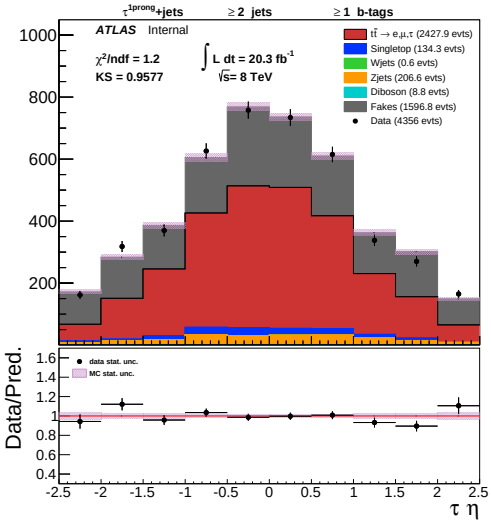

(b) η: $\tau_{\text{1-prong}}$

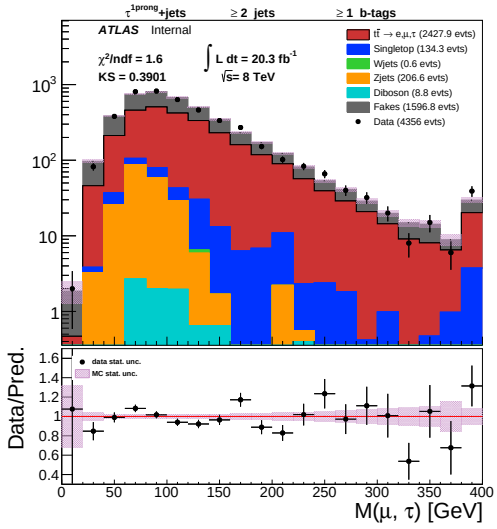

(c) invariant mass (μ, $\tau_{\text{1-prong}}$)

Figure 5.25: 2 inclusive jet and 1inclusive b-jet validation region for $\mu + \tau_{\text{1-prong}}$ final state. Only the uncertainty related to statistic is shown in the plots and the systematic uncertainties are not included.

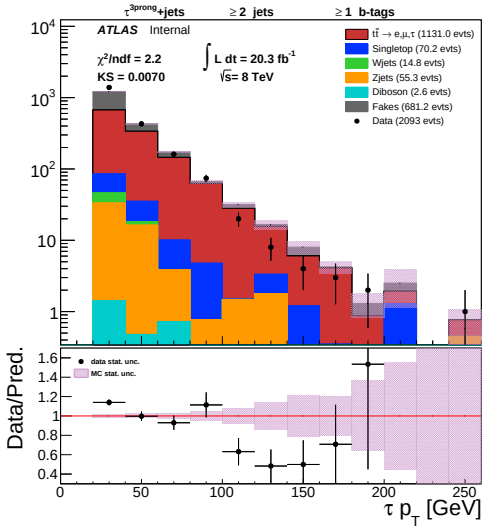

(a) p_T: $\tau_{\text{3-prong}}$

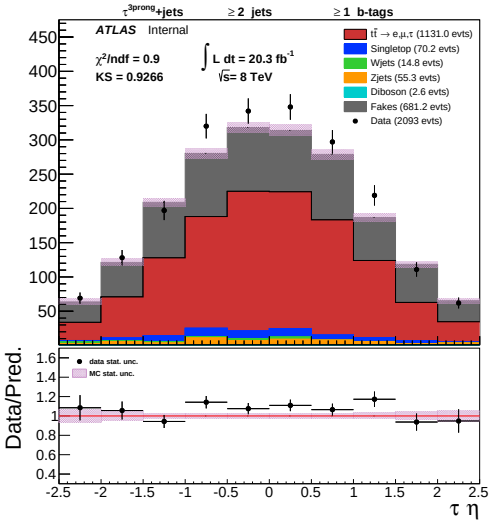

(b) η: $\tau_{\text{3-prong}}$

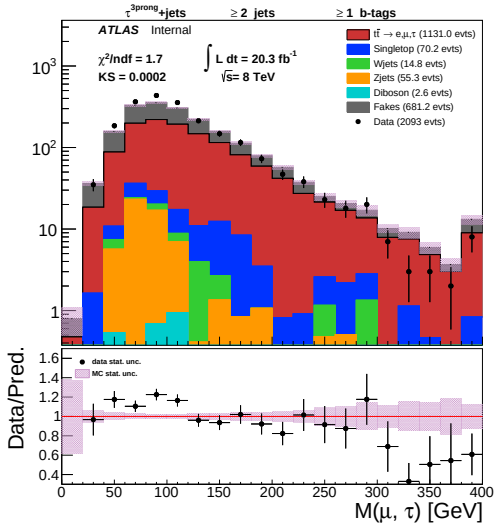

(c) invariant mass (μ, $\tau_{\text{3-prong}}$)

Figure 5.26: 2 inclusive jet and 1inclusive b-jet validation region for $\mu + \tau_{\text{3-prong}}$ final state. Only the uncertainty related to statistic is shown in the plots and the systematic uncertainties are not included.

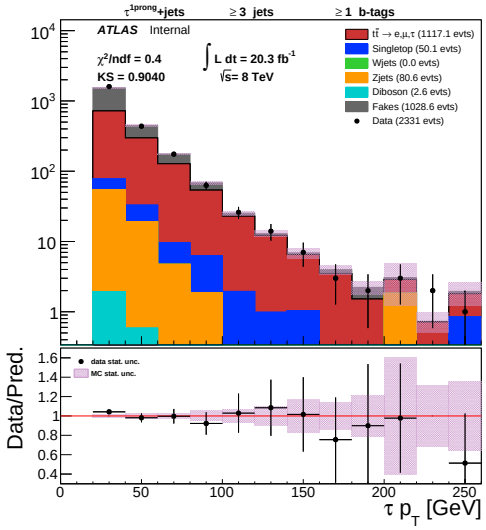

(a) p_T: $\tau_{\text{1-prong}}$

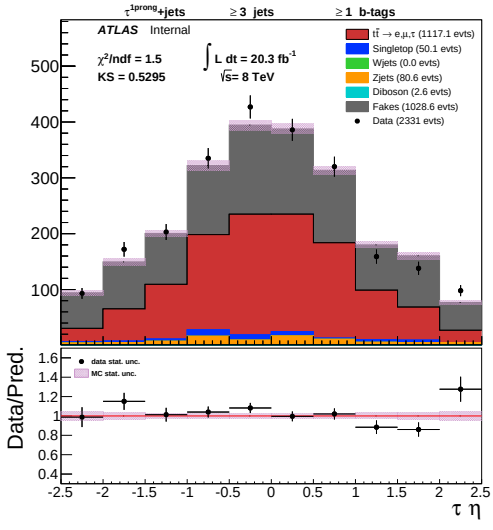

(b) η: $\tau_{\text{1-prong}}$

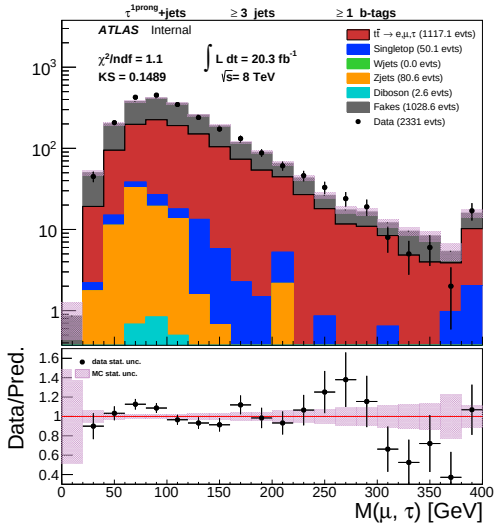

(c) invariant mass (μ, $\tau_{\text{1-prong}}$)

Figure 5.27: 3 inclusive jet and 1 inclusive b-jet validation region for $\mu + \tau_{\text{1-prong}}$ final state. Only the uncertainty related to statistic is shown in the plots and the systematic uncertainties are not included.

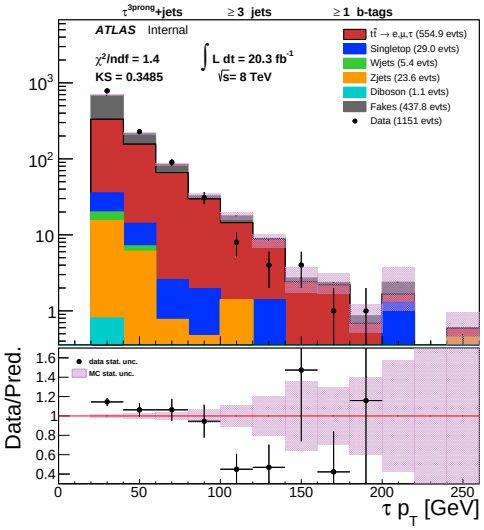

(a) p_T: $\tau_{3\text{-prong}}$

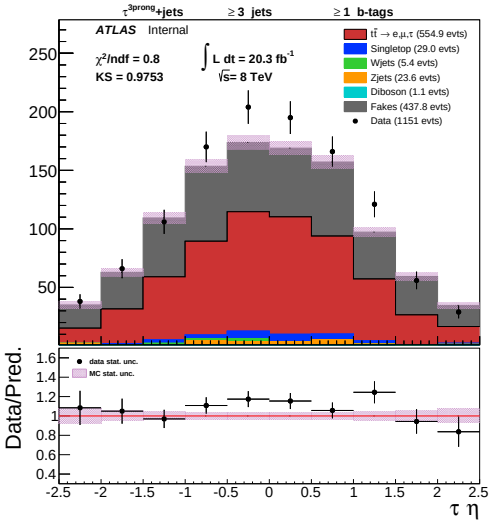

(b) η: $\tau_{3\text{-prong}}$

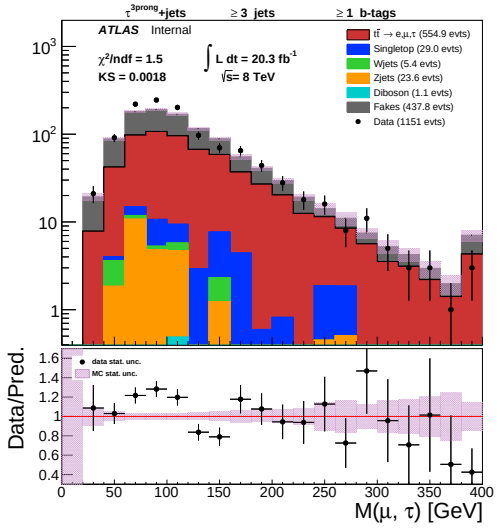

(c) invariant mass (μ, $\tau_{3\text{-prong}}$)

Figure 5.28: 3 inclusive jet and 1 inclusive b-jet validation region for $\mu + \tau_{3\text{-prong}}$ final state. Only the uncertainty related to statistic is shown in the plots and the systematic uncertainties are not included.

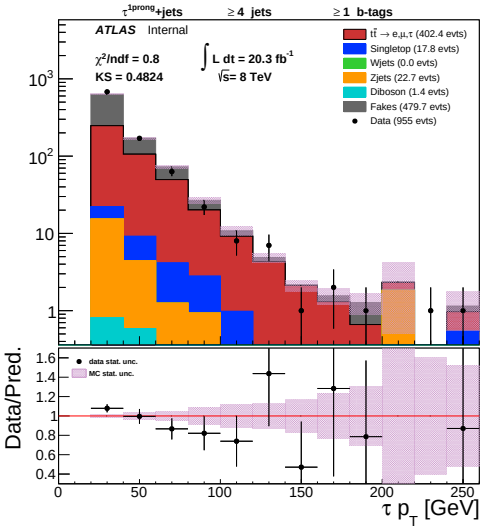

(a) p_T: $\tau_{\text{1-prong}}$

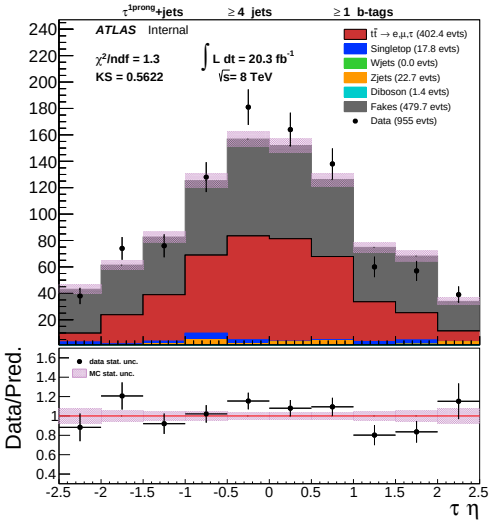

(b) η: $\tau_{\text{1-prong}}$

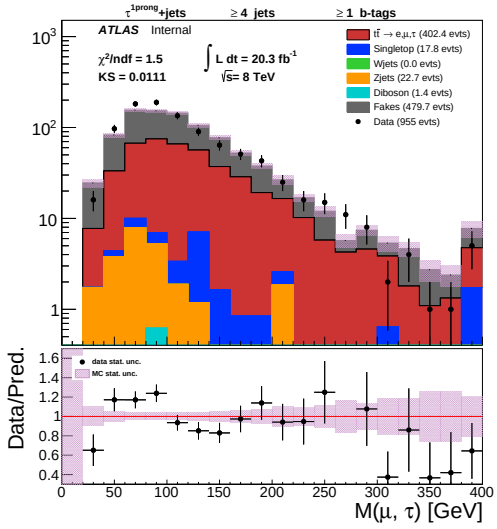

(c) invariant mass (μ, $\tau_{\text{1-prong}}$)

Figure 5.29: 4 inclusive jet and 1 inclusive b-jet validation region for $\mu + \tau_{\text{1-prong}}$ final state. Only the uncertainty related to statistic is shown in the plots and the systematic uncertainties are not included.

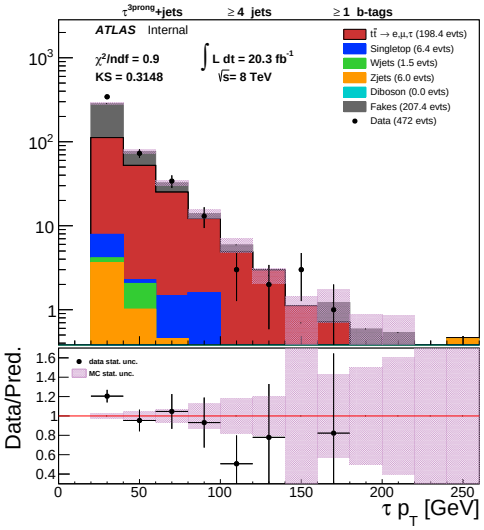

(a) p_T: $\tau_{\text{3-prong}}$

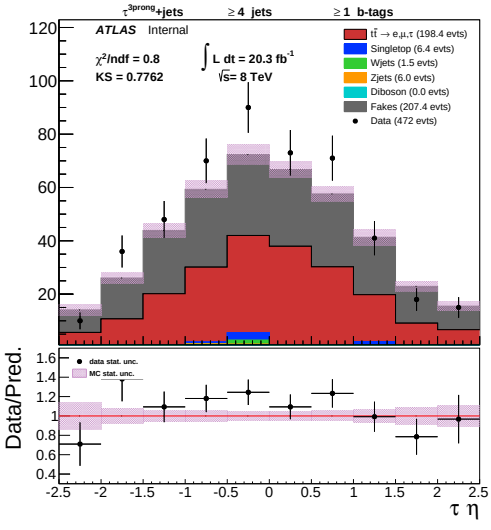

(b) η: $\tau_{\text{3-prong}}$

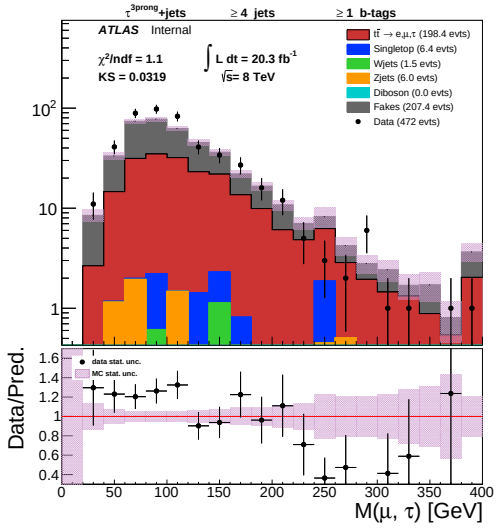

(c) invariant mass (μ, $\tau_{\text{3-prong}}$)

Figure 5.30: 4 inclusive jet and 1 inclusive b-jet validation region for $\mu + \tau_{\text{3-prong}}$ final state. Only the uncertainty related to statistic is shown in the plots and the systematic uncertainties are not included.

- $25 < p_T^{\mu} < 40$ GeV.

Figures 5.31 and 5.32 show the results of this validation region.

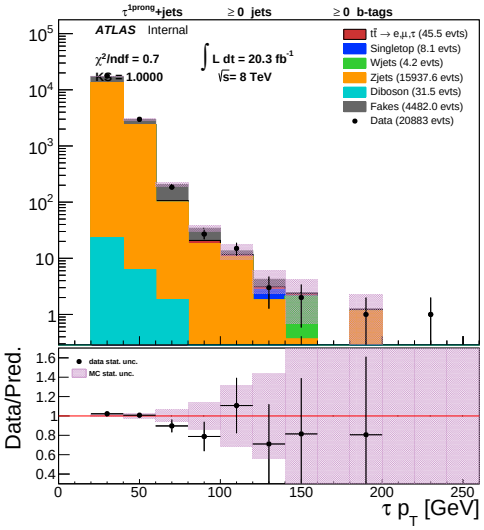

(a) p_T: $\tau_{\text{1-prong}}$

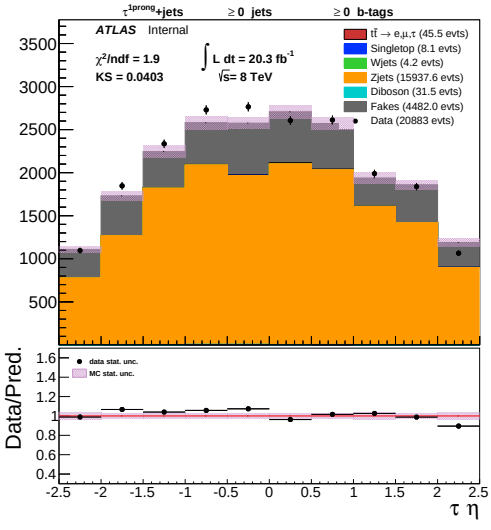

(b) η: $\tau_{\text{1-prong}}$

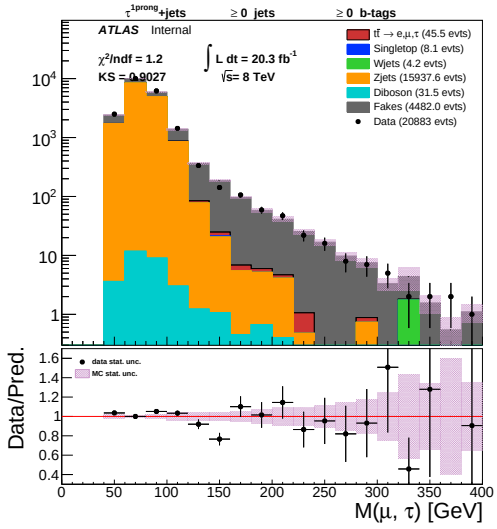

(c) invariant mass (μ, $\tau_{\text{1-prong}}$)

Figure 5.31: $Z \to \tau_\mu \tau_{\text{had}}$ validation region to test the true $\tau_{\text{1-prong}}$ selection. Only the uncertainty related to statistic is shown in the plots and the systematic uncertainties are not included.

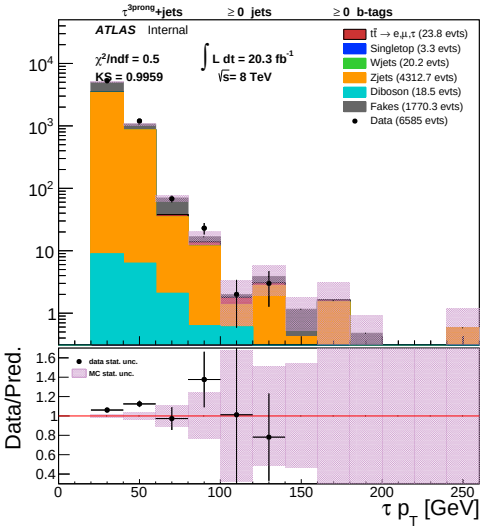

(a) p_T: $\tau_{\text{3-prong}}$

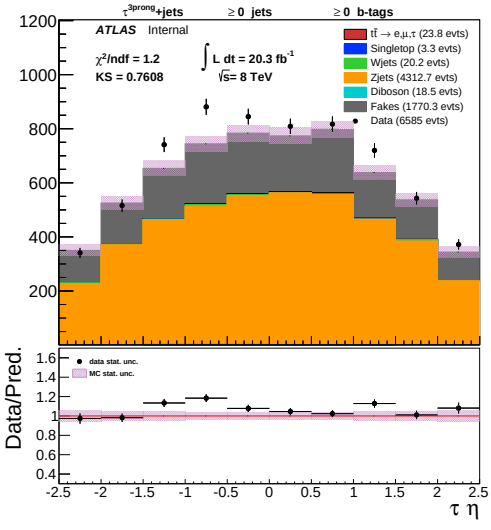

(b) η: $\tau_{\text{3-prong}}$

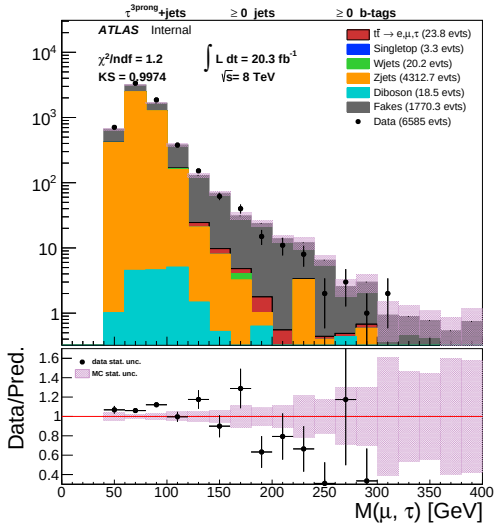

(c) invariant mass (μ, $\tau_{\text{3-prong}}$)

Figure 5.32: $Z \to \tau_\mu \tau_{\text{had}}$ validation region to test the true $\tau_{\text{3-prong}}$ selection. Only the uncertainty related to statistic is shown in the plots and the systematic uncertainties are not included.

5.6 Signal and background contributions in the signal region

The event pre-selection criteria are discussed in section 5.4. The estimation of the fake background is discussed in section 5.5. The prompt backgrounds are estimated in simulation and normalized to the data luminosity using the theoretical cross section corresponding to each process. Since the τ identification algorithm uses separate sets of requirement for $\tau_{\text{1-prong}}$ and $\tau_{\text{3-prong}}$ as discussed in section 5.3.2, different aspects of the analysis (agreement of data and simulation, cross section and uncertainties) are cross checked separately for $\tau_{\text{1-prong}}$ and $\tau_{\text{3-prong}}$ candidate. In general, the $\tau_{\text{3-prong}}$ has a better data/prediction agreement compared to $\tau_{\text{1-prong}}$, however, $\tau_{\text{3-prong}}$ is associated with larger systematic uncertainties.

The agreement between data and prediction in different kinematic distributions after pre-selection criteria are shown in Figs. 5.33 and 5.34 for $\tau_{\text{1-prong}}$, Figs. 5.35 and 5.36 for $\tau_{\text{3-prong}}$ and Figs. 5.37 and 5.38 for combined τ candidates in the final state. Good agreement between data and predictions have been observed as evident by the χ^2 and KS values. The fake background is further reduced by using the reconstructed W transverse mass.

The distribution of m_{WT} after pre-selection requirements is shown in Fig. 5.39. Different requirements on the value of the m_{WT} are studied and a requirement of $m_{WT} < 90$ GeV gives the largest ratio for the signal to background events, and selected for the definition of the SR.

The distributions of several kinematic and topological variables to compare the data with predicted backgrounds in the SR after final selection for the combined

$\tau_{\text{1-prong}}$ and $\tau_{\text{3-prong}}$ final state is shown in Fig. 5.44 and 5.45. The same distributions for $\tau_{\text{1-prong}}$ and $\tau_{\text{3-prong}}$ are shown in Figs. 5.40 to 5.43. Table 5.3 shows the signal and background yields for $\tau_{\text{1-prong}}$, $\tau_{\text{3-prong}}$ and combined τ candidates in the final state.

Process	combined $\tau_{\text{1-prong}}$ and $\tau_{\text{3-prong}}$	$\tau_{\text{1-prong}}$	$\tau_{\text{3-prong}}$
Observed data	6085	4603	1458
Total background	2440.7 ± 49.40	1880.3 ± 43.36	549.7 ± 23.44
$t\bar{t} \to l$	95.3 ± 9.76	68.0 ± 8.25	27.3 ± 5.22
Single top	552.1 ± 23.50	426.2 ± 20.64	125.3 ± 11.29
W+jets	1381.7 ± 37.17	1094.5 ± 33.08	287.2 ± 16.94
Z+jets	114.1 ± 10.68	97.7 ± 9.88	15.5 ± 3.94
Diboson	6.9 ± 2.62	5.2 ± 2.28	1.7 ± 1.30
Fakes	294.8 ± 17.17	191.0 ± 13.8	93.8 ± 9.68
Expected $t\bar{t} \to \tau$	3937.7 ± 62.91	3074.7 ± 55.45	879.7±29.66
Observed $t\bar{t} \to \tau$	3640.1	2720.4	907.2

Table 5.3: Number of events observed in data and simulation along with the associated statistical uncertainty for background and expected signal processes for different τ candidate in the final state in the SR after final selection.

The number of events and the associated efficiencies at each selection step for the SR for all processes are listed in Appendix C .

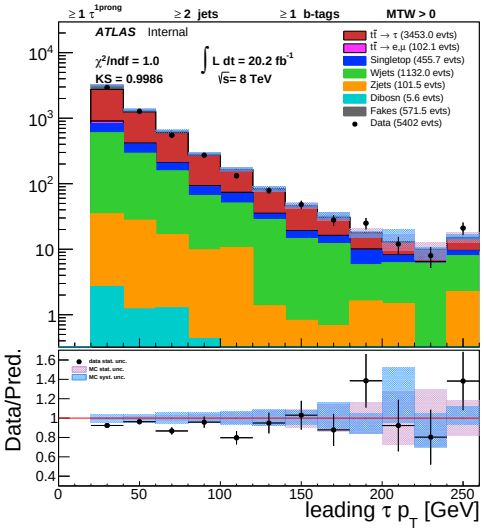

(a) $\tau_{\text{1-prong}}$- p_T

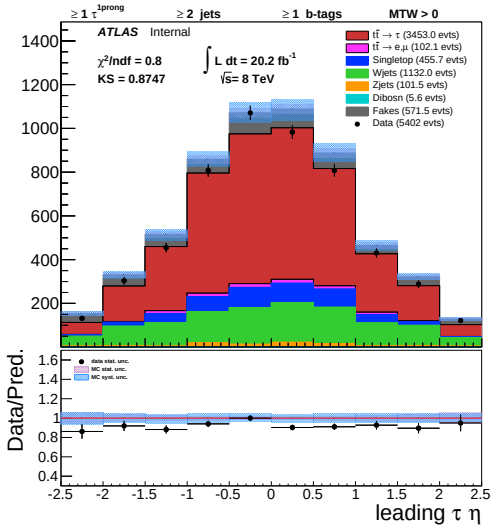

(b) $\tau_{\text{1-prong}}$- η

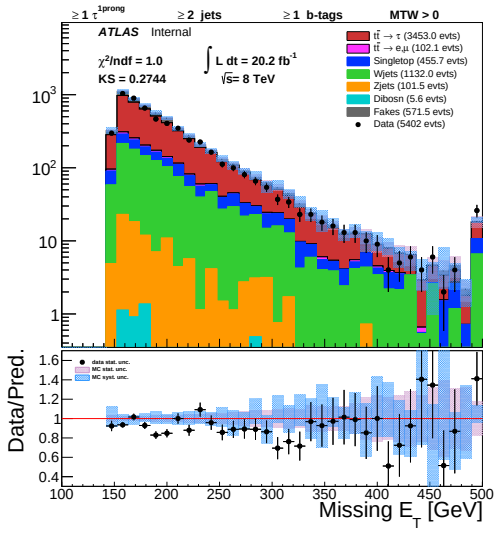

(c) $E_{\text{T}}^{\text{miss}}$

Figure 5.33: Control plots for tau p_{T}, tau η, and $E_{\text{T}}^{\text{miss}}$ distributions after pre-selection with $\tau_{\text{1-prong}}$ in the final state. Note the systematic uncertainty band only includes uncertainty related to detector simulation

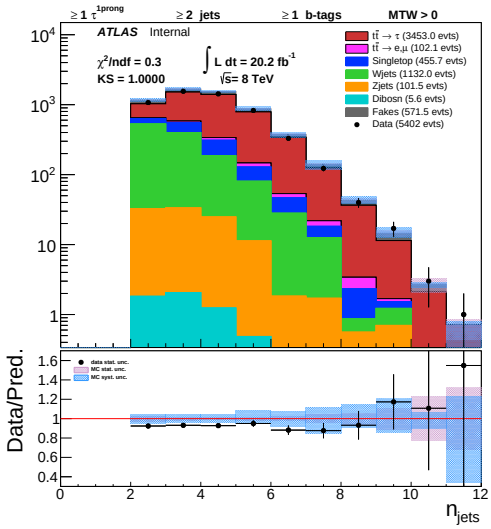

(a) all jet multiplicity

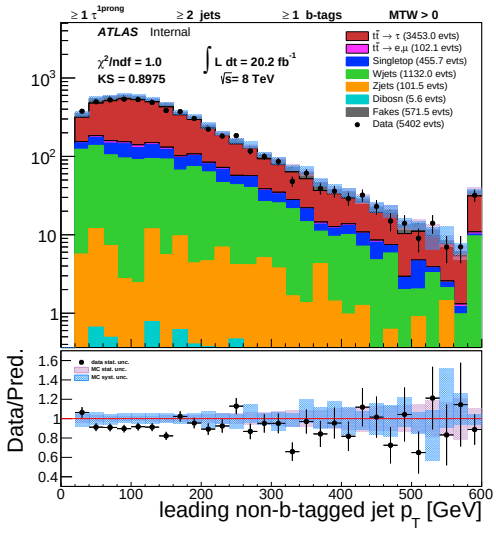

(b) leading light jet p_T

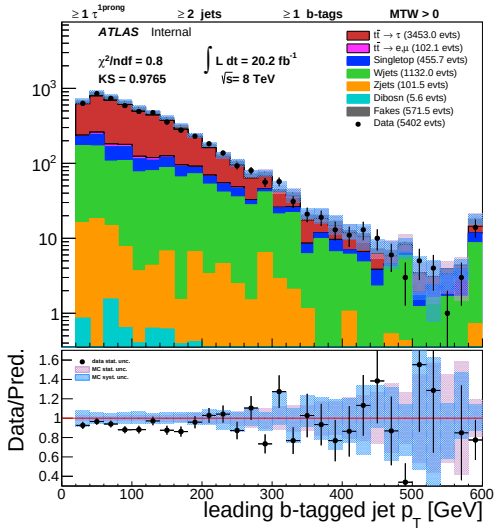

(c) leading b-jet p_T

Figure 5.34: Control plots for jet multiplicity, leading b-tagged jet p_{T} and leading non b-tagged jet p_{T} distributions after pre-selection with $\tau_{\text{1-prong}}$ in the final state. Note the systematic uncertainty band only includes uncertainty related to detector simulation

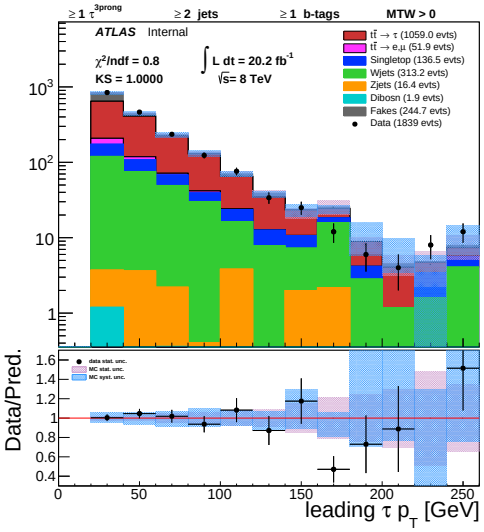

(a) $\tau_{\text{3-prong}}$- p_T

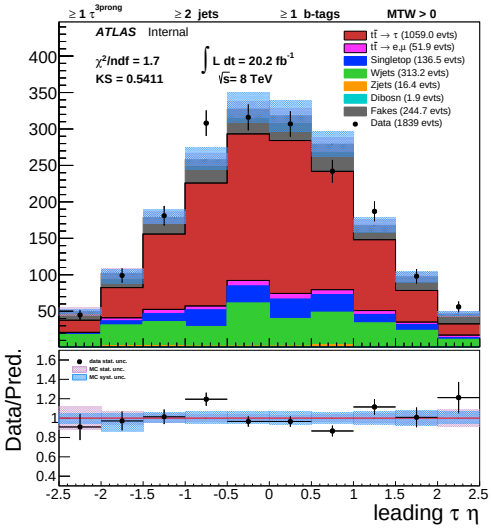

(b) $\tau_{\text{3-prong}}$- η

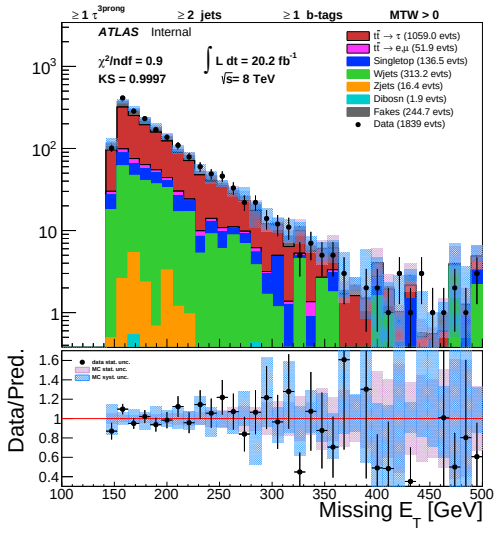

(c) $E_{\text{T}}^{\text{miss}}$

Figure 5.35: Control plots for tau p_{T}, tau η, and $E_{\text{T}}^{\text{miss}}$ distributions after pre-selection with $\tau_{\text{3-prong}}$ in the final state. Note the systematic uncertainty band only includes uncertainty related to detector simulation

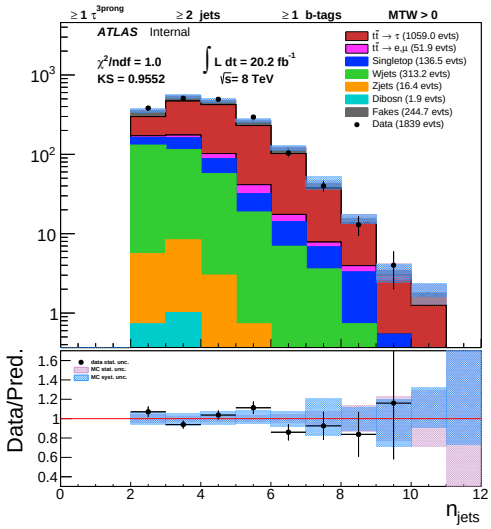

(a) all jet multiplicity

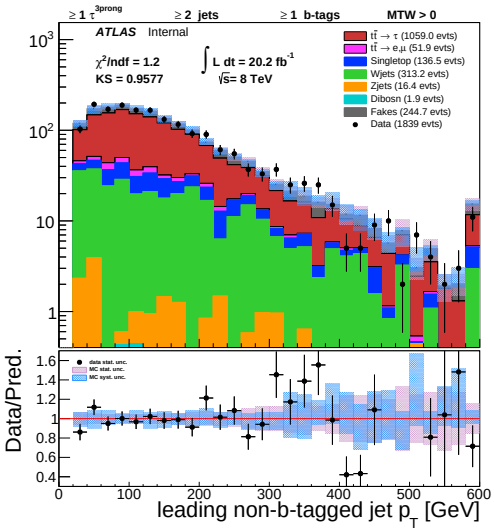

(b) leading light jet p_T

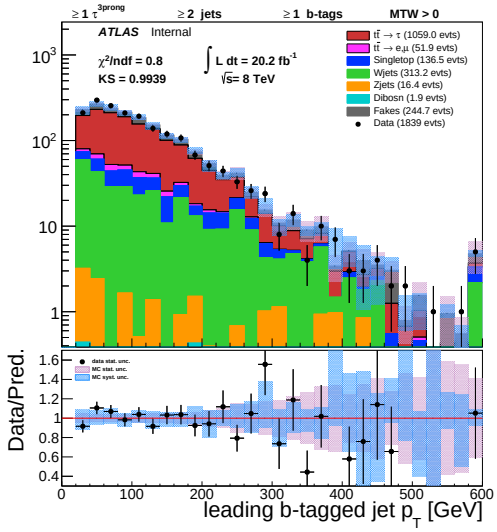

(c) leading b-jet p_T

Figure 5.36: Control plots for jet multiplicity, leading b-tagged jet p_{T} and leading non b-tagged jet p_{T} distributions after pre-selection with $\tau_{\text{3-prong}}$ in the final state. Note the systematic uncertainty band only includes uncertainty related to detector simulation

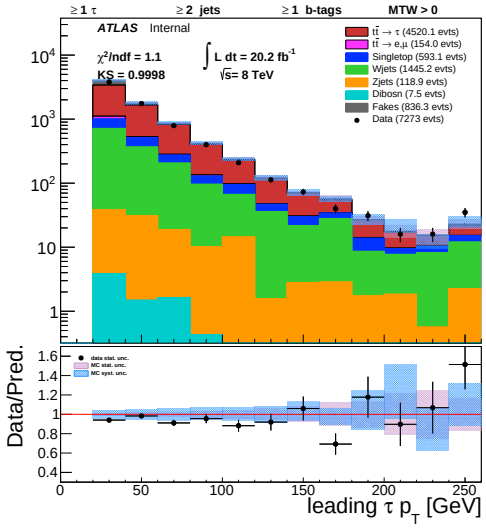

(a) τ- p_T

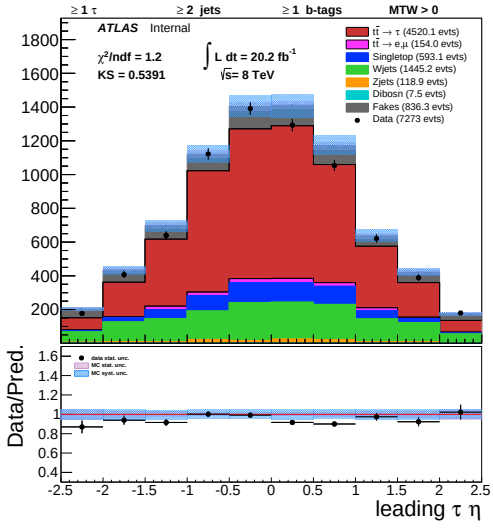

(b) τ- η

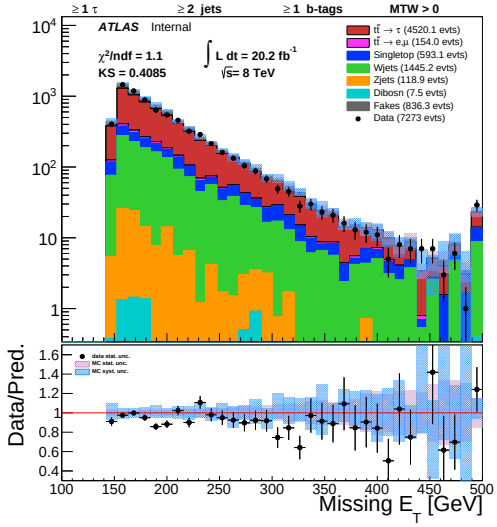

(c) $E_{\mathrm{T}}^{\mathrm{miss}}$

Figure 5.37: Control plots for tau p_{T}, tau η, and $E_{\mathrm{T}}^{\mathrm{miss}}$ distributions after pre-selection with τ (either $\tau_{\text{1-prong}}$ or $\tau_{\text{3-prong}}$) in the final state. Note the systematic uncertainty band only includes uncertainty related to detector simulation

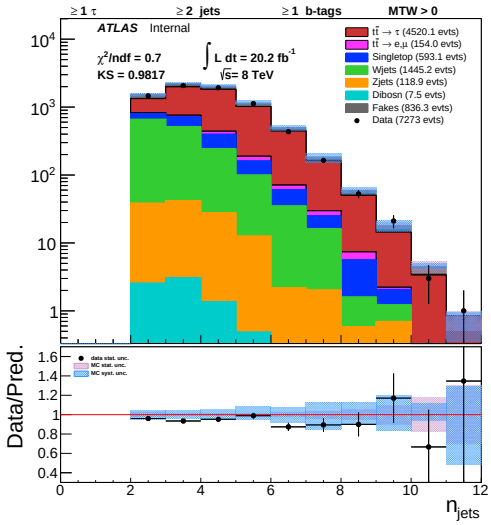

(a) all jet multiplicity

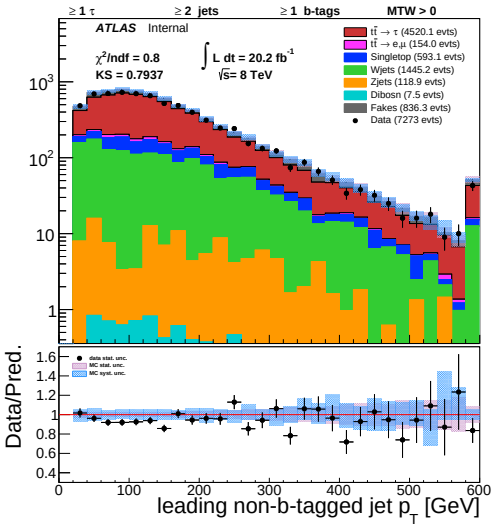

(b) leading light jet p_T

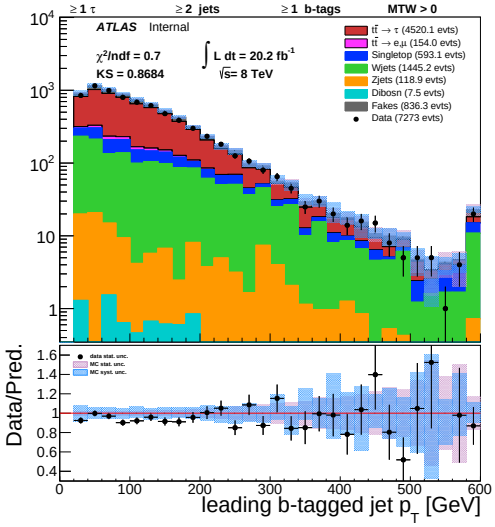

(c) leading b-jet p_T

Figure 5.38: Control plots for jet multiplicity, leading b-tagged jet p_{T} and leading non b-tagged jet p_{T} distributions after pre-selection with τ (either $\tau_{\text{1-prong}}$ or $\tau_{\text{3-prong}}$) in the final state. Note the systematic uncertainty band only includes uncertainty related to detector simulation

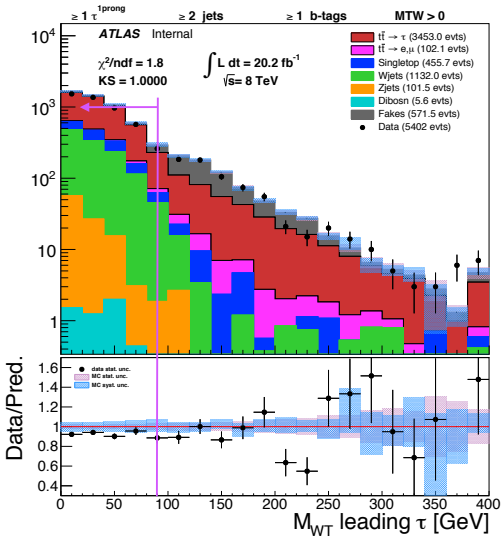

(a) $\tau_{\text{1-prong}}$

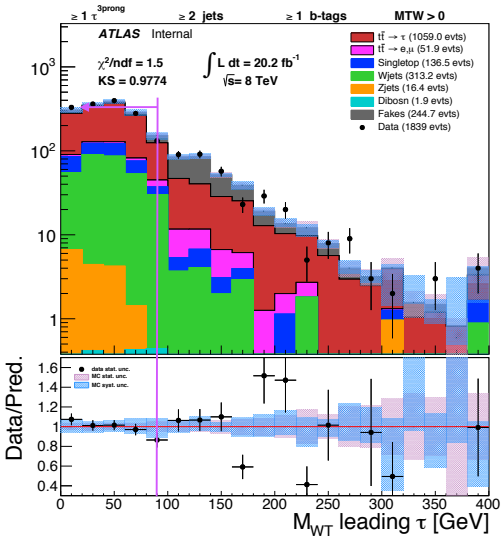

(b) $\tau_{\text{3-prong}}$

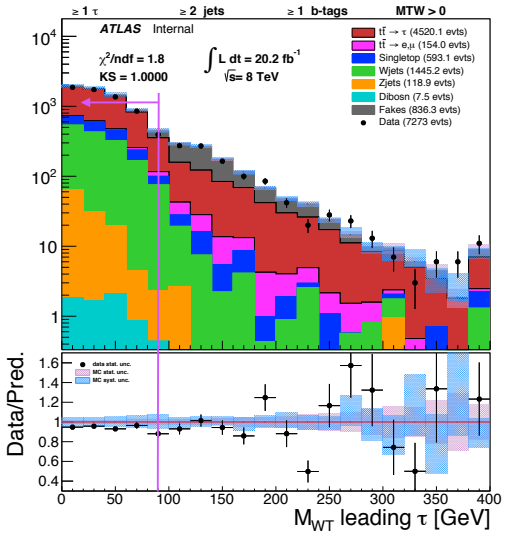

(c) combined $\tau_{\text{1-prong}}$ and $\tau_{\text{3-prong}}$

Figure 5.39: Distribution of the W transverse mass after pre-selection criteria. The arrow shows the SR selection.

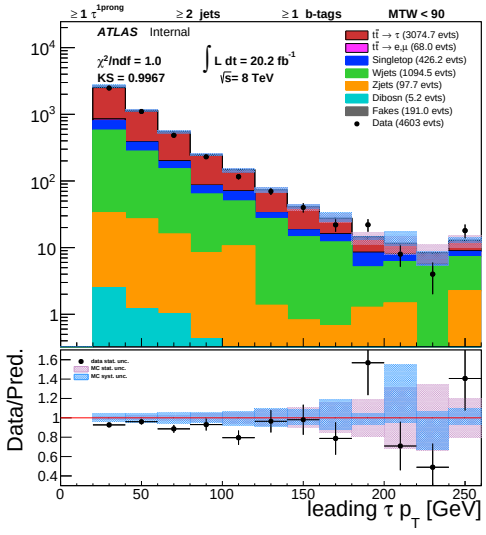

(a) $\tau_{\text{1-prong}}$- p_T

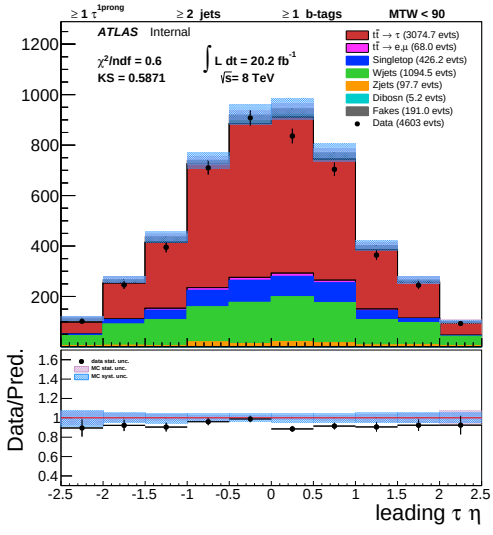

(b) $\tau_{\text{1-prong}}$- η

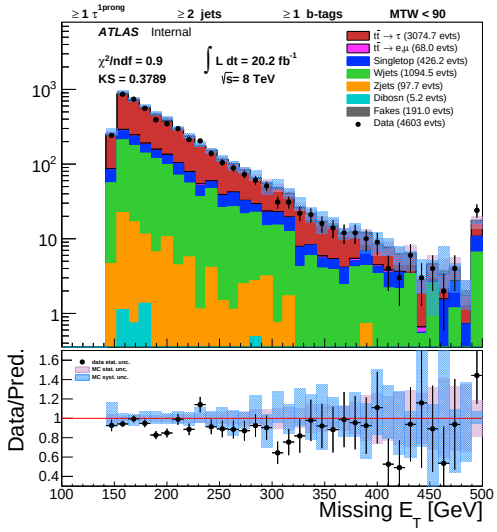

(c) $E_{\text{T}}^{\text{miss}}$

Figure 5.40: Control plots for signal region in tau p_{T}, η and $E_{\text{T}}^{\text{miss}}$ distributions with $\tau_{\text{1-prong}}$ in the final state. The uncertainties related to statistic and systematic are also shown. Note the systematic band only includes uncertainties related to detector simulation.

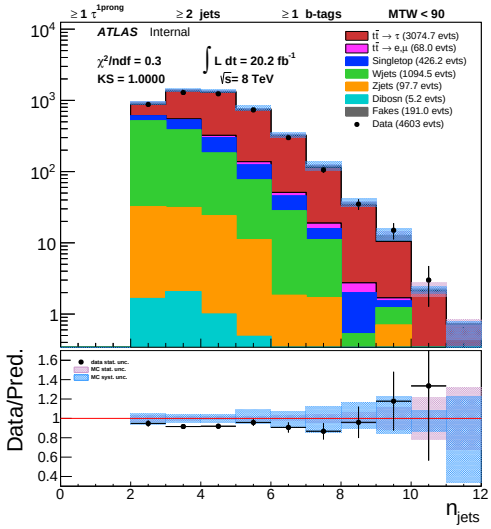

(a) all jet multiplicity

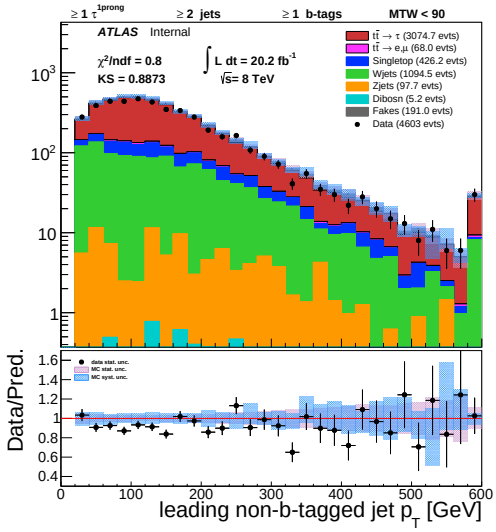

(b) leading light jet p_T

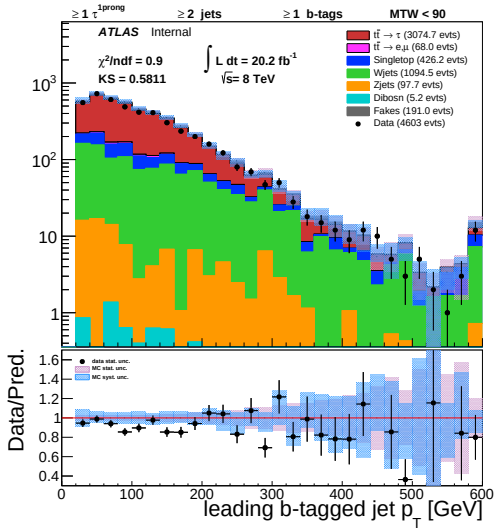

(c) leading b-jet p_T

Figure 5.41: Control plots for signal region in jet multiplicity, leading b-tagged jet p_{T} and leading non b-tagged jet p_{T} distributions with $\tau_{\text{1-prong}}$ in the final state. The uncertainties related to statistic and systematic are also shown. Note the systematic band only includes uncertainties related to detector simulation.

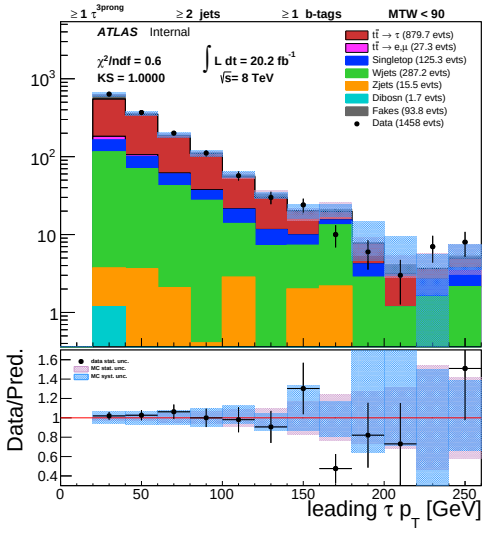

(a) $\tau_{\text{3-prong}}$- p_T

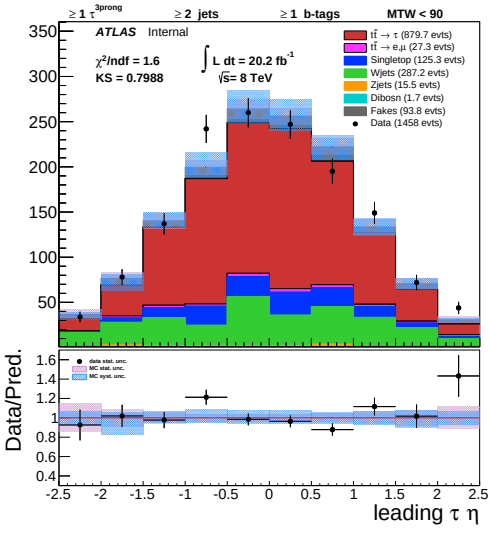

(b) $\tau_{\text{3-prong}}$- η

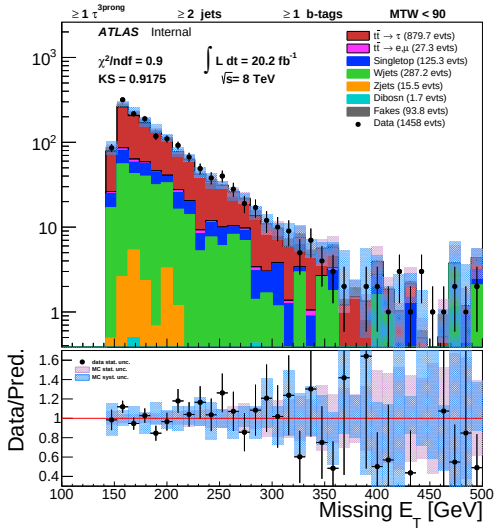

(c) $E_{\text{T}}^{\text{miss}}$

Figure 5.42: Control plots for signal region in tau p_{T}, η and $E_{\text{T}}^{\text{miss}}$ distributions with $\tau_{\text{3-prong}}$ in the final state. The uncertainties related to statistic and systematic are also shown. Note the systematic band only includes uncertainties related to detector simulation.

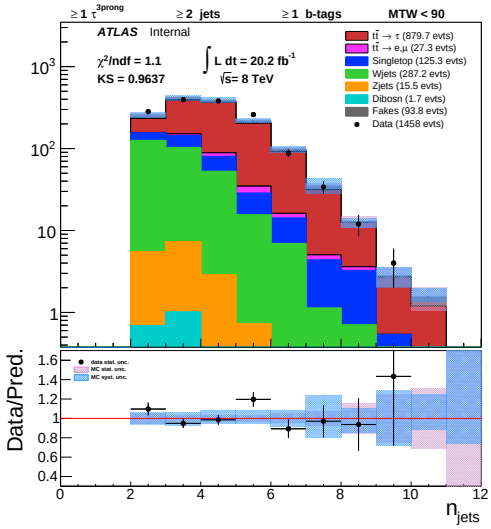

(a) all jet multiplicity

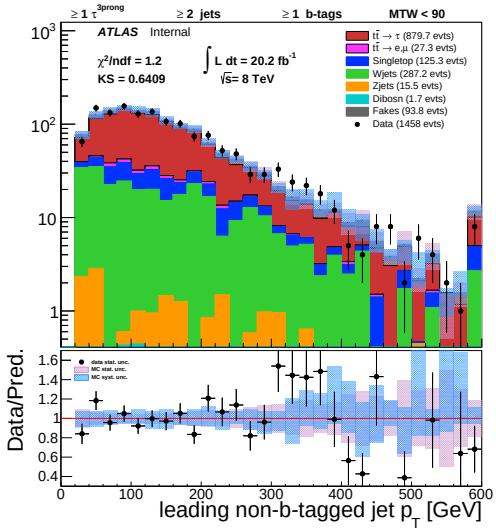

(b) leading light jet p_T

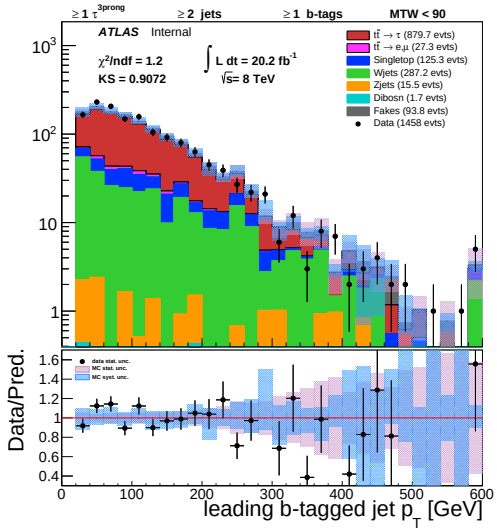

(c) leading b-jet p_T

Figure 5.43: Control plots for signal region in jet multiplicity, leading b-tagged jet p_{T} and leading non b-tagged jet p_{T} distributions with $\tau_{\text{3-prong}}$ in the final state. The uncertainties related to statistic and systematic are also shown. Note the systematic band only includes uncertainties related to detector simulation.

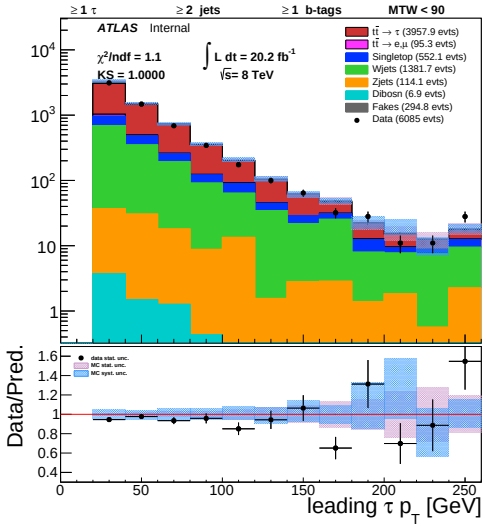

(a) τ- p_T

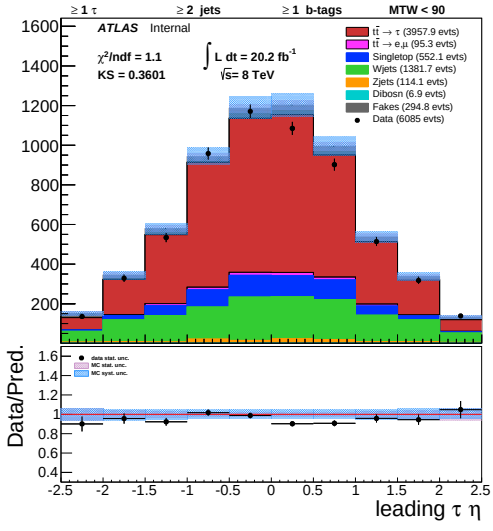

(b) τ- η

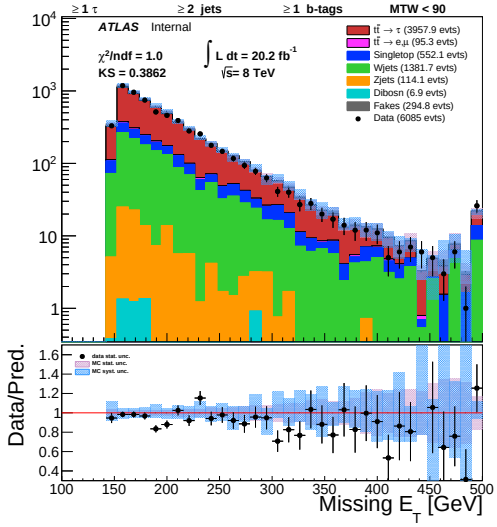

(c) $E_{\mathrm{T}}^{\mathrm{miss}}$

Figure 5.44: Control plots for signal region in tau p_{T}, η and $E_{\mathrm{T}}^{\mathrm{miss}}$ distributions with τ (either $\tau_{\text{1-prong}}$ or $\tau_{\text{3-prong}}$) in the final state. The uncertainties related to statistic and systematic are also shown. Note the systematic band only includes uncertainties related to detector simulation.

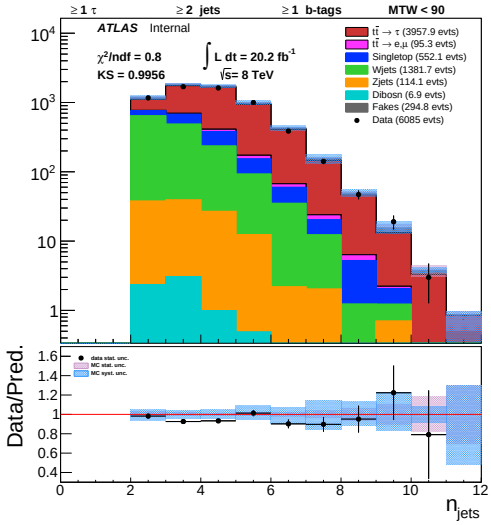

(a) all jet multiplicity

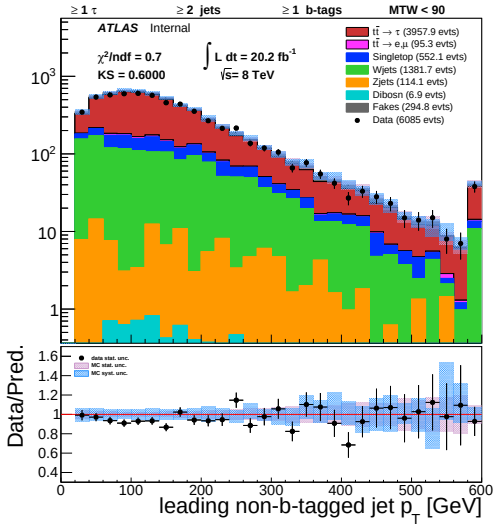

(b) leading light jet p_T

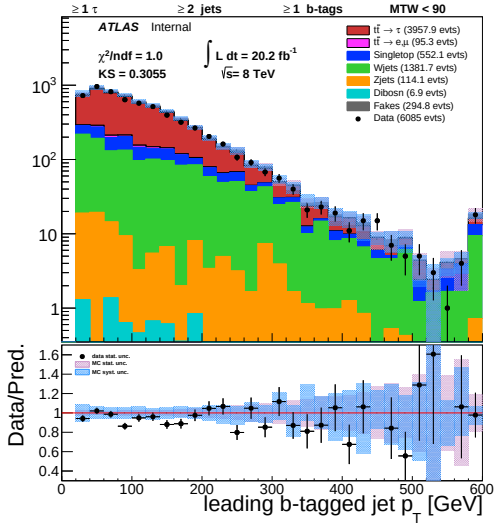

(c) leading b-jet p_T

Figure 5.45: Control plots for signal region in jet multiplicity, leading b-tagged jet p_{T} and leading non b-tagged jet p_{T} distributions with τ (either $\tau_{\text{1-prong}}$ or $\tau_{\text{3-prong}}$) in the final state. The uncertainties related to statistic and systematic are also shown. Note the systematic band only includes uncertainties related to detector simulation.

5.7 Measurement of $t\bar{t}$ production cross section

The cross section of a given process is calculated in general using the following equation:

$$\sigma\left(pp \to t\bar{t}\right) \times \mathrm{BR} = \frac{N_{\mathrm{data}} - N_{\mathrm{bkg}}}{\varepsilon_{t\bar{t}\to\tau} \cdot \int \mathcal{L}\left(t\right) dt} \tag{5.21}$$

where,

- N_{data} is the number of events passing the event selection criteria with data,
- N_{bkg} is number of events contributing to signal selection coming from processes other than $t\bar{t}$,
- $\varepsilon_{t\bar{t}\to\tau}$ is the signal efficiency with detector acceptance convoluted. The signal efficiency is measured in simulation as the fraction of events passing the signal selection to the total number of events in the sample,
- $\int \mathcal{L}\left(t\right) dt$ is the integrated luminosity for the year 2012 collected by the ATLAS detector and
- BR is the branching ratio, BR $\left(1 - \mathrm{BR}\left(t\bar{t} \to \mathrm{fullyhadronic}\right)\right) = 0.544$

The total number of backgrounds is the sum of the $t\bar{t} \to l$, single top, W + jets, Z + jets, diboson and the fake tau backgrounds. The fake background is estimated in data using equation 5.5 and the method described in 5.5. The contribution from real taus (prompt) in fake estimation are estimated in simulation and subtracted The total number of background contribution in SR is,

$$N_{\text{bkg}} = N_{t\bar{t}\to l} + N_{\text{singletop}} + N_{\text{W/Z+jets}} + N_{\text{diboson}} + (N_{\text{fakes,data}} - N_{\text{prompt,fakes}}) \quad (5.22)$$

where, $N_{\text{fakes,data}}$ is the number of fake events estimated in data while $N_{\text{prompt,fakes}}$ is the estimated number of prompt τ events in those data events. Prompt contributions come from $t\bar{t}$, W/Z+jets, single top and diboson processes,

$$N_{\text{prompt,fakes}} = N_{\text{prompt}-\text{t}\bar{\text{t}},\text{fakes}} + N_{\text{prompt}-\text{other,fakes}} \quad (5.23)$$

$N_{\text{prompt}-\text{t}\bar{\text{t}},\text{fakes}}$ however, is normalized using the $t\bar{t}$ cross section to the data luminosity and reweighted using fake-factors,

$$N_{\text{prompt},t\bar{t}} = \sigma\left(pp \to t\bar{t}\right) \cdot \int \mathcal{L}\left(t\right) dt \cdot \text{BR} \cdot \varepsilon_{\text{prompt},t\bar{t}} \cdot \text{FF} \quad (5.24)$$

Combining the above set of equations a modified cross section is written as,

$$\begin{aligned} \sigma\left(pp \to t\bar{t}\right) \times \text{BR} \;=\; & \{N_{\text{data}} - (N_{\text{fakes,data}} - N_{\text{prompt}-\text{other,fakes}}) \\ & - N_{t\bar{t}\to l} - N_{\text{singletop}} - N_{\text{W/Z+jets}} \\ & - N_{\text{diboson}}\} / \left(\varepsilon_{t\bar{t}\to\tau} - \varepsilon_{\text{prompt}-\text{t}\bar{\text{t}},\text{fakes}} \cdot \text{FF}\right) \cdot \int \mathcal{L}\left(t\right) \quad (5.25) \end{aligned}$$

The modified equation is used in order to avoid normalizing $N_{\text{prompt}-\text{t}\bar{\text{t}},\text{fakes}}$ with the theoretical $t\bar{t}$ cross section. Instead, the efficiency times fake-factor is calculated

for the prompt contribution associated to $t\bar{t}$ processes. For each systematic source of uncertainty, the cross section is re-calculated by re-estimating the relevant number of events and acceptances in the modified equation.

5.8 Systematic uncertainties

The analysis takes into account different sources of systematic uncertainty related to detector simulation, $t\bar{t}$ signal modeling and reducible background estimation.

For each source of systematic uncertainty, the error is estimated by making a variation of a parameter related to the uncertainty with respect to the nominal analysis. The procedure to determine each source of systematic uncertainty follows the recommendation of the Top Working Group [185] as implemented in `AnalysisTop-1.9`. Details on each uncertainty are discussed in the following sections.

Only the uncertainties for combined $\tau_{\text{1-prong}}$ and $\tau_{\text{3-prong}}$ candidates are presented here. The uncertainties for individual candidate are listed separately in appendix D.

5.8.1 Tau energy scale

The tau energy scale systematic uncertainties are measured using a *deconvolution* and a *in-situ* method [155]. To estimate the uncertainty of the tau energy scale in this analysis, the p_T of the τ candidate is scaled up and down according to the statistical and systematic uncertainties associated in those measurements. The effect of the variation is shown in Table 5.4.

Systematics [%]	$\Delta\varepsilon_{t\bar{t}}/\varepsilon_{t\bar{t}}$	$\Delta N_{obs}/N_{obs}$	$\Delta\sigma_{t\bar{t}}/\sigma_{t\bar{t}}$
Tau energy scale	-1.34 / +1.43	-0.70 / +0.81	-2.58 / +2.67

Table 5.4: Relative systematic uncertainties on $t\bar{t}$ production cross section associated to the tau energy scale with either a $\tau_{\text{1-prong}}$ or a $\tau_{\text{3-prong}}$ candidate in the final state. $\Delta\varepsilon_{t\bar{t}}$ is the uncertainty on the efficiency, ΔN_{obs} is the uncertainty on the number of observed events due to prompt subtraction in the background estimation, and the $\Delta\sigma_{t\bar{t}}$ is the uncertainty on the final cross section.

5.8.2 Tau identification and tau electron veto

In the nominal analysis, the tau identification and electron veto efficiencies are corrected to correspond to data by using scale factors. The uncertainties of these correction factors depend slightly on the tau identification working point and kinematic quantities [155]. These uncertainties are propagated through the cross section measurement by varying the scale factors by one standard deviation with respect to their central values. Table 5.5 gives the details of these uncertainties.

Systematics [%]	$\Delta\varepsilon_{t\bar{t}}/\varepsilon_{t\bar{t}}$	$\Delta N_{obs}/N_{obs}$	$\Delta\sigma_{t\bar{t}}/\sigma_{t\bar{t}}$
Tau ID scale factor statistics	-1.64 / +1.64	-0.77 / +0.77	-3.17 / +3.05
Tau ID scale factor systematics	-2.15 / +2.15	-0.92 / +0.92	-4.18 / +3.97
Tau electron veto	-0.04 / +0.04	-0.06 / +0.06	-0.07 / +0.07
Total, Tau ID , eVeto	-2.70 / +2.70	-1.20 / +1.20	-5.25/ +5.01

Table 5.5: Relative systematic uncertainties on $t\bar{t}$ production cross section associated to tau identification and tau electron veto with either $\tau_{\text{1-prong}}$ or $\tau_{\text{3-prong}}$ candidate in the final state. $\Delta\varepsilon_{t\bar{t}}$ is the uncertainty on efficiency, ΔN_{obs} is the uncertainty on the number of observed events due to prompt subtraction in the background estimation, and the $\Delta\sigma_{t\bar{t}}$ is the uncertainty on the final cross section.

5.8.3 Jet energy scale

The analysis is sensitive to the jet energy scale and is one of the dominant sources of systematic uncertainties. The jet energy scale measurements and all its associated uncertainties are described in reference [186]. For each source of uncertainty, the associated error is propagated in the analysis by introducing a variation on the energy of each jet in the relevant way and taking into account the correlations between all uncertainties.

The total uncertainty in the quadratic sum of all these uncertainties and are given in Table 5.6. In the table, the uncertainties called "JesEffective" correspond to the 15 reduced nuisance parameters given by *in-situ* measurements in the central region of the detector [186]. The other uncertainties propagated correspond to the relative calibration of the jet responses as function of pseudo rapidity ("EtaIntercalibration"), to the pile-up ("Pileup"), to the calibration extrapolation at high transverse momentum ("SinglePart") , to the energy leak outside the calorimeters("PunchThrough"), to the flavor composition of the jet ("Flavor comp"), to gluon initiated jet response ("Flavor response") and the response of b-jet from the inclusive jet response ("bJES").

Systematics [%]	$\Delta\varepsilon_{t\bar{t}}/\varepsilon_{t\bar{t}}$	$\Delta N_{obs}/N_{obs}$	$\Delta\sigma_{t\bar{t}}/\sigma_{t\bar{t}}$
BJesUnc	-0.54 / +0.50	-0.23 / +0.09	-1.02 / +0.92
EtaIntercalibrationModel	-0.49 / +0.56	-0.24 / +0.26	-0.93 / +1.06
EtaIntercalibrationTotalStat	-0.46 / +0.47	-0.28 / +0.28	-0.88 / +0.89
JesEffectiveDet1	-0.99 / +1.20	-0.35 / +0.68	-1.90 / +2.25
JesEffectiveDet2	-0.05 / +0.10	-0.01 / +0.10	-0.09 / +0.19
JesEffectiveDet3	-0.11 / +0.08	-0.05 / +0.01	-0.21 / +0.15
JesEffectiveMix1	-0.73 / +0.75	-0.31 / +0.30	-1.40 / +1.41
JesEffectiveMix2	-0.11 / +0.02	-0.05 / +0.06	-0.20 / +0.03
JesEffectiveMix3	-0.25 / +0.25	-0.12 / +0.12	-0.47 / +0.47
JesEffectiveMix4	-0.06 / +0.05	-0.03 / +0.02	-0.11 / +0.09
JesEffectiveModel1	-1.15 / +1.29	-0.49 / +0.66	-2.20 / +2.41
JesEffectiveModel2	-0.18 / +0.18	-0.08 / +0.07	-0.34 / +0.35
JesEffectiveModel3	-0.07 / +0.05	-0.02 / +0.01	-0.12 / +0.09
JesEffectiveModel4	-0.22 / +0.23	-0.12 / +0.11	-0.42 / +0.44
JesEffectiveStat1	-0.31 / +0.22	-0.32 / +0.12	-0.61 / +0.41
JesEffectiveStat2	-0.03 / +0.04	-0.01 / +0.01	-0.06 / +0.08
JesEffectiveStat3	-0.08 / +0.09	-0.05 / +0.01	-0.14 / +0.16
JesEffectiveStat4	-0.31 / +0.35	-0.15 / +0.17	-0.60 / +0.67
Pileup OffsetMu	-0.12 / +0.11	-0.09 / +0.08	-0.22 / +0.20
Pileup OffsetNPV	-0.09 / +0.16	-0.13 / +0.05	-0.16 / +0.30
Pileup Pt	-0.08 / +0.10	-0.04 / +0.07	-0.15 / +0.18
Pileup Rho	-0.92 / +0.91	-0.51 / +0.46	-1.77 / +1.70
PunchThrough	-0.02 / +0.07	-0.01 / +0.08	-0.03 / +0.14
SinglePart	-0.00 / +0.00	-0.00 / +0.00	-0.00 / +0.00
flavor comp	-0.90 / +1.00	-0.67 / +0.82	-1.75 / +1.91
flavor response	-0.92 / +0.89	-0.57 / +0.53	-1.73 / +1.72
Total JES	-2.56 / +2.73	-1.36 / +1.56	-4.87 / +5.15

Table 5.6: Relative systematic uncertainties on $t\bar{t}$ production cross section associated to jet energy scale with either $\tau_{\text{1-prong}}$ or $\tau_{\text{3-prong}}$ candidate in the final state. $\Delta\varepsilon_{t\bar{t}}$ is the uncertainty on efficiency, ΔN_{obs} is the uncertainty on the number of observed events due to prompt subtraction in the background estimation, and the $\Delta\sigma_{t\bar{t}}$ is the uncertainty on the final cross section.

5.8.4 b-tagging efficiency

In the nominal analysis, the b-tagging efficiency in the simulation is directly corrected to correspond to the data by using scale factors. These factors depend on the transverse momentum and the direction of the jets. They are defined from measurements of the b-tagging efficiency, of the mistag fraction of c-jets and of light jets [160, 187].

The uncertainties on these corrections are propagated in the cross section measurement by varying the scale factors by one standard deviation with respect to their central values. Table 5.7 shows the details of all these uncertainties.

Systematics [%]	$\Delta\varepsilon_{t\bar{t}}/\varepsilon_{t\bar{t}}$	$\Delta N_{obs}/N_{obs}$	$\Delta\sigma_{t\bar{t}}/\sigma_{t\bar{t}}$
BTAGSF BREAK0	-0.02 / +0.02	-0.02 / +0.01	-0.04 / +0.04
BTAGSF BREAK1	-0.03 / +0.03	-0.01 / +0.01	-0.05 / +0.05
BTAGSF BREAK2	-0.02 / +0.02	-0.00 / +0.00	-0.03 / +0.03
BTAGSF BREAK3	-0.00 / +0.00	-0.01 / +0.01	-0.00 / +0.01
BTAGSF BREAK4	-0.00 / +0.00	-0.03 / +0.03	-0.00 / +0.00
BTAGSF BREAK5	-0.17 / +0.17	-0.03 / +0.03	-0.31 / +0.31
BTAGSF BREAK6	-0.19 / +0.19	-0.11 / +0.11	-0.37 / +0.37
BTAGSF BREAK7	-0.90 / +0.92	-0.28 / +0.29	-1.67 / +1.75
BTAGSF BREAK8	-1.82 / +1.75	-0.45 / +0.45	-3.51 / +3.21
CTAUTAGSF BREAK0	-0.06 / +0.06	-0.06 / +0.06	-0.11 / +0.11
CTAUTAGSF BREAK1	-0.13 / +0.13	-0.15 / +0.15	-0.25 / +0.25
CTAUTAGSF BREAK2	-0.47 / +0.47	-0.74 / +0.74	-0.94 / +0.94
CTAUTAGSF BREAK3	-0.66 / +0.66	-1.00 / +1.00	-1.32 / +1.32
MISTAGSF BREAK0	-0.00 / +0.00	-0.00 / +0.00	-0.00 / +0.01
MISTAGSF BREAK1	-0.00 / +0.00	-0.00 / +0.00	-0.00 / +0.00
MISTAGSF BREAK2	-0.01 / +0.00	-0.01 / +0.01	-0.01 / +0.01
MISTAGSF BREAK3	-0.00 / +0.00	-0.00 / +0.00	-0.00 / +0.00
MISTAGSF BREAK4	-0.02 / +0.01	-0.02 / +0.02	-0.03 / +0.03
MISTAGSF BREAK5	-0.02 / +0.02	-0.03 / +0.03	-0.04 / +0.04
MISTAGSF BREAK6	-0.03 / +0.03	-0.05 / +0.05	-0.07 / +0.07
MISTAGSF BREAK7	-0.03 / +0.04	-0.06 / +0.06	-0.07 / +0.07
MISTAGSF BREAK8	-0.05 / +0.05	-0.08 / +0.08	-0.10 / +0.10
MISTAGSF BREAK9	-0.39 / +0.39	-0.63 / +0.63	-0.78 / +0.78
MISTAGSF BREAK10	-0.12 / +0.12	-0.17 / +0.17	-0.24 / +0.24
MISTAGSF BREAK11	-0.97 / +0.97	-1.53 / +1.53	-1.93 / +1.93
Total b tag eff	-2.05 / +2.00	-0.54 / +0.54	-3.91 / +3.69
Total c mistag	-0.82 / +0.82	-1.26 / +1.26	-1.64 / +1.64
Total light mistag	-1.05 / +1.05	-1.70 / +1.70	-2.10 / +2.10

Table 5.7: Relative systematic uncertainties on $t\bar{t}$ production cross section associated to b tagging efficiency with either $\tau_{\text{1-prong}}$ or $\tau_{\text{3-prong}}$ candidate in the final state. $\Delta\varepsilon_{t\bar{t}}$ is the uncertainty on efficiency, ΔN_{obs} is the uncertainty on the number of observed events due to prompt subtraction in the background estimation, and the $\Delta\sigma_{t\bar{t}}$ is the uncertainty on the final cross section.

5.8.5 Jet energy resolution

The systematic uncertainty on the jet energy resolution is estimated by smearing the energy of each reconstructed jet in the simulation before applying event selection.

The smearing is applied in such a way that the width of the energy distribution corresponds to the measured nominal resolution plus one sigma. Table 5.8 shows the estimated uncertainties.

Systematics [%]	$\Delta\varepsilon_{t\bar{t}}/\varepsilon_{t\bar{t}}$	$\Delta N_{obs}/N_{obs}$	$\Delta\sigma_{t\bar{t}}/\sigma_{t\bar{t}}$
JER	$\pm$ 0.55	$\pm$ 0.43	$\pm$ 0.97

Table 5.8: Relative systematic uncertainties on $t\bar{t}$ production cross section associated to jet energy resolution with either $\tau_{\text{1-prong}}$ or $\tau_{\text{3-prong}}$ candidate in the final state. $\Delta\varepsilon_{t\bar{t}}$ is the uncertainty on efficiency, ΔN_{obs} is the uncertainty on the number of observed events due to prompt subtraction in the background estimation, and the $\Delta\sigma_{t\bar{t}}$ is the uncertainty on the final cross section.

5.8.6 Jet reconstruction efficiency

The jet reconstruction efficiency has been measured by using the *tag and probe* method on di-jet events [186]. The difference of efficiency between data and simulation is around 0.2% for jets with a transverse momentum lower than 30 GeV. At higher transverse momentum, very good agreement is observed. The effect of this efficiency is propagated by randomly rejecting 0.2% of low p_T jets in the simulation. Table 5.9 shows the effect on this analysis.

Systematics [%]	$\Delta\varepsilon_{t\bar{t}}/\varepsilon_{t\bar{t}}$	$\Delta N_{obs}/N_{obs}$	$\Delta\sigma_{t\bar{t}}/\sigma_{t\bar{t}}$
JetEff	$\pm$ 0.04	$\pm$ 0.04	$\pm$ 0.08

Table 5.9: Relative systematic uncertainties on $t\bar{t}$ production cross section associated to jet reconstruction efficiency with either $\tau_{\text{1-prong}}$ or $\tau_{\text{3-prong}}$ candidate in the final state. $\Delta\varepsilon_{t\bar{t}}$ is the uncertainty on efficiency, ΔN_{obs} is the uncertainty on the number of observed events due to prompt subtraction in the background estimation, and the $\Delta\sigma_{t\bar{t}}$ is the uncertainty on the final cross section.

5.8.7 Pileup jet rejection efficiency

The efficiency of the rejection of jets from pile-up has been measured with an *in situ* analyses, especially with Z+jets event [188] on data and simulation. The differences between the efficiencies on data and simulation are lower than 0.5% on the whole kinematic region, except for $20 < p_T < 30$ GeV where it is around 1%. These differences are propagated in the analysis by varying the Jet Vertex Fraction (JVF) criteria such that the rejection efficiency in the simulation reaches the value observed in the data. The uncertainty related to JVF on the analysis is shown is Table 5.10.

Systematics [%]	$\Delta\varepsilon_{t\bar{t}}/\varepsilon_{t\bar{t}}$	$\Delta N_{obs}/N_{obs}$	$\Delta\sigma_{t\bar{t}}/\sigma_{t\bar{t}}$
JVF	-0.11 / +0.10	-0.10 / -0.05	-0.22 / +0.19

Table 5.10: Relative systematic uncertainties on $t\bar{t}$ production cross section associated to jet vertex fraction efficiency with either $\tau_{\text{1-prong}}$ or $\tau_{\text{3-prong}}$ candidate in the final state. $\Delta\varepsilon_{t\bar{t}}$ is the uncertainty on efficiency, ΔN_{obs} is the uncertainty on the number of observed events due to prompt subtraction in the background estimation, and the $\Delta\sigma_{t\bar{t}}$ is the uncertainty on the final cross section.

5.8.8 $E_{\text{T}}^{\text{miss}}$ soft-term resolution and scale

Energy scale variations of all physics objects affect the reconstructed $E_{\text{T}}^{\text{miss}}$ and it is recalculated after each variation. However, the systematic uncertainties on the scale and resolution of the $E_{\text{T}}^{\text{miss}}$ soft term is propagated separately through the cross section measurement. The results of these variations are listed in Table 5.11.

Systematics [%]	$\Delta\varepsilon_{t\bar{t}}/\varepsilon_{t\bar{t}}$	$\Delta N_{obs}/N_{obs}$	$\Delta\sigma_{t\bar{t}}/\sigma_{t\bar{t}}$
MET resolution soft	-0.06 / +0.15	-0.12 / +0.08	-0.12 / +0.29
MET scale soft	-0.29 / +0.41	-0.17 / +0.30	-0.55 / +0.79
Total, MET	-0.29 / +0.44	-0.20 / +0.31	-0.56 / +0.84

Table 5.11: Relative systematic uncertainties on $t\bar{t}$ production cross section associated to the soft term in missing energy calculation with either $\tau_{\text{1-prong}}$ or $\tau_{\text{3-prong}}$ candidate in the final state. $\Delta\varepsilon_{t\bar{t}}$ is the uncertainty on efficiency, ΔN_{obs} is the uncertainty on the number of observed events due to prompt subtraction in the background estimation, and the $\Delta\sigma_{t\bar{t}}$ is the uncertainty on the final cross section.

5.8.9 MC generator and hadronization model

The uncertainty on the $t\bar{t}$ production cross section associated to the choice of generator, parton showering and hadronization model is estimated. This is performed by estimating $t\bar{t}$ signal events and $t\bar{t}$ prompt contribution in background estimation using different generators and comparing with the nominal generator. The following generators are used for comparison:

- the generator POWHEG [121] interfaced with HERWIG/JIMMY [116, 165] to estimate the uncertainty associated to parton showering and hadronization models.

- the generator MC@NLO [120] interfaced with HERWIG/JIMMY

The above generators used to estimate the uncertainty are produced with damping factor, $h_{\text{damp}} = \infty$, introduced in section 5.2.2. For an unbiased comparison, a POWHEG+PYTHIA sample also produced with $h_{\text{damp}} = \infty$ is considered as nominal.

Table 5.12 shows the effect of these variations on the cross section measurement.

Systematics [%]	$\Delta\varepsilon_{t\bar{t}}/\varepsilon_{t\bar{t}}$	$\Delta N_{obs}/N_{obs}$	$\Delta\sigma_{t\bar{t}}/\sigma_{t\bar{t}}$
POWHEG+HERWIG vs MC@NLO	± 2.77	± 1.26	± 4.45
POWHEG+PYTHIA vs POWHEG+HERWIG	± 3.20	±0.85	± 4.54

Table 5.12: Relative systematic uncertainties on $t\bar{t}$ production cross section associated to the monte carlo generator and hadronization model with either $\tau_{\text{1-prong}}$ or $\tau_{\text{3-prong}}$ candidate in the final state. $\Delta\varepsilon_{t\bar{t}}$ is the uncertainty on efficiency, ΔN_{obs} is the uncertainty on the number of observed events due to prompt subtraction in the background estimation, and the $\Delta\sigma_{t\bar{t}}$ is the uncertainty on the final cross section.

5.8.10 Initial and final state radiation

The effect of additional jets due to initial and final state radiation on the cross section is studied with a $t\bar{t}$ simulation sample produced with POWHEG [121] generators. The generators are produced with the `AtlFast2` simulation for this case. The parton showering and hadronization processes are simulated with PYTHIA [114]. Two effects are considered in this study, the factorization and renormalization scales are varied by a factor of 0.5 and 2 and the h_{damp} parameter is set to the top mass and twice the top mass. In addition, the variation of scales are also applied in parton showering. The sample where the renormalization scale is varied by a factor of 2 and the h_{damp} parameter is set to the top mass is referred to as `radLo`, whereas, the sample with renormalization scale varied by 0.5 and the h_{damp} is set to two times the top mass is referred to as `radHi`.

The yield at each selection step is shown in Table 5.13 and compared to the nominal sample. The relative differences of the relative efficiencies of the `radLo` and `radHi` from the nominal sample is shown in Table 5.14. The `radLo` sample shows a large number of events compared to the nominal, while the number of events in the `radHi` sample is comparable to the nominal. As shown in Table 5.14, the large number of events in the `radLo` sample results from the jet multiplicity, $E_{\text{T}}^{\text{miss}}$ and tau identification and multiplicity requirements. The distributions of the kinematic and topological variables of these objects for `radLo` and `radHi` samples are compared to the nominal and shown in figures 5.46 and 5.47.

Cut	Yield nominal	Yield radLo	Yield radHi
INITIAL	2771946.5	2771946.5	2771946.5
GRL	2771946.5	2771946.5	2771946.5
HFOR/LAr	2771946.5	2771946.5	2771946.5
NPV ≥ 4	686432.5625	733730.3125	667879.5625
E-Mu OLR	686412	733705.9375	667862.1875
JET CLEAN	683196.0625	730101.6875	664957.9375
LEP VETO	374074.5625	400031.4375	365844.0938
≥ 2 JETS	238517.5625	265594.3438	238084.375
MET > 120 GeV	238517.5625	194576.3281	176119.6875
$\geq$ 1noIDTAU	159531.4219	133696.2344	115798.5234
≥ 2 JETS (after OLR)	159531.2188	133695.8438	115798.5234
$\geq$ BJET 70% WP	130496.4922	109972.4844	92897.44531
MET > 150 GeV	36346.48828	41339.57031	36157.54688
$\geq$ 1idTau	4492.54834	5229.254395	4324.074707
Truth Match	3970.769043	4533.684082	3870.525391
MWT < 90	3562.795654	4041.968018	3445.152344

Table 5.13: Comparison of yield at each selection step for $t\bar{t} \to \tau$ events in nominal, radiation low and radiation high samples.

Cut	relative eff(%) (radLo-Nom)/Nom	relative eff(%) (radHi-Nom)/Nom
INITIAL	-	-
GRL	0.0000	0.0000
HFOR/LAr	0.0000	0.0000
NPV ≥ 4	-0.0021	0.0067
E-Mu OLR	-0.0003	0.0004
JET CLEAN	-0.0228	0.0338
LEP VETO	0.0686	0.4822
≥ 2 JETS	4.1268	2.0640
MET > 120 GeV	-26.7393	-26.0264
$\geq$ 1noIDTAU	2.7314	-1.6964
≥ 2 JETS	-0.0002	0.0001
≥ 1 BJET 70% WP	0.5572	-1.9274
MET > 150 GeV	34.9641	39.7435
$\geq$ 1idTau	2.3396	-3.2471
Truth Match	-1.9089	1.2733
MWT < 90	-0.6369	-0.7976
Total jet	4.1266	2.0641
Total met	8.2248	13.7171
Total tau	3.1621	-3.6703

Table 5.14: Relative difference of the relative efficiencies at each selection from the nominal sample in $t\bar{t} \to \tau$ events. Positive sign indicates a increase of relative efficiency from the nominal. Different jet, met and tau requirements are applied at different stages of the selection. The bottom part of the table indicates the total difference in relative efficiency of each of these objects.

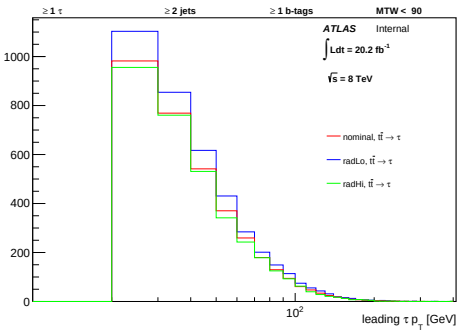

(a) leading τ- p_T: normalization comparison

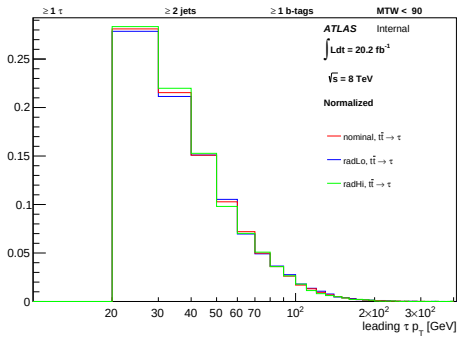

(b) leading τ- p_T: shape comparison

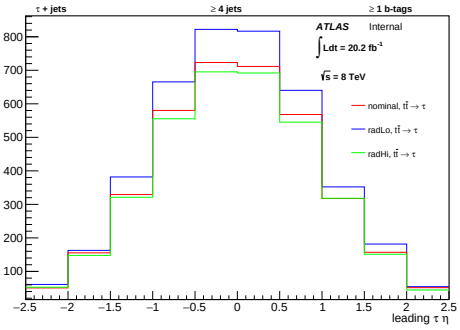

(c) leading τ- η: normalization comparison

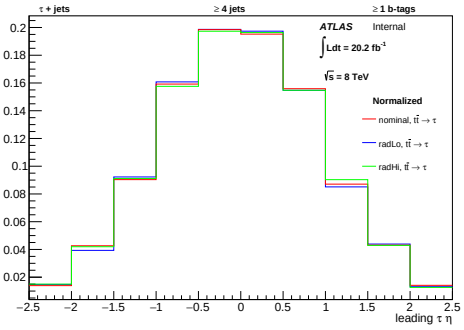

(d) leading τ- η: shape comparison

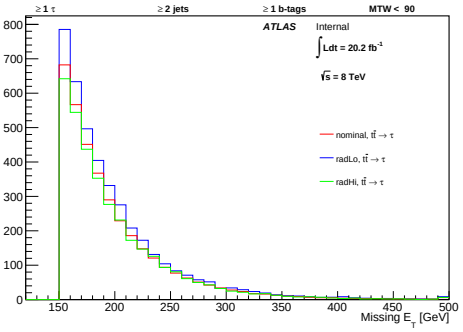

(e) $E_{\mathrm{T}}^{\mathrm{miss}}$: normalization comparison

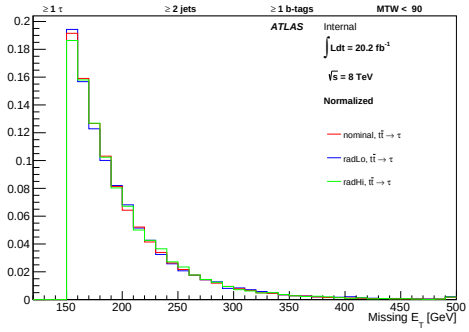

(f) $E_{\mathrm{T}}^{\mathrm{miss}}$: shape comparison

Figure 5.46: Normalization and shape comparison of $\tau - p_{\mathrm{T}}$, $\tau - \eta$ and $E_{\mathrm{T}}^{\mathrm{miss}}$ distributions in $t\bar{t} \to \tau$ events.

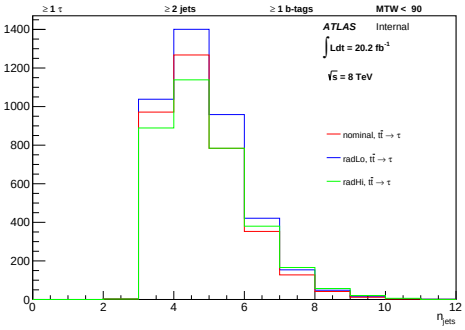

(a) jet multiplicity: normalization comparison

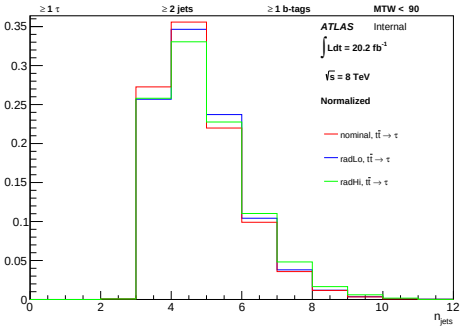

(b) jet multiplicity: shape comparison

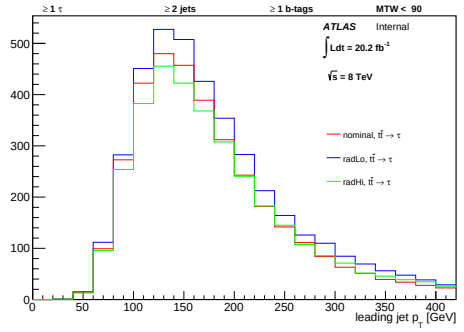

(c) leading jet- p_T: normalization comparison

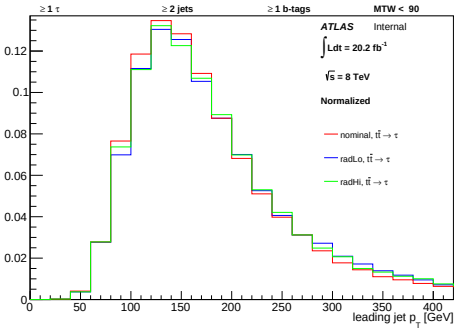

(d) leading jet- p_T: shape comparison

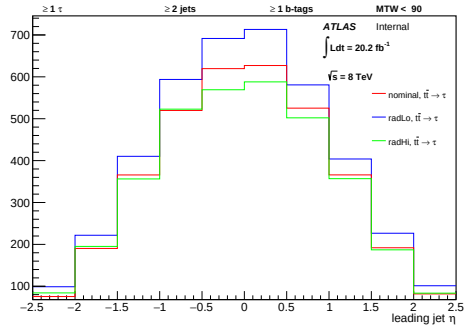

(e) leading jet- η: normalization comparison

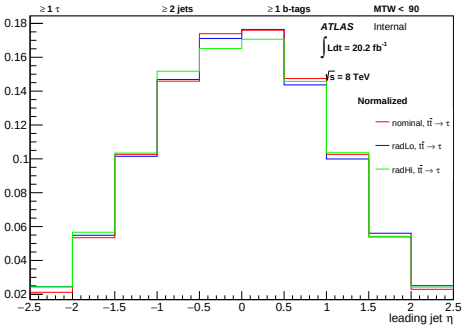

(f) leading jet- η: shape comparison

Figure 5.47: Normalization and shape comparison of jet multiplicity, leading jet $-\ p_{\mathrm{T}}$ and leading jet $-\ \eta$ distributions in $t\bar{t} \to \tau$ events.

The systematic uncertainties are calculated by comparing the `AtlFast2` simulated `radLo` and `radHi` samples with the `AtlFast2` nominal sample. Table 5.15 shows the calculated asymmetric uncertainties. However, since the asymmetric uncertainty does

not bracket the nominal, a symmetric uncertainty is also calculated by comparing `radLo` and `radHi` samples and is taken as the estimate of this uncertainty.

Systematics [%]	$\Delta\varepsilon_{t\bar{t}}/\varepsilon_{t\bar{t}}$	$\Delta N_{obs}/N_{obs}$	$\Delta\sigma_{t\bar{t}}/\sigma_{t\bar{t}}$
radLow vs Nominal	+3.63	-0.11	-6.52
radHigh vs Nominal	-0.37	+0.03	+0.72
radLow vs radHigh (symmetric)	± 1.97	± 0.07	± 3.69

Table 5.15: Relative systematic uncertainties on $t\bar{t}$ production cross section associated to initial and final state radiation with either $\tau_{\text{1-prong}}$ or $\tau_{\text{3-prong}}$ candidate in the final state. $\Delta\varepsilon_{t\bar{t}}$ is the uncertainty on efficiency, ΔN_{obs} is the uncertainty on the number of observed events due to prompt subtraction in the background estimation, and the $\Delta\sigma_{t\bar{t}}$ is the uncertainty on the final cross section.

5.8.11 Fake background estimation

The sources of systematic uncertainties related to the estimation of reducible background is discussed in section 5.5.6. A grid is created by adding all systematic uncertainties in quadrature for each $p_T - \eta$ range. The uncertainty is then propagated through the cross section measurement by varying the number of reducible events by $\pm 1\sigma$. Table 5.16 shows the effect of this variation.

Systematics [%]	$\Delta\varepsilon_{t\bar{t}}/\varepsilon_{t\bar{t}}$	$\Delta N_{obs}/N_{obs}$	$\Delta\sigma_{t\bar{t}}/\sigma_{t\bar{t}}$
Tau misidentification	-0.91 / +0.98	-1.59 / +1.72	-2.07 / +2.46

Table 5.16: Relative systematic uncertainties on $t\bar{t}$ production cross section associated to the estimation of jet misidentified as tau with either $\tau_{\text{1-prong}}$ or $\tau_{\text{3-prong}}$ candidate in the final state.. $\Delta\varepsilon_{t\bar{t}}$ is the uncertainty on efficiency, ΔN_{obs} is the uncertainty on the number of observed events due to prompt subtraction in the background estimation, and the $\Delta\sigma_{t\bar{t}}$ is the uncertainty on the final cross section.

5.8.12 Luminosity

The uncertainty on the integrated luminosity is 1.9%. It is derived following the same methodology as that detailed in reference [189], using a preliminary calibration of the luminosity scale derived from beam-separation scans performed in November 2012.

5.9 Results

The inclusive $t\bar{t}$ cross section is calculated using Eqn 5.25. The observed and expected number of $t\bar{t}$ events are listed in Table 5.3. The statistical and systematic uncertainties associated with the cross section measurement are also estimated. The total uncertainty is the quadratic sum of components.

The total systematic uncertainty associated to the combined $\tau_{\text{1-prong}}$ and $\tau_{\text{3-prong}}$ channel is shown in Table 5.17. The inclusive $t\bar{t}$ cross-section is measured to be

$$\sigma_{t\bar{t}\to\tau+\text{jets}} = 231 \pm 3(\text{stat.})^{+25}_{-25}(\text{syst.}) \pm 3(\text{lumi.})\text{pb}$$

Systematics [%]	$\Delta\varepsilon_{t\bar{t}}/\varepsilon_{t\bar{t}}$	$\Delta N_{\text{obs}}/N_{\text{obs}}$	$\Delta\sigma_{t\bar{t}}/\sigma_{t\bar{t}}$
JES	-2.55 / +2.73	-1.37 / +1.56	-4.87 / +5.15
b-tag eff	-2.05 / +2.00	-0.54 / +0.54	-3.92 / +3.69
c mistag	-0.82 / +0.82	-1.26 / +1.26	-1.64 / +1.64
light mistag	-1.05 / +1.05	-1.67 / +1.66	-2.10 / +2.10
MET	-0.29 / +0.44	-0.20 / +0.31	-0.56 / +0.84
Tau ID, electron veto	-2.70 / +2.70	-1.20 / +1.20	-5.25 / +5.01
TES	-1.34 / +1.43	-0.70 / +0.82	-2.58 / +2.68
JVF	-0.11 / +0.10	-0.10 / +0.05	-0.22 / +0.19
jeff	-0.04 / +0.04	-0.04 / +0.04	-0.08 / +0.08
jer	-0.55 / +0.55	-0.43 / +0.43	-0.97 / +0.97
Reducible	-0.91 / +0.98	-1.60 / +1.72	-2.08 / +2.46
Generator	-3.08 / +3.08	-0.85 / +0.85	-4.54 / +4.54
ISR/FSR	-2.04 / +2.04	-0.07 / +0.07	-3.69 / +3.69
Total Syst	-5.23 / +5.35	-4.62 / +4.75	-11.10 / +11.16

Table 5.17: Relative systematic uncertainties on $t\bar{t}$ production cross section associated to different sources with either $\tau_{\text{1-prong}}$ or $\tau_{\text{3-prong}}$ candidate in the final state. $\Delta\varepsilon_{t\bar{t}}$ is the uncertainty on efficiency, ΔN_{obs} is the uncertainty on the number of observed events due to the MC signal subtraction in the background estimation, and the $\Delta\sigma_{t\bar{t}}$ is the uncertainty on the final cross section.

The cross section and associated systematic uncertainties for $\tau_{\text{1-prong}}$ only and $\tau_{\text{3-prong}}$ only candidates in the final state are also calculated. Tables 5.18 and 5.19 show the total systematic uncertainty associated to $\tau_{\text{1-prong}}$ and $\tau_{\text{3-prong}}$ candidate, respectively. The cross section measured in these final states are the following:

$$\sigma_{t\bar{t}\to\tau_{\text{1-prong}}+\text{jets}} = 220.0 \pm 3(\text{stat.})^{+24}_{-24}(\text{syst.}) \pm 3(\text{lumi.})\text{pb}$$

$$\sigma_{t\bar{t}\to\tau_{\text{3-prong}}+\text{jets}} = 263.0 \pm 7(\text{stat.})^{+35}_{-35}(\text{syst.}) \pm 3(\text{lumi.})\text{pb}$$

Systematics [%]	$\Delta\varepsilon_{t\bar{t}}/\varepsilon_{t\bar{t}}$	$\Delta N_{\text{obs}}/N_{\text{obs}}$	$\Delta\sigma_{t\bar{t}}/\sigma_{t\bar{t}}$
JES	-2.28 / +2.57	-1.03 / +1.48	-4.41 / +4.96
b-tag eff	-2.03 / +1.98	-0.55 / +0.55	-3.94 / +3.72
c mistag	-0.85 / +0.85	-1.36 / +1.36	-1.78 / +1.77
light mistag	-1.03 / +1.03	-1.68 / +1.68	-2.14 / +2.16
MET	-0.32 / +0.42	-0.34 / +0.31	-0.64 / +0.82
Tau ID, electron veto	-2.37 / +2.37	-1.10 / +1.10	-4.69 / +4.50
TES	-1.54 / +1.45	-0.95 / +0.82	-3.06 / +2.77
JVF	-0.11 / +0.07	-0.12 / +0.01	-0.23 / +0.14
jeff	-0.03 / +0.03	-0.05 / +0.05	-0.07 / +0.07
jer	-0.21 / +0.21	-1.02 / +1.02	-0.26 / +0.26
Reducible	-0.77 / +0.83	-1.40 / +1.51	-2.05 / +2.46
Generator	-3.20 / +3.20	-1.43 / +1.43	-4.12 / +4.12
ISR/FSR	-1.98 / +1.98	-0.08 / +0.08	-3.83 / +3.83
Total Syst	-4.62 / +4.75	-5.07 / +5.18	-10.67 / +10.77

Table 5.18: Relative systematic uncertainties on $t\bar{t}$ production cross section associated to different sources with $\tau_{\text{1-prong}}$ candidate in the final state. $\Delta\varepsilon_{t\bar{t}}$ is the uncertainty on efficiency, ΔN_{obs} is the uncertainty on the number of observed events due to the MC signal subtraction in the background estimation, and the $\Delta\sigma_{t\bar{t}}$ is the uncertainty on the final cross section.

Systematics [%]	$\Delta\varepsilon_{t\bar{t}}/\varepsilon_{t\bar{t}}$	$\Delta N_{obs}/N_{obs}$	$\Delta\sigma_{t\bar{t}}/\sigma_{t\bar{t}}$
JES	-3.54 / +3.34	-2.53 / +1.91	-6.32 / +5.88
b-tag eff	-2.13 / +2.08	-0.52 / +0.53	-3.88 / +3.66
c mistag	-0.74 / +0.74	-0.97 / +0.97	-1.29 / +1.29
light mistag	-1.17 / +1.15	-1.70 / +1.66	-2.04 / +2.00
MET	-0.41 / +0.54	-0.51 / +0.32	-0.72 / +0.96
Tau ID, electron veto	-3.86 / +3.86	-1.53 / +1.53	-7.12 / +6.66
TES	-0.65 / +1.37	-0.03 / +0.82	-1.18 / +2.40
JVF	-0.11 / +0.18	-0.05 / +0.16	-0.20 / +0.32
jeff	-0.07 / +0.07	-0.04 / +0.04	-0.13 / +0.13
jer	-1.78 / +1.78	-1.35 / +1.35	-3.11 / +3.11
Reducible	-1.30 / +1.38	-2.05 / +2.18	-2.11 / +2.37
Generator	-2.48 / +2.48	-0.57 / +0.57	-6.44 / +6.44
ISR/FSR	-1.85 / +1.85	-0.1 / +0.1	-3.15 / +3.15
Total Syst	-6.54 / +6.56	-5.01 / +4.83	-13.46 / +13.17

Table 5.19: Relative systematic uncertainties on $t\bar{t}$ production cross section associated to different sources with either $\tau_{\text{3-prong}}$ candidate in the final state. $\Delta\varepsilon_{t\bar{t}}$ is the uncertainty on efficiency, ΔN_{obs} is the uncertainty on the number of observed events due to the MC signal subtraction in the background estimation, and the $\Delta\sigma_{t\bar{t}}$ is the uncertainty on the final cross section.

5.10 Interpretation and model independent limit

The number of events observed in the $t\bar{t}$ signal region is compared to the expected rate using a frequentist significance test. The expected rate is computed using a fit based on profile likelihood, according to the SM plus a generic beyond SM (BSM) signal present in the SR to derive model-independent limits on the number of BSM events in the SR.

A likelihood function is defined as follows:

$$\mathcal{L}\left(n_s;\mu,b,\theta\right) = \text{Poiss}\left(n_s|s\left(\mu,b,\theta\right)\right) \times N_{\text{syst}}\left(\theta_0,\theta\right). \tag{5.26}$$

$\text{Poiss}\left(n_s\right)$ is a Poisson probability density function (pdf) describing the expected event counts n_s in the signal region, given the expectation s. μ is the signal strength of any BSM process, b is the number of SM background events, and θ describes the systematic uncertainties as nuisance parameters. N_{syst} model the different systematic uncertainties described in section 5.8. Each parameter θ can be varied around the nominal values θ_0.

To determine the model independent upper limit on the number of BSM events, the signal expectation is set to 1 event. That way any upper limit on the signal strength is exactly the upper limit on a possible BSM number of events. No signal uncertainties are taken into account. The total SM background uncertainties including detector response, generator, luminosity and $t\bar{t}$ NNLO cross section uncertainty are taken into account in the N_{syst} and modelled by a Gaussian pdf.

Upper limit at 95% confidence level (CL) on the number of BSM events for

$t\bar{t}$ SR is derived using the `RooStat` [190] program, with the CL_s likelihood ratio prescription as described in reference [191]. Figure 5.48 shows the observed CL_b and CL_s as a function of the number of BSM events. Dividing the limit on the number of BSM events by the integrated luminosity of the data sample, this can be interpreted as upper limit on the visible BSM cross section, $\sigma_{\mathrm{vis}} = \sigma \times \mathcal{A} \times \varepsilon$, where σ is the production cross section of the BSM signal, $\mathcal{A}$ is the acceptance defined as the fraction of events passing the geometric and kinematic selections, and ε is the detector reconstruction, identification and trigger efficiency. Table 5.20 summarizes the observed number of events, the expected SM background yield, and the expected and observed upper limit on event yields from a BSM signal and on σ_{vis}. The confidence level observed for the background only hypothesis (CL_b) and the discovery p-value ($p(s = 0)$) is also shown.

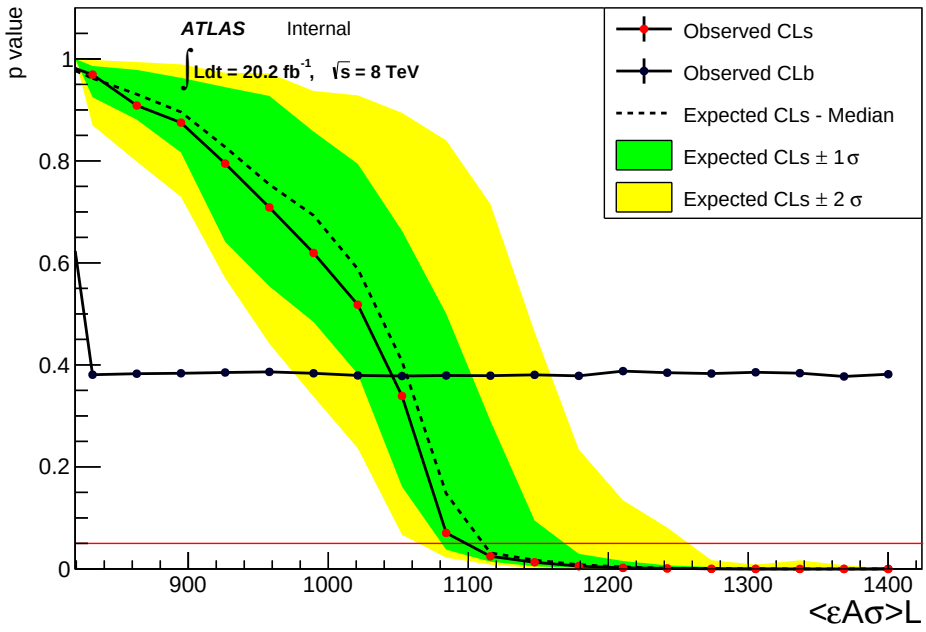

Figure 5.48: p-value as a function of $\langle \varepsilon \mathcal{A} \sigma \rangle \cdot L$ taking systematic uncertainties into account. The observed CL_s and CL_b is shown in red dotted line and black dotted line respectively . Also shown is the expected CL_b under the background-only hypothesis (black dashed line) along with the ± 1 and ± 2 standard deviation bands (green and yellow respecteviely). The red solid line at p-value $= 0.05$ represents the 95% CL.

Signal region: $t\bar{t}$	
Expected background	6378.4
Observed data	6085
$S^{95}_{\text{obs.(exp.)}}$	1098.37 $\left(1110.72^{+58.34}_{-29.65}\right)$
$\langle \mathcal{A}\epsilon\sigma \rangle^{95}_{\text{obs.(exp.)}}$[fb]	54.37 $\left(54.99^{+2.89}_{-1.47}\right)$
CL_b	0.62
$p(s=0)$	0.38

Table 5.20: Top to bottom: Expected background, number of observed events, 95% CL observed (expected) upper limits on the number of BSM events and the visible cross section ($\langle \mathcal{A}\epsilon\sigma \rangle^{95}_{\text{obs.(exp.)}}$). The last two rows indicate the CL_b value, i.e. the confidence level observed for the background-only hypothesis, and the discovery p-value ($p(s=0)$).

Process	Acceptance ($\mathcal{A}\epsilon$)
$t\bar{t} \to \tau$	1.43×10^{-3}
$t\bar{t} \to l$	3.44×10^{-5}
Single top	4.98×10^{-4}
W+jets	5.58×10^{-6}
Z+jets	3.70×10^{-6}
Diboson	1.25×10^{-5}
	No. of events
Fakes (estimated in data)	294.8
Data	6085

Table 5.21: Acceptance for each processes estimated in simulation, the number of fake background events (estimated in data) and the number of observed data events in the $t\bar{t}$ signal region used to estimate the model independent upper limit on the visible cross section of any BSM processes.

CHAPTER 6

Upper limit on the branching ratio of $t \to cH$

This chapter investigates the flavor changing neutral Higgs interaction of the top quark in association with a charm quark. First, the topology of the events of interest is discussed, followed by the analysis strategy and event selection requirements. The statistical model and the method to set an upper limit on the branching ratio along with the results are then presented.

6.1 Introduction

Flavor changing neutral current (FCNC) interactions of the Higgs boson to the top quark is forbidden at the tree level, and with respect to the dominant decay mode $t \to Wb$, very much suppressed at higher orders due to the Glashow-Iliopoulos-Maiani (GIM) mechanism [192]. For example, the branching ratio of $t \to cH$ is $BR(t \to cH) \sim 10^{-15}$ at one-loop level. Observation of FCNC decays of the top quark would therefore provide a clear signal of new physics. If FCNC decays of $t \to cH$ is allowed and the $H \to \tau\tau$ decay mode with branching ratio 6.3% is

considered, an excess of $t \to \tau +$ jets events can be observed relative to the SM.

In models beyond the SM, the GIM suppression can be relaxed, and loop diagrams mediated by new bosons may contribute, yielding effective couplings orders of magnitude larger than those of the SM. In two-Higgs double model (2HDM) without explicit flavor conservation (type III) [74,193,194], the predicted branching ratio for $t \to cH$, is $\sim 10^{-3}$.

Considering, BR$(t \to cH) \equiv$ B , the expected number of $t\bar{t}$ events is written as,

$$\begin{aligned} N^{t\bar{t}} = & \; 2B(1-B)\varepsilon_{cHWb} \cdot BR(H \to \tau\tau) \cdot \sigma^{t\bar{t}} \int \mathcal{L}\,(t)\,dt \\ & + (1-B)^2 \varepsilon_{WbWb} \cdot \sigma^{t\bar{t}} \int \mathcal{L}\,(t)\,dt \\ & + B^2 \varepsilon_{cHcH} \cdot BR^2\,(H \to \tau\tau) \cdot \sigma^{t\bar{t}} \int \mathcal{L}\,(t)\,dt \end{aligned} \tag{6.1}$$

where,

$\sigma^{t\bar{t}}$ is the $t\bar{t}$ production cross section

ε_{cHWb} is the efficiency of $t\bar{t} \to cHWb \to c\tau\tau bqq$

ε_{WbWb} is the efficiency of $t\bar{t} \to WbWb \to \tau bbqq$

Figure 6.1 shows the fractional number of event for each of the term in equation 6.1 corresponding to each possible combination of $t\bar{t}$ decay mode as a function of BR$(t \to cH)$. The number of events in $t\bar{t} \to cHcH$ decay mode is expected to be very small due to small BR$(t \to cH)$ and the signal model is generated for only the $t\bar{t} \to cHWb \to c\tau\tau bqq$ decay mode. The Feynman diagram of the final state considered is shown in Fig. 6.2. The MC sample (DSID 110594) is produced with

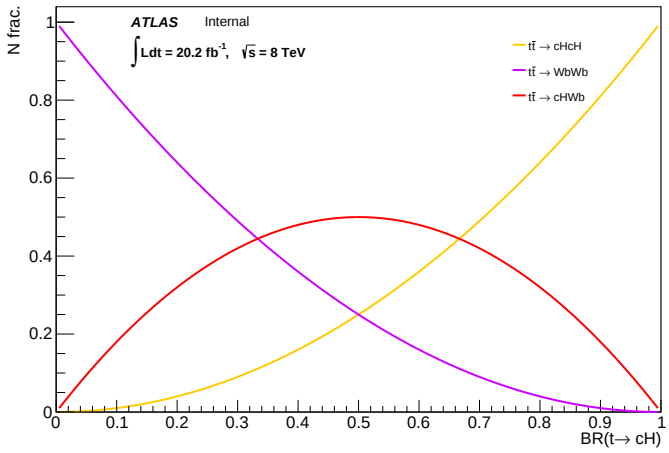

Figure 6.1: Fractional number of event for the three posible combination of $t\bar{t}$ decay mode as a function of the $t \to cH$ branching ratio.

PROTOS [195] interfaced to PYTHIA with Perugia 2011C for parton showering. A leading order PDF, CTEQ6L1 is used to calculate the matrix element.

6.1.1 Event Selection and analysis strategy

The analysis uses the ratio of two independent regions to set an upper limit on $BR(t \to cH)$, thereby benefiting from the cancellation of correlated uncertainties in these two regions. The first region requires exactly 1 tau and referred to as `tau1exR`, while the second region uses exactly 2 taus requirement, referred to as `tau2exR`. In addition, a model independent upper limit on the visible cross section on any BSM processes are also calculate using only the `tau2exR` region.

The events in these two regions are selected according to $t\bar{t} \to cHWb$ topology in the final state of $c\tau\tau qqb$. The event selection is applied once all physics objects are selected based on the definitions described in section 5.3 and the geometric overlap removal discussed in 5.3.5 is performed. The following steps are implemented to

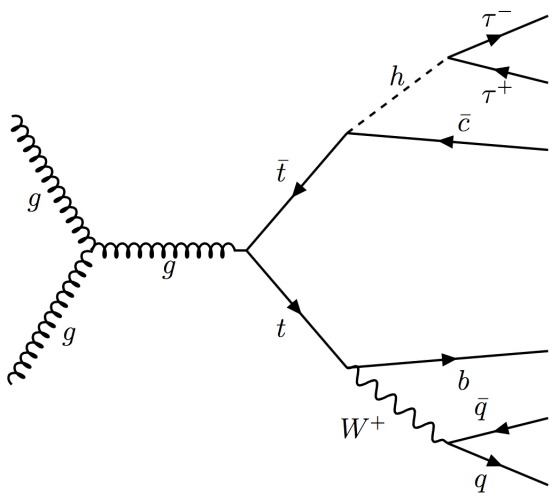

Figure 6.2: Feynman diagram of the flavor changing neutral Higgs interaction of the top quark. One of the top quark decay to a W boson and b quark the top quark decay through FCNC process to a Higgs boson and a c quark. Only the hadronic decay mode of the W boson and the $H \to \tau\tau$ final state is considered as the signal point.

select a signal event:

- The event must pass a trigger requirement. Events are required to pass trigger `EF_xe80_tclcw` OR `EF_xe75_tclcw`, discussed in details in section 5.2.1.

- The event must have a well defined primary vertex. Candidate events are selected if the reconstructed primary vertex has at least four associated tracks.

- An event is rejected if there is a `LooseBad` jet following the recommendation of jet cleaning [182].

- An event with either a reconstructed electron or a reconstructed muon defined in sections 5.3.3 and 5.3.4 is rejected.

- The event must have 2 inclusive jets and exactly one must be identified as a b-jet, defined in section 5.3.1. Exactly one b-jet requirement is motivated to veto

$H \to bb$ events in data. No attempts are made to identify a c-quark initiated jet.

- Each event is required to pass a threshold, $E_{\mathrm{T}}^{\mathrm{miss}} > 150$ GeV defined in 5.3.6. The requirement is influenced by the trigger efficiencies in data and simulation samples discussed in section 5.2.1.

- The event must have the following number of τ as defined in section 5.3.2:

  (a) Exactly one identified-τ for `tau1exR`

  (b) Exactly two identified-τ for `tau2exR`

The prompt backgrounds are estimated directly using simulation samples and normalized using the cross section for the respective processes while the fake background is estimated following the method described in section 5.5. Table 6.1 shows the number of observed events along with the expected signal and background yields for the two regions.

Process	`tau1exR`	`tau2exR`
Observed data	5155 ± 71.8	53 ± 7.3
$t\bar{t} \to cHWb$	450 ± 21.2	28 ± 5.3
$t\bar{t} \to WbWb$	3009.7 ± 54.9	14.6 ± 3.8
Single top	443.6 ± 21.1	1.2 ± 1.1
W+jets	1339.7 ± 36.6	0.0 ± 0.0
Z+jets	103.1 ± 10.2	6.9 ± 2.6
Diboson	6.0 ± 2.4	0.0 ± 0.0
Fakes	575.7 ± 24	40.1 ± 6.3

Table 6.1: Number of events observed in data and simulation along with the associated statistical uncertainty for expected background and signal processes for exactly one tau (`tau1exR`) and exactly two tau (`tau2exR`) final state.

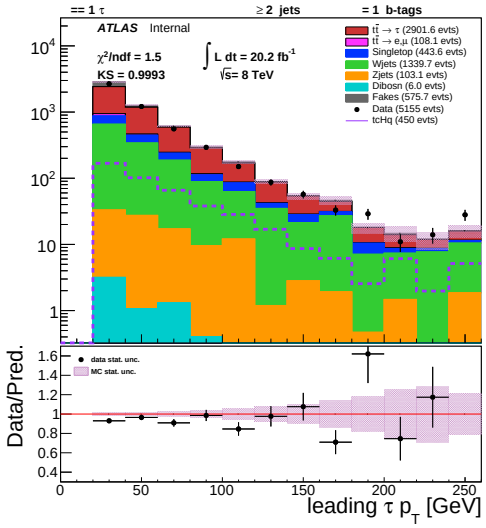

(a) τ- p_T

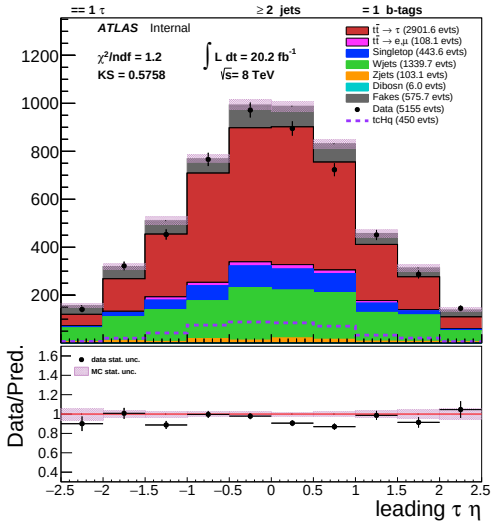

(b) τ- η

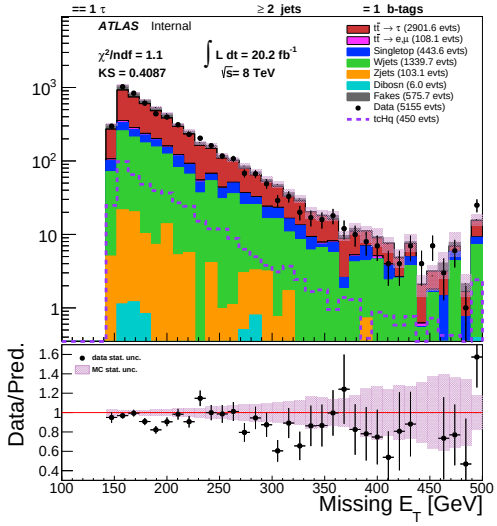

(c) $E_{\mathrm{T}}^{\mathrm{miss}}$

Figure 6.3: Control plots for the region with exactly 1 tau (`tau1exR`) in tau p_{T}, η and $E_{\mathrm{T}}^{\mathrm{miss}}$ distributions with τ (either $\tau_{\text{1-prong}}$ or $\tau_{\text{3-prong}}$) in the final state. The dashed line represent the $t\bar{t} \to qqbc\tau\tau$ final state considering $BR(t \to cH) = 100\%$. Note only the statistical uncertainty is shown in the plot.

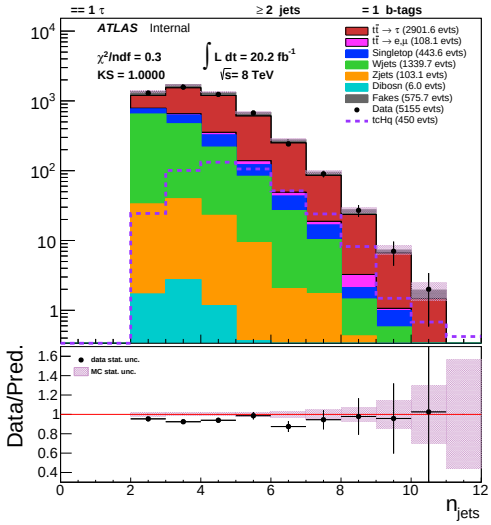

(a) all jet multiplicity

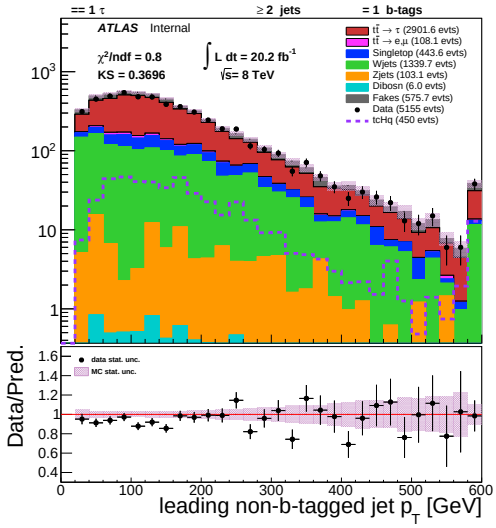

(b) leading light jet p_T

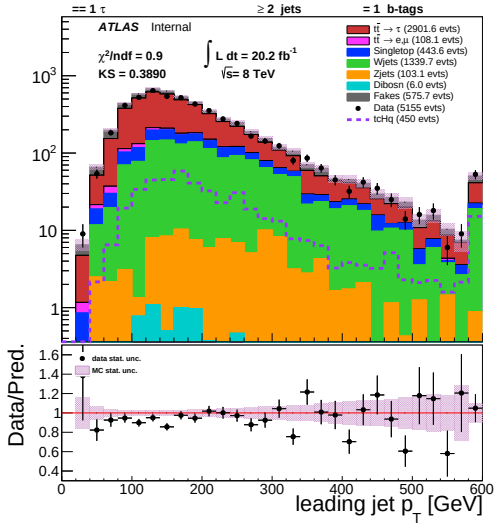

(c) leading b-jet p_T

Figure 6.4: Control plots for the region with exactly 1 tau (`tau1exR`) in jet multiplicity, leading b-tagged jet p_{T} and leading non b-tagged jet p_{T} distributions with τ (either $\tau_{\text{1-prong}}$ or $\tau_{\text{3-prong}}$) in the final state. The dashed line represent the $t\bar{t} \to qqbc\tau\tau$ final state considering $BR(t \to cH) = 100\%$. Note only the statistical uncertainty is shown in the plot.

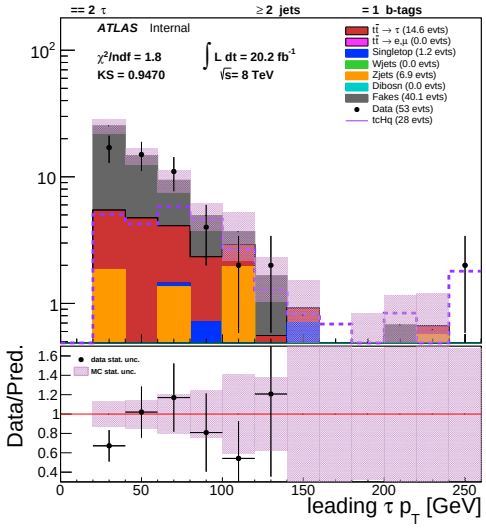

(a) τ- p_T

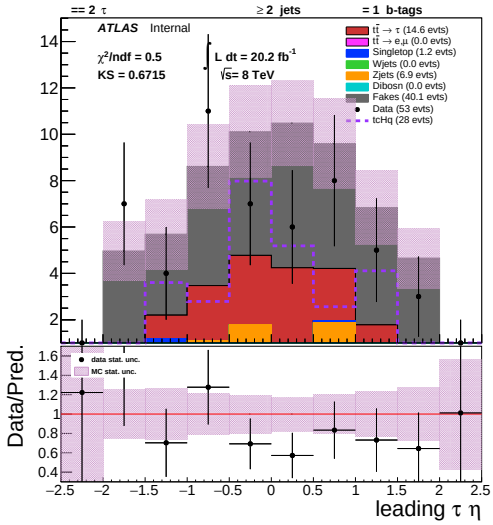

(b) τ- η

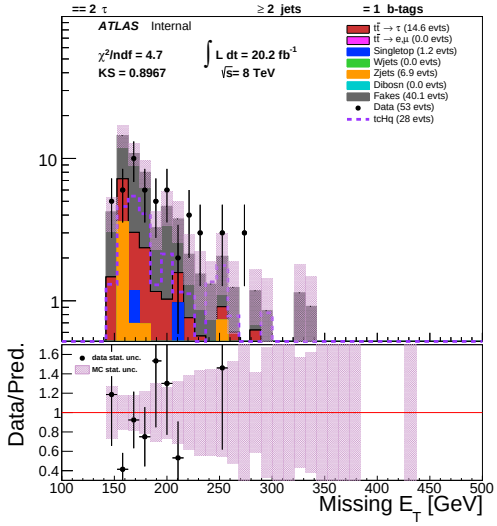

(c) $E_{\mathrm{T}}^{\mathrm{miss}}$

Figure 6.5: Control plots for the region with exactly 1 tau (`tau2exR`) in tau p_{T}, η and $E_{\mathrm{T}}^{\mathrm{miss}}$ distributions with τ (either $\tau_{\text{1-prong}}$ or $\tau_{\text{3-prong}}$) in the final state. The dashed line represent the $t\bar{t} \to qqbc\tau\tau$ final state considering $BR(t \to cH) = 100\%$. Note only the statistical uncertainty is shown in the plot.

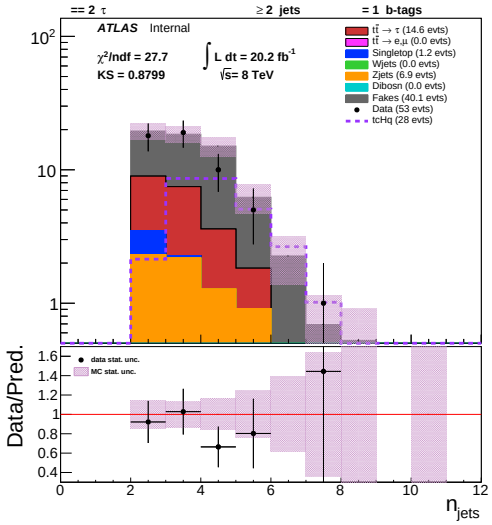

(a) all jet multiplicity

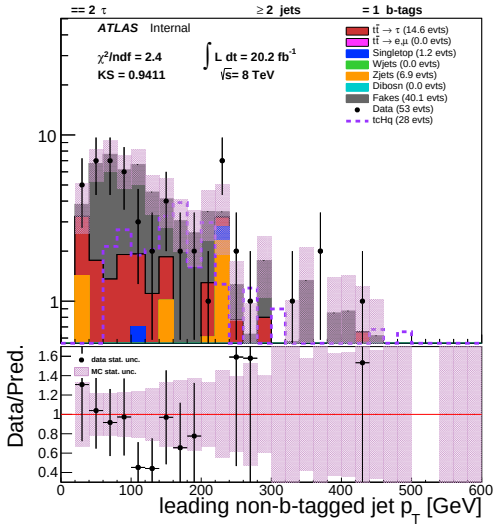

(b) leading light jet p_T

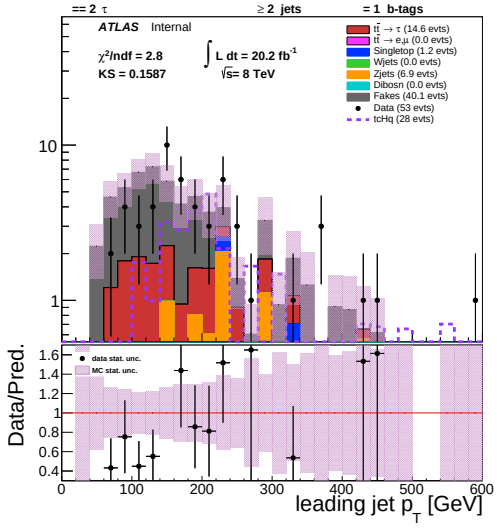

(c) leading b-jet p_T

Figure 6.6: Control plots for the region with exactly 1 tau (`tau2exR`) in jet multiplicity, leading b-tagged jet p_{T} and leading non b-tagged jet p_{T} distributions with τ (either $\tau_{\text{1-prong}}$ or $\tau_{\text{3-prong}}$) in the final state. The dashed line represent the $t\bar{t} \to qqbc\tau\tau$ final state considering $BR(t \to cH) = 100\%$. Note only the statistical uncertainty is shown in the plot.

6.1.2 Model independent upper limit

A model independent upper limit is also calculated using the `tau2exR` region following the same method described in section 5.10. Only the total SM background yields and observed number of events are used in this procedure. The total statistical and systematic uncertainties including detector response, generator and luminosity uncertainty on the backgrounds are taken into account. Upper limit at 95% confidence level (CL) on the number of BSM events is derived using the `RooStat` [190] program, with the CL_s likelihood ratio prescription as described in reference [191]. Dividing the limit on the number of BSM events by the integrated luminosity of the data sample, this can be interpreted as upper limit on the visible BSM cross section, $\sigma_{\text{vis}} = \sigma \times \mathcal{A} \times \varepsilon$, where σ is the production cross section of the BSM signal, $\mathcal{A}$ is the acceptance defined as the fraction of events passing the geometric and kinematic selections, and ε is the detector reconstruction, identification and trigger efficiency. Table 6.2 summarizes the observed number of events, the expected SM background yield, and the expected and observed upper limit on event yields from a BSM signal and on σ_{vis}. The confidence level observed for the background only hypothesis (CL_b) and the discovery p-value ($p(s = 0)$) is also shown.

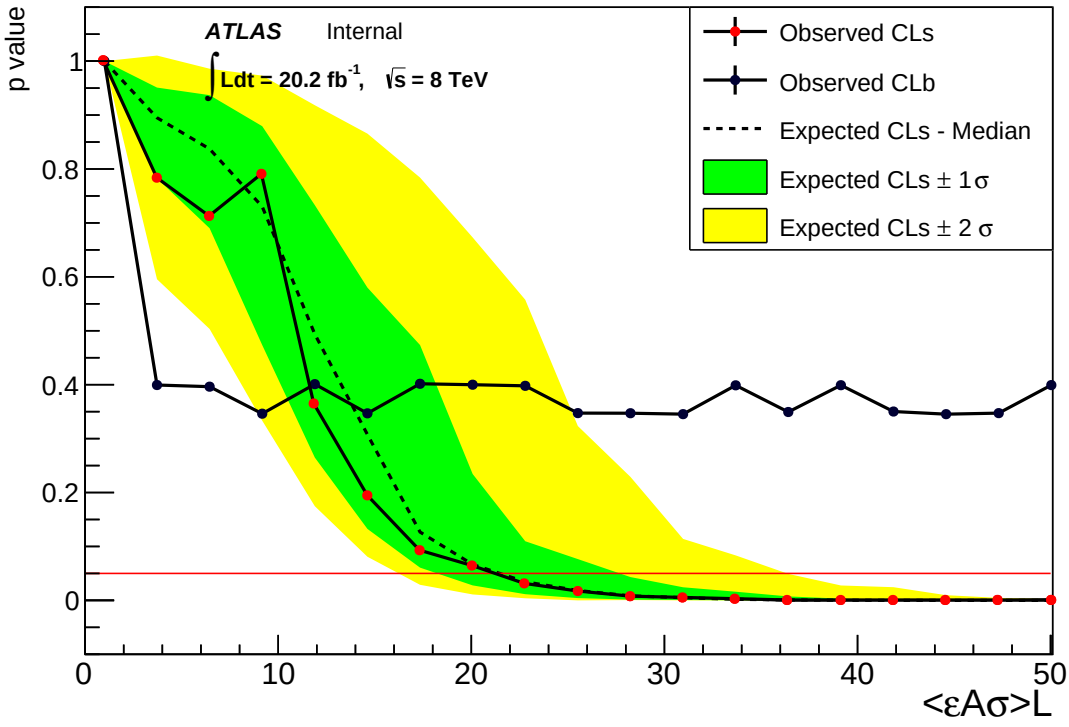

Figure 6.7: p-value as a function of $\langle \varepsilon \mathcal{A} \sigma \rangle \cdot L$ taking systematic uncertainties into account. The observed CL_s and CL_b is shown in red dotted line and black dotted line respectively . Also shown is the expected CL_b under the background-only hypothesis (black dashed line) along with the ± 1 and ± 2 standard deviation bands (green and yellow respecteviely). The red solid line at p-value $= 0.05$ represents the 95% CL.

The observed data and SM expectation is in good agreement and an upper limit is set on the branching ratio, BR($t \to cH$) using the `RooFit/RooStat` [190, 196] program, with the CL$_s$ likelihood ratio prescription as described in reference [191].

6.1.3 Statistical model

The expected number of signal plus background events in each independent region, tau1exR and tau2exR can be parameterized in terms of BR($t \to cH$).

Signal region: `tau2exR`	
Expected background	59.40 ± 5.94
Observed data	53
$S^{95}_{\text{obs.(exp.)}}$	$21.22\ \left(21.47^{+6.21}_{-9.45}\right)$
$\langle \mathcal{A}\epsilon\sigma \rangle^{95}_{\text{obs.(exp.)}}$[fb]	$1.05\ \left(1.06^{+0.31}_{-0.46}\right)$
CL_b	0.65
$p(s=0)$	0.35

Table 6.2: Top to bottom: Expected background, number of observed events, 95% CL observed (expected) upper limits on the number of BSM events and the visible cross section ($\langle \mathcal{A}\epsilon\sigma \rangle^{95}_{\text{obs.(exp.)}}$). The last two rows indicate the CL_b value, i.e. the confidence level observed for the background-only hypothesis, and the discovery p-value ($p(s=0)$).

Process	Acceptance ($\mathcal{A}\epsilon$)
$t\bar{t} \to e, \mu, \tau$	5.27×10^{-6}
Single top	0
W+jets	4.23×10^{-7}
Z+jets	0
Diboson	2.74×10^{-7}
	No. of events
Fakes (estimated in data)	40.1
Data	53

Table 6.3: Acceptance for each processes estimated in simulation, the number of fake background events (estimated in data) and the number of observed data events in the `tau2exR` signal region used to estimate the model independent upper limit on the visible cross section of any BSM processes.

$$
\begin{aligned}
N^{\text{expected}} &= N^{t\bar{t}} + N^{\text{singletop}} + N^{\text{V+jets,VV}}_{\text{irred.bkg}} + N_{\text{reduc.bkg}} - N_{\text{prompt}} \\
&= \underbrace{2B(1-B)\varepsilon_{cHWb} \cdot BR(H \to \tau\tau) \cdot \sigma^{t\bar{t}} \int \mathcal{L}\,(t)\,dt / (1 - BR(t\bar{t} \to \text{fullyhadronic}))}_{\text{expected signal contribution}} \\
&+ \underbrace{(1-B)^2 \varepsilon_{WbWb} \cdot \sigma^{t\bar{t}} \int \mathcal{L}\,(t)\,dt}_{t\bar{t}\text{ background contribution}} \\
&+ \underbrace{(1-B) \cdot N^{\text{singletop}}}_{\text{single top background contribution}} \\
&+ \underbrace{N^{\text{V+jets,VV}}}_{\text{W/Z + jets, diboson backgrounds}} \\
&+ \underbrace{N^{\text{data}}_{\text{fake}}}_{\text{fake bkg estimate from data includes prompt contribution}} \\
&- \underbrace{2B(1-B) \cdot BR(H \to \tau\tau) \cdot \frac{\Sigma FF}{N_{\text{gen}}} \cdot \sigma^{t\bar{t}} \int \mathcal{L}\,(t)\,dt / (1 - BR(t\bar{t} \to \text{fullyhadronic}))}_{\text{prompt contribution from } t\bar{t} \to cHWb} \\
&- \underbrace{(1-B)^2 \cdot \frac{\Sigma FF}{N_{\text{gen}}} \cdot \sigma^{t\bar{t}} \int \mathcal{L}\,(t)\,dt}_{\text{prompt contribution from } t\bar{t} \to WbWb} \\
&- \underbrace{(1-B) \cdot N^{\text{singletop}}_{\text{prompt}}}_{\text{prompt contribution from single top}} \\
&- \underbrace{N^{\text{V+jets,VV}}_{\text{prompt}}}_{\text{prompt contribution from W/Z+jets, diboson}}
\end{aligned}
\tag{6.2}
$$

where,

B is the $t \to cH$ branching ratio

$\sigma^{t\bar{t}}$ is the $t\bar{t}$ production cross section

ε_{cHWb} is the efficiency of $t\bar{t} \to cHWb \to c\tau\tau bqq$

ε_{WbWb} is the efficiency of $t\bar{t} \to WbWb \to \tau bbqq$

ΣFF is the sum of the fake factors

	tau1exR	tau2exR
N_{data}	5155	53
ε_{cHWb}	0.002665364127	0.0001664946798
ε_{WbWb}	0.00108566459	0.000006144454944
$N_{\text{singletop}}$	443.59	1.18917
N_{Wjets}	1339.7	0
N_{Zjets}	103.073	6.85913
N_{VV}	5.95475	0
N_{fake}	1245.79	42.6819
$\Sigma FF^{cHWb}_{\text{prompt}}$	172.964	11.3038
$\Sigma FF^{WbWb}_{\text{prompt}}$	7998.18	81.8308
$N^{\text{singletop}}_{\text{prompt}}$	52.119	0.106471
$N^{\text{Wjets}}_{\text{prompt}}$	164.587	0
$N^{\text{Zjets}}_{\text{prompt}}$	14.2958	0.235145
$N^{\text{VV}}_{\text{prompt}}$	0.820547	0

Table 6.4: Nominal values of different parameters in the statistical model calculated either in data or in simulation, for regions with exactly one tau (tau1exR) and exactly two taus (tau2exR).

N_{gen} is the number of generated events

For the $t\bar{t}$ process, the efficiency, while for single top, W/Z+jets, and diboson processes the yields are calculated directly in simulation. For the fake background the yield is calculated in data and the prompt contributions are subtracted by calculating the sum of the fake factor weights in simulation. Table 6.4 lists the nominal values of these parameters for tau1exR and tau2exR.

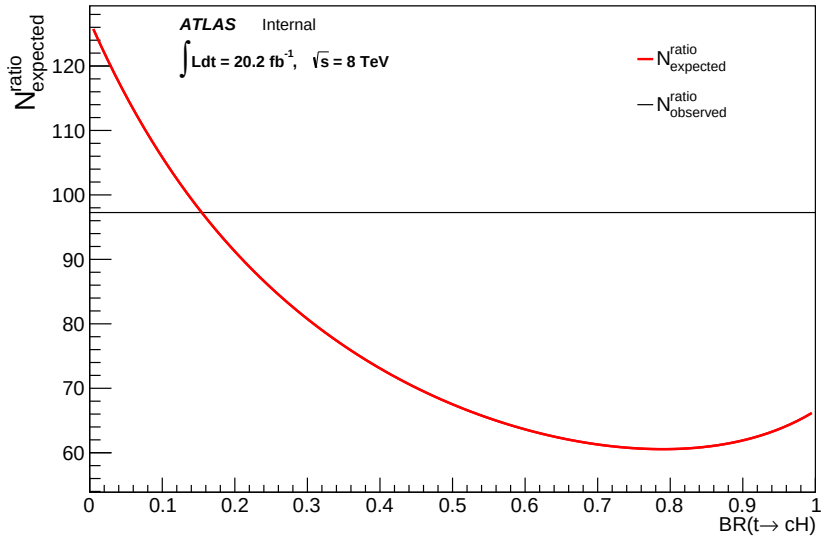

Figure 6.8: Distribution of the expected (red) and observed (black) number of events in the ratio analysis as a function of the $t \to cH$ branching ratio.

The expected and observed number of events in the ratio analysis is defined as,

$$N^{\text{ratio}}_{\text{expected}} = \frac{N^{\text{tau1exR}}_{\text{expected}}}{N^{\text{tau2exR}}_{\text{expected}}}, \tag{6.3}$$

$$N^{\text{ratio}}_{\text{observed}} = \frac{N^{\text{tau1exR}}_{\text{data}}}{N^{\text{tau2exR}}_{\text{data}}} \tag{6.4}$$

and their distribution as a function of BR($t \to cH$) is shown in Fig. 6.8.

In equations 6.3 and 6.4, the expected and observed number of events are ratios of two poisson distribution. Such distributions can be represented as a binomial probability density function (pdf) as discussed in the references [197, 198]. However, $N^{\text{ratio}}_{\text{observed}} = 5155/53 \sim 97$ and in the large N limit, the binomial pdf can be approximated with a gaussian distribution.

A likelihood function is thus defined as follows:

$$\mathcal{L}\left(N_{\text{obs.}}; N_{\text{exp.}}, \sqrt{N_{\text{exp.}}}, \theta\right) = Gauss\left(N_{\text{obs.}}|N_{\text{exp.}}, \sqrt{N_{\text{exp.}}}\right) \times N_{\text{syst.}}\left(\theta_0, \theta\right). \quad (6.5)$$

$N_{\text{syst.}}$ contains the different systematic uncertainties described in section 6.1.4 and modeled as a gaussian distribution. Each parameter θ can be varied around the nominal value θ_0.

6.1.4 Systematic uncertainties

The effect of systematic uncertainties on the total number of expected events defined in equation 6.2 are taken into account. The uncertainties are evaluated for each of the parameters listed in Table 6.4, associated to different sources discussed in section 5.8. For each source of systematic uncertainty, the error is estimated by making a variation of the parameter related to the uncertainty with respect to the nominal analysis. Table 6.5 shows the systematic uncertainties for the tau1exR while Table 6.6 shows the same for the tau2exR.

6.1.5 Upper limit estimation

The likelihood function defined in equation 6.5 is used to fit the expected number of signal and background events with associated systematic uncertainties to the observed data. The corresponding correlation matrix for the fitted nuisance parameters are shown in Fig. 6.9.

Systematics [%]	$\varepsilon_{\mathrm{cHWb}}$	$\varepsilon_{\mathrm{WbWb}}$	$N_{\mathrm{singletop}}$	N_{Wjets}	N_{Zjets}	N_{diboson}
JES	+4.47 /-3.17	+3.34 /-3.30	+3.36 /-5.36	+4.57 /-3.99	+7.95 /-7.59	+6.82 /-8.32
b-tag eff	+2.74 /-2.73	+0.46 /-0.45	+1.59 /-1.77	+0.94 /-0.95	+1.07 /-1.11	+2.08 /-1.95
c mistag	+0.44 /-0.44	+0.25 /-0.25	+0.10 /-0.10	+3.27 /-3.28	+3.26 /-3.28	+2.70 /-2.73
light mistag	+0.31 /-0.34	+0.11 /-0.11	+0.08 /-0.08	+4.62 /-4.59	+4.03 /-4.03	+0.26 /-0.25
MET	+0.69 /-0.90	+0.37 /-0.30	+0.54 /-1.31	+1.11 /-0.25	+0.78 /-1.60	+3.74 /-1.31
Tau ID, electron veto	+3.13 /-3.13	+3.17 /-3.17	+3.19 /-3.19	+3.22 /-3.22	+3.19 /-3.19	+2.57 /-2.57
jeff	+0.10 /-0.10	+0.01 /-0.01	+0.28 /-0.28	+0.06 /-0.06	0.00 / 0.00	0.00 / 0.00
jer	+3.24 /-3.24	+1.57 /-1.57	+0.64 /-0.64	+0.24 /-0.24	+3.89 /-3.89	+8.95 /-8.95
JVF	+0.02 /-0.09	+0.05 /-0.06	+0.09 /-0.29	+0.32 /-0.41	+0.00 / 0.00	0.00 / 0.00
Total	+6.97/-6.24	+4.91/-4.88	+4.98/-6.66	+8.09/-7.70	+10.83/-10.66	+12.60/-13.00

Systematics [%]	$\Sigma\mathrm{FF}^{\mathrm{prompt}}_{\mathrm{cHWb}}$	$\Sigma\mathrm{FF}^{\mathrm{prompt}}_{\mathrm{WbWb}}$	$N^{\mathrm{prompt}}_{\mathrm{singletop}}$	$N^{\mathrm{prompt}}_{\mathrm{Wjets}}$	$N^{\mathrm{prompt}}_{\mathrm{Zjets}}$	$N^{\mathrm{prompt}}_{\mathrm{diboson}}$
JES	+4.44 /-1.96	+3.60 /-3.63	+5.18 /-4.32	+4.27 /-6.13	+10.62 /-13.37	+0.24 /-0.23
b-tag eff	+2.74 /-2.71	+0.40 /-0.40	+1.49 /-1.62	+1.05 /-1.06	+1.01 /-0.99	+2.99 /-3.05
c mistag	+0.40 /-0.40	+0.23 /-0.23	+0.17 /-0.17	+3.07 /-3.09	+3.37 /-3.38	+3.35 /-3.38
light mistag	+0.13 /-0.10	+0.09 /-0.10	+0.16 /-0.17	+4.55 /-4.53	+4.03 /-4.04	+0.75 /-0.79
MET	+1.02 /-1.21	+0.33 /-0.33	+0.82 /-0.68	+0.32 /-0.37	+0.85 /-3.72	+3.08 /-8.11
Tau ID, electron veto	+2.85 /-2.85	+2.73 /-2.73	+2.72 /-2.72	+2.94 /-2.94	+2.96 /-2.96	+2.15 /-2.15
jeff	+0.19 /-0.19	+0.00 /-0.00	+0.21 /-0.21	0.00 / 0.00	0.00 / 0.00	0.00 / 0.00
jer	+5.02 /-5.02	+1.63 /-1.63	+1.64 /-1.64	+1.86 /-1.86	+11.86 /-11.86	+13.24 /-13.24
JVF	0.00 /-0.10	+0.08 /-0.03	+0.38 /-0.00	+0.29 /-0.33	+0.00 / 0.00	+0.02 /- 0.00
Total	+7.86/-6.79	+4.84/-4.86	+6.33/-5.66	+7.85/-9.00	+17.07/-19.26	+14.50/-16.35

Table 6.5: Relative systematic uncertainty on each parameter of $N_{\mathrm{exp.}}$ from various sources in exactly one tau region (tau1exR). The total uncertainty is calculated by adding the individual uncertainties in quadrature.

Systematics [%]	$\varepsilon_{\mathrm{cHWb}}$	$\varepsilon_{\mathrm{WbWb}}$	$N_{\mathrm{singletop}}$	N_{Wjets}	N_{Zjets}	N_{diboson}
JES	+4.50/-3.32	+2.71/-4.39	+1.99/-2.15	0.00/ 0.00	+0.02/-0.02	0.00 /0.00
b-tag eff	+2.12/-2.13	+0.93/-0.83	+7.24/-7.31	0.00/ 0.00	+2.26/-2.18	0.00 /0.00
c mistag	+0.82/-0.82	+0.10/-0.10	0.00/0.00	0.00/0.00	+1.06/-1.06	0.00/0.00
light mistag	+0.37/-0.38	+0.20/-0.20	+0.15/-0.15	0.00/0.00	+7.77 /-7.76	0.00/0.00
MET	+2.22/-0.82	+1.05/-0.93	+1.00 /-0.70	0.00/0.00	+3.84/-4.02	0.00/0.00
Tau ID, electron veto	+6.26/-6.11	+6.28/-6.14	+7.25/-7.07	0.00/ 0.00	+5.94 /-5.81	0.00/0.00
jeff	0.00/0.00	0.00/0.00	0.00 /0.00	0.00/0.00	0.00/0.00	0.00/0.00
jer	+1.33/-1.33	+1.70/-1.70	+40.71/-40.71	0.00/ 0.00	+12.30 /-12.30	0.00/0.00
JVF	0.00/-0.01	+0.51/-0.00	0.00/0.00	0.00/0.00	0.00/0.00	0.00/0.00
Total	+8.45/-7.50	+7.21/-7.84	+42.04/-42.02	0.00/0.00	+16.37/-16.35	0.00/0.00

Systematics [%]	$\Sigma\mathrm{FF}^{\mathrm{prompt}}_{\mathrm{cHWb}}$	$\Sigma\mathrm{FF}^{\mathrm{prompt}}_{\mathrm{WbWb}}$	$N^{\mathrm{prompt}}_{\mathrm{singletop}}$	$N^{\mathrm{prompt}}_{\mathrm{Wjets}}$	$N^{\mathrm{prompt}}_{\mathrm{Zjets}}$	$N^{\mathrm{prompt}}_{\mathrm{diboson}}$
JES	+5.03/-10.12	+9.76/-8.18	0.00/0.00	0.00/0.00	+0.14/-0.07	0.00/0.00
b-tag eff	+2.29/-2.33	+1.06/-1.00	+6.55/-6.55	0.00/0.00	+0.20/-0.20	0.00/0.00
c mistag	+0.95/-0.95	+0.05/-0.05	0.00/0.00	0.00/0.00	+3.02/-3.02	0.00/0.00
light mistag	+0.18/-0.18	+0.11/-0.11	+0.55/-0.55	0.00/0.00	+8.42/-8.40	0.00/0.00
MET	+1.47/-4.39	+3.29/-1.33	0.00/0.00	0.00/0.00	0.00/0.00	0.00/0.00
Tau ID, electron veto	+5.67/-5.55	+4.73/-4.65	+2.93/-2.91	0.00/0.00	+6.06/-5.92	0.00/0.00
jeff	0.00/0.00	0.00/0.00	0.00 /0.00	0.00/ 0.00	0.00/ 0.00	0.00/0.00
jer	+7.46 /-7.46	+7.18 /-7.18	+27.03/-27.03	0.00/ 0.00	+0.09/-0.09	0.00/ 0.00
JVF	+0.01/-0.00	+0.36/-0.42	0.00/0.00	0.00/ 0.00	0.00/ 0.00	0.00/0.00
Total	+11.02/-14.65	+13.46/-11.97	+27.97/-27.97	0.00/0.00	+10.81/-10.71	0.00/0.00

Table 6.6: Relative systematic uncertainty on each parameter of $N_{\mathrm{exp.}}$ from various sources in exactly two tau region (tau2exR). The total uncertainty is calculated by adding the individual uncertainties in quadrature.

The test statistics is calculated using the profile log likelihood ratio,

$$\tilde{q}_B = -2\ln\frac{\mathcal{L}\left(\text{data}|B,\hat{\theta}_B\right)}{\mathcal{L}\left(\text{data}|\hat{B},\hat{\theta}\right)} \tag{6.6}$$

$$= -2\ln\lambda \tag{6.7}$$

where,

B is the branching ratio of $t \to cH$ – the parameter of interest. $\hat{\theta}_B$ is the conditional maximum-likelihood estimator of θ and is a function of B itself. The denominator is maximized in an unconditional way, thus $\hat{B}$, $\hat{\theta}$ are the true maximum likelihood estimators. Figure 6.10 shows the evolution of -2lnλ.

Using the CLs method [191] the null hypothesis (H_0) is defined as the SM prediction (= sum of W+jets, Z+jets, single top, diboson and $t\bar{t}$ with B = 0). The test hypothesis (H_1) is defined as the sum of W+jets, Z+jets, single top, dibson and $t\bar{t}$ including $t\bar{t} \to cHWb$ decay.

The p-value of the two hypotheses are,

$$CL_{s+b} = p_{s+b} = P\left(\tilde{q}_B \geq \tilde{q}_B^{\text{obs.}}|H_1\right) = \int_{\tilde{q}_B^{\text{obs.}}}^{\infty} f\left(\tilde{q}_B|B,\hat{\theta}^{\text{obs.}}\right)d\tilde{q}_B \tag{6.8}$$

$$CL_b = 1 - p_b = P\left(\tilde{q}_B \geq \tilde{q}_B^{\text{obs.}}|H_0\right) = \int_{\tilde{q}_0^{\text{obs.}}}^{\infty} f\left(\tilde{q}_B|0,\hat{\theta}_0^{\text{obs.}}\right)d\tilde{q}_B \tag{6.9}$$

and the corresponding CL_s value is defined as,

$$CL_s = \frac{CL_{s+b}}{CL_b} \tag{6.10}$$

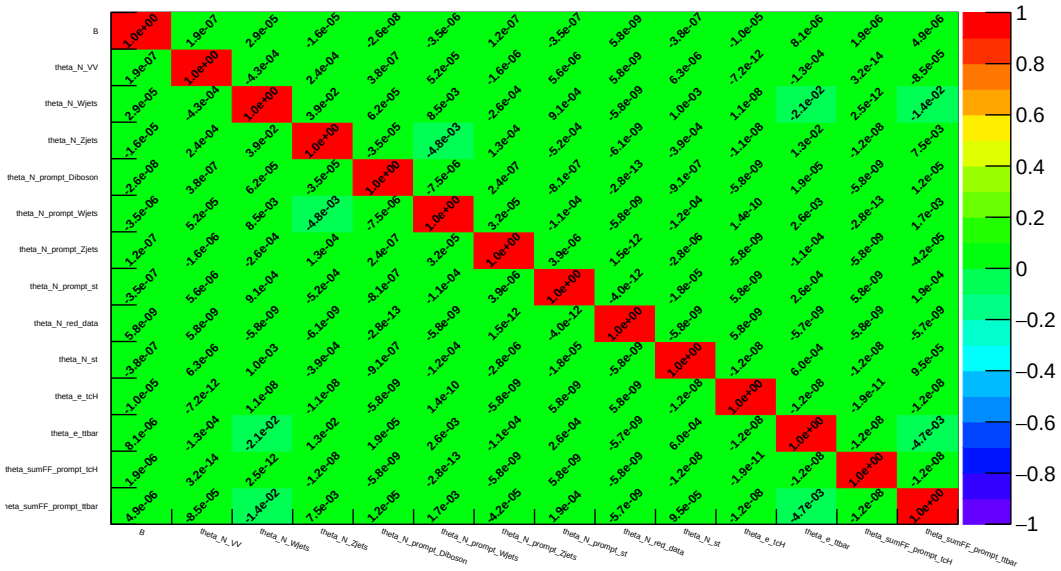

Figure 6.9: Correlation matrix for the fitted nuisance parameters.

Figure 6.11 shows the observed CL_{s+b}, CL_b and the CL_s values as a function of the branching ratio along with the expected upper limits. Figure 6.12 shows the generated test statistics to set this upper limit for signal plus background, background-only and data. Table 6.7 shows the observed and expected median upper limit along with the expected limit at one standard deviation.

Upper limit	Value
observed limit	0.100464
expected limit (median)	0.152624
expected limit (-1σ)	0.101192
expected limit (+1σ)	0.25284

Table 6.7: The observed and expected median upper limit along with expected limit at ± 1 standard deviation.

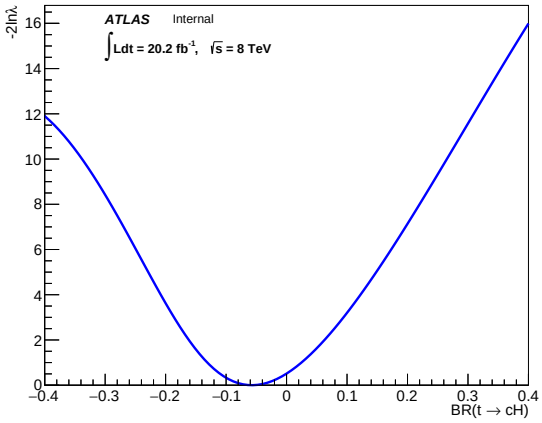

Figure 6.10: Evolution of $-2\ln\lambda$ as a function of the parameter of interest, BR($t \to cH$).

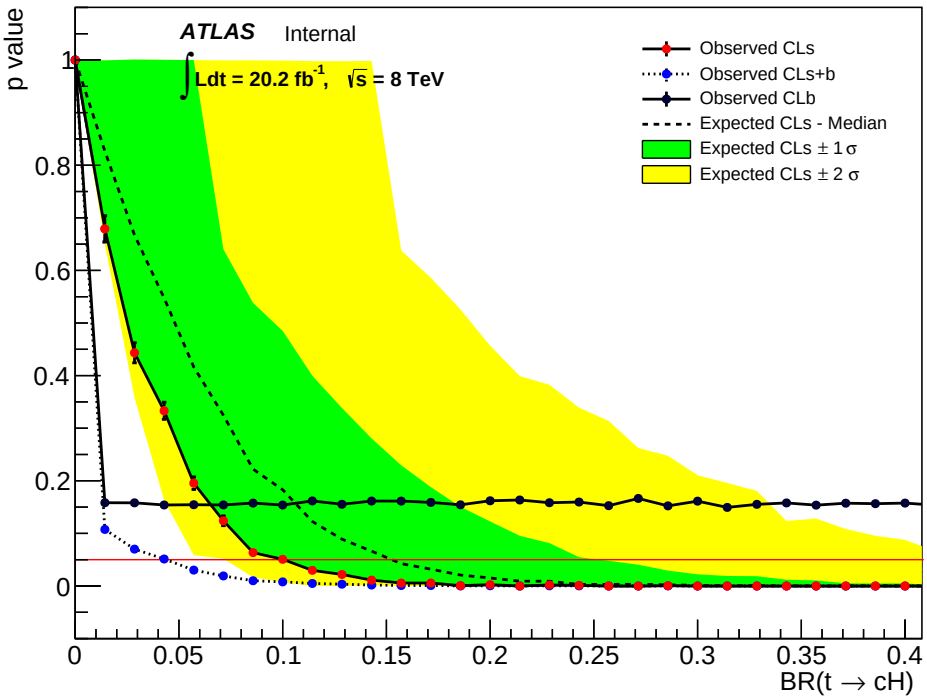

Figure 6.11: p-value as a function of BR($t \to cH$) taking systematic uncertainties into account. The observed CL_{s+b} (blue dot), CL_b (black dot), CL_s (red dot) are shown. Also shown the expected CL_s under the background-only hypothesis (black dashed line) along with the ± 1 and ± 2 standard deviation bands (green and yellow respectively). The red solid line at p-value $= 0.05$ represents the 95% CL. The observed upper limit on BR($t \to cH$) is at 10%.

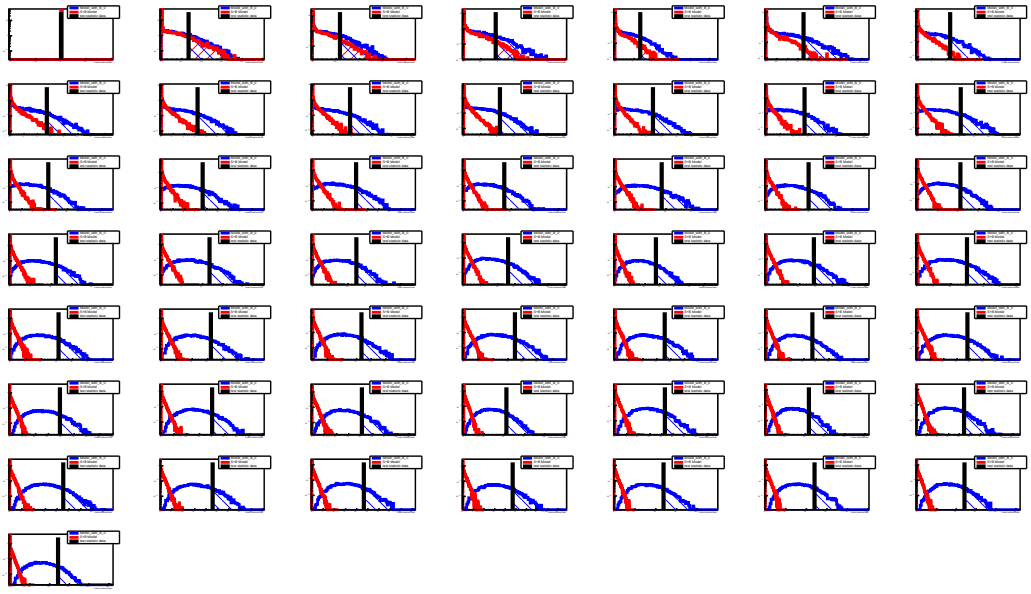

Figure 6.12: The generated test statistics for the signal plus background (red), background-only (blue) and data (black) to set the upper limit on BR($t \to cH$).

CHAPTER 7

Conclusion

7.1 Conclusion

The measurement of the top quark pair production cross section in the final state of a tau lepton with associated jets is presented in this dissertation. In calculating the production cross section the mass of the top quark is considered to be 172.5 GeV. The dataset used in this dissertation is collected using the ATLAS detector from proton-proton collisions during the 2012 operation of the Large Hadron Collider at the center-of-mass energy of 8 TeV. The integrated luminosity of the dataset corresponds to (20.2 ± 0.4) fb^{-1}.

The signal events are selected by requiring a set of selection criteria that corresponds to the topology of the final state of interest. The background contribution from different processes in data events after applying the set of selection requirements is estimated either from data or from simulation. The backgrounds that are

estimated in simulation are normalized to the integrated luminosity of the dataset using the theoretical cross section associated with each processes. The modeling of the background processes is well understood and a good agreement between data and predictions is observed. The inclusive production cross section is calculated using the branching ratio of the top quark to the final state of interest and the number of signal events in data corresponding to this final state. Due to the large integrated luminosity of the dataset, the statistical uncertainty on the measured cross section is only 1.3%. The uncertainty on the luminosity measured by ATLAS is 1.9%, which results to an uncertainty of 1.3% on the measured cross section. The systematic uncertainties on the cross section originating from theoretical and experimental sources are also taken into account. The largest source of theoretical uncertainty is associated to the choice of the generator, parton showering and hadronization model, and is estimated to be 4.5%. The largest experimental uncertainty comes from the identification of tau leptons, which is at 5.25%. The total systematic uncertainty on the measured cross section is estimated to be 11%. The measured inclusive $t\bar{t}$ cross section in the final state of a tau lepton with associated jets is:

$$\sigma_{t\bar{t}\to\tau+\text{jets}} = 231 \pm 3(\text{stat.})^{+25}_{-25}(\text{syst.}) \pm 3(\text{lumi.})\text{pb}$$

The theoretical prediction for the top quark pair production cross section is also calculated at the center-of-mass energy of 8 TeV, considering a top quark mass of 172.5 GeV. The calculation is performed at the next-to-next-to leading order (NNLO) in QCD including resummation of next-to-next-to leading logarithmic (NNLL) soft

gluon terms with Top++2.0 [38–44]. The PDF and α_s uncertainty is calculated using the PDF4LHC prescription [45] with the MSTW2008 68% CL NNLO [46, 47], CT10 NNLO [48, 49] and NNPDF 2.35f [36] PDF sets, added in quadrature to the scale uncertainty. The central value of the calculated prediction is,

$$\sigma_{t\bar{t}} = 252.89^{+6.39}_{-8.64}\,(\text{scale}) \pm 11.67\,(\text{PDF} + \alpha_s)$$

The measured cross section is consistent with the Standard Model prediction. The result is also compatible with the measurements performed in different final states by the ATLAS and CMS collaborations as shown in Fig. 7.1. A statistical analysis is also performed to check the consistency of the observed number of events in data with the predicted number of events from various Standard Model processes. Following frequentist approach, the confidence level observed with background-only hypothesis is 0.62 and the calculated p-value is 0.38, which indicates good agreement of the Standard Model prediction with the observed data. A model independent upper limit on the visible cross section on any non Standard Model processes is also calculated. The observed (expected) upper limit at 95% CL on the visible cross section of any non Standard Model processes is $54.37\,\left(54.99^{+2.89}_{-1.47}\right)$ fb.

The flavor changing neutral Higgs interaction of the top quark in association with a charm quark in the context of Type 3 two Higgs doublet model is also investigated. This analysis considers, one of the top quark pair decay via the Standard Model to the hadronic final state, while the other top quark undergoes flavor changing decay to a charm quark and a Higgs boson. Only the decay mode of the Higgs boson

to two tau leptons is considered. A statistical analysis is performed following the frequentist approach with CL_s method to set an upper limit on the branching ratio of $t \to ch^0$. The observed (expected) upper limit on the branching ratio at 95% CL is $\mathrm{BR}\,(t \to ch^0) < 10\%$ (15%).

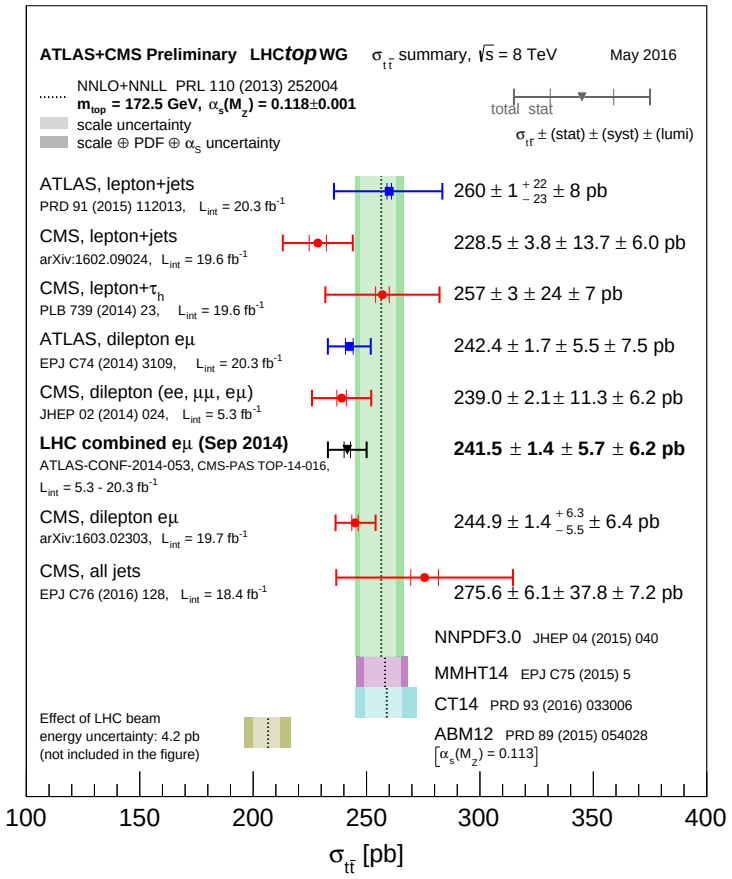

Figure 7.1: Summary of measurements of the top-pair production cross-section at 8 TeV compared to the exact NNLO QCD calculation complemented with NNLL resummation (top++2.0) using four different PDF sets. The theory bands represent uncertainties due to renormalisation and factorisation scale, parton density functions and the strong coupling. The measurements and the theory calculation are quoted at $m_t = 172.5\,\mathrm{GeV}$.

References

[1] F. Jegerlehner, *The hierarchy problem of the electroweak Standard Model revisited*, arXiv:1305.6652 [hep-ph]. 1

[2] D0 Collaboration, S. Abachi et al., *Observation of the top quark*, Phys. Rev. Lett. **74** (1995) 2632–2637, arXiv:hep-ex/9503003 [hep-ex]. 1

[3] CDF Collaboration, F. Abe et al., *Observation of top quark production in $\bar{p}p$ collisions*, Phys. Rev. Lett. **74** (1995) 2626–2631, arXiv:hep-ex/9503002 [hep-ex]. 1

[4] C. P. Yuan, *Top quark and electroweak symmetry breaking mechanism*, in *Quarks. Proceedings, 10th International Seminar on High Energy Physics, QUARKS'98, Suzdal, Russia, May 18-24, 1998*. 1998. arXiv:hep-ph/9809536 [hep-ph]. http://quarks.inr.ac.ru/1998/proc/yuan.tex.gz. 1

[5] *Top-pair production at hadron colliders with next-to-next-to-leading logarithmic soft-gluon resummation*, Physics Letters B **710** (2012) no. 4âĂŞ5, 612 – 622. 1

[6] P. Bärnreuther, M. Czakon, and A. Mitov, *Percent-Level-Precision Physics at the Tevatron: Next-to-Next-to-Leading Order QCD Corrections to $q\bar{q} \to t\bar{t}+X$*, Phys. Rev. Lett. **109** (Sep, 2012) 132001. 1

[7] *NNLO corrections to top-pair production at hadron colliders: the all-fermionic scattering channels*, Journal of High Energy Physics **2012** (2012) no. 12, . 1

[8] *NNLO corrections to top pair production at hadron colliders: the quark-gluon reaction*, Journal of High Energy Physics **2013** (2013) no. 1, . 1

[9] M. Czakon, P. Fiedler, and A. Mitov, *Total Top-Quark Pair-Production Cross Section at Hadron Colliders Through $\mathcal{O}(\alpha_S^4)$*, Phys. Rev. Lett. **110** (Jun, 2013) 252004. 1

[10] *Top++: A program for the calculation of the top-pair cross-section at hadron colliders*, Computer Physics Communications **185** (2014) no. 11, 2930 – 2938. 1

[11] ATLAS Collaboration, *Measurement of the top pair production cross section in 8 TeV proton-proton collisions using kinematic information in the lepton+jets final state with ATLAS*, Phys. Rev. **D91** (2015) no. 11, 112013, arXiv:1504.04251 [hep-ex]. 1

[12] ATLAS Collaboration, ATLAS Collaboration, *Measurement of the $t\bar{t}$ production cross-section using $e\mu$ events with b -tagged jets in pp collisions at $\sqrt{s} = 7$ and 8 TeV with the ATLAS detector*, Eur. Phys. J. **C74** (2014) no. 10, 3109, arXiv:1406.5375 [hep-ex]. 1

[13] ATLAS Collaboration, *Measurement of the ttbar production cross section in the tau+jets channel using the ATLAS detector*, Eur. Phys. J. **C73** (2013) no. 3, 2328, arXiv:1211.7205 [hep-ex]. 1

[14] CMS Collaboration, *Measurement of the top-antitop production cross section in the tau+jets channel in pp collisions at sqrt(s) = 7 TeV*, Eur. Phys. J. **C73** (2013) no. 4, 2386, arXiv:1301.5755 [hep-ex]. 1

[15] V. Barger and R. J. N. Phillips, *Hidden top quark with charged-Higgs-boson decay*, Phys. Rev. D **41** (Feb, 1990) 884–887. 1

[16] M. Cacciari, S. Frixione, M. L. Mangano, P. Nason, and G. Ridolfi, *Updated predictions for the total production cross sections of top and of heavier quark pairs at the Tevatron and at the LHC*, JHEP **0809** (2008) 127, arXiv:0804.2800 [hep-ph]. 1

[17] N. Kidonakis and R. Vogt, *The Theoretical top quark cross section at the Tevatron and the LHC*, Phys.Rev. **D78** (2008) 074005, arXiv:0805.3844 [hep-ph]. 1

[18] S. Moch and P. Uwer, *Theoretical status and prospects for top-quark pair production at hadron colliders*, Phys.Rev. **D78** (2008) 034003, arXiv:0804.1476 [hep-ph]. 1

[19] J. Aguilar-Saavedra, *Top flavor-changing neutral interactions: Theoretical expectations and experimental detection*, Acta Phys.Polon. **B35** (2004) 2695–2710, arXiv:hep-ph/0409342 [hep-ph]. 1

[20] S. L. Glashow, *Partial-symmetries of weak interactions*, Nuclear Physics **22** (1961) no. 4, 579 – 588. http://www.sciencedirect.com/science/article/pii/0029558261904692. 2.1

[21] S. Weinberg, *A Model of Leptons*, Phys. Rev. Lett. **19** (1967) 1264–1266. 2.1

[22] H. Georgi and S. L. Glashow, *Unified Weak and Electromagnetic Interactions without Neutral Currents*, Phys. Rev. Lett. **28** (May, 1972) 1494–1497. http://link.aps.org/doi/10.1103/PhysRevLett.28.1494. 2.1

[23] H. D. Politzer, *Reliable Perturbative Results for Strong Interactions?*, Phys. Rev. Lett. **30** (Jun, 1973) 1346–1349. http://link.aps.org/doi/10.1103/PhysRevLett.30.1346. 2.1

[24] H. D. Politzer, *Asymptotic freedom: An approach to strong interactions*, Physics Reports **14** (1974) no. 4, 129 – 180. http://www.sciencedirect.com/science/article/pii/0370157374900143. 2.1

[25] D. J. Gross and F. Wilczek, *Asymptotically Free Gauge Theories. I*, Phys. Rev. D **8** (Nov, 1973) 3633–3652. http://link.aps.org/doi/10.1103/PhysRevD.8.3633. 2.1

[26] S. Weinberg, *The making of the Standard Model*, The European Physical Journal C - Particles and Fields **34** (2004) no. 1, 5–13. http://dx.doi.org/10.1140/epjc/s2004-01761-1. 2.1

[27] G. Hooft, *Renormalizable Lagrangians for massive Yang-Mills fields*, Nuclear Physics B **35** (1971) no. 1, 167 – 188. http://www.sciencedirect.com/science/article/pii/0550321371901398. 2.1

[28] G. 't Hooft and M. J. G. Veltman, *Regularization and Renormalization of Gauge Fields*, Nucl. Phys. **B44** (1972) 189–213. 2.1

[29] G. 't Hooft and M. J. G. Veltman, *Combinatorics of gauge fields*, Nucl. Phys. **B50** (1972) 318–353. 2.1

[30] F. Englert and R. Brout, *Broken Symmetry and the Mass of Gauge Vector Mesons*, Phys. Rev. Lett. **13** (Aug, 1964) 321–323. http://link.aps.org/doi/10.1103/PhysRevLett.13.321. 2.1

[31] P. W. Higgs, *Broken Symmetries and the Masses of Gauge Bosons*, Phys. Rev. Lett. **13** (Oct, 1964) 508–509. http://link.aps.org/doi/10.1103/PhysRevLett.13.508. 2.1

[32] Particle Data Group Collaboration, K. Olive et al., *Review of Particle Physics*, Chin.Phys. **C38** (2014) 090001. 2.1, 2.2, 2.3, 2.2.3, 4.5, 5.1

[33] N. Cabibbo, *Unitary Symmetry and Leptonic Decays*, Phys. Rev. Lett. **10** (1963) 531–533. [,648(1963)]. 2.1, 2.2.3

[34] M. Kobayashi and T. Maskawa, *CP Violation in the Renormalizable Theory of Weak Interaction*, Prog. Theor. Phys. **49** (1973) 652–657. 2.1, 2.2.3

[35] *Asymptotic freedom in parton language*, Nuclear Physics B **126** (1977) no. 2, 298 – 318. 2.2.1

[36] B. Richard et al.Nucl. Phys. B **867** (Jul, 2012) 244–289. 56 p. http://cds.cern.ch/record/1460337. 2.1, 2.2.2, 7.1

[37] M. A. Dobbs et al., *Les Houches guidebook to Monte Carlo generators for hadron collider physics*, in *Physics at TeV colliders. Proceedings, Workshop, Les Houches, France, May 26-June 3, 2003*, pp. 411–459. 2004. arXiv:hep-ph/0403045 [hep-ph]. http://lss.fnal.gov/cgi-bin/find_paper.pl?conf-04-183. 2.2

[38] M. Beneke et al., *Hadronic top-quark pair production with NNLL threshold resummation*, Nucl. Phys. **B855** (2012) 695–741, arXiv:1109.1536 [hep-ph]. 2.2.2, 7.1

[39] M. Cacciari et al., *Top-pair production at hadron colliders with next-to-next-to-leading logarithmic soft-gluon resummation*, Phys. Lett. **B710** (2012) 612–622, arXiv:1111.5869 [hep-ph]. 2.2.2, 7.1

[40] P. Barnreuther et al., *Percent Level Precision Physics at the Tevatron: First Genuine NNLO QCD Corrections to $q\bar{q} \to t\bar{t} + X$*, Phys. Rev. Lett. **109** (2012) 132001, arXiv:1204.5201 [hep-ph]. 2.2.2, 7.1

[41] M. Czakon and A. Mitov, *NNLO corrections to top-pair production at hadron colliders: the all-fermionic scattering channels*, JHEP **12** (2012) 054, arXiv:1207.0236 [hep-ph]. 2.2.2, 7.1

[42] M. Czakon and A. Mitov, *NNLO corrections to top pair production at hadron colliders: the quark-gluon reaction*, JHEP **01** (2013) 080, arXiv:1210.6832 [hep-ph]. 2.2.2, 7.1

[43] M. o. Czakon, *Total Top-Quark Pair-Production Cross Section at Hadron Colliders Through $O(\frac{4}{S})$*, Phys. Rev. Lett. **110** (2013) 252004, arXiv:1303.6254 [hep-ph]. 2.2.2, 7.1

[44] M. Czakon et al., *Top++: A Program for the Calculation of the Top-Pair Cross-Section at Hadron Colliders*, Comput. Phys. Commun. **185** (2014) 2930, arXiv:1112.5675 [hep-ph]. 2.2.2, 7.1

[45] M. Botje et al., *The PDF4LHC Working Group Interim Recommendations*, arXiv:1101.0538 [hep-ph]. 2.2.2, 7.1

[46] A. Martin et al., *Parton distributions for the LHC*, Eur. Phys. J. **C63** (2009) 189–285, arXiv:0901.0002 [hep-ph]. 2.2.2, 7.1

[47] A. Martin et al., *Uncertainties on alpha(S) in global PDF analyses and implications for predicted hadronic cross sections*, Eur. Phys. J. **C64** (2009) 653–680, arXiv:0905.3531 [hep-ph]. 2.2.2, 7.1

[48] H. o. Lai, *New parton distributions for collider physics*, Phys. Rev. **D82** (2010) 074024, arXiv:1007.2241 [hep-ph]. 2.2.2, 7.1

[49] J. Gao et al., *CT10 next-to-next-to-leading order global analysis of QCD*, Phys. Rev. **D89** (2014) no. 3, 033009, arXiv:1302.6246 [hep-ph]. 2.2.2, 7.1

[50] ATLAS Collaboration, *Top Working Group summary plots*, https://atlas.web.cern.ch/Atlas/GROUPS/PHYSICS/CombinedSummaryPlots/TOP. 2.4, 2.5, 2.8

[51] ARGUS Collaboration, H. Albrecht et al., *Observation of B0 - anti-B0 Mixing*, Phys. Lett. **B192** (1987) 245–252. [,51(1987)]. 2.2.3

[52] Particle Data Group Collaboration, S. O. et al., $B^0 - \bar{B}^0$ *mixing*, Chin. Phys. **C38** (2014) 090001. 2.2.3

[53] CDF Collaboration, A. Abulencia et al., *Observation of* $B_s^0 - \bar{B}_s^0$ *Oscillations*, Phys. Rev. Lett. **97** (2006) 242003, arXiv:hep-ex/0609040 [hep-ex]. 2.2.3

[54] LHCb Collaboration, R. Aaij et al., *Precision measurement of the* B_s^0-$\bar{B}_s^0$ *oscillation frequency with the decay* $B_s^0 \to D_s^- \pi^+$, New J. Phys. **15** (2013) 053021, arXiv:1304.4741 [hep-ex]. 2.2.3

[55] S. Aoki et al., *Review of lattice results concerning low-energy particle physics*, Eur. Phys. J. **C74** (2014) 2890, arXiv:1310.8555 [hep-lat]. 2.2.3

[56] CDF Collaboration, D. Acosta et al., *Measurement of* $B(t \to Wb)/B(t \to Wq)$ *at the Collider Detector at Fermilab*, Phys. Rev. Lett. **95** (2005) 102002, arXiv:hep-ex/0505091 [hep-ex]. 2.2.3

[57] D0 Collaboration, V. M. Abazov et al., *Precision measurement of the ratio* $\mathrm{B}(t \to Wb)/\mathrm{B}(t \to Wq)$ *and Extraction of* V_{tb}, Phys. Rev. Lett. **107** (2011) 121802, arXiv:1106.5436 [hep-ex]. 2.2.3

[58] A. Ivanov, *CMS results on top physics*, PoS **IHEP-LHC-2012** (2012) 030. 2.2.3

[59] D0 Collaboration, V. M. Abazov et al., *Evidence for s-channel single top quark production in* $p\bar{p}$ *collisions at* $\sqrt{s} = 1.96$ *TeV*, Phys. Lett. **B726** (2013) 656–664, arXiv:1307.0731 [hep-ex]. 2.2.3

[60] CMS Collaboration, S. Chatrchyan et al., *Measurement of the single-top-quark t-channel cross section in pp collisions at* $\sqrt{s} = 7$ *TeV*, JHEP **12** (2012) 035, arXiv:1209.4533 [hep-ex]. 2.2.3

[61] ATLAS Collaboration, G. Aad et al., *Measurement of the t-channel single top-quark production cross section in pp collisions at* $\sqrt{s} = 7$ *TeV with the ATLAS detector*, Phys. Lett. **B717** (2012) 330–350, arXiv:1205.3130 [hep-ex]. 2.2.3

[62] I. I. Y. Bigi, *The QCD perspective on lifetimes of heavy flavor hadrons*, arXiv:hep-ph/9508408 [hep-ph]. 2.2.3

[63] ATLAS, CMS Collaboration, G. Aad et al., *Combined Measurement of the Higgs Boson Mass in pp Collisions at $\sqrt{s} = 7$ and 8 TeV with the ATLAS and CMS Experiments*, Phys. Rev. Lett. **114** (2015) 191803, arXiv:1503.07589 [hep-ex]. 2.3

[64] S. Weinberg, *Gauge hierarchies*, Physics Letters B **82** (1979) no. 3, 387 – 391. http://www.sciencedirect.com/science/article/pii/037026937990248X. 2.3

[65] E. Gildener, *Gauge-symmetry hierarchies*, Phys. Rev. D **14** (Sep, 1976) 1667–1672. 2.3

[66] G. L. Kane and M. A. Shifman, *Introduction to 'the supersymmetric world: The Beginnings of the theory'*, arXiv:hep-ph/0102298 [hep-ph]. 2.3

[67] G. Branco et al., *Theory and phenomenology of two-Higgs-doublet models*, Phys. Rept. **516** (2012) 1–102, arXiv:1106.0034 [hep-ph]. 2.3

[68] ATLAS Collaboration, G. Aad et al., *Search for $t\bar{t}$ resonances in the lepton plus jets final state with ATLAS using 4.7 fb^{-1} of pp collisions at $\sqrt{s} = 7$ TeV*, Phys. Rev. **D88** (2013) no. 1, 012004, arXiv:1305.2756 [hep-ex]. 2.3

[69] ATLAS Collaboration, G. Aad et al., *A search for $t\bar{t}$ resonances in lepton+jets events with highly boosted top quarks collected in pp collisions at $\sqrt{s} = 7$ TeV with the ATLAS detector*, JHEP **09** (2012) 041, arXiv:1207.2409 [hep-ex]. 2.3

[70] ATLAS Collaboration, G. Aad et al., *A search for $t\bar{t}$ resonances using lepton-plus-jets events in proton-proton collisions at $\sqrt{s} = 8$ TeV with the ATLAS detector*, JHEP **08** (2015) 148, arXiv:1505.07018 [hep-ex]. 2.3

[71] CMS Collaboration Collaboration, *Search for ttbar resonances in dilepton+jets final states in pp collisions at 8 TeV*, Tech. Rep. CMS-PAS-B2G-12-007, CERN, Geneva, 2014. https://cds.cern.ch/record/1955525. 2.3

[72] CMS Collaboration, S. Chatrchyan et al., *Search for resonant $t\bar{t}$ production in lepton+jets events in pp collisions at $\sqrt{s} = 7$ TeV*, JHEP **12** (2012) 015, arXiv:1209.4397 [hep-ex]. 2.3

[73] S. L. Glashow, J. Iliopoulos, and L. Maiani, *Weak Interactions with Lepton-Hadron Symmetry*, Phys. Rev. D **2** (Oct, 1970) 1285–1292. http://link.aps.org/doi/10.1103/PhysRevD.2.1285. 2.3.1

[74] J. A. Aguilar-Saavedra, *Top flavor-changing neutral interactions: Theoretical expectations and experimental detection*, Acta Phys. Polon. **B35** (2004) 2695–2710, arXiv:hep-ph/0409342 [hep-ph]. 2.4, 2.5, 6.1

[75] J. L. Díaz-Cruz, R. Martínez, M. A. Pérez, and A. Rosado, *Flavor-changing radiative decay of the t quark*, Phys. Rev. D **41** (Feb, 1990) 891–894. http://link.aps.org/doi/10.1103/PhysRevD.41.891. 2.4, 2.5

[76] G. Eilam, J. L. Hewett, and A. Soni, *Rare decays of the top quark in the standard and two-Higgs-doublet models*, Phys. Rev. D **44** (Sep, 1991) 1473–1484. http://link.aps.org/doi/10.1103/PhysRevD.44.1473. 2.4, 2.5

[77] G. Eilam, J. L. Hewett, and A. Soni, *Erratum: Rare decays of the top quark in the standard and two-Higgs-doublet models [Phys. Rev. D **44** , 1473 (1991)]*, Phys. Rev. D **59** (Dec, 1998) 039901. http://link.aps.org/doi/10.1103/PhysRevD.59.039901. 2.4, 2.5

[78] B. Mele, S. Petrarca, and A. Soddu, *A New evaluation of the t —> cH decay width in the standard model*, Phys. Lett. **B435** (1998) 401–406, arXiv:hep-ph/9805498 [hep-ph]. 2.4, 2.5

[79] CMS Collaboration, C. Collaboration, *Search for top quark decays t rightarrow qH with H rightarrow gammagamma in pp collisions at sqrts = 8 TeV*, . **??**

[80] CMS Collaboration, C. Collaboration, *Search for top quark decays via Higgs-boson-mediated flavor changing neutral currents in pp collisions at* $\sqrt{s}$ *= 8 TeV*, . **??**

[81] ATLAS Collaboration, G. Aad et al., *Search for top quark decays* $t \to qH$ *with* $H \to \gamma\gamma$ *using the ATLAS detector*, JHEP **06** (2014) 008, arXiv:1403.6293 [hep-ex]. **??**

[82] D. Hohn, M. Kuna, R. Narayan, P. Onyisi, and F. Seifert, *Reinterpretation of multilepton* $t\bar{t}H$ *search as a limit on the flavor-changing decay* $t \to Hq$, Tech. Rep. ATL-COM-PHYS-2015-562, CERN, Geneva, Jun, 2015. https://cds.cern.ch/record/2026565. **??**

[83] A. Juste, E. Le Menedeu, J. Montejo, F. Rubbo, S. Tsiskaridze, S. Grinstein, and H. Yang, *Search for flavor-changing neutral current* $t \to Hq$ $(q = u, c)$ *decays, with* $H \to b\bar{b}$*, in the lepton+jets final state in pp collisions at* $\sqrt{s} = 8$ *TeV with the ATLAS detector*, Tech. Rep. ATL-COM-PHYS-2014-809, CERN, Geneva, Jul, 2014. https://cds.cern.ch/record/1742309. **??**

[84] B. Lemmer, *Overview of FCNC Searches in Top Events from CMS and ATLAS*, Tech. Rep. ATL-PHYS-PROC-2015-189, CERN, Geneva, Dec, 2015. https://cds.cern.ch/record/2114091. 2.7

[85] CMS Collaboration, C. Collaboration, *Search for anomalous Wtb couplings and top FCNC in t-channel single-top-quark events*, . 2.3.1

[86] ATLAS Collaboration, G. Aad et al., *Search for single top-quark production via flavour-changing neutral currents at 8 TeV with the ATLAS detector*, Eur. Phys. J. **C76** (2016) no. 2, 55, arXiv:1509.00294 [hep-ex]. 2.3.1

[87] CMS Collaboration, V. Khachatryan et al., *Search for anomalous single top quark production in association with a photon in pp collisions at* $\sqrt{s} = 8$ *TeV*, JHEP **04** (2016) 035, arXiv:1511.03951 [hep-ex]. 2.3.1

[88] ATLAS Collaboration, G. Aad et al., *Search for flavour-changing neutral current top-quark decays to qZ in pp collision data collected with the ATLAS detector at* $\sqrt{s} = 8$ *TeV*, Eur. Phys. J. **C76** (2016) no. 1, 12, arXiv:1508.05796 [hep-ex]. 2.3.1

[89] CMS Collaboration, S. Chatrchyan et al., *Search for Flavor-Changing Neutral Currents in Top-Quark Decays* $t \to Zq$ *in pp Collisions at* $\sqrt{s} = 8$*âĂĽâĂĽTeV*, Phys. Rev. Lett. **112** (2014) no. 17, 171802, arXiv:1312.4194 [hep-ex]. 2.3.1

[90] L. Evans and P. Bryant, *LHC Machine*, JINST **3** (2008) S08001. 3.1

[91] A. Team, *The scale of the LHC. Vue aérienne du CERN avec le tracé du tunnel LHC*, https://cds.cern.ch/record/42370, Jan, 2001. 3.1

[92] ATLAS Collaboration, *The ATLAS Experiment at the CERN Large Hadron Collider*, JINST **3** (2008) S08003. 3.1, 3.2, 3.2.1, 3.2.1, 3.4

[93] CMS Collaboration, S. Chatrchyan et al., *The CMS experiment at the CERN LHC*, JINST **3** (2008) S08004. 3.1

[94] ALICE Collaboration, K. Aamodt et al., *The ALICE experiment at the CERN LHC*, JINST **3** (2008) S08002. 3.1

[95] LHCb Collaboration, A. A. Alves, Jr. et al., *The LHCb Detector at the LHC*, JINST **3** (2008) S08005. 3.1

[96] LHCf Collaboration, O. Adrian et al., *The LHCf detector at the CERN Large Hadron Collider*, JINST **3** (2008) no. 08, S08006. http://stacks.iop.org/1748-0221/3/i=08/a=S08006. 3.1

[97] MoEDAL Collaboration, B. Acharya et al., *The Physics Programme Of The MoEDAL Experiment At The LHC*, Int. J. Mod. Phys. **A29** (2014) 1430050, arXiv:1405.7662 [hep-ph]. 3.1

[98] TOTEM Collaboration, G. Anelli et al., *The TOTEM Experiment at the CERN Large Hadron Collider*, JINST **3** (2008) no. 08, S08007. http://stacks.iop.org/1748-0221/3/i=08/a=S08007. 3.1

[99] CERN, *The Accelerator Complex*, http://home.cern/about/accelerators. 3.1.1

[100] C. Lefévre, *The CERN accelerator complex. Complexe des accélérateurs du CERN*, https://cds.cern.ch/record/1260465, Dec, 2008. 3.2, 3.1

[101] W. Stirling, *Tevatron and LHC parton luminosity comparison plots*, http://www.hep.ph.ic.ac.uk/~wstirlin/plots/plots.html. 3.3

[102] ATLAS Collaboration, LHC, *ATLAS Data Summary*, https://atlas.web.cern.ch/Atlas/GROUPS/DATAPREPARATION/DataSummary/2012/run-table.html. 3.2

[103] ATLAS Collaboration, *Luminosity Results*, https://twiki.cern.ch/twiki/bin/view/AtlasPublic/LuminosityPublicResults. 3.4

[104] ATLAS Collaboration, *ATLAS detector and physics performance: Technical Design Report, 1.* Technical Design Report ATLAS. CERN, Geneva, 1999. https://cds.cern.ch/record/391176. Electronic version not available. 3.2, 3.12, 3.13

[105] ATLAS Collaboration, *ATLAS detector and physics performance: Technical Design Report, 2.* Technical Design Report ATLAS. CERN, Geneva, 1999. https://cds.cern.ch/record/391177. Electronic version not available. 3.2, 3.12, 3.13

[106] ATLAS Collaboration, *Cutview of ATLAS detector*, http://www.atlas.ch/photos/full-detector-cgi.html. 3.5

[107] J. Pequenao, *Event Cross Section in a computer generated image of the ATLAS detector.*, https://cds.cern.ch/record/1096081, Mar, 2008. 3.6

[108] ATLAS Collaboration, *Alignment of the ATLAS Inner Detector and its Performance in 2012*, Tech. Rep. ATLAS-CONF-2014-047, CERN, Geneva, Jul, 2014. https://cds.cern.ch/record/1741021. 3.7, 3.3

[109] ATLAS Collaboration, *The ATLAS Experiment at the CERN Large Hadron Collider*, Journal of Instrumentation **3** (2008) no. 08, S08003. http://stacks.iop.org/1748-0221/3/i=08/a=S08003. 3.8

[110] J. Pequenao, *Computer Generated image of the ATLAS calorimeter*, https://cds.cern.ch/record/1095927, Mar, 2008. 3.10

[111] ATLAS Collaboration, *Commissioning of the ATLAS Muon Spectrometer with Cosmic Rays*, Eur. Phys. J. **C70** (2010) 875–916, arXiv:1006.4384 [physics.ins-det]. 3.2.3

[112] J. Pequenao, *Computer generated image of the ATLAS Muons subsystem*, Mar, 2008. 3.11

[113] ATLAS Collaboration, *Trigger Operation Public Results*, https://twiki.cern.ch/twiki/bin/view/AtlasPublic/TriggerOperationPublicResults, 2015. 3.4

[114] T. Sjostrand, S. Mrenna, and P. Z. Skands, *PYTHIA 6.4 Physics and Manual*, JHEP **0605** (2006) 026, arXiv:hep-ph/0603175 [hep-ph]. 3.2.5, 5.2.2, 5.8.10

[115] T. Gleisberg, S. Hoeche, F. Krauss, M. Schonherr, S. Schumann, F. Siegert, and J. Winter, *Event generation with SHERPA 1.1*, JHEP **02** (2009) 007, arXiv:0811.4622 [hep-ph]. 3.2.5

[116] G. Corcella, I. Knowles, G. Marchesini, S. Moretti, K. Odagiri, et al., *HERWIG 6: An Event generator for hadron emission reactions with interfering gluons (including supersymmetric processes)*, JHEP **0101** (2001) 010, arXiv:hep-ph/0011363 [hep-ph]. 3.2.5, 5.2.2, 5.8.9

[117] J. Alwall, P. Demin, S. de Visscher, R. Frederix, M. Herquet, F. Maltoni, T. Plehn, D. L. Rainwater, and T. Stelzer, *MadGraph/MadEvent v4: The New Web Generation*, JHEP **09** (2007) 028, arXiv:0706.2334 [hep-ph]. 3.2.5

[118] J. Alwall, M. Herquet, F. Maltoni, O. Mattelaer, and T. Stelzer, *MadGraph 5 : Going Beyond*, JHEP **06** (2011) 128, arXiv:1106.0522 [hep-ph]. 3.2.5

[119] M. L. Mangano, M. Moretti, F. Piccinini, R. Pittau, and A. D. Polosa, *ALPGEN, a generator for hard multiparton processes in hadronic collisions*, JHEP **0307** (2003) 001, arXiv:hep-ph/0206293 [hep-ph]. 3.2.5

[120] S. Frixione and B. R. Webber, *Matching NLO QCD computations and parton shower simulations*, JHEP **0206** (2002) 029, arXiv:hep-ph/0204244 [hep-ph]. 3.2.5, 5.2.2, 5.8.9

[121] S. Frixione, P. Nason, and C. Oleari, *Matching NLO QCD computations with Parton Shower simulations: the POWHEG method*, JHEP **0711** (2007) 070, arXiv:0709.2092 [hep-ph]. 3.2.5, 5.2.2, 5.8.9, 5.8.10

[122] S. Agostinelli et al., *Geant4 simulation toolkit*, Nuclear Instruments and Methods in Physics Research **506** (2003) no. 3, 250 – 303. 3.2.5

[123] G. Folger and J. P. Wellisch, *String parton models in GEANT4*, eConf **C0303241** (2003) MOMT007, arXiv:nucl-th/0306007 [nucl-th]. 3.2.5

[124] H. Pi, *An event generator for interactions between hadrons and nuclei FRITIOF version 7.0*, Computer Physics Communications **71** (1992) no. 1 - 2, 173 – 192. 3.2.5

[125] J. Chapman et al., *The ATLAS detector digitization project for 2009 data taking*, Journal of Physics: Conference Series **219** (2010) no. 3, 032031. http://stacks.iop.org/1742-6596/219/i=3/a=032031. 3.2.5

[126] ATLAS Collaboration, *Concepts, Design and Implementation of the ATLAS New Tracking (NEWT)*, Tech. Rep. ATL-SOFT-PUB-2007-007. ATL-COM-SOFT-2007-002, CERN, Geneva, Mar, 2007. https://cds.cern.ch/record/1020106. 4.1

[127] ATLAS Collaboration, *Performance of the ATLAS Silicon Pattern Recognition Algorithm in Data and Simulation at* $\sqrt{s} = 7$ *TeV*, Tech. Rep. ATLAS-CONF-2010-072, CERN, Geneva, Jul, 2010. https://cds.cern.ch/record/1281363. i, 4.1, 4.2

[128] W. Waltenberger, R. FrÃijhwirth, and P. Vanlaer, *Adaptive vertex fitting*, Journal of Physics G: Nuclear and Particle Physics **34** (2007) no. 12, N343. http://stacks.iop.org/0954-3899/34/i=12/a=N01. 4.1

[129] ATLAS Collaboration, *Measurement of the Inelastic Proton-Proton Cross-Section at* $\sqrt{s} = 7$ *TeV with the ATLAS Detector*, Nature Commun. **2** (2011) 463, arXiv:1104.0326 [hep-ex]. 4.1

[130] ATLAS Collaboration, *ATLAS Inner Detector Tracking Performance Guidelines*, https://twiki.cern.ch/twiki/bin/view/AtlasProtected/TrackingCPMC12. 4.1

[131] ATLAS Collaboration, *ATLAS Data Preparation 2014*, https://twiki.cern.ch/twiki/bin/viewauth/Atlas/MC12bWiki. 4.1

[132] W. Lampl, S. Laplace, D. Lelas, P. Loch, H. Ma, S. Menke, S. Rajagopalan, D. Rousseau, S. Snyder, and G. Unal, *Calorimeter Clustering Algorithms: Description and Performance*, Tech. Rep. ATL-LARG-PUB-2008-002. ATL-COM-LARG-2008-003, CERN, Geneva, Apr, 2008. https://cds.cern.ch/record/1099735. 4.2

[133] ATLAS Collaboration, *Electron performance measurements with the ATLAS detector using the 2010 LHC proton-proton collision data*, Eur. Phys. J. **C72** (2012) 1909, arXiv:1110.3174 [hep-ex]. 4.2

[134] ATLAS Collaboration, *Electron efficiency measurements with the ATLAS detector using the 2012 LHC proton-proton collision data*, Tech. Rep. ATLAS-CONF-2014-032, CERN, Geneva, Jun, 2014. https://cds.cern.ch/record/1706245. 4.3, 4.4

[135] ATLAS Collaboration, *Photon Conversions at* $\sqrt{s} = 900$ GeV *measured with the ATLAS Detector*, Tech. Rep. ATLAS-CONF-2010-007, CERN, Geneva, Jun, 2010. https://cds.cern.ch/record/1274001. 4.2

[136] ATLAS Collaboration, *Electron and photon energy calibration with the ATLAS detector using LHC Run 1 data*, The European Physical Journal C **74** (2014) no. 10, . http://dx.doi.org/10.1140/epjc/s10052-014-3071-4. 4.2

[137] ATLAS Collaboration, *Preliminary results on the muon reconstruction efficiency, momentum resolution, and momentum scale in ATLAS 2012 pp collision data*, Tech. Rep. ATLAS-CONF-2013-088, CERN, Geneva, Aug, 2013. https://cds.cern.ch/record/1580207. 4.5, 4.6, 4.3

[138] ATLAS Collaboration, *Expected Performance of the ATLAS Experiment - Detector, Trigger and Physics*, arXiv:0901.0512 [hep-ex]. 4.4.1

[139] M. Cacciari, G. P. Salam, and G. Soyez, *The Anti-k(t) jet clustering algorithm*, JHEP **04** (2008) 063, arXiv:0802.1189 [hep-ph]. 4.4.1

[140] ATLAS Collaboration, *Jet energy measurement and its systematic uncertainty in proton-proton collisions at $\sqrt{s} = 7$ TeV with the ATLAS detector*, Eur. Phys. J. **C75** (2015) 17, arXiv:1406.0076 [hep-ex]. 4.4.2, 4.4.2, 4.4.2

[141] ATLAS Collaboration, *Monte Carlo Calibration and Combination of In-situ Measurements of Jet Energy Scale, Jet Energy Resolution and Jet Mass in ATLAS*, Tech. Rep. ATLAS-CONF-2015-037, CERN, Geneva, Aug, 2015. https://cds.cern.ch/record/2044941. 4.7, 4.4.2, 4.8, 4.9, 4.10, 4.12, 4.13

[142] ALTAS Collaboration, *Pile-up subtraction and suppression for jets in ATLAS*, Tech. Rep. ATLAS-CONF-2013-083, CERN, Geneva, Aug, 2013. https://cds.cern.ch/record/1570994. 4.4.2

[143] ATLAS Collaboration, *Jet global sequential corrections with the ATLAS detector in proton-proton collisions at sqrt(s) = 8 TeV*, Tech. Rep. ATLAS-CONF-2015-002, CERN, Geneva, Mar, 2015. https://cds.cern.ch/record/2001682. 4.4.2, 4.11

[144] ATLAS Collaboration, *Data-driven determination of the energy scale and resolution of jets reconstructed in the ATLAS calorimeters using dijet and multijet events at $\sqrt{s} = 8$ TeV*, Tech. Rep. ATLAS-CONF-2015-017, CERN, Geneva, Apr, 2015. https://cds.cern.ch/record/2008678. 4.4.2

[145] ATLAS Collaboration, *Calibration of the performance of b-tagging for c and light-flavour jets in the 2012 ATLAS data*, Tech. Rep. ATLAS-CONF-2014-046, CERN, Geneva, Jul, 2014. https://cds.cern.ch/record/1741020. 4.14, 4.4.4, 4.15, 4.4.4

[146] ATLAS Collaboration, *Performance of the ATLAS Secondary Vertex b-tagging Algorithm in 900 GeV Collision Data*, Tech. Rep. ATLAS-CONF-2010-004, CERN, Geneva, Jun, 2010. https://cds.cern.ch/record/1273194. 4.14

[147] ATLAS Collaboration, *b-Jet Tagging Efficiency Calibration using the System8 Method*, Tech. Rep. ATLAS-CONF-2011-143, CERN, Geneva, Oct, 2011. https://cds.cern.ch/record/1386703. 4.15, 4.4.4

[148] M. L. Perl et al., *Evidence for Anomalous Lepton Production in $e^+ - e^-$ Annihilation*, Phys. Rev. Lett. **35** (Dec, 1975) 1489–1492. 4.5

[149] M. L. Perl et al., *Properties of the Proposed tau Charged Lepton*, Phys. Lett. **B70** (1977) 487. 4.5

[150] ALEPH Collaboration, *A precise determination of the number of families with light neutrinos and of the Z boson partial widths*, Physics Letters B **235** (1990) no. 3 - 4, 399 – 411. 4.5

[151] K. Kodama et al., *Observation of tau neutrino interactions*, Physics Letters B **504** (2001) no. 3, 218 – 224. 4.5

[152] ATLAS Collaboration, *Measurement of inclusive jet and dijet cross sections in proton-proton collisions at 7 TeV centre-of-mass energy with the ATLAS detector*, Eur. Phys. J. **C71** (2011) 1512, arXiv:1009.5908 [hep-ex]. 4.5

[153] ATLAS Collaboration, *Measurement of the $W \to \tau\nu_\tau$ cross section in pp collisions at $\sqrt{s}$ =7 TeV with the ATLAS experiment*, Phys. Lett. **B706** (2012) 276–294, arXiv:1108.4101 [hep-ex]. 4.5

[154] C. Limbach, *Reconstruction and Identification of Tau Leptons in ATLAS*, Nuclear and Particle Physics Proceedings **260** (2015) 195 – 198. The 13th International Workshop on Tau Lepton PhysicsThe 13th International Workshop on Tau Lepton Physics (Tau2014). 4.17

[155] ATLAS Collaboration, *Identification and energy calibration of hadronically decaying tau leptons with the ATLAS experiment in pp collisions at $\sqrt{s}$=8 TeV*, Eur. Phys. J. **C75** (2015) no. 7, 303, arXiv:1412.7086 [hep-ex]. 4.5, 4.5.1, 4.19, 4.20, 4.21, 4.5.2, 4.1, 4.23, 4.24, 4.25, 4.5.3, 4.26, 4.27, 4.28, 4.29, 5.1, 5.3.2, 5.5, 5.8.1, 5.8.2

[156] ATLAS Collaboration, *Performance of the Reconstruction and Identification of Hadronic Tau Decays in ATLAS with 2011 Data*, Tech. Rep. ATLAS-CONF-2012-142, CERN, Geneva, Oct, 2012. https://cds.cern.ch/record/1485531. 4.18

[157] ATLAS Collaboration, *Stand-Alone Event Displays* , https://twiki.cern.ch/twiki/bin/view/AtlasPublic/EventDisplayStandAlone. 4.22

[158] B. P. Roe, H.-J. Yang, J. Zhu, Y. Liu, I. Stancu, and G. McGregor, *Boosted decision trees, an alternative to artificial neural networks*, Nucl. Instrum. Meth. **A543** (2005) no. 2-3, 577–584, arXiv:physics/0408124 [physics]. 4.5.2

[159] ATLAS Collaboration, *Performance of Missing Transverse Momentum Reconstruction in ATLAS studied in Proton-Proton Collisions recorded in 2012 at 8 TeV*, Tech. Rep. ATLAS-CONF-2013-082, CERN, Geneva, Aug, 2013. https://cds.cern.ch/record/1570993. 4.6, 4.30, 5.3.6

[160] *Calibration of the performance of b-tagging for c and light-flavour jets in the 2012 ATLAS data*, Tech. Rep. ATLAS-CONF-2014-046, CERN, Geneva, Jul, 2014. ?, 5.8.4

[161] ATLAS Collaboration, *The ATLAS Simulation Infrastructure*, Eur.Phys.J. **C70** (2010) 823–874, arXiv:1005.4568 [physics.ins-det]. 5.2.2

[162] H.-L. Lai, M. Guzzi, J. Huston, Z. Li, P. M. Nadolsky, et al., *New parton distributions for collider physics*, Phys.Rev. **D82** (2010) 074024, arXiv:1007.2241 [hep-ph]. 5.2.2

[163] P. Z. Skands, *Tuning Monte Carlo Generators: The Perugia Tunes*, Phys.Rev. **D82** (2010) 074018, arXiv:1005.3457 [hep-ph]. 5.2.2

[164] J. Pumplin, D. Stump, J. Huston, H. Lai, P. M. Nadolsky, et al., *New generation of parton distributions with uncertainties from global QCD analysis*, JHEP **0207** (2002) 012, arXiv:hep-ph/0201195 [hep-ph]. 5.2.2

[165] J. Butterworth, J. R. Forshaw, and M. Seymour, *Multiparton interactions in photoproduction at HERA*, Z.Phys. **C72** (1996) 637–646, arXiv:hep-ph/9601371 [hep-ph]. 5.2.2, 5.8.9

[166] ATLAS Collaboration, *Object selection and calibration, background estimations and MC samples for top quark analyses using the full 2012 data set*, Tech. Rep. ATL-COM-PHYS-2013-1016, CERN, Geneva, Jul, 2013. 5.3

[167] M. Cacciari, G. P. Salam, and G. Soyez, *The anti-k(t) jet clustering algorithm*, JHEP **0804** (2008) 063, arXiv:0802.1189. 5.3.1

[168] M. Cacciari and G. P. Salam, *Dispelling the N**3 myth for the k(t) jet-finder*, Phys. Lett. B **641** (2006) 57, arXiv:hep-ph/0512210. 5.3.1

[169] ATLAS Collaboration, *Local Hadronic Calibration*, ATL-LARG-PUB-2009-001. 5.3.1

[170] ATLAS Collaboration, *Jet energy measurement with the ATLAS detector in proton-proton collisions at* $\sqrt{s} = 7$ *TeV*, Eur. Phys. J **C73** (2013) 2304, arXiv:1112.6426 [hep-ex]. 5.3.1

[171] M. Cacciari, G. P. Salam, and G. Soyez, *The catchment area of jets*, JHEP **0804** (2008) 005, arXiv:0802.1188 [hep-ex]. 5.3.1

[172] ATLAS Collaboration, *Pile-up subtraction and suppression for jets in ATLAS*, ATLAS-CONF-2013-083. 5.3.1

[173] ATLAS Collaboration, *Jet global sequential corrections with the ATLAS detector in proton-proton collisions at sqrt(s) = 8 TeV*, Tech. Rep. ATLAS-CONF-2015-002, CERN, Geneva, Mar, 2015. 5.3.1

[174] ATLAS Collaboration, *Measurement of the b-tag efficiency in a sample of jets containing muons with 5* fb^{-1} *of data from the ATLAS detector*, ATLAS-CONF-2012-043. 5.3.1

[175] ATLAS Collaboration, *Electron performance measurements with the ATLAS detector using the 2010 LHC proton-proton collision data*, Eur. Phys. J. C **72** (2012) 1909, arXiv:1110.3174 [hep-ex]. 5.3.3

[176] W. Lampl et al., *Calorimeter clustering algorithms: description and performance*, ATL-LARG-PUB-2008-002. 5.3.3

[177] J. Hartert and I. Ludwig, *Electron isolation in the ATLAS experiment*, ATL-PHYS-INT-2010-052. 5.3.3

[178] SVN: root/Reconstruction/egamma/egammaAnalysis/egammaAnalysisUtils. 5.3.3

[179] ATLAS Collaboration, *Muon reconstruction efficiency in reprocessed 2010 LHC proton-proton collision data recorded with the ATLAS detector*, ATLAS-CONF-2011-063. 5.3.4

[180] ATLAS Collaboration, *A measurement of the muon reconstruction efficiency in 2010 ATLAS data using j/psi decays*, ATLAS-CONF-2012-125. 5.3.4

[181] https://twiki.cern.ch/MCPAnalysisGuidelinesData2012. 5.3.4

[182] Top Jet Liaison, *Jet recommendations for 2012 dataset*, . ?, ?, ?

[183] C. Boddy, D. Capriotti, D. Cavalli, E. Coniavitis, S. Consonni, S. Dhaliwal, D. Evangelakou, S. Farrington, F. Friedrich, J. Griffiths, A. Kaczmarska, J. Kretzschmar, S. Kuehn, S. Lai, A. Larner, Z. Liang, J. Novakova, X. Prudent, E. Ptacek, R. Reece, F. Seifert, T. Schwindt, M. Trottier-McDonald, T. Vickey, M. Wolter, and S. Yacoob, *Measurement of Z to tautau production cross-section in proton-proton collisions at sqrts=7 TeV with the ATLAS detector - Support Note for lep-had channels*, Tech. Rep. ATL-PHYS-INT-2012-032, CERN, Geneva, Apr, 2012. 5.5.7

[184] E. Barberio, S. Bedikian, E. Coniavitis, M. Dam, W. Davey, E. N. Dawe, S. Demers, M. Flechl, F. Friedrich, J. Godfrey, K. Hanawa, M. Janus, D. Jennens, J. Keller, S. Lai, M. Morgenstern, K. Nakamura, D. C. O'Neil, M. I. Pedraza Morales, R. Reece, N. Rompotis, M. Simonyan, A. Saavedra, K. G. Tan, M. Trottier-McDonald, S. Tsuno, D. Varouchas, M. Volpi, M. Wolter, S. Xella, and D. Zanzi, *Identification of Hadronic Tau Decays for Summer 2011*, Tech. Rep. ATL-PHYS-INT-2011-090, CERN, Geneva, Nov, 2011. 5.5.7

[185] Top Working Group, *Top recommendation on systematic uncertainties*, . 5.8

[186] ATLAS Collaboration, G. Aad et al., *Jet energy measurement and its systematic uncertainty in proton-proton collisions at $\sqrt{s} = 7$ TeV with the ATLAS detector*, Eur.Phys.J. **C75** (2015) no. 1, 17, arXiv:1406.0076 [hep-ex]. 5.8.3, 5.8.6

[187] ATLAS Collaboration Collaboration, *Commissioning of the ATLAS high-performance b-tagging algorithms in the 7 TeV collision data*, Tech. Rep. ATLAS-CONF-2011-102, CERN, Geneva, Jul, 2011. 5.8.4

[188] *Pile-up subtraction and suppression for jets in ATLAS*, Tech. Rep. ATLAS-CONF-2013-083, CERN, Geneva, Aug, 2013. 5.8.7

[189] ATLAS Collaboration, G. Aad et al., *Improved luminosity determination in pp collisions at sqrt(s) = 7 TeV using the ATLAS detector at the LHC*, Eur.Phys.J. **C73** (2013) no. 8, 2518, arXiv:1302.4393 [hep-ex]. 5.8.12

[190] L. Moneta, K. Cranmer, G. Schott, and W. Verkerke, *The RooStats project*, in *Proceedings of the 13th International Workshop on Advanced Computing and Analysis Techniques in Physics Research. February 22-27, 2010, Jaipur, India. http://acat2010.cern.ch/. Published online at <A href="http://pos.sissa.it/cgi-bin/reader/conf.cgi?confid=93">http://pos.sissa.it/cgi-bin/reader/conf.cgi?confid=93</A>, p.57*, p. 57. 2010. arXiv:1009.1003 [physics.data-an]. 5.10, 6.1.2, 6.1.2

[191] A. L. Read, *Presentation of search results: the CL s technique*, Journal of Physics G: Nuclear and Particle Physics **28** (2002) no. 10, 2693. http://stacks.iop.org/0954-3899/28/i=10/a=313. 5.10, 6.1.2, 6.1.2, 6.1.5

[192] S. L. Glashow, J. Iliopoulos, and L. Maiani, *Weak Interactions with Lepton-Hadron Symmetry*, Phys. Rev. D **2** (Oct, 1970) 1285–1292. http://link.aps.org/doi/10.1103/PhysRevD.2.1285. 6.1

[193] K.-F. Chen, W.-S. Hou, C. Kao, and M. Kohda, *When the Higgs meets the Top: Search for $t \to ch^0$ at the LHC*, Phys. Lett. **B725** (2013) 378–381, arXiv:1304.8037 [hep-ph]. 6.1

[194] D. Atwood, S. K. Gupta, and A. Soni, *Constraining the flavor changing Higgs couplings to the top-quark at the LHC*, JHEP **10** (2014) 57, arXiv:1305.2427 [hep-ph]. 6.1

[195] J. A. Aguilar-Saavedra, *Protos: Program for Top Simulation (User Manual, version 2.1)*, . https://jaguilar.web.cern.ch/jaguilar/protos/. 6.1

[196] W. Verkerke and D. Kirkby, *The RooFit toolkit for data modeling*, ArXiv Physics e-prints (June, 2003) , physics/0306116. 6.1.2

[197] R. D. Cousins, K. E. Hymes, and J. Tucker, *Frequentist evaluation of intervals estimated for a binomial parameter and for the ratio of Poisson means*, Nuclear Instruments and Methods in Physics Research A **612** (Jan., 2010) 388–398, arXiv:0905.3831 [physics.data-an]. 6.1.3

[198] CMS Collaboration Collaboration, *Search for Quark Compositeness with the Dijet Centrality Ratio in pp Collisions at $\sqrt{s} = 7$ TeV*, Phys. Rev. Lett. **105** (Dec, 2010) 262001. http://link.aps.org/doi/10.1103/PhysRevLett.105.262001. 6.1.3

APPENDIX A

Simulation samples

The Monte Carlo simulation samples associated to different processes are used either in nominal analysis or for estimating systematic uncertainties are listed in tables A.1 to A.5.

Process	DSID	$\sigma(pb)$	$k-$factor	Generator
$t\bar{t}$	110404	114.47	1.1996	POWHEG+PYTHIA, $h_{\text{damp}} = \text{m}_{\text{top}}$
$t\bar{t}$	117050	114.51	1.1992	POWHEG+PYTHIA, $h_{\text{damp}} = \infty$
$t\bar{t}$	105200	112.94	1.2158	MC@NLO+HERWIG
$t\bar{t}$ (AFII)	105860	115.56	1.1883	POWHEG+HERWIG
$t\bar{t}$ (AFII)	110407	137.32	1.00	POWHEG+PYTHIA, $\mu = 2$, $h_{\text{damp}} = m_{\text{top}}$
$t\bar{t}$ (AFII)	110408	137.32	1.00	POWHEG+PYTHIA, $\mu = 0.5$, $h_{\text{damp}} = 2 * m_{\text{top}}$

Table A.1: The simulation samples related to $t\bar{t}$ processes used in the analysis. A GEANT4 simulation is used for all samples unless mentioned otherwise.

Process	DSID	$\sigma(pb)$	$k-$factor	Generator
W $\to$ eν+Np0	147025	8127.3	1.1330	ALPGEN+PYTHIA
W $\to$ eν+Np1	147026	1792.7	1.1330	ALPGEN+PYTHIA
W $\to$ eν+Np2	147027	542.18	1.1330	ALPGEN+PYTHIA
W $\to$ eν+Np3	147028	147.65	1.1330	ALPGEN+PYTHIA
W $\to$ eν+Np4	147029	37.736	1.1330	ALPGEN+PYTHIA
W $\to$ eν+Np5incl.	147030	11.962	1.1330	ALPGEN+PYTHIA
W $\to \mu\nu$+Np0	147033	8127.1	1.1330	ALPGEN+PYTHIA
W $\to \mu\nu$+Np1	147034	1792.9	1.1330	ALPGEN+PYTHIA
W $\to \mu\nu$+Np2	147035	542.24	1.1330	ALPGEN+PYTHIA
W $\to \mu\nu$+Np3	147036	147.66	1.1330	ALPGEN+PYTHIA
W $\to \mu\nu$+Np4	147037	37.745	1.1330	ALPGEN+PYTHIA
W $\to \mu\nu$+Np5incl.	147038	11.970	1.1330	ALPGEN+PYTHIA
W $\to \tau\nu$+Np0	147041	8127.1	1.1330	ALPGEN+PYTHIA
W $\to \tau\nu$+Np1	147042	1792.2	1.1330	ALPGEN+PYTHIA
W $\to \tau\nu$+Np2	147043	542.27	1.1330	ALPGEN+PYTHIA
W $\to \tau\nu$+Np3	147044	147.64	1.1330	ALPGEN+PYTHIA
W $\to \tau\nu$+Np4	147045	37.781	1.1330	ALPGEN+PYTHIA
W $\to \tau\nu$+Np5incl.	147046	11.959	1.1330	ALPGEN+PYTHIA
W+bb+Np0	200256	52.237	1.1330	ALPGEN+PYTHIA
W+bb+Np1	200257	45.628	1.1330	ALPGEN+PYTHIA
W+bb+Np2	200258	23.955	1.1330	ALPGEN+PYTHIA
W+bb+Np3incl.	200259	13.633	1.1330	ALPGEN+PYTHIA
W+cc+Np0	200156	149.39	1.1330	ALPGEN+PYTHIA
W+cc+Np1	200157	143.90	1.1330	ALPGEN+PYTHIA
W+cc+Np2	200158	84.227	1.1330	ALPGEN+PYTHIA
W+cc+Np3incl.	200159	44.277	1.1330	ALPGEN+PYTHIA
W+c+Np0	200056	758.93	1.5200	ALPGEN+PYTHIA
W+c+Np1	200057	274.47	1.52000	ALPGEN+PYTHIA
W+c+Np2	200058	71.643	1.5200	ALPGEN+PYTHIA
W+c+Np3	200059	16.482	1.5200	ALPGEN+PYTHIA
W+c+Np4incl.	200060	4.7824	1.5200	ALPGEN+PYTHIA

Table A.2: The simulation samples related to W+jets processes used in the analysis. A GEANT4 simulation is used for all samples unless mentioned otherwise.

Process	DSID	$\sigma(pb)$	$k-$factor	Generator
Z $\rightarrow$ ee+Np0	147105	718.97	1.1800	ALPGEN+PYTHIA
Z $\rightarrow$ ee+Np1	147106	175.70	1.1800	ALPGEN+PYTHIA
Z $\rightarrow$ ee+Np2	147107	58.875	1.1800	ALPGEN+PYTHIA
Z $\rightarrow$ ee+Np3	147108	15.636	1.1800	ALPGEN+PYTHIA
Z $\rightarrow$ ee+Np4	147109	4.0116	1.1800	ALPGEN+PYTHIA
Z $\rightarrow$ ee+Np5incl.	147110	1.2592	1.1800	ALPGEN+PYTHIA
Z $\rightarrow \mu\mu$+Np0	147113	719.16	1.1800	ALPGEN+PYTHIA
Z $\rightarrow \mu\mu$+Np1	147114	175.74	1.1800	ALPGEN+PYTHIA
Z $\rightarrow \mu\mu$+Np2	147115	58.882	1.1800	ALPGEN+PYTHIA
Z $\rightarrow \mu\mu$+Np3	147116	15.673	1.1800	ALPGEN+PYTHIA
Z $\rightarrow \mu\mu$+Np4	147117	4.0057	1.1800	ALPGEN+PYTHIA
Z $\rightarrow \mu\mu$+Np5incl.	147118	1.2544	1.1800	ALPGEN+PYTHIA
Z $\rightarrow \tau\tau$+Np0	147121	718.87	1.1800	ALPGEN+PYTHIA
Z $\rightarrow \tau\tau$+Np1	147122	175.76	1.1800	ALPGEN+PYTHIA
Z $\rightarrow \tau\tau$+Np2	147123	58.856	1.1800	ALPGEN+PYTHIA
Z $\rightarrow \tau\tau$+Np3	147124	15.667	1.1800	ALPGEN+PYTHIA
Z $\rightarrow \tau\tau$+Np4	147125	4.0121	1.1800	ALPGEN+PYTHIA
Z $\rightarrow \tau\tau$+Np5incl.	147126	1.2560	1.1800	ALPGEN+PYTHIA
Z $\rightarrow$ ee+bb+Np0	200332	6.5083	1.18000	ALPGEN+PYTHIA
Z $\rightarrow$ ee+bb+Np1	200333	3.2927	1.1800	ALPGEN+PYTHIA
Z $\rightarrow$ ee+bb+Np2	200334	1.2544	1.1800	ALPGEN+PYTHIA
Z $\rightarrow$ ee+bb+Np3incl.	200335	0.61711	1.1800	ALPGEN+PYTHIA
Z $\rightarrow \mu\mu$+bb+Np0	200340	6.5056	1.1800	ALPGEN+PYTHIA
Z $\rightarrow \mu\mu$+bb+Np1	200341	3.2904	1.1800	ALPGEN+PYTHIA
Z $\rightarrow \mu\mu$+bb+Np2	200342	1.2601	1.1800	ALPGEN+PYTHIA
Z $\rightarrow \mu\mu$+bb+Np3incl.	200343	0.61882	1.1800	ALPGEN+PYTHIA
Z $\rightarrow \tau\tau$+bb+Np0	200348	6.5062	1.1800	ALPGEN+PYTHIA
Z $\rightarrow \tau\tau$+bb+Np1	200349	3.2935	1.1800	ALPGEN+PYTHIA
Z $\rightarrow \tau\tau$+bb+Np2	200350	1.2485	1.1800	ALPGEN+PYTHIA
Z $\rightarrow \tau\tau$+bb+Np3incl.	200351	0.61363	1.1800	ALPGEN+PYTHIA
Z $\rightarrow$ ee+cc+Np0	200432	11.763	1.1800	ALPGEN+PYTHIA
Z $\rightarrow$ ee+cc+Np1	200433	7.1280	1.1800	ALPGEN+PYTHIA
Z $\rightarrow$ ee+cc+Np2	200434	3.3603	1.1800	ALPGEN+PYTHIA
Z $\rightarrow$ ee+cc+Np3incl.	200435	1.7106	1.1800	ALPGEN+PYTHIA
Z $\rightarrow \mu\mu$+cc+Np0	200440	11.795	1.1800	ALPGEN+PYTHIA
Z $\rightarrow \mu\mu$+cc+Np1	200441	7.1123	1.1800	ALPGEN+PYTHIA
Z $\rightarrow \mu\mu$+cc+Np2	200442	3.3708	1.1800	ALPGEN+PYTHIA
Z $\rightarrow \mu\mu$+cc+Np3incl.	200443	1.7059	1.1800	ALPGEN+PYTHIA
Z $\rightarrow \tau\tau$+cc+Np0	200448	11.760	1.1800	ALPGEN+PYTHIA
Z $\rightarrow \tau\tau$+cc+Np1	200449	7.1410	1.1800	ALPGEN+PYTHIA
Z $\rightarrow \tau\tau$+cc+Np2	200450	3.3582	1.1800	ALPGEN+PYTHIA
Z $\rightarrow \tau\tau$+cc+Np3incl.	200451	1.7046	1.1800	ALPGEN+PYTHIA

Table A.3: The simulation samples related to Z+jets processes used in the analysis. A GEANT4 simulation is used for all samples unless mentioned otherwise.

Process	DSID	$\sigma(pb)$	$k-$factor	Generator
t-channel top	110090	17.519	1.0501	POWHEG+PYTHIA
t-channel antitop	110091	9.3964	1.0613	POWHEG+PYTHIA
s-channel	110119	1.6424	1.1067	POWHEG+PYTHIA
Wt-channel (incl.)	110140	20.461	1.0933	POWHEG+PYTHIA

Table A.4: The simulation samples related to single top processes used in the analysis. A GEANT4 simulation is used for all samples unless mentioned otherwise.

Process	DSID	$\sigma(pb)$	$k-$factor	Generator
WW	105985	12.416	1.6833	HERWIG
ZZ	105986	0.99244	1.5496	HERWIG
WZ	105987	3.6666	1.9011	HERWIG

Table A.5: The simulation samples related to diboson processes used in the analysis. A GEANT4 simulation is used for all samples unless mentioned otherwise.

APPENDIX B

Signal region optimization

The definition of signal region is based on a set of selection criteria. A set of selections are used without any optimization to define the SR. The following steps were applied:

- Trigger `EF_xe80_tclcw` OR `EF_xe75_tclcw`.
- Number of tracks associated to a primary vertex > 4.
- Reject events with a `LooseBad` jet.
- Reject evens with a reconstructed electron or muon.
- $N_{\text{jets}} > 4$, at least one of which is b-tagged.
- $E_{\text{T}}^{\text{miss}} > 150$ GeV.
- $N_{\tau} = 1$.

These set of selections referred to as `j4inb1intau1ex`, however, is associated with large systematic uncertainties. The total systematic uncertainty is $\sim$15% with the

dominant source of uncertainty being the jet energy scale (JES) ∼7.5%. In addition, this defintion of SR has a large reducible background. To reduce the systematic uncertainties and the reducible background, different selection requirements are studied extensively.

To reduce the JES uncertainty a higher p_{T} cut compared to the nominal, $p_{\mathrm{T}} >$ 25 GeV, on the leading jet is investigated. Subsequent increase in the leading jet p_{T} showed no improvement in the uncertainty. Since the JES uncertainty is lower for jets with high p_{T}, a requirement on the 4th leading jet in p_{T} is also investigated. However, requiring 4th leading jet to be large in p_{T}, not only lowers the available statistics but also shifts the flavor composition of the SR towards gluon domination. Thus the fake factor which is calculated in a region where no requirement on the 4th leading jet p_{T} is applied, overestimates the reducible background. To suppress the reducible background at cut on the sum of p_{T} of all jets, referred to as H_T, is also studied. However, the variable H_T does not provide sufficient discrimination between the signal events and reducible backgrounds. A cut on H_T, although reduces the reducible background but at the same time reduces a significant number of signal events without lowering the total uncertainty.

Alternate selection criteria based on lowering the jet multiplicity are then investigated and the set of selection presented in section 5.4 is found to be optimal to reduce the JES uncertainty. To reduce the reducible background, the W transverse mass, M_{WT}, defined in equation 5.4 is used. Several upper limit on M_{WT} is also studied and a requirement of $M_{WT} < 90$ GeV is found to be optimal. In addition, to increase the available statistics, the exactly one tau requirement is relaxed to at

least one tau requirement. These set of selections are then used to define the SR and is referred to as `j2inb1intau1inMTW90`.

Table B.1 shows the comparison of the number of events and signal significance between the `j4inb1intau1ex` and `j2inb1intau1inMTW90` definitions of the SR. The `j2inb1intau1inMTW90` definition of SR has higher signal significance and lower reducible background compared to the other definition. Table B.2 shows the comparison of the systematic uncertainties from different sources between these two definitions. The JES , JER and total uncertainties are found to be significantly lower compared to the previous definition of the SR. The `j2inb1intau1inMTW90` definition is then taken as a default for the SR.

	Data	$t\bar{t} \to \tau$	$t\bar{t} \to l$	Single top	W+jets	Z+jets	Diboson	Reducible	$S/\sqrt{S+B}$
`j4inb1intau1ex`	3705	2717.96	86.42	255.36	350.76	41.17	1.84	395.08	43.81
`j2inb1intau1inMTW90`	6085	3957.89	95.31	552.15	1381.72	114.11	6.89	290.56	49.47

Table B.1: Number of events observed in data and simulation associated to each definition of the SR. The `j2inb1intau1inMTW90` definition shows a higher signal significance and a lower reducible background.

Systematics ($\Delta\sigma_{t\bar{t}}/\sigma_{t\bar{t}}$) [%]	`j4inb1intau1ex`	`j2inb1intau1inMTW90`
JES	-7.14 / +7.49	-4.87 / +5.15
b-tag eff	-3.20 / +2.99	-3.91 / +3.69
c mistag eff	-0.58 / + 0.58	-1.64 / +1.64
light mistag eff	-0.79 / +0.79	-2.10 / +2.10
MET	-0.32 / +0.53	-0.56 / +0.84
Tau ID, electron Veto	-4.17 / +3.98	-5.24 / +5.00
Tau Energy Scale	-2.34 / +2.29	-2.58 / +2.67
Jet Vertex Fraction	-0.85 / +0.71	-0.22 / +0.19
Jet efficiency	-0.01 / +0.01	-0.08 / +0.08
Jet energy resolution	-4.34 / +4.34	-0.97 / +0.97
Reducible background	-3.66 / +4.48	-2.07 / +2.46
Generator	-4.49 / +4.49	-4.54/ +4.54
ISR/FSR	-9.06 / +9.06	-3.69 / +3.69
Total Systematic Unc.	-14.85 / +15.13	-11.10 / + 11.16

Table B.2: Systematic uncertainties associated to different sources for each definition of the SR. The `j2inb1intau1inMTW90` definition shows a overall reduction in total uncertainty.

APPENDIX C

Signal region selection efficiencies and yields

The selection efficiencies for each cut of the SR is shown is table C.1, whereas, the yield at each cut is listed in Table C.2 for combined $\tau_{\text{1-prong}}$ and $\tau_{\text{3-prong}}$ candidates.

	Cut	Data	$t\bar{t} \to \tau$	$t\bar{t} \to l$	Single top	W+jets	Z+jets	Diboson	prompt $t\bar{t}$	prompt other	Fakes
C0	INITIAL	-	-	-	-	-	-	-	-	-	-
C1	GRL	0.9576	1.0000	1.0000	1.0000	1.0000	1.0000	1.0000	1.0000	1.0000	0.9576
C2	HFOR/LAr	0.9973	1.0000	1.0000	1.0000	1.0000	1.0000	1.0000	1.0000	1.0000	0.9973
C3	TRIGGER	0.0452	0.2437	0.2437	0.1163	0.0093	0.0064	0.0821	0.2437	0.0092	0.0452
C4	NPV ≥ 4	0.9986	0.9996	0.9996	0.9986	0.9976	0.9986	0.9922	0.9996	0.9976	0.9986
C5	E-Mu OLR	1.0000	1.0000	1.0000	1.0000	1.0000	0.9999	0.9999	1.0000	1.0000	1.0000
C6	JET CLEAN	0.9474	0.9986	0.9986	0.9985	0.9987	0.9978	0.9980	0.9986	0.9987	0.9474
C7	LEP VETO	0.9304	0.5473	0.5473	0.5994	0.6251	0.2397	0.3848	0.5473	0.6004	0.9304
C8	≥ 2 JETS	0.5927	0.9805	0.9805	0.8430	0.5594	0.6673	0.6957	0.9805	0.5669	0.5927
C9	MET > 120 GeV	0.1389	0.5568	0.5568	0.4940	0.4878	0.3346	0.4871	0.5568	0.4837	0.1389
C10	$\geq$ 1noIDTAU	0.4247	0.5901	0.5901	0.4960	0.4465	0.5970	0.4722	0.5901	0.4507	0.4247
C11	HFOR	1.0000	1.0000	1.0000	1.0000	0.7748	0.7996	1.0000	1.0000	0.7825	1.0000
C12	≥ 2 JETS (after OLR)	0.9794	0.9965	0.9965	0.9863	0.9465	0.8960	0.9838	0.9957	0.9548	0.9758
C13	≥ 1 BJET 70% WP	0.2640	0.7728	0.7728	0.6680	0.0749	0.0939	0.1300	0.7741	0.1036	0.2660
C14	MET > 150 GeV	0.4038	0.5275	0.5275	0.5029	0.5145	0.4807	0.5212	0.5276	0.5104	0.4054
C15	$\geq$ 1idTau	0.0617	0.1052	0.1052	0.1240	0.0974	0.2545	0.0455	0.0225	0.0162	0.0150
C16	Truth Match	1.0000	0.8895	0.0303	0.9478	0.9579	0.9792	0.8269	0.6401	0.7190	1.0000
C27	MWT < 90	0.8367	0.8756	0.6191	0.9309	0.9561	0.9597	0.9241	0.8097	0.9178	0.6154

Table C.1: Relative efficiency at each step of the signal region selection for all processes. Here, Fakes represent the reducible background estimated in data. Fakes include contributions from prompt events which are subtracted. The prompt $t\bar{t}$ represents prompt $t\bar{t} \to \tau, e, \mu$ events and prompt other represents prompt single top, W+jets, Z+jets, diboson $\to \tau, e, \mu$ events.

	Cut	Data	$t\bar{t} \to \tau$	$t\bar{t} \to l$	Single top	W+jets	Z+jets	Diboson	prompt $t\bar{t}$	prompt other	Fakes
C0	INITIAL	848879104.00	2771946.50	2771946.50	1060926.48	778530252.44	72031149.15	593645.04	2771946.50	852215973.11	848879104.00
C1	GRL	812901568.00	2771946.50	2771946.50	1060926.48	778530252.44	72031149.15	593645.04	2771946.50	852215973.11	812901568.00
C2	HFOR/LAr	810730240.00	2771946.50	2771946.50	1060926.48	778530252.44	72031149.15	593645.04	2771946.50	852215973.11	810730240.00
C3	TRIGGER	36649728.00	675444.69	675444.69	123353.51	7220556.11	463884.60	48747.01	675444.69	7856541.23	36649728.00
C4	NPV ≥ 4	36597376.00	675150.63	675150.63	123185.98	7203070.44	463241.08	48365.48	675150.63	7837862.98	36597376.00
C5	E-Mu OLR	36597224.00	675129.81	675129.81	123182.59	7202896.27	463189.11	48362.84	675129.81	7837630.80	36597224.00
C6	JET CLEAN	34671544.00	674172.13	674172.13	122998.99	7193756.73	462182.58	48267.45	674172.13	7827205.76	34671544.00
C7	LEP VETO	32257620.00	368969.00	368969.00	73723.13	4496515.38	110772.04	18573.72	368969.00	4699584.27	32257620.00
C8	≥ 2 JETS	19118216.00	361776.94	361776.94	62148.11	2515378.39	73917.36	12921.43	361776.94	2664365.29	19118216.00
C9	MET > 120 GeV	2656152.00	201423.27	201423.27	30699.26	1227045.66	24729.50	6294.66	201423.27	1288769.08	2656152.00
C10	$\geq$ 1noIDTAU	1128136.00	118860.11	118860.11	15227.78	547921.23	14764.20	2972.29	118860.11	580885.51	1128136.00
C11	HFOR	1128136.00	118856.98	118856.98	15227.78	424541.42	11804.76	2972.29	118856.98	454546.26	1128136.00
C12	≥ 2 JETS (after OLR)	1104911.00	118441.90	118441.90	15019.76	401817.47	10576.86	2924.04	118340.47	434018.57	1100824.00
C13	≥ 1 BJET 70% WP	291677.00	91530.79	91530.79	10033.38	30102.85	992.77	380.19	91602.36	44959.64	292863.00
C14	MET > 150 GeV	117787.00	48283.41	48283.41	5045.56	15487.19	477.18	198.15	48328.80	22948.09	118718.00
C15	$\geq$ 1idTau	7273.00	5081.42	5081.42	625.78	1508.69	121.42	9.02	1087.50	371.16	1786.14
C16	Truth Match	7273.00	4520.06	153.96	593.12	1445.23	118.90	7.46	696.06	266.88	1786.14
C17	MWT < 90	6085.00	3957.89	95.31	552.15	1381.72	114.11	6.89	563.62	244.95	1099.13

Table C.2: Number of events at each step of the signal region selection for all processes. Here, Fakes represent the reducible background estimated in data. Fakes include contributions from prompt events which are subtracted. The prompt $t\bar{t}$ represents prompt $t\bar{t} \to \tau, e, \mu$ events and prompt other represents prompt single top, W+jets, Z+jets, diboson $\to \tau, e, \mu$ events.

APPENDIX D

Systematic uncertainties for $\tau_{\text{1-prong}}$ and $\tau_{\text{3-prong}}$ candidate

Different sources of systematic uncertainties are explained in section 5.8 where the uncertainties related to the combined $\tau_{\text{1-prong}}$ and $\tau_{\text{3-prong}}$ channel is presented. Here, simply the estimated uncertainties for each sources are presented for $\tau_{\text{1-prong}}$ only and $\tau_{\text{3-prong}}$ only channels without any explanations.

D.1 Tau energy scale

Systematics [%]	$\Delta\varepsilon_{t\bar{t}}/\varepsilon_{t\bar{t}}$	$\Delta N_{\text{obs}}/N_{\text{obs}}$	$\Delta\sigma_{t\bar{t}}/\sigma_{t\bar{t}}$
Tau energy scale	-1.54 / +1.45	-0.95 / +0.82	-3.06 / +2.77

Table D.1: Relative systematic uncertainties on $t\bar{t}$ production cross section associated to tau energy scale with $\tau_{\text{1-prong}}$ candidate in the final state. $\Delta\varepsilon_{t\bar{t}}$ is the uncertainty on efficiency, ΔN_{obs} is the uncertainty on the number of observed events due to prompt subtraction in the background estimation, and the $\Delta\sigma_{t\bar{t}}$ is the uncertainty on the final cross section.

Systematics [%]	$\Delta\varepsilon_{t\bar{t}}/\varepsilon_{t\bar{t}}$	$\Delta N_{obs}/N_{obs}$	$\Delta\sigma_{t\bar{t}}/\sigma_{t\bar{t}}$
Tau energy scale	-0.65 / +1.37	-0.03 / +0.82	-1.18 / +2.40

Table D.2: Relative systematic uncertainties on $t\bar{t}$ production cross section associated to tau energy scale for $\tau_{\text{3-prong}}$ in the final state. $\Delta\varepsilon_{t\bar{t}}$ is the uncertainty on efficiency, ΔN_{obs} is the uncertainty on the number of observed events due to prompt subtraction in the background estimation, and the $\Delta\sigma_{t\bar{t}}$ is the uncertainty on the final cross section.

D.2 Tau identification and tau electron veto

Systematics [%]	$\Delta\varepsilon_{t\bar{t}}/\varepsilon_{t\bar{t}}$	$\Delta N_{obs}/N_{obs}$	$\Delta\sigma_{t\bar{t}}/\sigma_{t\bar{t}}$
Tau ID scale factor statistics	-1.38 / +1.38	-0.67 / +0.67	-2.72 / +2.63
Tau ID scale factor systematics	-1.93 / +1.93	-0.86 / +0.86	-3.83 / +3.65
Tau electron veto	-0.05 / +0.05	-0.08 / +0.08	-0.09 / +0.09
Total, Tau ID , eVeto	-2.37 / +2.37	-1.10 / +1.10	-4.69 / +4.50

Table D.3: Relative systematic uncertainties on $t\bar{t}$ production cross section associated to tau identification and tau electron veto for $\tau_{\text{1-prong}}$ in the final state. $\Delta\varepsilon_{t\bar{t}}$ is the uncertainty on efficiency, ΔN_{obs} is the uncertainty on the number of observed events due to prompt subtraction in the background estimation, and the $\Delta\sigma_{t\bar{t}}$ is the uncertainty on the final cross section.

Systematics [%]	$\Delta\varepsilon_{t\bar{t}}/\varepsilon_{t\bar{t}}$	$\Delta N_{obs}/N_{obs}$	$\Delta\sigma_{t\bar{t}}/\sigma_{t\bar{t}}$
Tau ID scale factor statistics	-2.54 / +2.54	-1.05 / +1.05	-4.68 / +4.40
Tau ID scale factor systematics	-2.91 / +2.91	-1.11 / +1.11	-5.37 / +5.01
Tau electron veto	0.00 / 0.00	0.00 / 0.00	0.00 / 0.00
Total, Tau ID , eVeto	-3.86 / +3.86	-1.53 / +1.53	-7.12 / +6.66

Table D.4: Relative systematic uncertainties on $t\bar{t}$ production cross section associated to tau identification and tau electron veto for $\tau_{\text{3-prong}}$ in the final state. $\Delta\varepsilon_{t\bar{t}}$ is the uncertainty on efficiency, ΔN_{obs} is the uncertainty on the number of observed events due to prompt subtraction in the background estimation, and the $\Delta\sigma_{t\bar{t}}$ is the uncertainty on the final cross section.

D.3 Jet energy scale

Systematics [%]	$\Delta\varepsilon_{t\bar{t}}/\varepsilon_{t\bar{t}}$	$\Delta N_{obs}/N_{obs}$	$\Delta\sigma_{t\bar{t}}/\sigma_{t\bar{t}}$
BJesUnc	-0.50 / +0.50	-0.17 / +0.10	-0.98 / +0.94
EtaIntercalibrationModel	-0.43 / +0.55	-0.16 / +0.28	-0.83 / +1.06
EtaIntercalibrationTotalStat	-0.35 / +0.44	-0.11 / +0.28	-0.68 / +0.86
JesEffectiveDet1	-0.92 / +1.09	-0.24 / +0.55	-1.78 / +2.09
JesEffectiveDet2	-0.05 / +0.07	-0.01 / +0.07	-0.09 / +0.15
JesEffectiveDet3	-0.10 / +0.08	-0.03 / +0.02	-0.19 / +0.14
JesEffectiveMix1	-0.63 / +0.72	-0.14 / +0.28	-1.22 / +1.36
JesEffectiveMix2	-0.12 / +0.04	-0.08 / +0.03	-0.23 / +0.07
JesEffectiveMix3	-0.26 / +0.24	-0.16 / +0.10	-0.51 / +0.46
JesEffectiveMix4	-0.04 / +0.02	-0.01 / +0.01	-0.08 / +0.04
JesEffectiveModel1	-1.05 / +1.24	-0.37 / +0.70	-2.03 / +2.38
JesEffectiveModel2	-0.15 / +0.14	-0.05 / +0.02	-0.30 / +0.26
JesEffectiveModel3	-0.06 / +0.06	-0.03 / +0.01	-0.11 / +0.11
JesEffectiveModel4	-0.20 / +0.22	-0.11 / +0.11	-0.39 / +0.42
JesEffectiveStat1	-0.26 / +0.22	-0.24 / +0.16	-0.51 / +0.42
JesEffectiveStat2	-0.01 / +0.04	-0.05 / +0.01	-0.01 / +0.07
JesEffectiveStat3	-0.06 / +0.10	-0.08 / +0.03	-0.10 / +0.19
JesEffectiveStat4	-0.30 / +0.32	-0.15 / +0.13	-0.58 / +0.61
Pileup OffsetMu	-0.13 / +0.09	-0.14 / +0.07	-0.25 / +0.17
Pileup OffsetNPV	-0.08 / +0.12	-0.13 / +0.00	-0.14 / +0.22
Pileup Pt	-0.09 / +0.10	-0.06 / +0.07	-0.17 / +0.19
Pileup Rho	-0.83 / +0.83	-0.38 / +0.39	-1.61 / +1.59
Punch Through	-0.03 / +0.07	-0.04 / +0.08	-0.06 / +0.14
Single Part	-0.00 / +0.00	-0.00 / +0.00	-0.00 / +0.00
Flavor comp	-0.79 / +0.94	-0.52 / +0.84	-1.55 / +1.85
Flavor response	-0.78 / +0.84	-0.42 / +0.47	-1.51 / +1.65
Total JES	-2.28 / +2.57	-1.03 / +1.48	-4.41 / +4.96

Table D.5: Relative systematic uncertainties on $t\bar{t}$ production cross section associated to jet energy scale for $\tau_{\text{1-prong}}$ in the final state. $\Delta\varepsilon_{t\bar{t}}$ is the uncertainty on efficiency, ΔN_{obs} is the uncertainty on the number of observed events due to prompt subtraction in the background estimation, and the $\Delta\sigma_{t\bar{t}}$ is the uncertainty on the final cross section.

Systematics [%]	$\Delta\varepsilon_{t\bar{t}}/\varepsilon_{t\bar{t}}$	$\Delta N_{obs}/N_{obs}$	$\Delta\sigma_{t\bar{t}}/\sigma_{t\bar{t}}$
BJesUnc	-0.65 / +0.51	-0.41 / +0.05	-1.17 / +0.91
EtaIntercalibrationModel	-0.69 / +0.61	-0.48 / +0.21	-1.23 / +1.07
EtaIntercalibrationTotalStat	-0.83 / +0.57	-0.76 / +0.31	-1.48 / +1.01
JesEffectiveDet1	-1.25 / +1.58	-0.66 / +1.06	-2.24 / +2.75
JesEffectiveDet2	-0.05 / +0.18	-0.03 / +0.20	-0.09 / +0.32
JesEffectiveDet3	-0.15 / +0.10	-0.09 / +0.00	-0.26 / +0.18
JesEffectiveMix1	-1.09 / +0.89	-0.81 / +0.38	-1.94 / +1.57
JesEffectiveMix2	-0.08 / +0.05	-0.02 / +0.17	-0.14 / +0.09
JesEffectiveMix3	-0.22 / +0.28	-0.01 / +0.17	-0.39 / +0.50
JesEffectiveMix4	-0.11 / +0.14	-0.11 / +0.12	-0.19 / +0.24
JesEffectiveModel1	-1.51 / +1.46	-0.85 / +0.57	-2.73 / +2.57
JesEffectiveModel2	-0.26 / +0.34	-0.16 / +0.24	-0.46 / +0.60
JesEffectiveModel3	-0.09 / +0.02	-0.01 / +0.02	-0.16 / +0.03
JesEffectiveModel4	-0.27 / +0.28	-0.16 / +0.12	-0.48 / +0.51
JesEffectiveStat1	-0.51 / +0.23	-0.57 / +0.01	-0.90 / +0.40
JesEffectiveStat2	-0.10 / +0.05	-0.11 / +0.02	-0.18 / +0.09
JesEffectiveStat3	-0.15 / +0.05	-0.02 / +0.05	-0.27 / +0.09
JesEffectiveStat4	-0.37 / +0.48	-0.15 / +0.29	-0.65 / +0.85
Pileup OffsetMu	-0.08 / +0.17	-0.04 / +0.12	-0.14 / +0.30
Pileup OffsetNPV	-0.13 / +0.30	-0.12 / +0.19	-0.24 / +0.54
Pileup Pt	-0.04 / +0.08	-0.01 / +0.08	-0.08 / +0.15
Pileup Rho	-1.25 / +1.19	-0.91 / +0.66	-2.24 / +2.08
Punch Through	-0.03 / +0.07	-0.05 / +0.11	-0.05 / +0.13
Single Part	-0.00 / +0.00	-0.00 / +0.00	-0.00 / +0.00
Flavor comp	-1.30 / +1.21	-1.14 / +0.77	-2.33 / +2.13
Flavor response	-1.39 / +1.07	-1.01 / +0.73	-2.44 / +1.91
Total JES	-3.54/ +3.34	-2.53 / +1.91	-6.31 / +5.88

Table D.6: Relative systematic uncertainties on $t\bar{t}$ production cross section associated to jet energy scale for $\tau_{\text{3-prong}}$ in the final state. $\Delta\varepsilon_{t\bar{t}}$ is the uncertainty on efficiency, ΔN_{obs} is the uncertainty on the number of observed events due to prompt subtraction in the background estimation, and the $\Delta\sigma_{t\bar{t}}$ is the uncertainty on the final cross section.

D.4 b-tagging efficiency

Systematics [%]	$\Delta\varepsilon_{t\bar{t}}/\varepsilon_{t\bar{t}}$	$\Delta N_{obs}/N_{obs}$	$\Delta\sigma_{t\bar{t}}/\sigma_{t\bar{t}}$
BTAGSF BREAK0	-0.03 / +0.02	-0.02 / +0.02	-0.05 / +0.05
BTAGSF BREAK1	-0.02 / +0.02	-0.00 / +0.00	-0.04 / +0.04
BTAGSF BREAK2	-0.02 / +0.02	-0.01 / +0.01	-0.04 / +0.03
BTAGSF BREAK3	-0.00 / +0.00	-0.01 / +0.01	-0.00 / +0.00
BTAGSF BREAK4	-0.00 / +0.00	-0.02 / +0.02	-0.00 / +0.00
BTAGSF BREAK5	-0.17 / +0.17	-0.04 / +0.04	-0.32 / +0.32
BTAGSF BREAK6	-0.18 / +0.18	-0.08 / +0.08	-0.35 / +0.35
BTAGSF BREAK7	-0.90 / +0.92	-0.30 / +0.30	-1.71 / +1.79
BTAGSF BREAK8	-1.80 / +1.73	-0.46 / +0.45	-3.52 / +3.22
CTAUTAGSF BREAK0	-0.05 / +0.05	-0.06 / +0.06	-0.10 / +0.11
CTAUTAGSF BREAK1	-0.12 / +0.12	-0.15 / +0.15	-0.25 / +0.25
CTAUTAGSF BREAK2	-0.50 / +0.50	-0.81 / +0.81	-1.04 / +1.04
CTAUTAGSF BREAK3	-0.68 / +0.68	-1.08 / +1.08	-1.42 / +1.41
MISTAGSF BREAK0	-0.00 / +0.00	-0.01 / +0.01	-0.01 / +0.01
MISTAGSF BREAK1	-0.00 / +0.00	-0.00 / +0.00	-0.00 / +0.00
MISTAGSF BREAK2	-0.00 / +0.00	-0.01 / +0.00	-0.01 / +0.01
MISTAGSF BREAK3	-0.00 / +0.00	-0.00 / +0.00	-0.00 / +0.00
MISTAGSF BREAK4	-0.02 / +0.01	-0.02 / +0.02	-0.03 / +0.03
MISTAGSF BREAK5	-0.02 / +0.02	-0.04 / +0.04	-0.05 / +0.05
MISTAGSF BREAK6	-0.04 / +0.04	-0.06 / +0.06	-0.08 / +0.08
MISTAGSF BREAK7	-0.04 / +0.04	-0.07 / +0.07	-0.08 / +0.08
MISTAGSF BREAK8	-0.05 / +0.05	-0.07 / +0.07	-0.10 / +0.10
MISTAGSF BREAK9	-0.41 / +0.42	-0.70 / +0.70	-0.87 / +0.87
MISTAGSF BREAK10	-0.10 / +0.10	-0.13 / +0.13	-0.20 / +0.20
MISTAGSF BREAK11	-0.93 / +0.93	-1.51 / +1.52	-1.94 / +1.95
Total b tag eff	-2.03 / +2.00	-0.55 / +0.55	-3.94 / +3.72
Total c mistag	-0.85 / +0.85	-1.36 / +1.36	-1.78 / + 1.78
Total light mistag	-1.03 / +1.03	-1.68 / +1.68	-2.14 / +2.15

Table D.7: Relative systematic uncertainties on $t\bar{t}$ production cross section (τ is reconstructed using 1 associated track) associated to b tagging efficiency. $\Delta\varepsilon_{t\bar{t}}$ is the uncertainty on efficiency, ΔN_{obs} is the uncertainty on the number of observed events due to prompt subtraction in the background estimation, and the $\Delta\sigma_{t\bar{t}}$ is the uncertainty on the final cross section.

Systematics [%]	$\Delta\varepsilon_{t\bar{t}}/\varepsilon_{t\bar{t}}$	$\Delta N_{obs}/N_{obs}$	$\Delta\sigma_{t\bar{t}}/\sigma_{t\bar{t}}$
BTAGSF BREAK0	-0.02 / +0.01	-0.00 / +0.00	-0.03 / +0.03
BTAGSF BREAK1	-0.04 / +0.04	-0.02 / +0.02	-0.06 / +0.06
BTAGSF BREAK2	-0.00 / +0.00	-0.02 / +0.02	-0.01 / +0.01
BTAGSF BREAK3	-0.01 / +0.01	-0.02 / +0.02	-0.02 / +0.02
BTAGSF BREAK4	-0.01 / +0.01	-0.04 / +0.04	-0.02 / +0.02
BTAGSF BREAK5	-0.16 / +0.16	-0.00 / +0.00	-0.29 / +0.29
BTAGSF BREAK6	-0.24 / +0.24	-0.18 / +0.18	-0.42 / +0.42
BTAGSF BREAK7	-0.88 / +0.90	-0.24 / +0.25	-1.55 / +1.64
BTAGSF BREAK8	-1.92 / +1.85	-0.42 / +0.43	-3.52 / +3.23
CTAUTAGSF BREAK0	-0.07 / +0.07	-0.07 / +0.07	-0.13 / +0.13
CTAUTAGSF BREAK1	-0.15 / +0.15	-0.18 / +0.18	-0.26 / +0.26
CTAUTAGSF BREAK2	-0.38 / +0.38	-0.53 / +0.53	-0.66 / +0.67
CTAUTAGSF BREAK3	-0.61 / +0.61	-0.79 / +0.79	-1.07 / +1.06
MISTAGSF BREAK0	-0.00 / +0.00	-0.00 / +0.00	-0.00 / +0.00
MISTAGSF BREAK1	-0.00 / +0.00	-0.00 / +0.00	-0.01 / +0.00
MISTAGSF BREAK2	-0.01 / +0.01	-0.01 / +0.01	-0.01 / +0.01
MISTAGSF BREAK3	-0.00 / +0.00	-0.00 / +0.00	-0.00 / +0.00
MISTAGSF BREAK4	-0.02 / +0.01	-0.02 / +0.02	-0.03 / +0.03
MISTAGSF BREAK5	-0.01 / +0.01	-0.01 / +0.01	-0.01 / +0.01
MISTAGSF BREAK6	-0.02 / +0.02	-0.02 / +0.02	-0.03 / +0.03
MISTAGSF BREAK7	-0.03 / +0.03	-0.04 / +0.04	-0.05 / +0.05
MISTAGSF BREAK8	-0.06 / +0.06	-0.09 / +0.09	-0.11 / +0.11
MISTAGSF BREAK9	-0.30 / +0.30	-0.42 / +0.42	-0.52 / +0.52
MISTAGSF BREAK10	-0.20 / +0.20	-0.31 / +0.31	-0.36 / +0.35
MISTAGSF BREAK11	-1.11 / +1.08	-1.61 / +1.57	-1.93 / +1.89
Total b tag eff	-2.13 / +2.08	-0.52 / +0.53	-3.88 / +3.66
Total c mistag	-0.74 / +0.74	-0.97 / +0.97	-1.29 / +1.29
Total light mistag	-1.17 / +1.15	-1.70 / +1.66	-2.04 / +2.00

Table D.8: Relative systematic uncertainties on $t\bar{t}$ production cross section (τ is reconstructed using 3 associated track) associated to b tagging efficiency. $\Delta\varepsilon_{t\bar{t}}$ is the uncertainty on efficiency, ΔN_{obs} is the uncertainty on the number of observed events due to prompt subtraction in the background estimation, and the $\Delta\sigma_{t\bar{t}}$ is the uncertainty on the final cross section.

D.5 Jet energy resolution

Systematics [%]	$\Delta\varepsilon_{t\bar{t}}/\varepsilon_{t\bar{t}}$	$\Delta N_{obs}/N_{obs}$	$\Delta\sigma_{t\bar{t}}/\sigma_{t\bar{t}}$
JER	$\pm$ 0.21	$\pm$ 1.02	$\pm$ 0.26

Table D.9: Relative systematic uncertainties on $t\bar{t}$ production cross section (τ is reconstructed using 1 associated track) associated to jet energy resolution. $\Delta\varepsilon_{t\bar{t}}$ is the uncertainty on efficiency, ΔN_{obs} is the uncertainty on the number of observed events due to prompt subtraction in the background estimation, and the $\Delta\sigma_{t\bar{t}}$ is the uncertainty on the final cross section.

Systematics [%]	$\Delta\varepsilon_{t\bar{t}}/\varepsilon_{t\bar{t}}$	$\Delta N_{obs}/N_{obs}$	$\Delta\sigma_{t\bar{t}}/\sigma_{t\bar{t}}$
JER	$\pm$ 1.78	$\pm$ 1.35	$\pm$ 3.11

Table D.10: Relative systematic uncertainties on $t\bar{t}$ production cross section (τ is reconstructed using 3 associated track) associated to jet energy resolution. $\Delta\varepsilon_{t\bar{t}}$ is the uncertainty on efficiency, ΔN_{obs} is the uncertainty on the number of observed events due to prompt subtraction in the background estimation, and the $\Delta\sigma_{t\bar{t}}$ is the uncertainty on the final cross section.

D.6 Jet reconstruction efficiency

Systematics [%]	$\Delta\varepsilon_{t\bar{t}}/\varepsilon_{t\bar{t}}$	$\Delta N_{obs}/N_{obs}$	$\Delta\sigma_{t\bar{t}}/\sigma_{t\bar{t}}$
JetEff	$\pm$ 0.03	$\pm$ 0.05	$\pm$ 0.07

Table D.11: Relative systematic uncertainties on $t\bar{t}$ production cross section (τ is reconstructed using 1 associated track) associated to jet reconstruction efficiency. $\Delta\varepsilon_{t\bar{t}}$ is the uncertainty on efficiency, ΔN_{obs} is the uncertainty on the number of observed events due to prompt subtraction in the background estimation, and the $\Delta\sigma_{t\bar{t}}$ is the uncertainty on the final cross section.

Systematics [%]	$\Delta\varepsilon_{t\bar{t}}/\varepsilon_{t\bar{t}}$	$\Delta N_{obs}/N_{obs}$	$\Delta\sigma_{t\bar{t}}/\sigma_{t\bar{t}}$
JetEff	± 0.07	± 0.04	± 0.13

Table D.12: Relative systematic uncertainties on $t\bar{t}$ production cross section (τ is reconstructed using 3 associated track) associated to jet reconstruction efficiency. $\Delta\varepsilon_{t\bar{t}}$ is the uncertainty on efficiency, ΔN_{obs} is the uncertainty on the number of observed events due to prompt subtraction in the background estimation, and the $\Delta\sigma_{t\bar{t}}$ is the uncertainty on the final cross section.

D.7 Pileup jet rejection efficiency

Systematics [%]	$\Delta\varepsilon_{t\bar{t}}/\varepsilon_{t\bar{t}}$	$\Delta N_{obs}/N_{obs}$	$\Delta\sigma_{t\bar{t}}/\sigma_{t\bar{t}}$
JVF	-0.11 / +0.07	-0.12 / +0.01	-0.23 / +0.14

Table D.13: Relative systematic uncertainties on $t\bar{t}$ production cross section (τ is reconstructed using 1 associated track) associated to jet vertex fraction efficiency. $\Delta\varepsilon_{t\bar{t}}$ is the uncertainty on efficiency, ΔN_{obs} is the uncertainty on the number of observed events due to prompt subtraction in the background estimation, and the $\Delta\sigma_{t\bar{t}}$ is the uncertainty on the final cross section.

Systematics [%]	$\Delta\varepsilon_{t\bar{t}}/\varepsilon_{t\bar{t}}$	$\Delta N_{obs}/N_{obs}$	$\Delta\sigma_{t\bar{t}}/\sigma_{t\bar{t}}$
JVF	+0.11 / -0.18	-0.05 / -0.16	+0.20 / -0.32

Table D.14: Relative systematic uncertainties on $t\bar{t}$ production cross section (τ is reconstructed using 3 associated track) associated to jet vertex fraction efficiency. $\Delta\varepsilon_{t\bar{t}}$ is the uncertainty on efficiency, ΔN_{obs} is the uncertainty on the number of observed events due to prompt subtraction in the background estimation, and the $\Delta\sigma_{t\bar{t}}$ is the uncertainty on the final cross section.

D.8 $E_{\mathrm{T}}^{\mathrm{miss}}$ soft-term resolution and scale

Systematics [%]	$\Delta\varepsilon_{t\bar{t}}/\varepsilon_{t\bar{t}}$	$\Delta\mathrm{N_{obs}}/\mathrm{N_{obs}}$	$\Delta\sigma_{t\bar{t}}/\sigma_{t\bar{t}}$
MET resolution soft	-0.15 / +0.12	-0.31 / +0.05	-0.32 / +0.24
MET scale soft	-0.29 / +0.40	-0.14 / +0.31	-0.56 / +0.78
Total, MET	-0.14 / +0.18	-0.06 / +0.05	-0.56 / +0.81

Table D.15: Relative systematic uncertainties on $t\bar{t}$ production cross section (τ is reconstructed using 1 associated track) associated to the missing transverse energy. $\Delta\varepsilon_{t\bar{t}}$ is the uncertainty on efficiency, ΔN_{obs} is the uncertainty on the number of observed events due to prompt subtraction in the background estimation, and the $\Delta\sigma_{t\bar{t}}$ is the uncertainty on the final cross section.

Systematics [%]	$\Delta\varepsilon_{t\bar{t}}/\varepsilon_{t\bar{t}}$	$\Delta\mathrm{N_{obs}}/\mathrm{N_{obs}}$	$\Delta\sigma_{t\bar{t}}/\sigma_{t\bar{t}}$
MET resolution soft	-0.28 / +0.25	-0.44 / +0.14	-0.49 / +0.46
MET scale soft	-0.30 / +0.48	-0.26 / +0.28	-0.52 / +0.85
Total, MET	-0.62 / +0.33	-0.35 / +0.14	-0.62 / 0.33

Table D.16: Relative systematic uncertainties on $t\bar{t}$ production cross section (τ is reconstructed using 3 associated track) associated to the missing transverse energy. $\Delta\varepsilon_{t\bar{t}}$ is the uncertainty on efficiency, ΔN_{obs} is the uncertainty on the number of observed events due to prompt subtraction in the background estimation, and the $\Delta\sigma_{t\bar{t}}$ is the uncertainty on the final cross section.

D.9 MC generator and hadronization model

Systematics [%]	$\Delta\varepsilon_{t\bar{t}}/\varepsilon_{t\bar{t}}$	$\Delta\mathrm{N_{obs}}/\mathrm{N_{obs}}$	$\Delta\sigma_{t\bar{t}}/\sigma_{t\bar{t}}$
POWHEG+HERWIG vs MC@NLO	± 3.20	± 1.43	± 4.12
POWHEG+PYTHIA vs POWHEG+HERWIG	± 3.22	±0.85	± 4.34

Table D.17: Relative systematic uncertainties on $t\bar{t}$ production cross section (τ is reconstructed using 1 associated track) associated to theMC generator and hadronization model. $\Delta\varepsilon_{t\bar{t}}$ is the uncertainty on efficiency, ΔN_{obs} is the uncertainty on the number of observed events due to prompt subtraction in the background estimation, and the $\Delta\sigma_{t\bar{t}}$ is the uncertainty on the final cross section.

Systematics [%]	$\Delta\varepsilon_{t\bar{t}}/\varepsilon_{t\bar{t}}$	$\Delta N_{obs}/N_{obs}$	$\Delta\sigma_{t\bar{t}}/\sigma_{t\bar{t}}$
POWHEG+HERWIG vs MC@NLO	± 2.48	± 0.57	± 6.44
POWHEG+PYTHIA vs POWHEG+HERWIG	± 2.50	±0.45	± 6.04

Table D.18: Relative systematic uncertainties on $t\bar{t}$ production cross section (τ is reconstructed using 3 associated tracks) associated to the MC generator and hadronization model. $\Delta\varepsilon_{t\bar{t}}$ is the uncertainty on efficiency, ΔN_{obs} is the uncertainty on the number of observed events due to prompt subtraction in the background estimation, and the $\Delta\sigma_{t\bar{t}}$ is the uncertainty on the final cross section.

D.10 Initial and final state radiation

Systematics [%]	$\Delta\varepsilon_{t\bar{t}}/\varepsilon_{t\bar{t}}$	$\Delta N_{obs}/N_{obs}$	$\Delta\sigma_{t\bar{t}}/\sigma_{t\bar{t}}$
radLow vs Nominal	+3.28	0.12	-5.98
radHigh vs Nominal	-0.77	0.13	+1.52
radLow vs radHigh (symmetric)	± 2.00	± 0.01	± 3.83

Table D.19: Relative systematic uncertainties on $t\bar{t}$ production cross section (τ is reconstructed using 1 associated track) associated to initial and final state radiation. $\Delta\varepsilon_{t\bar{t}}$ is the uncertainty on efficiency, ΔN_{obs} is the uncertainty on the number of observed events due to prompt subtraction in the background estimation, and the $\Delta\sigma_{t\bar{t}}$ is the uncertainty on the final cross section.

Systematics [%]	$\Delta\varepsilon_{t\bar{t}}/\varepsilon_{t\bar{t}}$	$\Delta N_{obs}/N_{obs}$	$\Delta\sigma_{t\bar{t}}/\sigma_{t\bar{t}}$
radLow vs Nominal	+4.83	-0.53	-8.44
radHigh vs Nominal	+1.02	-0.33	-1.91
radLow vs radHigh (symmetric)	± 1.85	± 0.10	± 3.44

Table D.20: Relative systematic uncertainties on $t\bar{t}$ production cross section (τ is reconstructed using 3 associated track) associated to initial and final state radiation. $\Delta\varepsilon_{t\bar{t}}$ is the uncertainty on efficiency, ΔN_{obs} is the uncertainty on the number of observed events due to prompt subtraction in the background estimation, and the $\Delta\sigma_{t\bar{t}}$ is the uncertainty on the final cross section.

D.11 Fake background estimation

Systematics [%]	$\Delta\varepsilon_{t\bar{t}}/\varepsilon_{t\bar{t}}$	$\Delta N_{obs}/N_{obs}$	$\Delta\sigma_{t\bar{t}}/\sigma_{t\bar{t}}$
Reducible	-0.77 / +0.83	-1.40 / +1.51	-2.05 / +2.46

Table D.21: Relative systematic uncertainties on $t\bar{t}$ production cross section (τ is reconstructed using 1 associated track) associated to the estimation of jet misidentified as tau. $\Delta\varepsilon_{t\bar{t}}$ is the uncertainty on efficiency, ΔN_{obs} is the uncertainty on the number of observed events due to prompt subtraction in the background estimation, and the $\Delta\sigma_{t\bar{t}}$ is the uncertainty on the final cross section.

Systematics [%]	$\Delta\varepsilon_{t\bar{t}}/\varepsilon_{t\bar{t}}$	$\Delta N_{obs}/N_{obs}$	$\Delta\sigma_{t\bar{t}}/\sigma_{t\bar{t}}$
Reducible	-1.30 / +1.38	-2.05 / +2.18	-2.11 / +2.37

Table D.22: Relative systematic uncertainties on $t\bar{t}$ production cross section (τ is reconstructed using 3 associated track) associated to tau energy scale. $\Delta\varepsilon_{t\bar{t}}$ is the uncertainty on efficiency, ΔN_{obs} is the uncertainty on the number of observed events due to prompt subtraction in the background estimation, and the $\Delta\sigma_{t\bar{t}}$ is the uncertainty on the final cross section.